Development and characterization of a scintillation dosimeter dedicated to CBCT in image-guided radiotherapy and exploratory study of the CBCT doses effect in DNA repair

Christian Popotte

THESE de DOCTORAT DE L'UNIVERSITE CLAUDE BERNARD LYON 1

Ecole Doctorale N° 205
(EDISS :
Ecole Doctorale Interdisciplinaire Sciences et Santé)

Spécialité de doctorat : Ingénierie pour le vivant
Discipline : Physique Médicale

Soutenue publiquement le 14/09/2023 par :
POPOTTE Christian

Development and characterization of a scintillation dosimeter dedicated to CBCT in image-guided radiotherapy and exploratory study of the CBCT doses effect in DNA repair

Dr Delpon Gregory, ICO, IMT Atlantique, UMR CNRS 6457/IN2P3	Rapporteur
Pr Gschwind Régine, UBFC, UMR 6249 CNRS	Rapportrice
Pr Vogin Guillaume, Université de Lorraine, IMoPA, UMR 7365 CNRS	Rapporteur
Dr Bouchet Audrey, INSERM UMR 1296	Co-encadrante
Pr Lamartine Jérôme, Université Lyon 1, UMR5305 LBTI CNRS	Président
Dr Munier Mélodie, Fibermetrix, ALARA Group	Co-encadrante
Dr Paul Didier, CH de Haguenau	Directeur de thèse
Dr Pierrat Noëlle, CLCC Jean Perrin	Examinatrice

Développement et caractérisation d'un dosimètre à scintillation dédié au CBCT en IGRT et étude exploratoire de l'effet des doses CBCT dans la réparation de l'ADN

Remerciements :

Je tiens à remercier par ces quelques lignes, celles et ceux qui ont contribué de près ou de loin à l'aboutissement de ce travail de thèse.

En premier lieu, j'exprime toute ma gratitude à Mélodie Munier pour son encadrement, les échanges scientifiques, et son soutien tout au long de la thèse. Je la remercie également de m'avoir accueilli au sein de Fibermetrix pour y réaliser ma thèse. Merci pour ta résilience avec l'administration et pour ton accompagnement constant au cours de la thèse.

Je remercie Didier Paul de m'avoir accordé sa confiance au cours de mes travaux de thèse.

Un grand merci à Gregory Delpon, Régine Schwind, et Guillaume Vogin d'avoir accepté d'être mes rapporteurs. Leurs commentaires et remarques ont aidé à façonner le manuscrit dans sa version finale. Je les remercie également pour leurs échanges riches et pertinents avant et durant la soutenance.

Merci à Jérôme Lamartine d'avoir présidé mon jury de thèse. Je le remercie également pour les remarques et questions pertinentes au cours de la soutenance.

Je remercie également Noëlle Pierrat d'avoir accepté d'être examinatrice lors de ma soutenance de thèse et pour ces judicieux commentaires.

Mercie à Audrey Bouchet, d'avoir co-encadré ma thèse. Je la remercie également pour ses échanges et remarques pertinentes.

Je tiens à remercier également Marie-Claude Biston et Jean-Marc Bordy pour leur participation à mon comité de suivi individuel de thèse.

Toute ma reconnaissance à Fanny Carbillet pour m'avoir accueilli au sein du groupe ALARA. Merci pour nos discussions, formelles et parfois moins formelles ainsi que pour ta disponibilité tout au long de la thèse.

Merci à Philippe Frey de m'avoir accueilli au sein du groupe ALARA. Nos échanges m'ont permis de m'ouvrir au monde du marketing et du business. Merci également pour tes blagues toujours de très haut niveau.

J'exprime ma gratitude à Nicolas Foray de m'avoir accueilli au sein de son laboratoire. Un grand merci pour le temps passé lors de nos discussions et de nos nombreux échanges scientifiques.

J'ai eu la chance de rencontrer et de travailler avec des personnes exceptionnelles au cours de ma thèse. Je tiens à les remercier en leur dédiant les prochaines lignes.

Je tiens à remercier Sandrine Pereira, d'avoir partagé avec moi ses connaissances et pour m'avoir formé au passionnant monde de la radiobiologie. Je te remercie pour tes nombreuses heures passées à mes cotés durant les manips de radiobiologie et pour le temps que tu as passé à m'accompagner dans la rédaction de la partie radiobiologie de cette thèse. Merci également pour ces moments de rires, de poisse monumentale, et de résilience. A bientôt dans le sud.

Merci à Nicolas Guillochon. Travailler à tes cotés a été pour moi une vraie source d'enrichissement, tant sur le point professionnel que personnel. Ton esprit toujours claire, ta pédagogie et ton humilité font qu'il est très agréable d'échanger avec toi. Je te souhaite le meilleur. Ne change pas.

Un grand merci à Paul Rétif de m'avoir ouvert les portes du service de physique médicale du CHR de Metz Thionville. Merci également pour les nombreux échanges et la bonne humeur toujours au rendez-vous lorsque je venais effectuer des mesures.

Merci tout particulièrement à Romain Letellier de m'avoir accompagné lors de mes nombreuses sessions de mesures au CHR de Metz-Thionville. Je te remercie également pour ta disponibilité à toute épreuve. J'ai été heureux de travailler avec toi et j'espère qu'on se recroisera bientôt.

À mes compagnons de bureau, Fred, Mamoutou, Arthur, Adrien, Guillaume pour nos discussions et moments de détente. Nos échanges et discussions ont su égayer mes journées au bureau et rendre les jours plus agréables. Une pensé particulière pour Fred et nos très très longues discussions musicales/cinématographiques/littéraires.

À Anthony et Anh-Thu, merci pour votre bonne humeur, vos rigolades et surtout pour l'alliance FMX dans MPG ;).

À Selena, ma stagiaire qui a le mieux réussi. Ça a été un véritable plaisir de te voir trouver ta place dans l'entreprise. Travailler avec toi était réellement enrichissant, tant tu a toujours su allier la rigueur et la bonne humeur. Je te souhaite le meilleur pour la suite de ta carrière.

À Eloi, l'un de mes premiers compagnons de bar à Strabsourg, avec qui on se souviendra longtemps du « comme d'habitude ? » destiné à un certain Quentin au garde fou. Tu as un vrai talent pour parler de n'importe quel sujet avec n'importe qui et tu sais mettre à profit ce talent tout les jours dans ton métier. Je te souhaite le meilleur pour la suite de ta carrière.

À Patrick, tu es un exemple de plus de la force et de la résilience du peuple libanais. Tu es quelqu'un avec un grand cœur et j'espère que tu réussiras dans tout tes projets. Merci pour tes rires, ton humeur parfois changeante, et surtout pour tes talents de cuisinier.

À Pierre B., merci à toi également pour tes nombreuses recommandations cinématographiques, musicales, et littéraires. Imbattable au blindtest de Brian, ta bonne humeur et ton rire ont su égayer les moments passés ensemble.

À Ramiro et Corentin, merci pour les moments de rigolades et les échanges scientifiques. Travailler avec vous deux était un réel plaisir. Ramiro toujours un instrument à la main pour chanter la bonne humeur Colombienne, et Corentin toujours un bon houblon à la main.

À tout ceux que j'ai rencontré et avec qui j'ai pu travailler au cours de ces années, au sein du groupe ALARA et à l'extérieur, un grand merci pour avoir rendu tout cela possible.

Ma famille et mes proches ont également rendu ces années plus agréables et ont contribué, à leur façon, à la réussite de cette thèse. Je leur dédie ces prochaines lignes.

Un immense merci à tout mes proches qui m'ont soutenu et ont été une source d'inspiration pour moi avant et pendant la thèse. Merci à Sara, de m'avoir soutenu et conseillé avec sagesse et attention. Merci à Suzie, Flavien, Pauline, Romaric, Florian S., Florian A., Eric, Julien, Maëlle, Yann, Patrick. Je ne compte plus les heures passées à vos côtés à rire, à profiter de la vie, à refaire le monde pour mieux le défaire encore une fois. Je sais également que je peux compter sur vous, dans les bons comme les moins bons moments.

Merci aux meilleurs des colocs, ceux du T19.3, pour leur accueil et nos souvenirs incroyables. Merci à Camo, Julien, Thibault et Eve qui ont été les colocs de la première génération, car sans vous ce confinement aurait été une toute autre aventure. Merci à Fede (« baguette »), Pierre, Morgane et Eric, Stéph, et Nour. Merci à vous tous pour nos discussions, nos rigolades, nos excursions, nos voyages au bout du monde et merci pour votre bonne humeur qui m'a accompagné pendant tout mon séjour à Strasbourg.

Mon immense gratitude à mes compagnons de la première heure, Aythami et Annthomy. Le destin nous a réuni il y a de ça plus de la moitié de nos vies. Depuis cette rencontre, ce même feu qui brûle en chacun de nous a tantôt été notre moteur, tantôt une lanterne pour éclairer nos pas. Puissent l'avenir nous réserver encore de nombreux moments de fraternité et d'amitié. À l'Alcyone,

Un grand merci à celui qui a été mon modèle étant petit, mon grand frère, Jérémy. Tu as été une source d'inspiration pour moi et tu as contribué à me maintenir « sur le droit chemin » lorsque je m'en écartais. Je te dois une grande partie de mon aisance à l'oral (même en anglais), de mon esprit critique, et de mon envie d'accomplir de belles choses. Merci pour tout.

Enfin, je tiens à conclure ces remerciements en remerciant tout particulièrement ma mère pour son éducation, sa force, et son amour. Merci à toi, pour tes choix de vie parfois compliqués mais qui ont menés aux hommes que nous sommes aujourd'hui Jérémy et moi. La vie n'a pas toujours été simple, mais tu as toujours réussi à nous donner le meilleur et nous transmettre l'envie d'accomplir de grandes choses. Merci de nous avoir transmis ton amour de la lecture, ton goût pour le sport, et la valeur du travail. Cette thèse c'est aussi la tienne.

Résumé :

L'utilisation du kV cone-beam computed tomography (CBCT) en radiothérapie a augmenté depuis le début des années 2000, permettant la visualisation volumétrique des patients pendant les traitements de radiothérapie, mais entraînant des dépôts de doses plus élevés par rapport à l'imagerie 2D traditionnelle. La radiothérapie guidée par l'image (IGRT) utilisant le CBCT est devenue essentielle pour l'administration précise du traitement, permettant la vérification de l'installation du patient pour tenir compte des variations anatomiques, des mouvements et d'autres facteurs. Cependant, la dose provenant de l'imagerie est souvent négligée dans la planification du traitement et dans les rapports de dose, malgré les effets cumulatifs potentiels. Pour relever ces défis, il est essentiel de mettre en œuvre des systèmes d'assurance qualité rapides et précis, de rapporter les doses d'imagerie tout au long du traitement et de développer des méthodologies de dosimétrie appropriées.

En raison des doses délivrées pouvant aller jusqu'à 3% de la dose prescrite[6], cette thèse s'est concentrée sur la dosimétrie du CBCT et vise à développer un système de dosimétrie compatible avec l'environnement de la radiothérapie, à valider un dosimètre et une méthodologie, à évaluer les performances dosimétriques et à étudier la réponse adaptative en IGRT. L'étude comprenait l'analyse du comportement de la fibre en présence de fortes doses, l'amélioration du système de photodétection de Fibermetrix avec l'intégration des SiPM, le développement d'un dispositif de mesure de dose CBCT et l'exploration des doses et des mécanismes de réparation de l'ADN dans le cadre de l'IGRT. Cette collaboration interdisciplinaire entre Fibermetrix et l'INSERM U1296 visait à combiner l'expertise de l'industrie, de la clinique et de la recherche pour faire progresser la dosimétrie pour le kV-CBCT en radiothérapie.

A l'issue de ce travail, la dégradation des fibres optiques plastiques a été étudiée en fonction de leur dose absorbée cumulée. En raison de ces nombreux désavantages (problème d'approvisionnement, prix, et dimensions), le précédent photodétecteur (tube photomultiplicateur) fut remplacé par des photodétecteurs SiPM. L'étude préliminaire à leur implémentation a été réalisée dans le cadre des travaux de cette thèse. Additionnellement à cela, un dosimètre et une méthodologie ont été validés pour le contrôle qualité dosimétrique kV-CBCT en radiothérapie. Enfin, une étude préliminaire a été menée afin d'étudier l'effet radiobiologique des doses de kV-CBCT et MV-CT en IGRT en IGRT.

Abstract:

The use of kV cone-beam computed tomography (CBCT) in radiotherapy has increased since the early 2000s, enabling volumetric patient visualization during radiotherapy treatments but resulting in higher radiation doses compared to traditional 2D imaging. Image-guided radiotherapy (IGRT) using kV-CBCT has become essential for precise treatment delivery, enabling verification of patient setup to account for variations in anatomy, movement, and other factors. However, the dose from imaging is often neglected in treatment planning and reporting, despite the potential cumulative effects. To address these challenges, it is crucial to implement fast and accurate quality assurance systems, report imaging doses throughout treatment, and develop suitable dosimetry methodologies.

Because the doses from kV-CBCT can reach up to 3% of the prescribed dose[6], this thesis focused on the dosimetry of CBCT and aimed to develop a dosimetry system compatible with the radiotherapy environment, validate a dosimeter and methodology, evaluate dosimetric performance, and investigate the Adaptive Response. The study involved investigation on the fiber behavior under high radiation doses, improving the photodetection system with SiPM integration, developing a CBCT imaging dose measurement device, and exploring doses and DNA repair mechanisms in IGRT. This interdisciplinary collaboration between Fibermetrix, INSERM U1296, aimed to combine industry, clinical, and research expertise in advancing dosimetry for kV-CBCT in radiotherapy.

Consequent to these efforts, the degradation of plastic optical fibers was studied relative to their cumulative absorbed dose. Owing to numerous drawbacks (supply issues, cost, and dimensions), the prior photodetector (photomultiplier tube) was substituted with SiPM photodetectors. Preliminary assessment of their implementation was conducted within the scope of this thesis work. Furthermore, a dosimeter and associated methodology were validated for kV-CBCT dosimetric quality assurance in radiotherapy. Lastly, a preliminary study was conducted to examine the radiobiological effect of kV-CBCT and MV-CT doses in the context of IGRT.

Mots clés :

CBCT ; Dosimètre à scintillation ; Radiothérapie ; IGRT ; Faibles doses ; Réponse Adaptative

Keywords:

CBCT ; Scintillation dosimeter ; Radiotherapy ; IGRT ; Low doses ; Adaptive Response

Unité INSERM U1296 :

Radiations : Défense, Santé, Environnement

Centre Léon Bérard

Bâtiment Cheney A, 1er étage

28, rue Laënnec

69008 LYON

TABLE OF CONTENTS

List of figures

List of main abbreviations

CBCT: Cone Beam Computed Tomography

CT: Computed Tomography

Gy: Gray

CTDI: Computed Tomography Dose Index

POF: Plastic Optical Fiber

PSF: Plastic Scintillating Fiber

QA: Quality Assurance

AR: Adaptive Response

IGRT: Image Guided RadioTherapy

Linac: Linear Accelerator

IMRT: Intensity-modulated radiotherapy

VMAT: Volumetric Modulated Arc Therapy

EPID: Electronic Portal Imaging Detector

aSi: Amorphous Silicon

SNR: Signal Noise Ratio

PMMA: PolyMethylMethAcrylate

PM: PhotoMultiplier

SiPM: Silicon photomultiplier

DCR: Dark current rate

RIA: Radiation-Induced Attenuation

SSB: Single Strand Break

DSB: Double Strand Break

DNA: Deoxyribonucleic acid

ATM: Ataxia Telangiectasia Mutated gene

I. Introduction

Since the early 2000s, kV-cone beam computed tomography (CBCT) has been more and more used in radiotherapy for periodic volumetric visualization of the patient anatomy during the treatment course with the benefit of enhanced visualization of soft tissue at the cost of a higher dose compared to 2D kV or MV imaging. As modern radiotherapy (RT) is increasingly using intensity modulation or stereotactic techniques with a high degree of conformity in multiple areas of the body, the use of image-guided procedures in RT, namely image-guided radiotherapy (IGRT), increases as well. During these treatments, several patient-related parameters can modify the dose distribution at each fraction: variations in patient setup, anatomy, or movement during treatment. It is therefore of utmost importance to verify the patient setup at each treatment fraction to ensure precision in the delivery of RT. The dose resulting from imaging in RT has historically often been omitted in the planning process and is rarely reported at the end of the treatment because it is two orders of magnitude smaller than the therapeutic doses, between 1 and 10 cGy for a scan[43, 91, 62, 103, 153, 87, 76, 146]. Cumulated doses of repeated scans can however be consequential. It has been reported that kV-CBCT procedures employed for pelvic imaging can add a cumulative dose of 1-3% of the prescription dose (e.g. up to 2.3 Gy for a 78 Gy prostate treatment)[6]. Moreover, during an imaging procedure, the portions of the body that are irradiated are often larger than the treatment fields resulting in unintended irradiation of nearby organs and leading to radiation-induced pathologies[44, 84, 101, 106, 135, 159].

CBCT imaging is available on various radiation delivery units of different vendors for example Varian (Varian, a Siemens Healthineers Company, Palo Alto, USA) or Elekta (Elekta AB Stockholm, Sweden). Lately, some medical accelerators (e.g. Radixact (Accuray Incorporated, Sunnyvale, USA)) have also been able to acquire computed tomography (CT) images with the advantage of potentially acquiring longer longitudinal field-of-view. Each vendor has its acquisition protocols which are generally related to the acquired part of the body, the image quality, or the field-of-view. These protocols can be used as-is or can be optimized by the local physics team. Thus, there is a variety of volumetric imaging protocols within radiotherapy centers. Each one has its protocol for both frequency of CBCT and the acquisition parameters. Some centers use daily volumetric images while others might acquire them daily during the first week and then once a week to check that the patient follows the nutritional guidelines or whether there is a need to do a new treatment planning[120].

Therefore, as it has been recommended by multiple institutions[63, 173, 85], it appears necessary to: (i) implement fast and accurate quality assurance (QA) systems that can check whether the X-ray tube is delivering the attended dose or not ; (ii) work towards an easy reporting of the imaging dose given through RT treatment courses. Besides, the dosimetry of CBCT is all the more complex that it involves the presence of large collimations and requires a specific measurement methodology. This latter issue highlighting also the complexity when it comes to the choice of the dosimetric quantities and methods to describe the dose from an imaging device in an RT environment depending on the purpose (*i.e.* QA or patient dose). In addition, it is

interesting to point out that the doses schemes involved in IGRT (low imaging doses + repositioning time + high treatment dose) could be consistent with an unintuitive radiobiological phenomenon known as the Adaptive Response (AR)[34, 94, 130, 147] which, to our knowledge, has not been studied in these conditions yet. This phenomenon describes the protective effect that a priming low dose delivered before a challenging intermediate or high dose can have on the DNA repair mechanisms.

Focusing on these concerns, the Fibermetrix company (specialized in in-vivo and QA dosimetry solutions) and the INSERM U1296 (specialized in the radiobiological study of DNA repair mechanisms) joined their expertise during this CIFRE thesis to develop a dosimetry system for IGRT applications.

Fibermetrix is a French start-up founded in 2014 specializing in designing and producing advanced solutions to manage radiation risks in medical imaging and radiotherapy. Based on a patented fiber optic technology[168, 174–177], the company developed a dosimetry technology capable of measuring the delivered dose in real-time, especially in complex environments. The first detector commercialized by the company in 2019 is named IVIscan. It is the first real-time in vivo dosimetry system dedicated to CT imaging and is designed to measure and visualize patient-delivered doses in real-time, detect abnormalities, and bad practices (e.g. dose alerts, repetitive exams, etc.) evaluate and verify the proper functioning of the scanner (usable tool for image and dose quality controls) and archive patient dose reports. In this context, the main objective of this CIFRE thesis was to adapt the device called IVI-CBCT, originally developed for CT applications under the name IVIscan, to radiotherapy kV-CBCT applications.

The Unit 1296 "Radiation: Defense, Health Environment" was created in January 2019 with the support of the National Institute of Health and Medical Research (INSERM), the Ministry of the Armed Forces, and the Armed Forces Health Service (SSA), and the Léon-Bérard Center in Lyon (CLB). The main mission of this Unit is to better understand the biological consequences of exposure to radiation DNA-breaking agents in a clinical, military, environmental, space, or professional context, by studying more particularly the impact of the individual factor in the repair and signaling of DNA damage. By extension, this innovative Research Unit also deals with aspects of human and social sciences (risk perception, law, and regulation, history of science), commercialization (partnership with many companies), and develops teaching projects aimed at the public, health professionals, institutional decision-makers, and scientific journalists. The Unit is based on two sites: the "Health" site on the CLB campus in Lyon and the "Defense" site on the campus of the Institut de Recherche Biomédicale des Armées (IRBA/SSA) in Brétigny-sur-Orge.

Thus, centering on the main source of imaging dose in RT, the CBCT, the subsequent requirements, were identified in the dosimetry system's early stage of development:

- To be compatible with an RT environment (e.g. material resistance under radiations; no interference on treatment or imaging beams) and clinical constraints.
- Validate a dosimeter and associated methodology suitable to measure the dose from CBCT dosimetric QA using a scintillating fiber dosimeter.
- Measure the CBCT dosimetric performances when changing the acquisition parameters of acquisition protocols (e.g. when optimizing the acquisition protocols).
- Evaluate the dose delivered during treatment courses involving imaging and treatment dose in RT.
- Evaluate the dose delivered in radiobiological studies on AR involving imaging and treatment doses in RT.

Following this rationale, the main external elements interacting with the dosimeter were defined such as the users (e.g. medical physicists, measurement technicians), the physical environment (e.g. treatment beam, imaging system beams, treatment table), the patients, and the medical and hospital staff. Based on these assumptions, the dosimeter functions can be divided into two groups: the primary functions, and the secondary functions (Cf. Table 1). The primary functions here are the reasons why the detector exists, and the secondary functions are coming because the dosimeter exists. All the rest of the detector's functions can be described as optional or unnecessary and will not be described here.

Table *1*: Dosimeter's primary and secondary functions.

Primary functions	Secondary functions
Measure the dose from CBCT imaging systems in RT	Having little or no influence on treatment and imaging beams
Display a signal proportional to the delivered dose	No obstruction to the patient's, or radiation therapist's movements
Dose measurement is at least as accurate as the reference dosimeter for the same applications	Access to the follow-up of the measurements
Display good repeatability	

Once the dosimeter's primary and secondary functions are defined, the design and development aiming at fulfilling these functions started. Following these specifications, this CIFRE thesis worked driven by both applicative and research goals in an interdisciplinary environment combining industry, clinics, and public research. To achieve each point of the specifications, the thesis was divided into the following steps:

- Firstly, the behavior of different types of fibers was studied in the presence of a high cumulated dose (up to 1 kGy) both with kV and MV photons beam to evaluate the evolution of transmission and emission properties of plastic optical fibers. Then, this thesis work

emphasized the improvement of the photodetection system by the integration of a new photodetector, the SiPM, into the detection chain.

- The innovative measurement device capable of measuring the imaging dose of CBCT (*i.e.* the air Kerma and the computed tomography dose index (CTDI)) was developed in partnership with the Metz-Thionville hospital radiotherapy service. Alongside this development, the methodology for large collimations dosimetry during this thesis. Initially planned to assess patient dosimetry as well, further limitations appeared during the development and the dosimeter was eventually suitable only for dosimetric QA.
- Finally, the dose and DNA repair mechanisms involved in IGRT were studied in the frame of a preliminary study of the AR phenomenon in IGRT using the IVInomad dosimeter. This interdisciplinary work between Fibermetrix and INSERM U1296 was realized in partnership with Neolys Diagnostics, a company specializing in biotechnologies that develops tests for medical purposes allowing personalized medicine in radiation oncology.

This manuscript details the steps aforementioned and the considerations raised during this thesis. In order to present this work, the manuscript is divided such as the first section resumes the state of the art in IGRT, scintillation dosimetry, and the technical obstacles raised by the dosimeter development. Once the technical constraints are stated, the following section details the experimental development realized to investigate these limitations and develop and characterize the fiber dosimeter to implement it in IGRT dosimetry. Then the radiobiological aspect of the IGRT dose is investigated in a preliminary study. And finally, the conclusion and general perspectives are detailed in the last section.

II. State of the art

II.A. Radiation-matter interactions

Radiation interactions with matter can be divided into two main groups: neutral particles (photons, neutrons, neutrinos) and charged particles (electron, proton, ion, atom) interactions. Depending on the energy and the nature of the incident particle, various interactions are possible. Among these interactions, the most used in medical physics are the photon and charged particle interactions with matter. This section describes the main interactions found in RT, *i.e.* photons and secondary electrons interactions with matter.

II.A.1. Photons interactions with particles

Photons, contrary to charged particles, in general, have few interactions and are exponentially attenuated in the medium. At the energy range used in medical physics, the photons' energy loss (considering Rayleigh scatter as non-significative) can be described by three main interactions.

II.A.1.a. Photoelectric effect

The photoelectric effect occurs when an incident photon with energy ≥ ionization potential transfers the totality of its energy to an atom's electron (Cf. Figure 1).

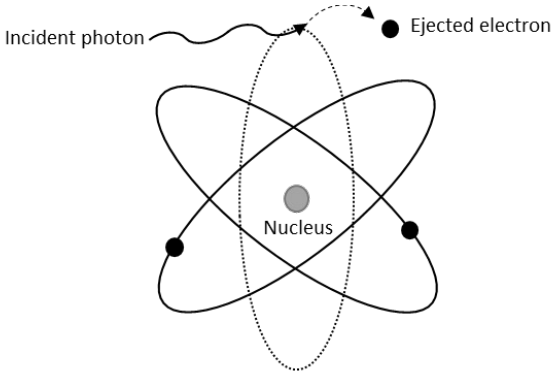

Figure *1*: Photoelectric effect.

The photoelectric probability varies in Z^5 (particularly for K layer electrons).

II.A.1.b. Compton effect

The Compton effect occurs when a photon interacts with an outer shell orbital electron and partially loses its energy during the interaction. The interaction results in the creation of a scattered photon and an ejected Compton electron (Cf. Figure 2).

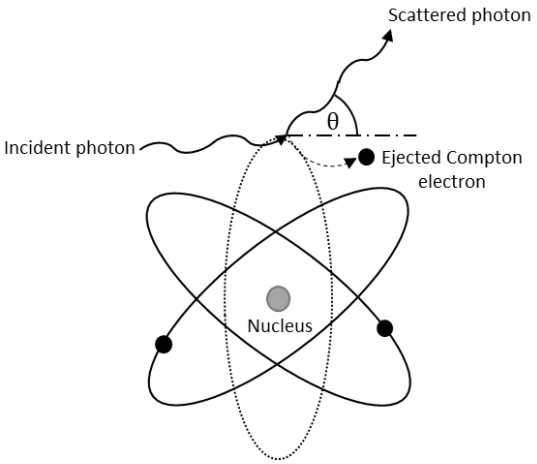

Figure *2*: Compton effect.

The Compton effect probability increases with the energy of the incident photon and the density of the medium. The angle of the scattered photon depends on the energy transmitted during the interaction: at low energy, the angle scattering is equally probable; at high energy, forward angle scattering is more probable.

II.A.1.c. Pair production

This effect takes place when a photon with energy ≥ 1.022 MeV interacts with the atomic nucleus. The photon energy is converted into an electron-positron pair and kinetic energy (Cf. Figure 3). After slowing down in the medium, the positron will interact very quickly with a free electron and will produce a pair of annihilation photons emitted virtually in coincidence with the pair production interaction. The pair production probability increases with the Z^2 of the medium.

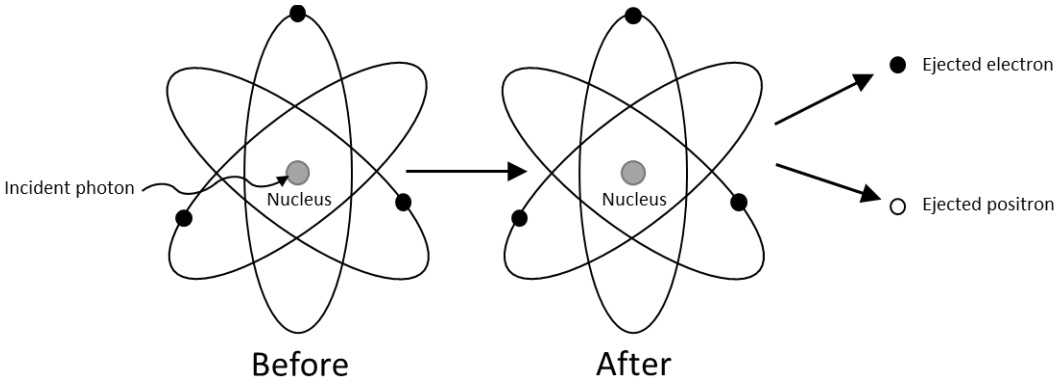

Figure *3*: Pair production.

The probability of each interaction depending on the energy and the medium mass attenuation coefficient is given in Figure 4.

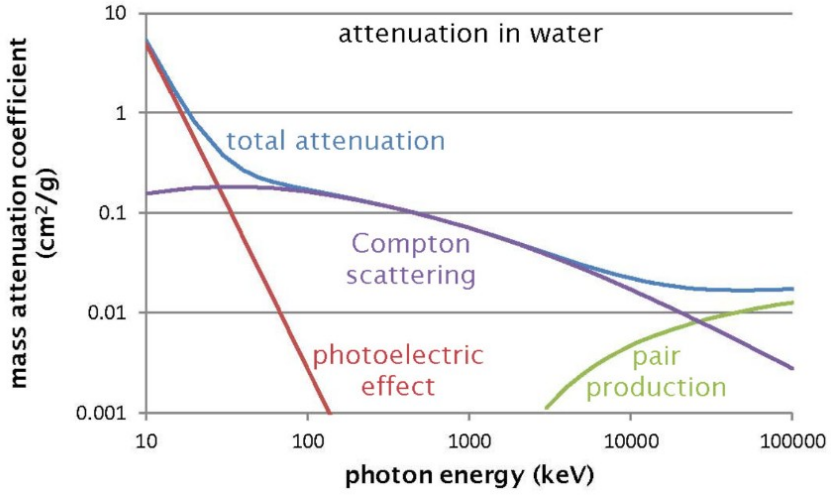

Figure *4*: Incident particle interaction proportion depending on their energy and the medium mass attenuation.

Following these interactions, secondary particles such as electrons can be generated. Depending on these secondary charged particles' energy, other interactions can occur, resulting in a succession of secondary particles generated and energy deposition in the medium.

II.A.2. Charged secondary particles interactions

Charged particles experience a large number of interactions when moving through a medium. Charged particles are normally considered into two groups, the heavy and the light-charged particles. Since this work focuses on conventional RT, only electron particle interactions will be detailed in this section. Considering incident charged particle interactions with an electron in the medium, the reaction will depend on the incident particle energy and the binding electron energy.

II.A.2.a. Excitation

This phenomenon is produced when an incident charged particle interacts with an orbital electron of higher liaison energy than the incident charged particle ($E < E_i$ with E the incident charged particle energy and E_i the minimum liaison energy of the electron). In this case, due to an elastic collision, the incident charged particle transfers a part of its energy to an orbital electron, but not enough energy to free it (Cf. Figure 5).

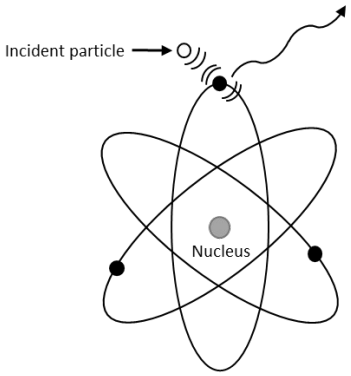

Figure *5*: Atom's excitation.

The former orbital electron, due to its increase in energy, reaches an excited state and releases its energy into a photon emission (Cf. Figure 5). The emitted photon's energy will depend on the energy difference between the different states. This interaction can be described as:

$$M + Energy \rightarrow M^{*} \quad \text{[Eq. 1]}$$

With M the molecule, M^{*} the molecule in an excited state.

II.A.2.b. Ionization

It occurs following the interaction of a charged particle with an orbital electron. The energy from the incident particle is transferred to the electron. If the transferred energy is greater than the electron ionization potential ($E > E_i$), the electron is freed (Cf. Figure 6).

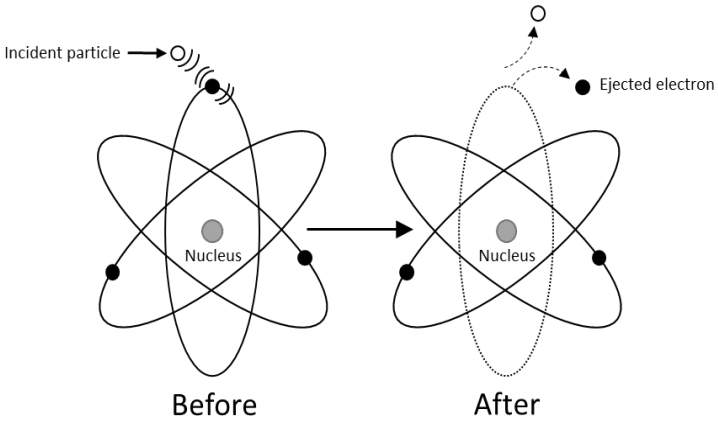

Figure *6*: Atom's ionization.

The ejected electron's energy will be equal to the difference between the incident electron's energy and the orbital electron's ionization potential. Depending on its energy, the ejected electron can interact with

another element of the medium and potentially causes a secondary ionization. This interaction can be described as:

$$M + e^{-} \rightarrow \qquad \text{[Eq. 2]}$$

$$M + e^{-} \rightarrow M^{*} + e^{-} \qquad \text{[Eq. 3]}$$

With M the molecule, M^{+} the resulting ion, M^{*} the molecule in a superexcited state.

II.A.2.c. Bremsstrahlung

If the incident electron interacts with the nucleus, the particle will be deflected by the electrical forces and will lose a part of its energy when decelerating. The energy loss will take the form of the emission of a photon. The emitted photon's energy will be equal to the energy loss of the incident electron (Cf. Figure 7).

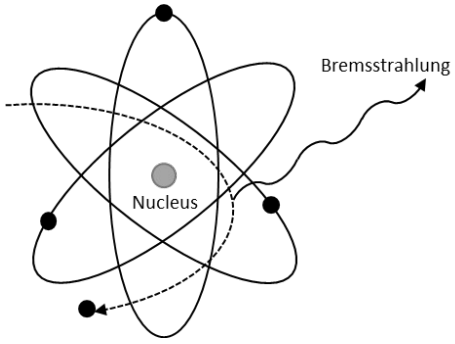

Figure 7: Bremsstrahlung schematized.

The Bremsstrahlung radiation loss increase with increasing particle energy and increasing atomic number of the absorbing material. It is a key reaction in photons production in medical physics (e.g. X-Ray tube, or Linac).

II.A.2.d. Cherenkov and transition radiation effects

Cherenkov radiation is emitted when a charged particle in a medium exceeds the speed of light in that same medium. Nothing can travel faster than the speed of light in a vacuum. However, when light travels through a transparent medium such as water, its speed is slowed down by the refractive index of the medium: the refractive index of water at room temperature is 1.33 so light in water is traveling at about 3/4 of the speed of light in a vacuum.

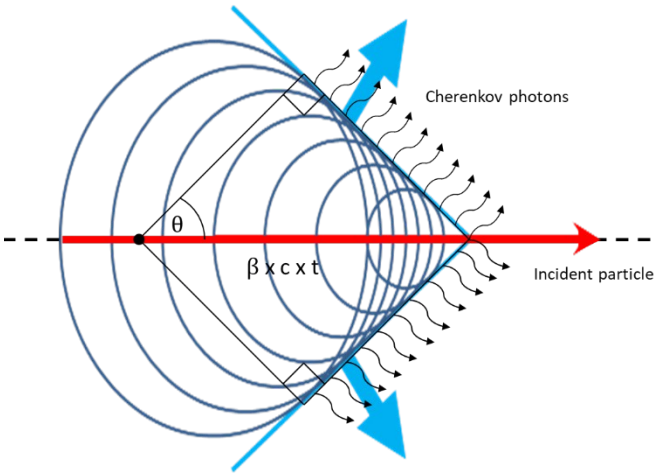

Figure *8*: Cherenkov emission.

Charged particles, however, are not slowed down by the refractive index. A conical electromagnetic wavefront, similar to a sonic shock, is produced (Cf. Figure 8).

The coherent wave is emitted at a specific angle described in the following formulas:

$$\cos\cos(\theta) = \frac{1}{\beta \times n} \qquad \text{[Eq. 4]}$$

With

$$\beta = \frac{Vp}{c} \qquad \text{[Eq. 5]}$$

And n the medium refractive index, V_p the particle speed, and c the speed of light in vacuum.

The fundamental interactions described above form the basic principles of radiation medical physics. Based on this, physicists have lifted the technological barriers to bring the benefit of radiation physics to the patient. One of their numerous applications is their use in RT and medical imaging.

II.B. A brief history of radiotherapy

On July 4, 1896, Victor Despeignes, a physician in the village of Les Echelles in Savoie, France, made history by using X-rays to treat cancer for the first time[71]. This was only six months after the discovery of X-rays by Wilhelm Roentgen, a German scientist. Despeignes was trying to cure his friend, Eugène-Constant Colliat, who had been diagnosed with cancer. At the time, it was widely believed that cancer was a microbial disease, and Despeignes was inspired by the successful use of X-ray treatments on tubercular animals that had been conducted in Lyon, France, earlier that year.

This marked the beginning of a new era in cancer treatment, known as radiotherapy.

In 1900, two Germans, Otto Walkhof and Friedrich Giesel, reported their observations on the biological effects of radium on the skin and established a parallel with the action of X-rays. In 1901, Pierre Curie and Henri Becquerel published a note[16] on the "physiological action of radium rays.", and a dermatologist from the Saint Louis Hospital in Paris, Henri Danlos, published his results on the treatment of lupus with radium. The radium used by Danlos for these experiments was given to him by Pierre Curie. Following these discoveries, physicians also conducted numerous tests on other pathologies.

From 1904 to 1906, Jean Bergonié (a radiologist) and Louis Tribondeau (a histologist) showed that cancerous cells were more sensitive to X-rays than healthy cells[23, 24]. They thus provided the first biological basis for the use of X-ray RT. In 1905, the beneficial effects of radium rays for the treatment of skin and cervical tumors were recognized, marking the birth of brachytherapy. In 1906, Armet de Lisle (a radium industrialist) financed the creation of the first laboratory devoted to the study of the biological and medical effects of radium. This was the beginning of significant developments in radiation therapy.

RT has seen major advancements in treatment efficiency and complexity since the 1950s when high-energy treatments using $Cobalt^{60}$ were first introduced. In 1968, radiosurgery was developed, followed by 3D conformal radiotherapy in 1974 which then became the standard treatment for most cases until the early 2000s. However, in 2000, a new technique called Intensity-modulated radiotherapy (IMRT) was introduced, which allowed for more accurate treatment plans by using dose gradients generated by a succession of complex beam geometries created by the primary jaws and multi-leaf collimators (MLC). The accuracy of IMRT is heavily dependent on the performance of the Linac and the patient positioning. To address this latter issue, kV Cone Beam Computed Tomography (kV-CBCT) Image-Guided RadioTherapy was introduced by Jaffray et al.[92] in 1999 and became commercially available in 2005, allowing for patient 3D repositioning while on the treatment table. In 2007, Volumetric Modulated Arc Therapy (VMAT) was introduced, further improving treatment modulations and accuracy (Cf. Figure 9).

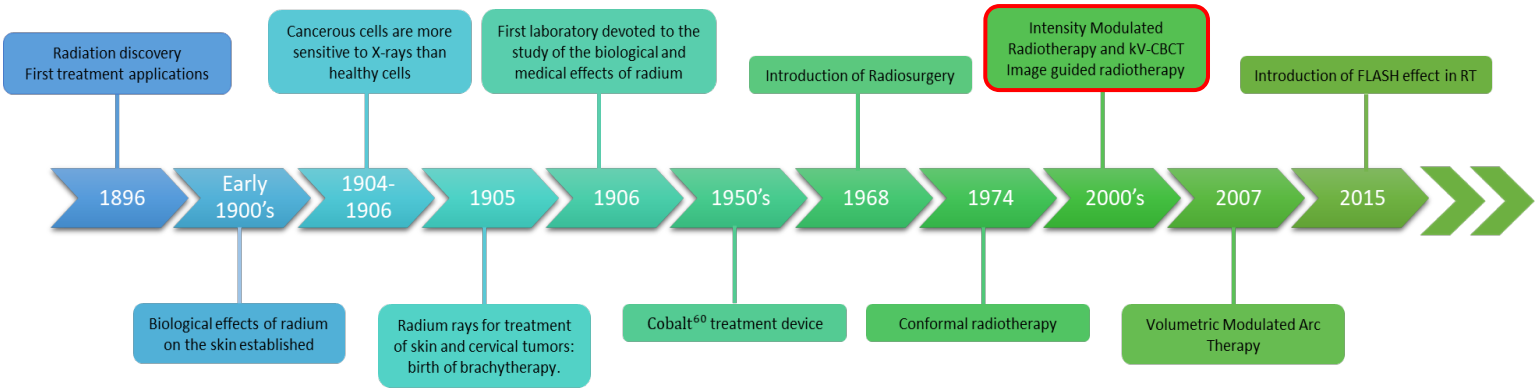

Figure *9*: Radiotherapy history timeframe

Since these breakthroughs, radiotherapy has continued to evolve, with advancements being made in fields such as physics, radiobiology, modelization, and information science. Although radiotherapy can be achieved by using different types of particles, this manuscript will assess only the field of photon radiotherapy.

II.C. kV-based in room imaging systems

The types of equipment dedicated to radiotherapy have made enormous progress in recent years allowing the distribution of physical doses better limited to the tumor as well as better protection of healthy tissue. The treatment quality is significantly improved by ensuring that the patient is properly positioned during treatment thanks to in room imaging systems. The principle of Image-guided Radiotherapy (IGRT) is based on the registration of an acquired image with the planification image (CT in most cases) or a digital radiology reconstruction (DRR). The comparison between images is done either manually or automatically by registration algorithms. The registration can be rigid (translation only) or non-rigid (deformation). The distance between the two image structures is evaluated using software analysis tools. Depending on the level of accuracy desired, thresholds can be defined in 3 levels of difference such as : 1) Acceptable difference. When the patient position and anatomy do not differ significantly from the planification image. 2) Significant difference requiring patient repositioning. The operator can move the treatment couch manually on 3 degrees of freedom, or automatically on 3 to 6 degrees of freedom depending on the treatment couch. 3) Difference outside the acceptable threshold, requiring investigation to determine the difference origin and possibly a treatment re-planification.

II.C.1.Interest and limitations

Regarding the justification principle, imaging in radiotherapy considerably increases the quality of treatment. It is therefore not simply a matter of reducing the dose received from imaging examinations, but of optimizing it. To do so, a simple estimate of the imaging dose received during radiotherapy sessions is no longer sufficient. It is necessary to measure and quantify the dose for several examinations, imaging modalities, and incidences. Indeed, because of the different imaging systems using either 2D or 3D acquisitions, kV or MV beams, and the variety of protocols, it has been a challenging task to find dose indicators and/or methods to assess the delivered dose due to imaging systems in radiotherapy[4, 35, 44, 64, 66, 92, 123, 158, 180]. In addition, when reporting the dose, it is a matter of high importance to indicate if it is a QA dose indicator (give information on the imaging system’s performances at a given time) or a patient dose indicator (gives information on the received dose by the patient during the imaging protocol). Furthermore, since epidemiological studies are based on dosimetric data, providing unanimous indicators for patient imaging dose monitoring would also have a clear benefit on epidemiological applications.

Modern radiotherapy is increasingly using modulated dose delivery techniques to deliver radiation doses with a high degree of conformity in multiple areas of the body. Several patient-related parameters can modify the dose distribution at each fraction: variations in patient setup, anatomy, or movement during treatment. It is therefore of utmost importance to verify the patient setup at each treatment fraction to ensure precision in the delivery of radiotherapy. Since the early 2000s, kV-cone beam computed tomography (CBCT) has been more and more used in radiotherapy[96] for periodic volumetric visualization of the patient anatomy during the treatment course with the benefit of enhanced visualization of soft tissue. While the justification of this acquisition is certain, it also delivers a higher dose compared to traditional 2D kV or MV imaging.

The dose resulting from imaging in radiotherapy has historically often been omitted in the planning process and is rarely reported at the end of the treatment since it is two orders of magnitude smaller than the therapeutic doses, between 1 and 10 cGy for a scan[35]. Cumulated doses of repeated scans can however be significant. It has been reported that kV-CBCT procedures employed for pelvic imaging can add a cumulative dose of 1-3% of the prescription dose (e.g. up to 2.3 Gy for a 78 Gy prostate treatment)[4, 7, 95, 106, 133, 142]. Moreover, during an imaging procedure, the region of the body that are irradiated are often larger than the treatment fields resulting in unintended irradiation of nearby organs and leading to radiation-induced pathologies[106]. Among these organs, the bones, due to their high absorption power, can receive up to 1.5 to 3 Gy following daily exposure to CBCT[106]. Moreover, during an imaging procedure, the portions of the body that are irradiated are often larger than the treatment fields resulting in unintended irradiation of nearby organs and leading to radiation-induced pathologies[44, 84, 101, 106, 135, 159]. Given the variable frequency of CBCT and the high doses that can result at the end of treatment, it is therefore essential to correctly control and estimate the dose due to CBCT during treatment to adapt the imaging protocol based on the dosimetric information.

II.C.2.Description

II.C.2.a. kV-2D imaging systems

They are composed of an X-ray source providing X-rays with energy from tens to 150 kV and a detector. The detector is based on a-Si, but is slightly different from high-energy imaging systems (Cf. Figure 10). The assembly, which is positioned at a 90-degree angle to the Linac beam's axis, is connected to the treatment device with a support arm that can be moved and adjusted. The distance between the X-ray source and the patient, as well as the distance between the X-ray source and the image detector, can be adjusted. The rotation axis of the X-ray source-detector assembly is aligned with Linac’s axis. Low energy (kV) imaging systems can be used either for 2D-kV or kV-CBCT (3D) acquisitions.

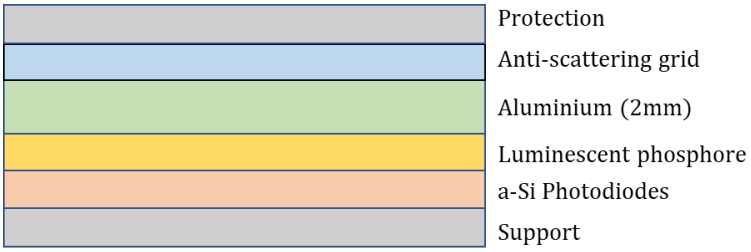

Figure *10*: Section of a kV a-Si detector.

The main features of most equipment available on the market can be found in the report[27] of the American Association of Physicists in Medicine's Task Group N. 179. Even though the delivered dose is relatively low compared to the MV system's delivered dose, it is difficult to quantify it and integrate it into the treatment plan or even record it[32, 127].

II.C.2.b. kV-CBCT and MV-CT imaging systems

The kV-CBCT systems are based on the same device as the kV-2D systems and are therefore available on most of them. Principal characteristics of this device can be found in working group number 179 of the AAPM[27]. With the EPIDs, the kV-CBCT is the most commonly used imaging modality in IGRT. kV-CBCT uses a cone-shaped X-ray beam to acquire an entire volume in a single, slow rotation. kV-CBCT uses flat-panel detectors to acquire multiple projections per second and can be reconstructed with submillimeter resolution. The image is obtained without moving the couch, by performing a single, relatively slow rotation (complete or partial) of the "X-ray tube-detector" set, which covers a variable length of the patient depending on the width of the beam chosen by the operator. The rotation axis is aligned with that of the accelerator. The image is produced using X-rays of 80 to 125 kV depending on the explored anatomical area. To avoid artifacts caused by inevitable arm bending in certain positions, manufacturers have integrated correction programs into the imaging system (bending compensated by a robotic movement of the arm on VARIAN accelerators or corrected through the reconstruction algorithm on ELEKTA accelerators). Despite this, the image is of lower quality than that provided by diagnostic scanners as it is generated by a wide cone beam instead of a thin X-ray beam. However, it is of sufficient quality to identify bone structures and some soft tissues. While kV-CBCT can produce a full CT dataset, the image quality is limited compared to traditional CT due to motion blur, scattered radiation, and image artifacts. Research is ongoing to improve these issues.

It is important to note that the couch doesn’t move during the acquisition. Despite the advantage of acquiring a 3D image of the patient in the treatment position and a direct comparison with 3D images from the TPS, this technology doesn’t provide an image of the treatment field and is often flowed by movement artifacts due to the acquisition duration. In addition, the delivered dose from kV-CBCT imaging systems is

difficult data to assess because of the large beam's width and often the partial rotation of the X-ray tube. In addition, 4D-CBCT has been introduced to provide spatiotemporal information on the organs moving during the breathing cycles[3]. Despite the advantage of providing 4D information, since the time of acquisition is longer than a usual CBCT acquisition, these exams could result in a higher delivered dose from the kV-CBCT. In this context, it appears crucial to investigate the dose indicators and methodology to use when assessing the delivered dose from kV-CBCT for quality assurance and patient dose monitoring purposes.

Regarding the Tomotherapy (Accuray Incorporated, CA, USA), as for the EPID, images are generated by the same photon source as the one used for treatments but with a lower average energy (about 1 MV) by using electrons of about 3.5 MV. Another parameter that differs from the treatment is the dose rate used which is significantly lower. The X-ray source describes a helicoidal movement around the patient with a rotation speed of 6 rotations per minute and a variable couch speed (pitch) depending on the wanted resolution. This is not the case for the new models of Radixact (Accuray Incorporated, CA, USA) incorporating kV-CT as well as the Halcyon (Varian Medical Systems, CA, USA) last models.

II.C.3. Dose quantities

According to the ICRU report n°80 definition, the Kerma represents for ionizing uncharged particles the quotient of transferred energy by mass unit and is defined by the following formula:

$$K[Gy] = \frac{dE_{p,tr}}{dm} \qquad \text{[Eq. 6]}$$

Where $dE_{p,tr}$ is the mean sum of the initial kinetic energies of all the charged particles liberated in a mass dm of a material by the uncharged particles incident on dm.

The unit of Kerma is $J.Kg^{-1}$= Gray [Gy]. Although Kerma is a quantity that concerns the initial transfer of energy to matter, it is sometimes used as an approximation to the absorbed dose. The numerical value of the Kerma approaches that of the absorbed dose when charged particle equilibrium exists, radiative losses are negligible, and the kinetic energy of the uncharged particles is large compared to the binding energy of the liberated charged particles. These conditions are reached in conventional and interventional radiology using low-energy photons (*i.e.* keV).

The absorbed dose D is the quotient of the mean energy imparted by ionizing radiation to matter of mass and is described by the following formula:

$$D[Gray] = \frac{d\bar{\varepsilon}}{dm} \qquad \text{[Eq. 7]}$$

With $d\bar{\varepsilon}$ the mean energy imparted. The unit of absorbed dose is $J.Kg^{-1}$ = Gray [Gy].

Other indexes and quantities are defined based on the absorbed dose depending on the application in medical physics. In radiotherapy, each beam is characterized by various dosimetric quantities and functions that provide information about its dose distribution. Different dose functions and quantities apply when it comes to imaging dosimetry.

Considering the 3-dimensional imaging dose in radiotherapy, the dose index commonly used is the CTDI used in scanography. It is a derivate measurement of the Dose (with Dose = Kerma at radiological energies) and is measured by a pencil ionization chamber of 100 mm in length in a CTDI phantom made of polymethylmethacrylate (PMMA) (Cf. Figure 12). Although it is now commonly used, the CTDI was not the first dose index used in CT dosimetry. This section proposes a short overview of the CTDI history and calculation formalism.

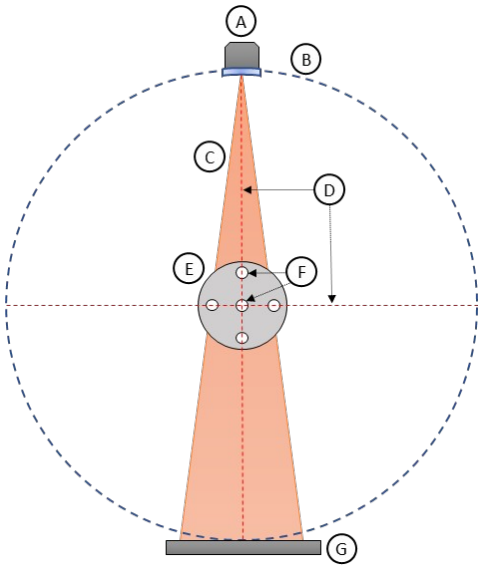

Figure *11*: Positioning of CTDI phantom within the scanned field. A: X-ray source. B: Rotational trajectory of the X-ray source. C: X-ray beam. D: Positioning lasers. E: CTDI phantom. F: Internal and external inserts. G: X-Ray detector.

The pencil ionization method was introduced in 1977 by Jucius and Kambic[97]. Before that, the dose repartition in CT was evaluated using thermoluminescent dosimetry. They derived an equation that showed that the integral of a single-slice dose profile could be used to predict the average dose about the central scan location (z=0) for multiple slices. Then Shope et al. reformulate the equation and defined the Multiple Slice Average Dose (MSAD)[149] as the dose resulting from a series of N identical axial dose profiles f(z) spaced at equal intervals of b = Δd along z such as:

$$MSAD\left[mGy\right]=D_L\left(0\right)=\frac{1}{b}\int_{-L/2}^{L/2} f\left(z'\right)dz' \qquad \text{[Eq. 8]}$$

With MSAD the average dose over ± b/2 from z = 0 and L = N x b. From this equation they stated that for L being long enough, the dose at the center of the scan length reaches its limiting "equilibrium value", therefore defining the CTDI as follows:

$$CTDI_{\infty}\left[mGy\right]=\frac{1}{T}\int_{-\infty}^{\infty} f\left(z'\right)dz' \qquad \text{[Eq. 9]}$$

With T "the slice thickness as stated by the manufacturer", and f(z) the dose profile generated by a single axial scan centered at z = 0. With the advent of multi-detector CT, T is replaced by N x T.

The measured dose $D_{measured}$ from the pencil ionization chamber is multiplied by the length Lc of the chamber to obtain the DLI (Dose-Length Integral) [Eq. 10]. The CTDI is then obtained by dividing the DLI by the collimation width in the upper-lower range [Eq. 11]. Then the CTDIw is obtained by weighting the values in the center and periphery [Eq. 12].

$$DLI\left[mGy.mm\right]=L_c\times D_{measured} \qquad \text{[Eq. 10]}$$

$$CTDI\left[mGy\right]=\frac{1}{coll}\times DLI \qquad \text{[Eq. 11]}$$

$$CTDI_w\left[mGy\right]=\frac{1}{3}CTDI_{100,central}+\frac{2}{3}CTDI_{100,peripheral} \qquad \text{[Eq. 12]}$$

Since the first introduction of CTDI in 1981 by Shope et al., CT technologies have evolved through tube current modulation, or wide collimations and CBCT, making the above-defined CTDI less accurate to estimate dose from a CT or a CBCT exam. As an example, due to the insufficient length of the detector compared to the length of the dose profile beyond 40 mm of collimation and because of the insufficient length of the phantom, the complete scattered dose is not measured and therefore results in an underestimation of the delivered dose[32]. This also causes a rise in the underestimation with the increase of the field size which can go up to 40 cm x 40 cm for CBCT[6]. Other proposed methods allow to avoid this defect will be discussed in the following section.

Therefore, as it has been recommended by multiple institutions[27, 88, 173], it appears necessary to: (i) work towards an easy reporting of the imaging dose given through radiotherapy treatment courses and (ii) implement quality control systems that can check whether the X-ray tube is delivering the attend dose or not.

To this aim, two different approaches exist: Monte Carlo dose calculations; Dose measurements. Numerous works have been conducted to evaluate Monte Carlo dose calculation tools[4, 41, 61, 152]. Unfortunately, such tools are hardly implementable into a clinical routine due to the time of calculation and the time needed to validate the generated models. The approach of the dose measurement with on-board detectors, or punctual detectors presents the advantage of assessing the real dose delivered by the imaging system either for quality control or patient dose purpose. Unfortunately, due to the lack of technical solutions and the absence of standardization for radiation dosimetry in CBCT applications, these measurements are rarely or never realized. This leads to a variety of formalisms being used to measure radiation output and perform QC. These include the Kerma Area Product (KAP), the air Kerma at the focus-to-detector distance (K_a(FDD)), and in-phantom dose indicators (such as traditional CTDI, cone-beam dose index (DSBI), IAEAw index, AAPM cumulative dose).

$K_{a,i}$(FDD): One phantom-less method to assess the CBCT dosimetric performances is by measuring the air Kerma ($K_{a,i}$ as abbreviated by the ICRU 80) using a flat probe to take a point measurement at the focal spot-to-detector distance (FDD)[89]. Solid-state probes are commonly used in projection radiography and mammography can be used in this measurement and are already available in most clinics. These probes should be back-shielded to prevent measurement of backscatter. The benefit of using solid-state dosimeters is that their calibration and results are not affected by room temperature or atmospheric pressure, unlike pencil IC. However, it should be noted that solid-state dosimeters have a non-negligible level of energy dependence, which limits their accuracy for estimating patient doses in situations involving scattered radiation from a phantom or patient.

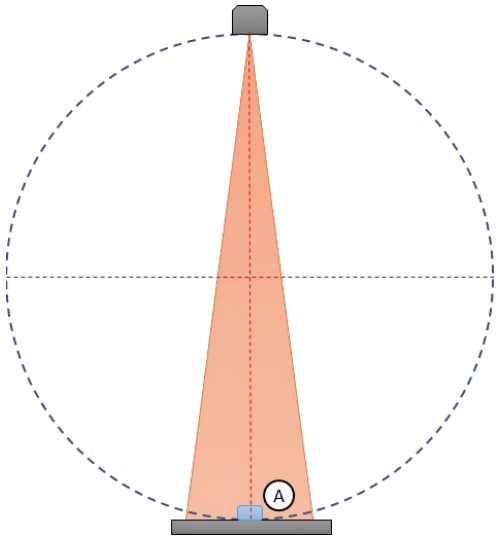

Figure *12*: Air Kerma $K_{a,i}$(FDD) measurement with A: The dosimeter placed on the X-ray detector.

The $K_{a,i}$(FDD) is measured free-in-air without the use of a phantom, simulating an actual examination by placing the probe as close as possible to the plane of the imaging detector (Cf. Figure 13). The probe must be placed at the center of the imaging detector and, most importantly, its position must be marked (preferably on the detector) to ensure reproducibility. For data acquisition, the exposure parameters for a standard patient are used, following the manufacturer's recommendations. The measurement of the $K_{a,i}$(FDD) allows the calculation of another interesting dose index: D_{FOV}. The latter takes into account the geometry, size of the field of view, and rotation angle. This quantity represents the average dose calculated across the diameter of the FOV. It can be calculated using the following formula:

$$D_{FOV}[mGy] = K_{a,i} \frac{\frac{(FDD) * b}{a} * d}{c} \quad \text{[Eq. 13]}$$

Where a represents the distance from the focal spot to the isocenter, b the distance from the focal spot to the place of measurement, c the horizontal diameter of the scanned volume, and d the horizontal diameter of the radiation field at the place of measurement (Cf. Figure 14).

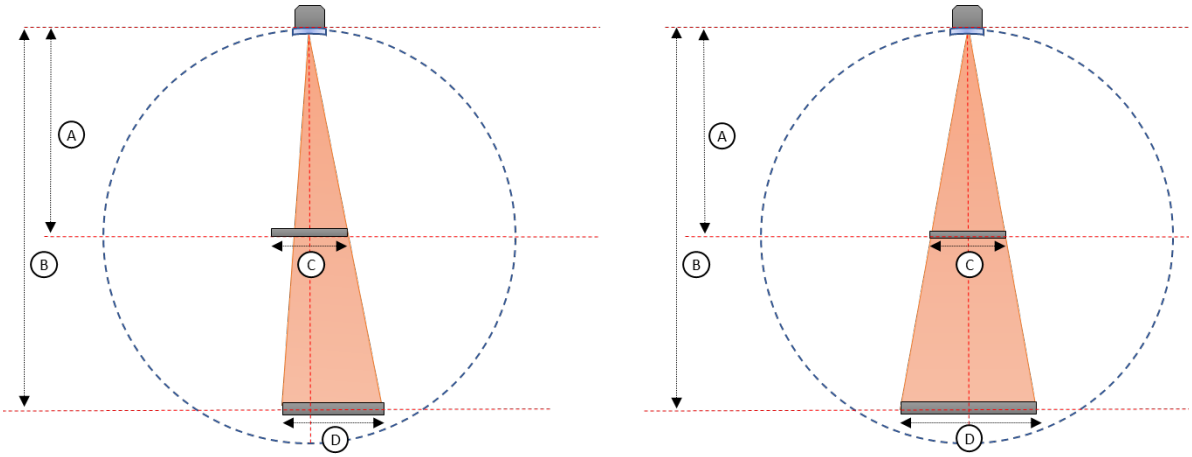

Figure *13*: Description of the quantities a,b,c,d for an acquisition in Full fan (left) and half fan (right).

CTDI: This method is well-known since it is the standard method in CT to assess the in-phantom (head or body) dose, based on the measurement of a 100 mm long pencil ionization chamber in a PMMA phantom.

DSBI: As for the CTDI, a head or body phantom, and a 100 mm pencil ionization chamber are required for measuring the DSBI. It is recommended to use an additional scattering volume in superior-inferior to collect the entire scattered photons dose in the irradiated volume and avoid dose underestimation [6,

32]. The difference is that the DSBI is obtained by dividing the DLI by the sensitive length Lc of the 100 mm IC [Eq. 15].

$$DSBI\left[mGy\right]=\frac{1}{L_c}\times DLI \qquad \text{[Eq. 14]}$$

Dw(AAPM TG number 111): This method uses a point detector (0.6 cc Farmer IC with a sensitive volume of 24 mm of length and 3.2 mm of radius). To meet the AAPM TG111 requirements, it is necessary to perform central and peripheral measurements in a PMMA phantom of 32 cm in diameter and 45 cm in length (Cf. Figure 15). A custom insert is required to place the Farmer chamber in the center of the phantom without the presence of an air gap. Unfortunately, this method can only be applied to protocols with a 360° rotation of the arm and requires a calibration of the Farmer IC for different half-attenuation-layer (HAL). In addition, a correction of the temperature and pressure is performed on the measured charge q to convert it into dose in the medium using the following formula:

$$D_w\left[mGy\right]=q\times N_k\times\left(\frac{\mu}{\rho}\right)_{air}^{material} \qquad \text{[Eq. 15]}$$

Where Dw is the dose in the medium, q is the collected charge, Nk is the calibration factor, $\frac{\mu}{\rho}$ the mean massic absorption factor.

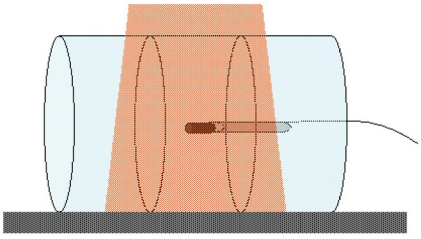

Figure *14*: PMMA phantom of 32 cm in diameter and 45 cm in length made with a point dosimeter placed in the central insert.

IAEAw method: The International Atomic Energy Agency (IAEA) HUMAN HEALTH REPORTS No. 5 methodology is based on the measurement of a CTDIref in a reference collimation (under 40 mm long, e.g. 20 mm) with a 10 mm pencil IC in a PMMA phantom (Cf. Figure 16). The CTDIref is then multiplied by the ratio of the CTDI in the air under the conditions of the tested protocol and the CTDI in the air at the reference collimation width (e.g. 20 mm) to obtain the IAEAw for a given protocol [Eq. 17]

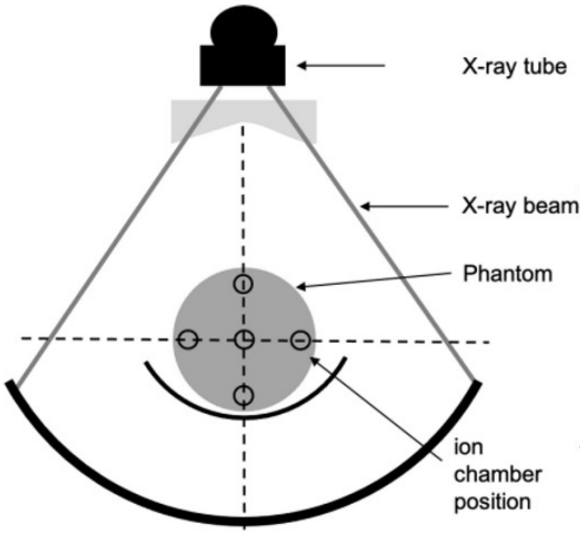

Figure *15*: Demonstrating position of ion chamber in x-y for all free-in-air measurements.

In the case of collimations exceeding the length of 4cm, when using the 100 mm pencil IC, the dose is underestimated[46, 57, 126]. In this case, it is then necessary to perform several acquisitions (3 to 5) by incrementing the position of the chamber at each acquisition to obtain an acquisition length of between 300 mm to 500 mm. The DLI obtained for each position is summed and then divided by the total collimation in the superior-inferior axis to obtain the CTDI in the air at the investigated collimation.

$$CTDI^{-air}_{protocol\,width}[mGy] = \frac{\sum_{i}^{n} DLI_i}{coll} \qquad \text{[Eq. 16]}$$

$$IAEA_w[mGy] = CTDI_{ref} \times \left(\frac{CTDI^{-air}_{protocol\,width}}{CTDI^{-air}_{reference\,width}} \right) \qquad \text{[Eq. 17]}$$

One of the limitations of this method can be the dosimeter activation threshold used. If settled too high, it can result in failing to acquire the low dose from the reference collimation in low-dose protocols.

When comparing the in-phantom methods, it has to be underlined that the CTDI method is suitable only for collimations not exceeding 10cm. Beyond 10cm it strongly underestimates the measured dose because the detection length is too small to capture the entire field profile and the phantom is too small to integer the whole scattered dose along the entire beam length. As CBCT protocols often have a conic shape along the z-axis with collimation exceeding 15cm, it appears that the dose distribution inside the CTDI phantom or the patient would take an ovoidal shape instead of a homogeneous cylindrical shape as it can be seen in CT dosimetry. Therefore, the CTDI is not the optimal indicator for CBCT dose measurement. Below 10cm the DSBI method underestimates the dose since it is divided by the sensitive length (100 mm) instead of

the collimation. Above 10 cm the DSBI method is an effective indicator of the CBCT dose despite a slight underestimation of the dose indicated by Buckley et al.[32] due to the lack of scatter volume. In addition, the DSBI method using a CTDI phantom shows relatively good agreement with the TG111 despite the lack of scatter mentioned by Buckley et al[32]. This method, although performing well for large collimations, is not suitable for a standardized CBCT dose measurement strategy because of its incompatibility with rotations of less than 360° (which may represent almost half of the available CBCT protocols). The IAEA report n°5 method shows a very small underestimation of the dose for collimations above 10 cm[32].

In-phantom dosimetry has two main issues: i) most of the phantoms used are not large enough to accurately mimic the radiation scatter from the large x-ray fields used in CBCT (larger phantoms are not commonly found), ii) positioning the phantom in a reproductive way can be difficult. However, instead of using phantoms, QC measurements can be done by obtaining a detailed description of the x-ray beam geometry from the manufacturer, which can be used to assess the radiation output and estimate patient radiation dose for a given unit. The air Kerma can also be used for regular and quick measurements of x-ray tube output. In the end, it has to be reminded that each of these formalisms can be helpful for a QC approach, but none of them are sufficient for determining patient radiation doses.

Regarding the patient dose in CBCT, there is presently no consensus on the standardization of dosimetry. Numerous studies have been published investigating the dose and dosimetry formalism regarding CBCT patient dose[118]. In-phantom quantities previously mentioned were proposed, along with the effective dose which seems to be the preferential choice when assessing patient dose[88]. Although, the use of the effective dose quantity can be questionable if the purpose is to report or add the imaging doses to the planning doses using the same dose quantities. For this reason, the patient imaging dose can be described as an organ dose [Gy] or an effective dose [mSv]. According to the review works of the EFOMP- ESTRO-IAEA[88] and Marinello et al.[118], the following table (Cf. Table 2) summarizes the $DSBI_w$ calculated from different CBCT manufacturers and protocols for the pelvic and thoracic area.

Table *2*: Example of $DSBI_w$ per exam for CBCT protocols.

CBCT Protocols	$DSBI_w$ [mGy]
Pelvis[88]	21.57 (Varian) 24.13 (Elekta)
Prostate[88]	17.2 (Varian)
Chest[88]	6.1 (Varian) 16.62 (Elekta)
Pelvis[118]	25
Spotlight[118]	25
Low dose chest[118]	7

Despite the variations of dose between manufacturers, both reviews accord on the dose range delivered. In addition, according to Marinello et al.[118] the dose from 3D MVCT is 10-100 mGy per acquisition and can reach up to 1.5 Gy at the end of a 30 fractions radiotherapy treatment.

While the question of dose from kV-imaging and MV-imaging in RT is still a matter of debate, other systems allow the imaging and repositioning of patients during RT treatments without irradiating the patient. These systems present the main advantage that they do not deliver doses to the patients while acquiring images or information with a sufficient level of confidence to reposition the patient. As they are outside the scope of this thesis work, they will not be developed in this manuscript.

II.D. Commercial dosimeters available and their limitations

II.D.1. Ionization chambers

One of the most commonly used dosimeters is the ionization chamber (Cf. Figure 18). It is made of a cavity of air or liquid between two parallel metallic electrodes on which a potential difference is applied to create an electric field in the volume. The space between the two electrodes filled with the gas or the liquid defines the sensitive volume of the chamber. Under the effect of ionizing radiation, the sensitive volume is ionized and the charges thus created will migrate toward the electrodes (Cf. Figure 18). The collected charges are measured by an electrometer connected to the ionization chamber. The number of charges collected in the cavity is then associated with an absorbed dose in the cavity and subsequently with an absorbed dose in the water.

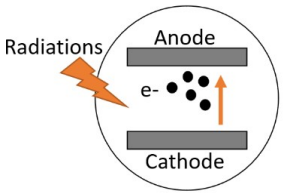

Figure *16*: Section of an ionization chamber general representation.

The ionization chambers offer a lot of advantages such as low dependency on energy, dose, and dose rate. Depending on the application, the sensitive volume and the shape of the ionization chamber can vary from cylinder to plate shapes with volumes from 0.6 cm^3 (Farmer, PTW)) to 0.007 cm3 (Micropoint A16, Exradin). In practice, due to the variety of volumes and shapes of detection available, these detectors are very polyvalent and therefore can be used for reference or relative dose measurement, and consistency checks (e.g. dose calibration, daily dose consistency check, dose quality assurance).

II.D.2. Semiconductor technology

These dosimeters are composed of a P-N junction made of a doped semiconductor P (positive carriers: holes) and a doped semiconductor N (negative carriers: electrons). The electrons are driven towards the P junction and conversely for the holes towards the N junction. The junction of these two semiconductors gives rise to a depletion zone (without free charge carriers) between the two semiconductors (Cf. Figure 19). Following the interaction of radiations with the depletion zone, electron-hole pairs are created and, under the action of an electric field, will migrate toward electrodes placed on each side of the junction. The electric current thus created by the displacement of the charges is then measured by an electrometer.

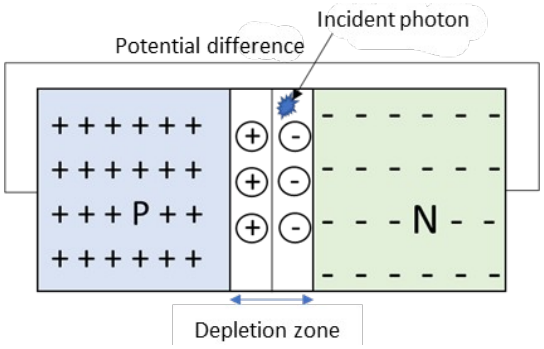

Figure *17*: General representation of a semiconductor dosemeter.

II.D.2.a. Diode

One type of semiconductor detector used in radiotherapy is the diode detector. These detectors can be operated with or without a bias voltage and are typically constructed from silicon, which has an atomic number Z = 14. Diode detectors are commonly used for in-vivo dosimetry (IVD) in radiotherapy due to their

ease of use, high sensitivity, capability for real-time measurement, and shapes. Despite a good reproducibility of response (standard deviation of ≈ 1 %[143]), the diodes lose sensitivity during irradiation (about 0.7 %/kGy[110]) and must be recalibrated regularly. Their sensitivity also shows a strong dependence on temperature since it varies up to 0.35 % per degree[158, 143, 110, 81]. Due to the high Z, the diodes over-attenuate low-energy photons resulting in an overestimation of the absorbed dose measured in Silicon compared to water (up to 11.5 %)[166].

II.D.2.b. Diamond detectors

The synthetic diamond detector has recently been introduced in radiotherapy. Its low sensitive volume and its atomic number (Z=6) close to that of water make it a detector of choice for small beam dosimetry. It works on the same detection principle as diodes due to the presence of P-N junctions and does not require an applied voltage. It has a dose rate dependence of up to 3.2% and requires pre-irradiation before use[49]. Without this pre-irradiation (which varies depending on the diamond detector model) the current under irradiation is not stable. This is one of the main limitations to the use of the diamond detector for step-and-shoot IMRT applications since this phenomenon leads to an underestimation of the dose between each segment[50]. Natural diamond detectors can also be used in radiotherapy. Due to the differences from one sample to another, the performance varies from one detector to another.

II.D.2.c. MOSFETs

Used for 50 years in space technology, they only appeared very late in medical physics[29]. The MOSFET (Metal-Oxide Semiconductor Field Effect Transistor) can be used in particular for the measurement of IVD. As shown in the following Figure 20, MOSFET dosimeters are composed of 4 electrodes: source, drain, gate, and substrate. The voltage Vt necessary to establish a current between the source and the drain is a known value and is applied between the two other electrodes of the system, *i.e.* the grid and the substrate. Under the effect of ionizing radiation, electron-hole pairs are formed within the silicon dioxide which will cause a rise in the threshold voltage Vt. It is this variation of Vt before and after irradiation that gives the measurement of the absorbed dose in the detector.

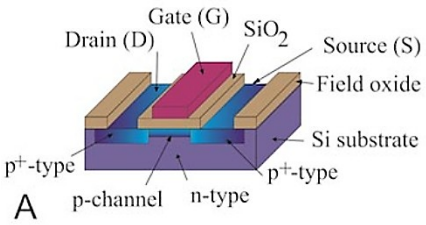

Figure *18*: MOSFET sensitive volume[104]

This detector is not dependent on dose rate, angle of incidence, nature of the radiation, and temperature. Its sensitivity remains stable above 1 MV. Below this value, the sensitivity of MOSFETs decreases rapidly and requires a specific calibration. Due to its small dimensions (MOSFET: 2 mm x 2 mm x 3.5 mm; microMOSFET: 1 mm x 1 mm x 3.5 mm; a sensitive volume of 0.2 mm^2) and its physical properties, this detector is used for the measurement of IVD in external radiotherapy with intensity modulation[30], in brachytherapy[140] and intraoperative radiotherapy[151]. Because of its detection principle based on an increase in threshold voltage, the sensitivity of the detector deteriorates with increasing irradiation (5.5 % up to 20 Gy; 6.5 % up to 74 Gy[30]). Despite a lower cost than diodes, it is not used in the clinical routine because of its limited lifetime, its fragility, and the need for an electronic equilibrium cap to be adapted.

II.D.3. Luminescent dosimeters

Under the effect of ionizing radiation, some solid materials will absorb part of the energy of the incident radiation and be brought to a metastable state (excitation or ionization). The absorbed energy is then restored either by calorific dissipation or by very fast photon emission: Fluorescence (ns) or phosphorescence.

II.D.3.a. Thermo-Luminescent dosimeters (TLD)

During an interaction with ionizing radiation, charges are trapped in the sensitive material. These electrons are retained in these traps until they receive an external excitation that releases them. These charges then emit a pulse of light proportional to the dose of radiation received. The emission of light causes the dosimeter to reset completely. TLDs are used for IVD because of their small volume (about a few mm^3). In addition, they have other advantages, namely that they are isotropic, tissue equivalent, and have no dependence on dose rate and temperature. Nevertheless, their use requires a delicate and time-consuming calibration/reading procedure: an annealing cycle of 1h at 400°C then 2h at 100°C for zeroing before reuse, as well as a 10 min annealing at 100°C to be performed before each reading. Moreover, it is a passive dosimeter, *i.e.* it allows only a delayed measurement of the absorbed dose. Despite this, TLDs are widely used for IVDs or external quality control (e.g. quality control performed by the Equal-Estro (Villejuif, France))[29, 45].

II.D.3.b. Radio photoluminescent detectors

Another luminescence phenomenon used for dosimetry is radio photoluminescence (RPL). Under the effect of ionizing radiation, the natural absorption spectrum of a material will be modified by the creation of absorption bands. However, its energy response is highly variable[86]. To make the reading, the material is subjected to a UV beam and will de-excite, emitting an orange luminescence (600-700 nm) proportional to the dose received. This type of dosimeter can be read several times before being reset by heating at a high temperature. The RPL dosimeter can measure a very wide dose range and has an excellent angular

response[86]. Like TLDs, they only allow for integrated dose measurement and not instantaneous dose[52]. A great advantage of this detector is that it can be read multiple times without a decrease in the measured signal.

II.D.3.c. Scintillating dosimeters

Scintillating dosimetry is based on the photon emission following an excitation in a material (Cf. section II.E). Among the commercially available solutions, the scintillating dosimeters can be divided into two categories: organic scintillators and inorganic scintillators. They can take different shapes (e.g. fibers or plates). For example, the Lynx 2D, based on a scintillating plate and a CCD camera, is used in RT for quality assurance applications. Recently, scintillating fiber detectors are used in RT and radiology[57]. Most often composed of PMMA and polystyrene (PS), scintillating fiber dosimeters are commercialized for quality assurance purposes on conventional Linacs (e.g. Exradin W1 and W2). Numerous studies confirm the use of organic scintillating fibers (e.g. Exradin W1 and W2) for radiotherapy Linac quality assurance applications in the presence of mini-beams or intensity-modulated beams[134, 74, 11]. According to the literature, this detector benefits from a density correction factor of 1 (water equivalent), a small sensible volume, a linear response with the number of doses, and a low dependence in temperature (0,0017%/°C between 6 °C and 50 °C). The W2 can also be used for scanning the irradiated field to characterize it. Inorganic scintillating fibers have also been proposed for similar applications[53]. Favaudon et al. also published[69] on the possible application of scintillating fibers for FLASH-RT and showed encouraging results for FLASH dosimetry beam quality assurance. Among the advantages of optical fiber is its principle of detection. As it is based on the measurement of a light signal, contrary to electronic dosimeters, it does not depend on the applied electromagnetic field. For this reason, scintillation dosimeters are insensitive to EMI, making them a good candidate for dosimetry in the presence of magnetic fields *i.e.* MR-Linac dosimetry. Recent studies have confirmed the scintillating fiber's equivalent or better performances when compared to electronic detectors in the presence of magnetic field variation[116]. If organized in a multidetector array solution integrating scintillating plastic fibers (mPSD) and optimized for High Dose Rate (HDR) brachytherapy, scintillating dosimeters allow localizing the source position during the irradiation[114]. To achieve this, one possible way is to use a single transport fiber for several measurement points, each measurement point using fibers with different emission wavelengths (e.g. BCF-60, BCF-10, BCF-12). Among the brachytherapy applications, BrachyFOD (Sydney University) is a solution dedicated to IVD in HDR prostate brachytherapy[107] with an accuracy on the dose measurement of 3%. It consists of a 16-point measurement (1 mm diameter fibers) placed around the applicator and connected to an electron-multiplying CCD camera. Recently, Archer et al. highlighted a possible application of scintillating detectors for applications in dosimetry and characterization of synchrotrons' treatment microbeam[12]. They have been able to achieve a good spatial resolution up to 10µm. On the other hand, the detector used was still limited by the spurious Cherenkov signals inherent to scintillating detectors. Finally, since it has been showed that Cherenkov signal is negligible when using

protons beam[48], studies have shown an interest in the use of scintillating fiber for dosimetry of protontherapy beams[5, 47, 48]. At the time of writing this manuscript, scintillating fiber dosimeters on the market are dedicated to brachytherapy or high-energy treatment beam quality assurance. None of them is used for IVD or kV dosimetry applications in radiotherapy. The physical principle of this dosimeter is explained in detail in the scintillating dosimetry section below.

II.D.3.d. Optically Stimulated Luminescent detectors (OSL)

Initially used in the medical field for the manufacturing of luminescent memory screens (ERLM), these detectors are also adapted to clinical use in radiotherapy. Most often composed of carbon-doped aluminum oxide ($Al_2O_3:C$), they have an independent response to beam energy, low dependence on dose rate[33] , wide dose range (10^{-7} to 100 Gy), and supralinear response with cumulative dose above 300 cGy[65], independent of angle of incidence, multiple readings possible without total loss of the measured signal (0.05% loss per reading)[98]. Very comparable to RPL, the reading is not done following a UV beam but following an illumination between 400 nm to 700 nm with a peak at 475 nm inducing a luminescence at 410-420 nm[29]. Illumination can be performed in two modes: continuous mode (simultaneous illumination and reading) and pulsed mode (asynchronous illumination and reading).

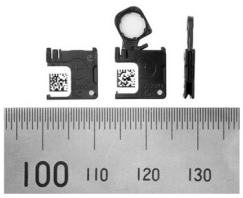

Figure *19*: OSL detectors.

One of the main advantages of this detector is its dimensions of 10 mm x 10 mm x 2 mm and sensitive volume of 5mm diameter and 0.3mm thickness[65] (Cf. Figure 21). Their better light output than scintillating fibers and higher time constant (33 ms) allows correcting the Cherenkov influence by time discrimination (delicate with fibers because constant = ns) only realizable for Linacs due to the known time pulse information.

II.D.4. Radiochromic films

Although there are two types of films used for ionizing radiation (radiochromic and radiographic), this description will focus only on radiochromic films because of their strong use in radiotherapy. The radiochromic films present on the market are the Gafchromic EBT3 films. They consist of a 27-µm-thick active layer protected on both sides by a 120 µm layer of transparent polyester. Within the active layer, the presence of yellow dye reduces the sensitivity to light polluting the measurements. Under the action of

ionizing radiation, the component present in the active layer undergoes a polymerization reaction: this chemical reaction results in a change in the optical density at the film level, *i.e.* a blackening. It is thus possible to link a certain blackening to a dose received by the film, provided that the film batch is calibrated beforehand. Another innovation is the presence of microscopic silicon particles in the polyester layer, which also prevents the formation of "Newtonian circle" artifacts on the film image. Despite this, they must be handled with care by the user to avoid fingerprints, scratches, or accidental irradiation. Moreover, the conservation of films requires particular attention concerning light, temperature, and humidity. The films have an excellent spatial resolution (<1 mm after digitization) and allow access to a 2-dimensional dose measurement. However, it is limited by the scanner used for the reading (spatial resolution, response non-uniformity). The reading is carried out according to a channel of color (red, green, blue). If one supposes that the defects of non-uniformities of the scanner and the film do not impact the 3 channels at the same time, it is possible to compensate them with a multi-channel reading[121]. In addition, Gafchromic EBT3 films have an atomic number (Z = 6.73) close to the effective atomic number of water (Z = 7.3). They have a measurement range from 1 cGy to 40 Gy and have a low energy dependence.

II.D.5. Transit dosimetry

With the increasing use of techniques such as IMRT, VMAT, Tomotherapy, and radiotherapy in stereotactic conditions, most of the detectors mentioned above do not allow a good estimation of the dose received by the patient in the presence of strong dose gradients. Transit dosimetry, based on the use of the portal imager placed in front of the irradiation beam (Cf. section II.C.2.a EPID), allows estimating the dose received by the patient by measuring the fluence. The portal imager is generally made of amorphous silicon (aSi) or semi-liquid cavity ionization chambers.

II.D.6. Main challenges and technical obstacles

Despite showing interesting characteristics, the dosimeters described in the section above have limitations regarding the measured beams, and therefore their application. Table 3 summarizes the detector's main characteristics. Following the technical properties detailed, the two main application limitations observed are the dosimetry for IGRT, and the IVD for intensity-modulated radiotherapy and stereotactic treatment. While this latter limitation is mainly compensated by the implementation of pretreatment QA, the lack of a suitable solution to evaluate the dose from imaging systems for both dosimetric QA and patient dosimetry purposes remains. Even though Monte Carlo simulations have shown promising results[1, 64, 148, 152] for both kV-CBCT and MV-CT devices, the use of Monte Carlo calculations is not yet suitable with utilization for every patient at each treatment fraction.

Table *3*: Main characteristics of the different dosimeter technologies.

Dosimeters technology	Direct reading	Water equivalent	Sensible volume	Dependencies	Main applications	Compatibles for kV-CBCT dosimetry
Ionization chamber	✓	X	Variable	Temperature ; Pressure ; Angulation ; Dose rate	Quality assurance; Commissioning	✓QC
Diodes	✓	X (High Z)	Small sensible volume	Temperature ; Angulation ; Dose rate ; Energy	IVD; Small field dosimetry	X
Diamond	✓	✓	1 mm^3	Dose rate	Small field dosimetry	X
MOSFET	✓	X	0,2 mm^3	Beam nature; Dose	IVD	X
TLD	X	✓	1mm^3	Fading	External quality assurance; IVD	✓ Punctual dosimetry
RPL	X	X (High Z)	/	Energy (keV); Detection threshold	Passive dosimeter	✓ Punctual dosimetry
OSL	X	X (High Z)	5 mm x 0,3 mm	The supralinear response above 300cGy	IVD	✓Punctual dosimetry

The dosimetry technology able to respond to this technical issue must present various characteristics such as live measurement, compatibility with patients and with clinical environment, water equivalence, no or few dependencies (temperature, pressure, angulation, dose rate, energy, beam nature), no or negligible interference with the treatment and the imaging beam. Considering these requirements and the interesting properties of scintillation dosimeters, they appear to be an interesting choice for the development of a dosimeter dedicated to IGRT dosimetry.

In this context, this thesis developed an innovative measurement device capable of measuring the imaging dose and calculating the correspondent dose metric (*i.e.* the air Kerma and the computed dose index (CTDI)) at each kV-CBCT exam. The device, a scintillation dosimeter originally developed for CT applications under the name IVIscan[57], was adapted to radiotherapy kV-CBCT applications to fit a Varian Linac installation. The detector is based on a plastic scintillating fiber (PSF) and a plastic optical fiber (POF) attached underneath the treatment couch. The device also allows monitoring of the output of the X-ray tube for QA and protocol optimization purposes.

To better understand the functioning and limitations of the scintillating dosimeter developed during this thesis, the next section details more precisely the functioning and general principles of scintillating dosimeters and the detection chain associated.

II.E. Scintillation dosimetry: application to organic scintillators

The first step toward the scintillating fiber dosimeter development was a deep understanding of the scintillation dosimeter principles. To this aim, this section provides a detailed reminder of scintillating dosimeters' physical properties and constraints.

Excited molecular states, which lead to fluorescence emissions, are formed by a series of elementary processes. When a molecule is excited or ionized, a hole is created in its electronic structure. This hole can be linked with an electron, forming an exciton. These excitons created in organic materials are unstable and typically convert a small proportion of their energy into radiant energy or luminescence. The release of light is the outcome of a complex series of physical and chemical processes that reduce the energy imparted to the medium by the ionizing particle. These energy degradation steps vary depending on the nature and energy of the incident particles.

Scintillation dosimeters can be used to measure a wide range of radiation doses, from low doses in medical imaging to high doses in radiation therapy and industrial radiography[9, 11, 14, 15, 18–20, 48, 51, 72, 74, 107, 109, 116, 161]. They are particularly useful for measuring doses in real-time, as they can provide a fast response and a high temporal resolution.

II.E.1. Scintillation dosimeters’ history and principles

II.E.1.a. A brief history of scintillation dosimetry

In 1903, Sir William Crookes constructed the first device that utilized a scintillator, called a spinthariscope[111]. It utilized a ZnS screen and the scintillations produced could be viewed through a microscope in a dark room with a count rate of about one per second. In 1909, Geiger and Marsden used this device to study the scattering of alpha particles. Despite being a significant breakthrough, the method was still time-consuming. In 1944, Curran and Baker improved upon the design by replacing the naked eye measurement with a photomultiplier (PM) tube, marking the beginning of the modern scintillation detector[105]. The first practical scintillation-based radiation therapy machine, the "Scintillation Field Unit", was developed by Dr. Robert Wilson at the University of California, Berkeley in 1946. During the 1950s and 1960s, scintillation detectors were used in the development of radiation protection instruments, such as

personal dosimeters, for use in the nuclear industry[105]. In the 1970s and 1980s, scintillation detectors were used in the development of medical imaging modalities such as Single Photon Emission Computed Tomography (SPECT) and Positron Emission Tomography (PET). Scintillation detectors were also used in the development of gamma cameras for diagnostic imaging. In recent years, advances in scintillation detector technology have led to the development of highly sensitive and precise detectors for use in a wide range of applications, including nuclear power plants, radiation protection, and medical imaging. Scintillation detectors are now widely used for radiation detection and imaging in nuclear medicine, radiation therapy, industrial radiography, and radiation protection. Today, scintillation detectors are made from materials like CsI, LaBr3, LSO, and LYSO, which have better light output and energy resolution. These detectors are used in modern technologies like Time-of-Flight PET, SPECT-CT, and high-energy particle detection.

II.E.1.b. Scintillation dosimetry principles

When a molecule is excited or ionized (Cf. section II.A), it creates a hole (h) which represents the absence of an electron in its electronic structure. An electron (of spin ½) and a hole (of spin ½) can be linked together, forming a specific type of excitation called an exciton. These two spin systems can reach various excited states depending on the respective excited states of the electron and the hole. Excited states are described as S_n and T_n respectively for singlets and triplets (Cf. Figure 22). Excitons formed during the irradiation of organic materials are highly unstable and typically convert only a small amount of their energy into radiant energy, or luminescence. This emission is the final stage of a complex set of physical and chemical processes that degrade the energy transferred to the medium by the ionizing particle. This energy degradation process can be broken down into several steps that vary depending on the type and energy of the incident particles.

The very fast excitation phenomenon ($10^{-15}s$) is followed by a decrease of the excitation centers, mainly by internal conversion or vibrational relaxation, to the S_1 state in $10^{-12}s$ (Cf. Figure 22). The phenomenon of visible fluorescence only appears during the deexcitation of the S_1 state to S_0 and lasts about $10^{-9}s$. The gap between these two states (3-4 eV) allows for a temperature dependence (changes in ambient temperature resulting in a variation of 0,025 eV). In addition, the emission energy being different from the absorption energy, organic scintillators are transparent to their radiation. It is also important to note the presence of a second deexcitation mechanism where electrons pass from the S_1 state to T_1 and then from T_1 to S_0. This less common and less useful phenomenon in dosimetry also leads to the creation of emission in the visible but with a longer life of the fluorescence centers (delayed phosphorescence).

The luminescent response (luminescent emitted energy) of a scintillator is described by the following formula:

$$L[eV] = E_{hv} = \langle N_{hv} \rangle \langle hv \rangle \qquad \text{[Eq. 18]}$$

With $\langle N_{hv} \rangle$ the mean number of photons emitted and $\langle hv \rangle$ their mean energy.

The intrinsic efficiency S describes the ratio of energy loss by the ionizing particle $E_{||}$ and converted into luminescent energy:

$$S = \frac{L}{E_{||}} \quad \text{[Eq. 19]}$$

The mean particle loss energy per emitted photons W is then calculated by:

$$W[eV] = \frac{E_{||}}{H_{hv}} = \frac{\langle hv \rangle}{S} \quad \text{[Eq. 20]}$$

And the differential scintillator response dL/dx defines the fluorescent energy emitted by the distance unit traveled by the ionizing particle.

$$\frac{dL}{dx}[eV.m^{-1}] = S\,d\frac{E_{||}}{dx} \quad \text{[Eq. 21]}$$

With $d\frac{E_{||}}{dx}$ the medium stopping power.

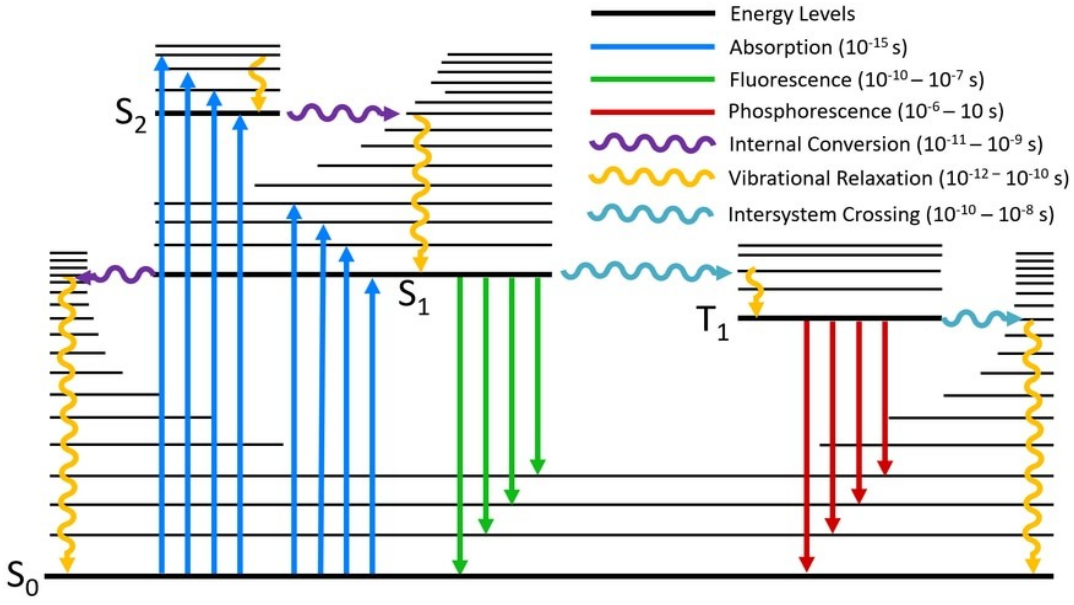

Figure *20*: Perrin-Jablonski diagram.

A scintillation detector is always made up of at least four elements: a scintillator, an optical guide, a photodetector, and a converter. The detection efficiency and linearity between the received dose and the number of detected photons, therefore, depend not only on the properties of the scintillator but also on the entire detection chain. For this reason, when characterizing a scintillation dosimeter, all these elements must be taken into account. The three main photodetectors on the market are the photomultipliers (PM) tube, the charge-coupled device (CCD), and the silicon photomultipliers (SiPM).

II.E.2. Organic scintillators

Scintillators are divided into two categories: organic and inorganic scintillators (Cf. Figure 23). They can take various shapes or states depending on their components. To guarantee a water equivalent measurement, only organic scintillators with a density close to the water were used in this thesis. Organic scintillators can be shaped into almost any desired shape (e.g. sheet, cylinder) or size (from 125 µm), and are relatively low-cost to produce, which can be useful for a variety of applications. However, organic scintillators also have some limitations. One limitation is that they are known to show light output saturation when exposed to very high energy density. This means that when exposed to very high levels of radiation, the scintillator will reach a point where it can no longer emit more photons, making it potentially less useful for detecting and measuring high-energy radiation.

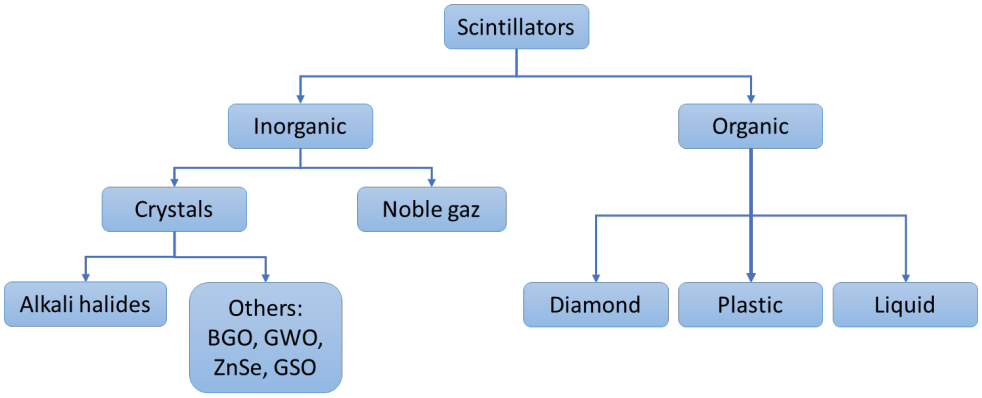

Figure *21*: Scintillators classification.

In addition, organic scintillators have generally a better scintillation decay (a few ns) than inorganic scintillators (from a few ns to 10 ms). Organic scintillators can be either liquid or solid. Among solid organic scintillators, plastic scintillators are generally made of a base (polystyrene $(C_8H_8)_n$) to which organic fluorine is added (fluors). Moreover, plastic scintillators also present a high degree of durability. The most frequently used base materials are polymers containing aromatic structures, with a distinction between scintillators made of polyvinyltoluene (PVT) and scintillating fibers made of polystyrene (PS) being the most widely common examples. The relatively low yield and poor transparency of these materials to their own emitted light

necessitate the incorporation of fluors to construct a functional scintillator. In addition to aromatic plastics, PMMA is also commonly used as a base material, owing to its high transparency to ultraviolet and visible light, as well as superior mechanical properties and increased resistance to brittleness. However, PMMA lacks inherent fluorescence, which can be mitigated by the inclusion of an aromatic co-solvent, such as naphthalene, resulting in a scintillator with improved transparency to emitted radiation and more efficient light collection. The fluors (or luminophores) are capable of absorbing the ultraviolet radiation emitted by a base and re-emitting it at a longer wavelength. This conversion of ultraviolet radiation into visible light improves the transfer efficiency of the light. The addition of a second Fluor, known as a spectrum shifter or converter, can further enhance the attenuation length and result in the emission of blue or green light. Among the shapes available for scintillators and in particular, for organic scintillators, optical fiber is one of the most promising for dosimetry applications. The following section gives a detailed description of the plastic fibers.

II.E.3. Plastic fibers

The first POF was developed by DuPont in the early 1960s and was made of PS and acrylics[163]. It had a high loss (between 500 to 1000 dB/km) and was mainly destined for illumination or automobile applications. It was years later, in 1978, when DuPont sell the POF business to Mitsubishi Rayon in Japan that they have been able to reduce the loss of the PMMA fibers to close to 150 dB/km at 650 nm[163]. More recently, several teams have demonstrated the utility of POF for medical dosimetric applications[7, 9, 10, 14, 15, 18, 19].

II.E.3.a. Clear fibers

Clear fibers, also called waveguide fibers, present many advantages compared to silica (inorganic) fibers such as lower cost, lightweight, higher flexibility, immunity to electromagnetic interference (EMI), and minor radio-induced luminescence[154] (in addition to other parasite signals present in all fibers, silica fibers emits photons from UV to 690 nm when exposed to radiations), but they also come with disadvantages such as a high loss during transmission, a small number of systems and suppliers, a lack of awareness among users of how to install and design with POFs. The cross-section of the fiber is occupied mainly by the core which allows the transmission of light. By utilizing a cladding material typically made of PMMA, the core's refractive index can be made greater than that of the cladding, enabling total internal reflection and allowing the transmission of light over a considerable distance. The light can thus be transmitted over a substantial distance. The cladding is also useful to protect the core from abrasion in different diameter sizes (a few tenths of millimeters to several millimeters) and shapes. Additionally, the cladding protects the core against abrasion and is available in various sizes and shapes ranging from a few tenths of a millimeter to several millimeters in diameter.

II.E.3.b. Plastic scintillating fibers

PSF are composed of a core, where the light is produced, and a cladding, having multiple functions similar to the POF's cladding, while simple scintillators only have what would correspond to a core[20] (Cf. Figure 24). To conserve the emitted scintillation photons, the scintillating core and an optical cladding with a lower refractive index ($n_{core} > n_{cladding}$). However, for both types of scintillators, self-absorption may become significant when the scintillator size is large. The core of scintillating fibers contains a combination of fluorescent dopants selected to produce the desired scintillation, optical (e.g. wavelength shifter), and radiation-resistance characteristics. Often, one property is enhanced while another is mildly compromised.

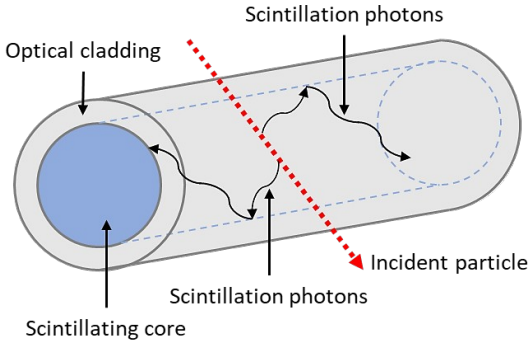

Figure *22*: Section of a scintillation optical scintillating fiber.

Regarding their performances, PSF presents an excellent temporal and spatial resolution. In addition, they allow access to a live dose measurement. The main drawback of these detectors is the presence, beyond a certain energy of Cherenkov radiation (in water, E=175 keV; in PMMA ~200 keV), a parasite signal in the non-scintillating fiber. This spurious signal must be extracted from the overall signal to make a meaningful measurement. The methods available to extract this signal are detailed in the following section alongside the other sources of noise that can be found in scintillation fiber dosimetry. Apart from the noise sources, other challenges and technological obstacles specific to scintillating fiber dosimetry should be considered when it comes to scintillating fiber dosimetry. Among these technical obstacles, the choice of the photodetector and the fiber's response to a high delivered dose should be taken into account since the chemical characteristics of the fiber are affected by the absorbed cumulated dose. These and other technical limitations will be detailed more precisely in the following section.

II.F. Scintillation dosimetry: challenges and technological obstacles

II.F.1. Noise sources in organic scintillators

II.F.1.a. Cherenkov

The Cherenkov effect is the main source of noise in the use of fiber optic detectors in medical physics[107]. As described in the Radiation-Matter interaction section, this phenomenon occurs when a charged particle travels at a speed greater than the speed of light in a medium due to a refraction factor n >1. In plastic scintillating optical fibers (refractive index n=1.48 – 1.6) this phenomenon occurs when the incident electrons exceed an energy between 145 keV and 180 keV. The electrons in the medium will relax by oscillations and emit visible photons. The light created, moving more slowly than the electrons in the medium, will give rise to a wavefront moving preferentially in the direction of the electrons, by constructive interference. The production of photons is emitted in the whole visible range, but the intensity of the emission is higher in the blue, that's why the Cherenkov emission is characterized by the blue color.

Various methods have been proposed to extract the Cherenkov signal from the scintillating fiber-collected light. These methods can be used separately or in combination to improve signal correction. Since the dosimeter developed here is intended for CBCT dosimetry application, the Cherenkov photons correction will not concern the development of the detector. Nevertheless, to assess the main issues present in plastic fiber RT dosimetry, a short description of Cherenkov and its correction methods is necessary. In that aim, the following section describes the methods existing to extract the Cherenkov signal[17, 19, 112, 18].

Subtraction Method: This technique consists in juxtaposing two collecting optical fibers next to each other with only one of the fibers coupled to a scintillating fiber[17, 19, 112]. The basic assumptions of this method are that the light collected by the "clear" fiber (the one without the scintillating element) comes only from Cherenkov radiation and that both fibers are exposed to the same dose. Although very simple, this method is not robust in the presence of strong gradients (e.g. IMRT, VMAT, stereotactic radiotherapy). Moreover, the presence of two optical fibers also implies the presence of at least two acquisition channels which leads to an increase in the detector's size and production cost.

Spectral filtration method: This technique implies partially reflecting the visible light collected while the other part is transmitted using two dichroic filters[51, 73]. As shown in Figure 25 below, the first "yellow" filter reflects the wavelengths below 500 nm (mainly Cherenkov radiation) and transmits the wavelengths above 500 nm to a second "magenta" filter. This one reflects the light below 600nm (mainly scintillation radiation: between 500nm and 650nm). To improve this filtration, De Boerr et al. suggested[51]

coupling it with the subtraction method. Nevertheless, the Cherenkov radiation being emitted on the visible spectrum, this approach does not allow to remove it completely.

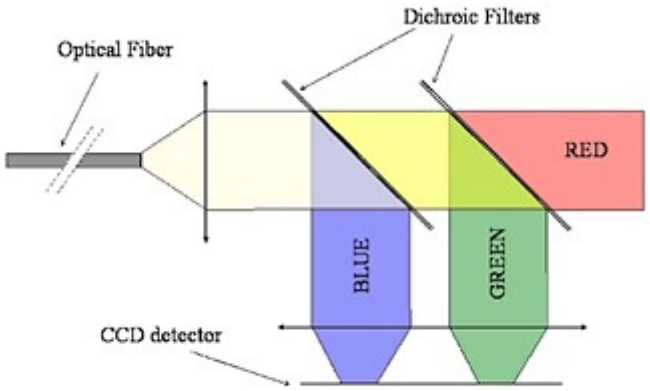

Figure *23*: Cherenkov spectral filtration method.

Chromatic filtration method: This method proposed by Fontbonne et al.[70] is based on the principle that the Cherenkov energy spectrum is known and unchanged during the irradiation so it is possible to separate the measurement into two wavelengths: the first one corresponding to the scintillation light, and the second one corresponding to the Cherenkov. By using this method, Frelin et al. proved that it is possible to remove the Cherenkov signal using a CCD camera. Yet, this method is limited by the CCD camera sensibility and temporal resolution.

Gating (temporal filter): This method is based on the pulsed characteristics of the beam produced by the accelerator and on the time constant of the scintillators[42]. It is mostly used for inorganic scintillators due to their longer time constant. The Cherenkov light, which has an extremely short time constant compared to that of scintillators, is separated from the overall signal by filtering the signal emitted right after the accelerator pulse. This method is particularly difficult to implement with organic scintillators because of their low luminescence time constant (about a few ns). According to literature[42], when correctly used, this method allows getting rid of 99.9% of the Cherenkov radiation. However, it requires an exact knowledge of the beam irradiation pulses and the implementation of a complex temporal filtering system. Moreover, the information related to the radiation pulses may depend on the Linac, the irradiation technique, or other parameters.

The air-core optical guide method: Since the Cherenkov signal is due to a parasite signal generated inside the optical guide fiber, rather than trying to reduce it, Lambert et al.[109] proposed to prevent its production by using an air light guide (Cf. Figure 26). A scintillating fiber is connected to an air-silvered core linked to a polymer fiber and a connector. Despite preventing the generation of Cherenkov in the first centimeters following the scintillating fiber, Cherenkov light may be generated in the fiber extension not by

the primary beam but by low-energy scattered photons. The use of a second "background" probe placed at the level of the extension fiber optic allows subtracting of the signal due to Cherenkov by simple signal subtraction. Because of the high attenuation of air, the choice of the length of the optical guide must be made with care. Indeed, the longer the length of the air optical guide, the more signal loss there will be, but there will be less extension optical fiber that will be subjected to scattered photons and therefore less Cherenkov[33, 108]. This solution is preferentially used in small fields because it allows for the reduction of the length of the optical air guide. In addition, this method also has the advantage of being independent of the incident beam angulation.

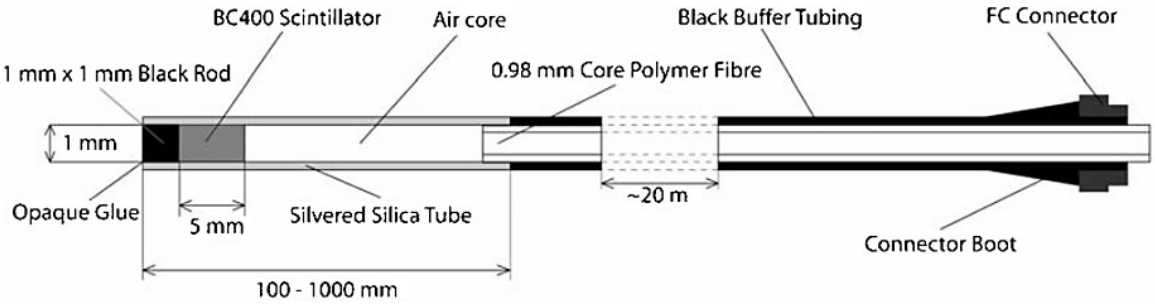

Figure *24*: The dosimeter in cross-section showing the scintillator and the air core silvered tube guiding the signal through the radiation field and the solid core polymer fiber[109].

Another strategy suggested by Archambault et al.[8] is to use a scintillating fiber emitting in a higher wavelength than Cherenkov light. This system would also have to be coupled with a photodetector measuring preferentially this wavelength. BCF-60 fibers commercialized by Saint-Gobain are emitting preferentially in the green. This could be used but it has to be noted that the BCF-60 fibers have a lower emission ratio than BCF-12 fibers (emitting in the blue), reducing also the scintillating light vs. Cherenkov light ratio.

Overall, it appears that the Cherenkov light cannot be effectively corrected by only a solution but by a combination of various methods.

II.F.1.b. Light leakage

This can occur if light enters the detector through the window or the back of the detector, leading to a signal that is not related to the scintillation light. This type of noise can be reduced by using a light-tight housing for the detector or by using light-blocking materials. In the case of fiber dosimeters, light leakage is prevented most of the time by the use of black plastic tubes or other optical insulators.

II.F.1.c. Quenching

Quenching in scintillators refers to the process by which the scintillation light produced by the scintillator material is reduced or suppressed. This can occur in several ways, but one common mechanism is through the formation of excited state complexes between the scintillator molecules and the ionizing radiation. These complexes are formed when the particles transfer some of their energy to the scintillator molecules, which then become excited and emit light. However, if the energy transfer is too large or the scintillator molecules are too close together, the excited state complexes can become quenched, meaning that the scintillation light is not emitted and is instead absorbed by the scintillator material. This results in a reduction of the overall light output of the scintillator, which can negatively impact the performance of detectors that use these materials.

One possible way to reduce the quenching effect is by using scintillators with a short decay time so that they return to their ground state quickly and emit light before the excited state complex can quench. To our knowledge, the quenching effect was not observed in the scintillators used in this thesis.

II.F.2. Radio-Induced Attenuation

When PMMA (which is the main material of scintillating fibers) is subjected to radiation damage, its chemical and physical characteristics are altered[13, 83]. As the PMMA is irradiated, a chemical change occurs in the molecular structures, affecting the physical properties of the material. One example of this alteration is the average molecular weight decreasing with the dose increase. The fracture behavior and the attenuation are the most altered characteristics after irradiation of the PMMA. On a molecular scale, the degradations induced by radiations can be divided into two categories: main-chain scission, and cross-linking. Although both processes happen in polymers, Yoshida and Ichikawa showed that the main-chain scission predominates in PMMA[110]. This mechanism is triggered by the creation of a radical in the side chain of PMMA following the irradiation. This radical forms a precursor for the main-chain scission. When irradiated with ionizing radiation such as the ones used in radiotherapy, a free radical is then generated inside the PMMA ester side-chain and can be described with the following equations.

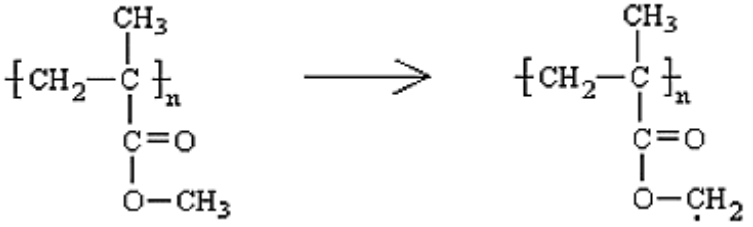

[Eq. 22]

This degradation in the polymer main chain results in an increase in the attenuation inside the PMMA. This phenomenon is called Radio-Induced Attenuation (RIA). It can be described by the Beer-Lambert Law with the following formula.

$$RIA\left[dB.m^{-1}\right]=\frac{-10}{L_0}\log\left\{\frac{P_T(\lambda,t)}{P_T^0(\lambda)}\right\} \quad \text{[Eq. 23]}$$

Where L_0 is the irradiated length of the fiber, $P_T(\lambda,t)$ is the measured optical power in the irradiated fiber and $P_T^0(\lambda)$ is the optical power of the reference fiber.

O'keefe et al. showed how RIA variates in PMMA regarding the delivered dose[129]. They highlighted the dependency of the RIA with the wavelength observed for different deposited doses (Cf. Figure 27). As the dose is delivered to the PMMA fiber, it appears that beyond 30Gy there is a steady, quantifiable increase in the radiation-induced attenuation.

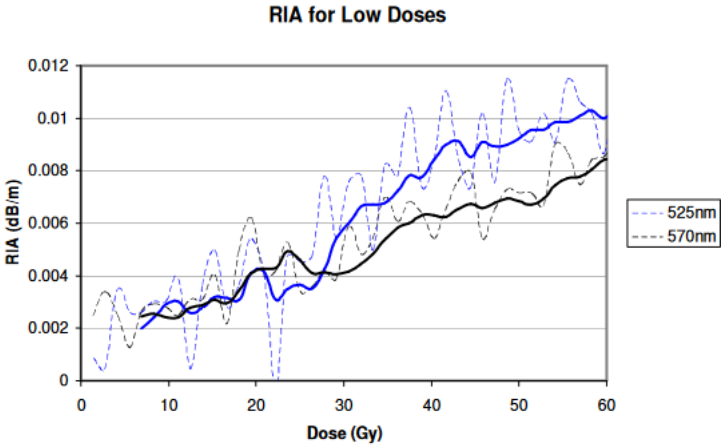

Figure *25*: RIA for doses of gamma radiation between 0 to 60 Gy[156].

Through their observations, they suggested the use of the RIA to quantify the deposited dose into the fiber. As the sensitivity of the PMMA fiber to ionizing radiation is directly related to the wavelength observed (high sensitivity for low wavelength, and low sensitivity for high wavelength), the idea suggested in their paper was to monitor over a wide dose range by selecting high sensitivity or low sensitivity wavelengths[156] (Cf. Figure 28). Saturation occurs after delivering a very high dose (about 10 kGy).

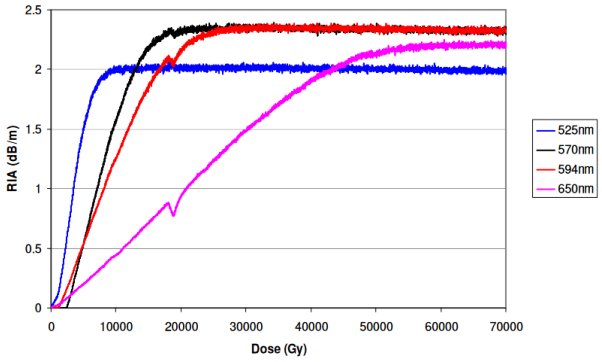

Figure *26*: RIA for high doses of gamma radiation[129].

Another interesting aspect of plastic fibers is the temporal and permanent aspect of the RIA. Kovacevic et al. showed that the plastic fiber starts to recover itself immediately after the end of irradiation but never fully recovers its initial properties due to permanent damage to the polymer (Cf. Figure 29).

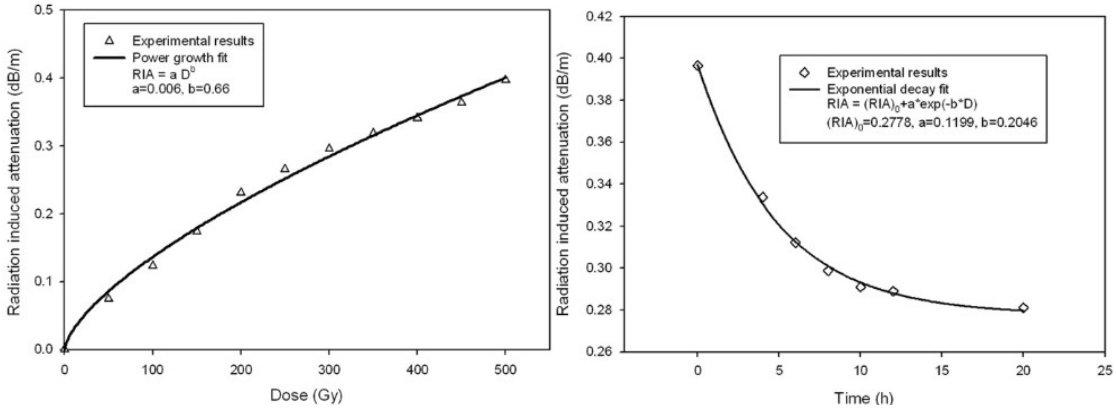

Figure *27*: RIA evolution with dose (right) with time after the end of the irradiation (left)[156].

As the figure shows, the optical signal improves 20 h after the end of the irradiation but doesn't fully come back to its original value. Other studies corroborate the recovering effect in optical fibers[59, 60, 90, 113], even using it to measure the delivered dose in different beams and applications. Di Francesca et al[60]. showed similar results concerning the partial recovery aspect with a 30 dB/m recovery after 22h. The permanent damage to the fiber outlined the necessity to recalibrate the optical fiber dosimeter after physicochemical changes due to the high deposited dose. Based on these, the literature suggests an interest in the use of the RIA as a dosimetric indicator in the presence of high doses[59, 60, 90] (e.g. synchrotron). Nevertheless, this interest is mitigated by the numerous parameters influencing the RIA, such as the wavelength and the fiber composition, but also the dose rate, temperature, or radiation-energy[78].

Following the signal path, from the scintillating fiber through the optical guide made of clear optical fiber, the next important component of the signal chain is the photodetector. Among the photodetectors

commercially available, the ones more suitable for scintillation dosimetry are the SiPM, the PM, and the CCD. Each one is based on different physical characteristics determining their suitability depending on the application. Until now, Fibermetrix laboratories had chosen PMs over SiPMs in their dosimeter development because in 2016 SiPMs were not as efficient as they are now. They opted for high sensitivity (enabling millisecond temporal resolution) with very thin fibers to minimize patient discomfort for in-vivo use in IVIscan. However, due to cost optimization and improved expertise in electronics and probes, we now decided to replace them with SiPMs. The next section provides comprehensive information regarding their physical principle limitations.

II.F.3. Photodetectors

II.F.3.a. SiPM

Based on the interaction of an incident particle with a depletion zone (Cf. Figure 19 in section II.D.1.b), a Silicon photomultiplier (SiPM), which will be integrated into the Fibermetrix technology to replace the current photodetector, is a type of photodetector that uses a large array of tiny avalanche photodiodes (APDs) to detect light (Cf. Figure 30). It is similar to a PM in that it converts light into an electrical current, but it is much smaller in size and more resilient. A SiPM consists of a silicon substrate with a large array of small APDs, typically on the order of tens of thousands or even millions of APDs (depending on the size of the APDs and SiPM). Each APD is a p-n junction diode that is operated in the reverse-bias mode, which means that a high voltage is applied across the diode. When a photon strikes an APD, it creates an electron-hole pair, which is accelerated by the high voltage and can produce a cascade of secondary electrons in the diode, similar to a PM. The silicon then breaks down and becomes conductive, effectively amplifying the original electron-hole pair into a macroscopic current. The electrons are then collected by a common electrode and create a current signal that is proportional to the number of photons detected. This process is called Geiger discharge, in analogy to the ionization discharge observed in a Geiger-Muller tube.

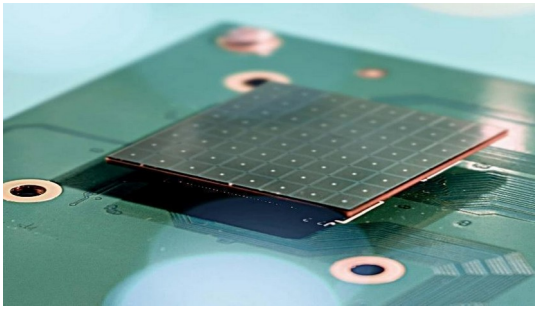

Figure *28*: SiPM.

The main advantage of SiPMs is their small size and high density of APDs, which allows them to detect very low levels of light and have a high sensitivity. They are also relatively robust and insensitive to

magnetic fields, making them well-suited for use in harsh environments. They also have relatively low power consumption and can be operated at room temperature. SiPMs are also very fast, with response times on the order of picoseconds, making them ideal for time-resolved measurements. However, SiPMs have some limitations, such as low quantum efficiency and a higher noise level compared to traditional PM modules. They also require a specialized high-voltage power supply and the output signal is not linear with the number of photons. Additionally, SiPMs are more sensitive to temperature changes and require temperature stabilization to minimize the noise and increase the stability of the measurement.

The SiPM noise sources are separated into three main categories:

- The dark current rate (DCR): This noise comes mainly from charge carriers thermally created in the depletion zone. The dark current limits the performances of the SiPM, especially at room temperature, when trying to detect weak light signals (Cf. Figure 31).

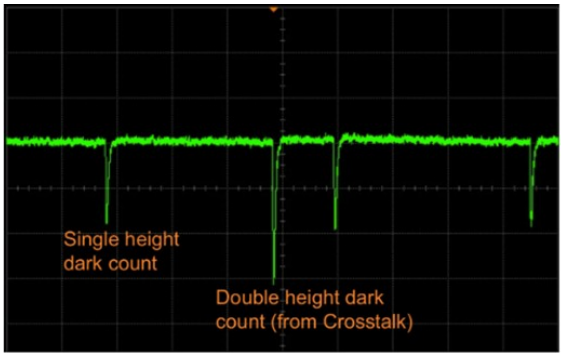

Figure *29*: Dark current counts on an oscilloscope.

- Crosstalk: This noise occurs when a photon escape from a pixel and triggers another pixel next to it, resulting in the emission of a pulse. One way to lower the crosstalk effect is to isolate each pixel from the other. Various ways in which a secondary photon can travel to neighboring microcells (pixels) and cause optical crosstalk are described in Figure 32.

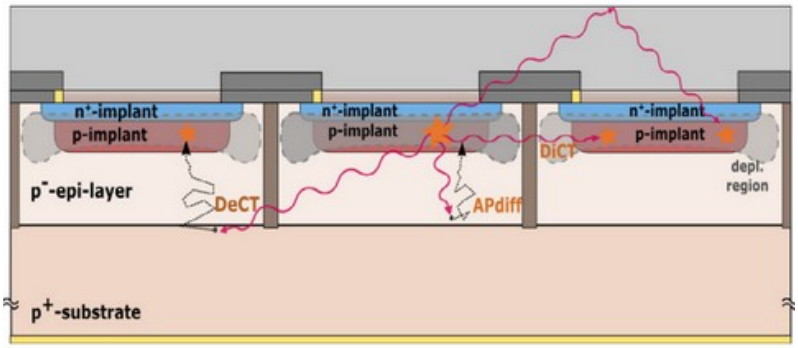

Figure *30*: Various ways of SiPM crosstalk: Direct (DiCT); Delayed (DeCT); Afterpulsing (APdiff); External crosstalk[2].

- After pulses interferences: These interferences are delayed pulses correlated with the main pulse. This delay can vary from several nanoseconds to a few tens of microseconds. The main cause of these delayed pulses is the trapping of electrons in the deep layers of a pixel during the breakdown and their release after the recovery time, *i.e.* after the diode has recharged. The electron thus released can again trigger an avalanche and cause a pulse. One possible cause of electron trapping could be a default during the diode manufacturing process.

II.F.3.b. Photomultiplier tube

PM module, which is the photodetector used in the actual Fibermetrix technology, is a type of photodetector that converts radiation into a measurable electrical signal. It is used in a wide range of applications, including scientific research, medical imaging, and industrial inspection. A PM consists of a vacuum tube with a photocathode on one end and an anode on the other (Cf. Figure 33). The photocathode is a material that emits electrons when exposed to light. When light strikes the photocathode, it releases electrons, which are then accelerated by an electric field toward the anode. The anode is typically made of a metal that can detect electrons and is divided into several sections called dynodes. The electrons that hit the anode produce a cascade of secondary electrons in each dynode. Each dynode is connected to the next one with a high voltage, allowing the electrons to be amplified as they move through the tube. The number of electrons can be multiplied by a factor of 100 or more. At the end of the cascade, the amplified electrons are collected by a final anode and create a current signal that is proportional to the number of photons detected.

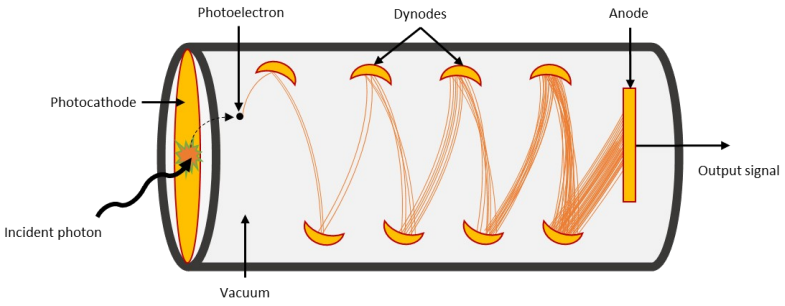

Figure *31*: Photomultiplier tube.

PMs have several advantages over other types of photodetectors, such as high sensitivity, wide dynamic range, and fast response time. They can detect very low levels of light and can detect a wide range of wavelengths. They are also able to detect single photons, making them useful in applications such as particle physics, fluorescence spectroscopy, and medical imaging. However, they are relatively bulky and fragile and require a high-voltage power supply which can introduce noise in the signal.

II.F.3.c. CCD

A charge-coupled device (CCD) is an electronic device that converts light into an electrical charge. The CCD is divided into several sections called a pixel, each of which corresponds to a photosite. These light-sensitive cells (photosites) are made of silicon. Each photosite is capable of collecting and holding a small electrical charge when exposed to light. The more light that falls on a cell, the greater the electrical charge it holds. The number of pixels in a CCD can vary, but most modern digital cameras have millions of pixels. When the CCD is exposed to light, each photosite collects an electrical charge proportional to the amount of light falling on it. The CCD then uses charge transfer to move the electrical charges from one photosite to the next. This process is done in a specific sequence and direction, with the last photosite in the sequence transferring its charge to an output amplifier.

The challenges and limitations presented in this section are particularly present when it comes to RT application but can be found in other applications too. Despite this, Fibermetrix company developed dosimeters for different applications using the unique physical characteristics of the scintillating fibers. The dosimetry technologies developed by Fibermetrix are detailed in the following section.

II.G. Fibermetrix dosimetric solutions

Fibermetrix is a French start-up founded in 2014 specializing in designing and producing advanced solutions to manage radiation risks in medical imaging and radiotherapy. Based on a patented fiber optic technology[168, 174–177], the company developed a dosimetry technology capable of measuring the delivered dose in real-time for patients undergoing CT exams. This detector, commercialized in 2019, is the first real-time in vivo dosimetry system dedicated to CT imaging. The dosimeter, named IVIscan is designed to measure and visualize delivered doses in real-time, detect abnormalities, evaluate and verify the proper functioning of the scanner, and evaluate good practices.

II.G.1. IVI solutions

These detectors are all based on scintillating optical fiber technology. For this reason, they have many advantages such as small dimensions (no or small interference with the incident beam in diagnostic or therapeutic), excellent signal linearity with dose and dose rate, a temporal resolution of 1ms allowing for real-time measurements, density close to water (PS density = 1.05 $g.cm^{-3}$) for water equivalent dose measurements.

II.G.1.a. IVIscan dosimeter

This dosimeter is made of a scintillating fiber 2m long and 2 optical guides made of clear optical fiber[57] connected at each fiber extremities. Both fibers are 0.5mm in diameter and isolated from outside light with an Hytrel sheath of 0.65mm in diameter. The photons emitted by the scintillating fiber are

transmitted to the photodetector by the optical guide through two channels corresponding to the two extremities of the scintillating fiber, before being amplified and transformed into electrical impulses by the photodetection system. The measured electrical signal corresponds to several counts or “Hits” and, depending on several factors, this number of hits is related to a dose deposited in the scintillating fiber using the formula:

$$K_a[mGy] = N_k \times Hits \quad \text{[Eq. 24]}$$

With K_a the Kerma in the air, and N_k the calibration factor.

The IVIscan dosimeter has been validated for quality control and patient dose evaluation on every CT scan manufacturer[124, 77, 82]. Thanks to this detector, the operator can compare the dose estimated by the CT scan calculations with the “real” dose delivered to the patient during the procedure and measured with the dosimeter.

II.G.1.b. IVIyou software

The IVIscan device works with dedicated software[132] where all the calibration and correction factors are configured, allowing the user to assess the dose depending on the patient’s area irradiated (Cf. Figure 34). A color scale from green to red facilitates the visualization of the dose repartition on the volume, along with a CTDI [mGy] repartition visualization depending on the position (Cf. Figure 34). This tool reveals itself very useful since all the CT scans are now equipped with an intensity modulation tool[141] modulating the mA, and therefore the delivered dose, depending on the tissue density. Using the IVIscan detector coupled with the IVIyou dedicated software, studies have been able to detect abnormalities in the dose repartition[137] (Cf. Figure 34) that were not detected by the CT-scan constructor’s dose estimator.

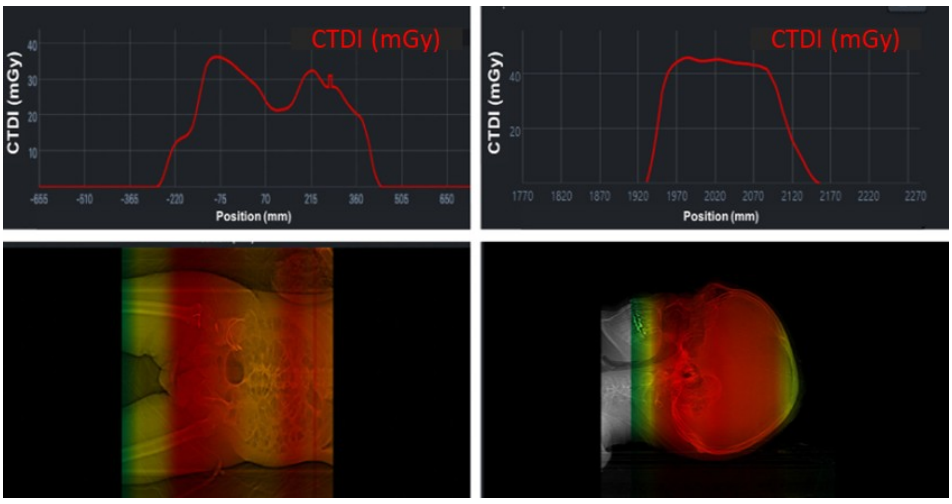

Figure *32*: Dose repartition visualization tool. Up: CTDI depending on the position. Down: Color scale dose visualization tool.

In addition to the visualization tool, the solution also allows for dose superposition and surveillance tools if the patient has undergone a CT exam in the same area several times. Recently, it also has been validated for several acquisition parameters including wide collimation beams, which is a major dosimetric issue in radiological dosimetry[138].

II.G.1.c. IVInomad dosimeter

This dosimeter can have a punctual or linear shape and is mostly used for R&D applications and the characterization of low-energy photon beams. Thanks to its shape and dimensions, it can achieve a spatial resolution of a few mm and can be used in many environments (e.g. conventional or interventional radiology, dental radiology, imaging RT). Indeed, several studies had been done during this thesis work using the IVInomad probe (Cf. Figure 35) and at the time of writing this manuscript, these works have resulted in national and international scientific participation such as oral communications[138] on the characterization of the eye lens dose during CT exams, the characterization of the dose delivered by different CT scanners, and the characterization of dose optimization tools in head CT. A scientific article is in progress on the characterization of the CT dose optimization tools.

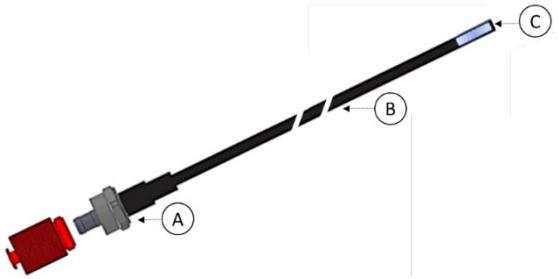

Figure *33*: IVInomad dosimeter. A: SMA connector. B: optical guide (variable length). C: Sensible volume made of scintillating fiber.

Although the development of this dosimeter and the IVIscan design helped in the development of the IVI-CBCT dosimeter, several issues specific to the radiotherapy environment had to be addressed such as the scintillating material response to high delivered dose, the influence of the detector on imaging and treatment beam, and the determination of the useful signal.

II.G.2. Previous validations of the Fibermetrix PSF technology

Previous studies realized by Fibermetrix aimed to investigate the performance of the IVIscan real-time dosimetry system in clinical use[57, 77]. In terms of metrological considerations, a detector should have favorable properties such as repeatability, dose, dose rate, energy independence, minimal angular dependence, independence from prior radiation exposure, minimal radiation damage, and minimal temperature response. For that purpose, they investigated the dosimetric characteristics of IVIscan for energies and filtration used for

CT imaging. These characteristics were repeatability, energy dependence in air kerma, dose-rate response linearity (in air kerma rate), angular dependence, and stability with cumulative doses. They also evaluated the response deviation for different PSF lengths. To achieve the most reliable repeatability, energy, and dose-rate dependence measurements, they needed stable and well-characterized radiation qualities. Considering this, they placed the IVIscan dosemeter in the calibration reference conditions at the CEA LIST LNHB (Laboratoire National Henry Becquerel), which is an independent French primary laboratory for the metrology of ionizing radiation. The references in terms of air kerma are obtained with a free-air ionization chamber, in the domain of low- and medium-energy X-ray dosimetry. For this study, a large panel of radiation qualities was used to cover the entire radiology energy range. More detailed information can be found in ISO4037, IEC61267, and BIPM(RI)I-K3. Most popular CT manufacturers give the 1st HVL values between 5 and 15 mm Al for tube voltage of 70 to 140 kV, corresponding to effective energies between 42 and 100 keV.

Concerning the repeatability, the standard deviation observed was less than 0.039% and the expanded uncertainty of repeatability is between 0.017% and 0.025% depending on the radiation qualities and dose rates used (1.56 $mGy.s^{-1}$ and 0.55 $mGy.s^{-1}$). The uncertainty decreases as the dose rate increases. Given the range of dose rates found in CT imaging, this result demonstrates that the IVIscan dosemeter has very good measurement repeatability over the exposure range of interest in CT imaging.

The energy dependence study[57] realized by Fibermetrix showed a significant energy dependence from +22 to −32 % for the air kerma measurement compared to the RQT9 reference radiation quality for HVL from 6 to 15 mm Al (42 to 100 keV), respectively. This energy dependence is due to the variability of the ratios of the mass–energy-absorption coefficients of PSF to air in this energy range and is fitted here by an exponential law. It is therefore necessary to compensate for this effect in order to give accurate air kerma values in CT imaging with PSF dosemeter technology. Due to the considerable energy dependence, an automatic energy correction factor was included in the calculation of the dose with IVIscan. The correction function was established by considering the values of $N_{k,Q}$ over several batches of IVIscan dosemeters in order to take into account batch variability. After integrating this correction factor, the dose deviations were not exceeding ±2 % when varying the energy and filter of the scanning beam[57].

Following the results of the dose rate dependence study[57], the air kerma rate measured was directly proportional to the tube current, the fitting curves are then represented by a linear function, and the R^2 coefficient is equal to 1 for each one (Cf. Figure 36).

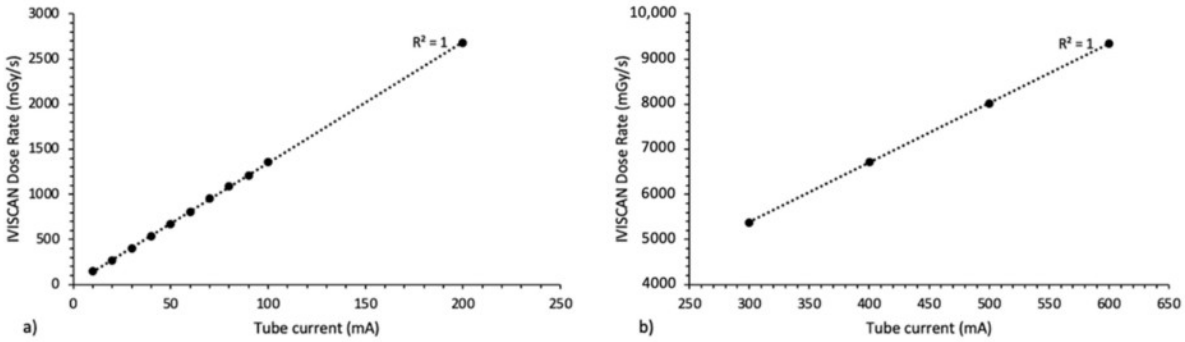

Figure 34: IVIscan response in air kerma rate for the whole range of X-ray tube current for (a) small focal spot and (b) large focal spot, on Canon Aquilion ONE™ Genesis.

The uniformity of the response along the PSF was also evaluated[57]. A comparison between the IVI scan dosemeter and reference measurements based on the z-axis irradiation position reveals a relatively stable deviation ΔDz ranging from -1.1% to +2.7%. These findings indicate good homogeneity in response across the entire exploration area of the CT scan. In comparison, conventional pencil ion chambers exhibit a typical deviation of 3% along a 10 cm probe. As this issue is also present in all the dosimeters involving fibers, it was also evaluated during the development of the IVI-CBCT dosimeter.

II.G.3. Limitations of IVI solutions for IGRT dosimetry

Due to IGRT particularities, the development of a dosimeter for this application requires to fulfill some requirements specific to RT while fulfilling all of the imaging dosimetry requirements. It is all the more true that a dosimeter for CBCT also involves a particular dosimetry methodology for large collimations. For these reasons, in addition to the methodology for large collimations, the following developments were essential when developing the dosimeter.

Firstly, the impact of the dosimeter on the treatment and imaging beams needed to be evaluated as well as the impact of the treatment beam's high doses on the fiber itself. Therefore, the elements of the dosimeter should be adapted to the RT environment and selected to be the more radiotransparent possible. In particular, the splice (made of a metallic tube on IVIscan) must be replaced. Moreover, the RIA of different fibers needs to be evaluated in order to estimate the fibers' resistance and performances in the presence of high cumulated doses. The choice of the probe's components will depend on this analysis. Additionally, the dosimeter's position inside the treatment room must be considered to : (i) collect and transfer the signal from the scintillating fiber to the computer at the treatment desk, (ii) receive the power supply, (iii) not obstructs the medical staff or the patient's movements. Moreover, depending on the length of the probe and its position, the uniformity of the signal generated inside the PSF must be evaluated and corrected if necessary.

Alongside this work, the perennity of each component of the dosimeter needs to be maintained. One of the identified parts concerned by this issue is the PM photodetector as a consequence of the absence of concurrence in the PM modules supplier (Hamamatsu, Shizuoka, Japan, owning 100% of the PM modules and 90% of the PM tubes global market). As a result, a replacement should be found for the PM modules, regardless of the dosimeter application.

Because of these reasons, the IVIscan and the IVInomad dosimeters could not be simply translated as is to IGRT dosimetry and needed supplementary development and characterization. The remainder of the manuscript describes the work realized during this thesis to solve most of the technical limitations identified. Naturally, all the issues and technical obstacles cannot be identified prior to the detector development and are thus not described here. Ultimately, as for every product, other issues will be identified after the commercialization of the dosimeter thanks to the users' feedback and will be corrected accordingly.

III. Experimental development and characterization

III.A. Probe's radiation degradation: Radio-Induced Attenuation

Since the IVI-CBCT detector is intended for an application in high doses environment, the detector had to maintain a certain level of performance in the presence of a high dose or high dose rate. For this reason, the RIA has been evaluated in the scintillating fiber and the optical guide for a high deposited dose (up to 1kGy) and at a relatively high dose rate at low and high energies.

At the time when this characterization was performed, COVID-19 epidemy was on-course as well as restrictive measures, making access to radiotherapy installations even more challenging than it is under the ordinary situation. For this reason, a significant part of the radiation-induced characterization work has been performed with an X-Ray generator delivering low-energy photons.

III.A.1. Irradiation devices and methods

The RIA measurements were performed at the Fibermetrix laboratory, at Entzheim in France, using a Faxitron X-ray generator (Faxitron bioptics, Tucson, Arizona, USA) made of a COMET AG CH-3097 (Comet X-Ray, Flamatt, Switzerland) X-ray tube (Cf. Figure 37) with a nominal voltage of 160 kV, a power of 640 W and an inherent filtration of 0.8 mm of Be^4. The X-Ray generator tension [kV], intensity [mA], and irradiation duration [min] can be controlled by an analogical interface on an MP1 controller (Cf. Figure 37) with preregistered irradiation programs or with homemade software. The filtrations were obtained by adding aluminum (Al) thin plates to the tube's exit. The irradiations were performed under controlled temperatures and at atmospheric pressure and humidity.

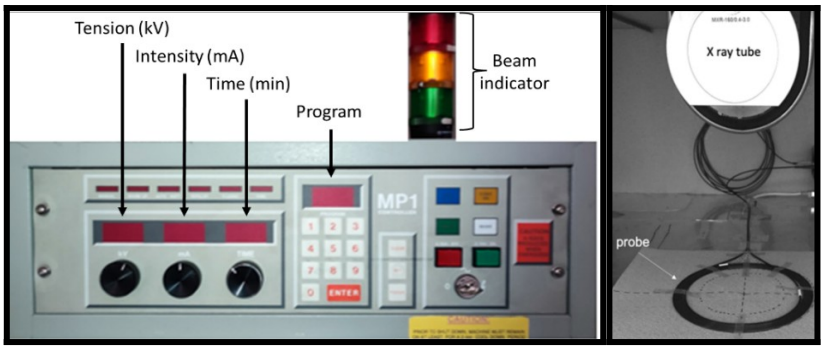

Figure *35*: MP1 X-Ray generator controller (left) and the X-ray tube from the X-ray generator with a fiber positioned in a spiral for the RIA measurements (right).

In a previous study, the X-Ray generator dose rate was evaluated depending on the tension [kV], the intensity [mA], and the variation in time [min] using an ionization chamber for two different aluminum filtrations (8 mm and 13 mm of Al) to find the optimal irradiation parameters. Following this study, the

irradiation parameters were set at 120 kV, 8.3 mA, and 8 mm, of Al and placed at a distance of 18 cm from the source, resulting in a dose rate of 635.5 mGy/min at the detector's position. The fiber probes were irradiated with a dose from 0 Gy to 1 kGy.

III.A.1.a. RIA measurements

The RIA was evaluated for both the optical guides and the scintillating fibers. Concerning the optical guide's RIA, the measurements were realized in total on 3 unirradiated fiber probes that were made specifically for this study. The plastic optical fibers were made of 5 m long and 0.5 mm diameter of BCF-98 (Saint-Gobain, Courbevoie, France) fibers and the extremities connections were made of SMA connectors. Concerning the scintillation fiber, the measurements were performed in total on 6 unirradiated scintillating probes made specifically for this study. The probes were made of 5 m long and 0.5 mm diameter of BCF-12 and BCF-60 (Saint-Gobain, Courbevoie, France) fibers (respectively 3 of each) with peak emissions respectively at 435 nm (blue) and 530 nm (green) (Cf. Figure 38), and the extremities connections were made of SMA connectors. The RIA was studied in both scintillators because the BCF-12 scintillator is supposed to boast higher scintillation outputs and faster decay times compared to the BCF-60 scintillator, while it lacks the radiation resistance found in BCF-60, which includes 3-hydroxyflavone.

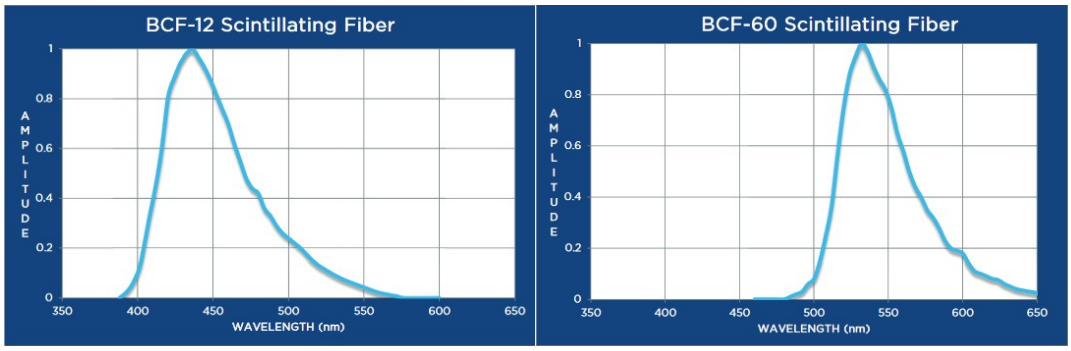

Figure *36*: Emission wavelength of the BCF-12 and BCF-60 fibers.

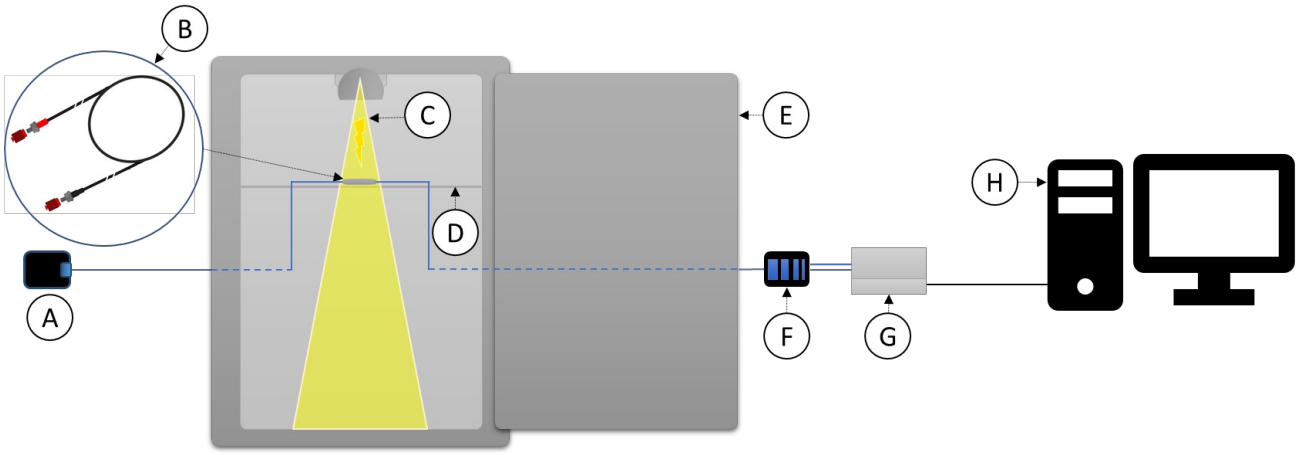

Figure *37*: RIA measurement experimental setup. A: Thorlabs LED light source. B: Zoom on the fiber probe positioned in a spiral shape into the X-ray generator. C: X-ray beam from the X-ray tube. D: 0.8mm plexiglass support. E: Lead radioprotective door. F: Attenuator. G: Fibermetrix photocounting system. H: Computer with in-house signal processing software.

The fibers were arranged into a spiral shape on an 8 mm plexiglass plate to reduce the backscattered dose from the support as much as possible (Cf. Figure 39). One extremity of the fiber is connected to an M455F1 Fiber-Coupled LED (Thorlabs, Newton, New Jersey, USA) with a peak wavelength at 455 nm (Cf. Figure 40), and the other extremity is connected to an attenuator, itself connected by two optical guides (respectively channel 1 and 2) to a Fibermetrix photocounting system.

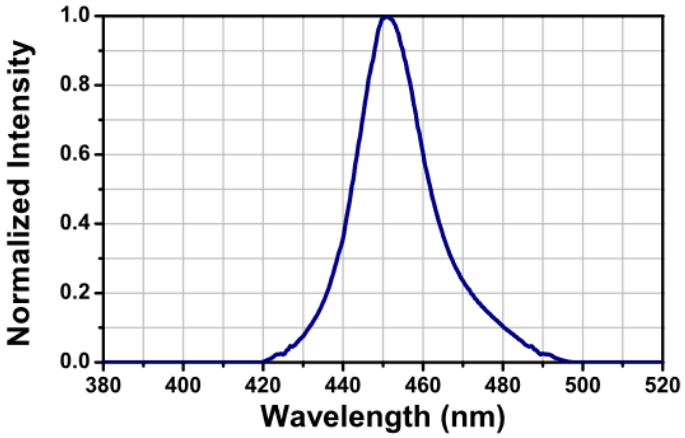

Figure *38*: M455F1 Fiber-Coupled LED spectrum.

The reference signal $I_T^0(\lambda)$ is measured before the first irradiation by measuring the signal emitted by the LED then transmitted through the probe to the Fibermetrix photocounting system. The signal on each channel is defined as the mean value of the hits [counts] measured every 1 ms for a duration of 30 s (Cf. Figure 41). The intensity is measured independently on channels 1 and 2, then the mean normalized intensity and RIA of the two-channel is represented.

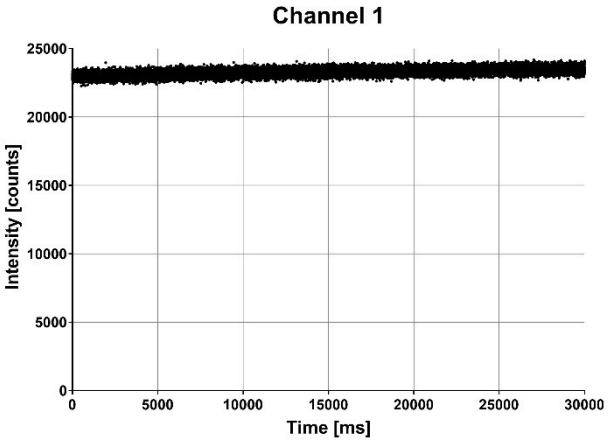

Figure *39*: Example of the measured signal during the 30s with a 1ms sampling.

For each measurement after the beginning of the irradiation, a length L_0 = 1 m of the probe is irradiated by the X-Ray generator and $I_T(\lambda,t)$ is measured as the length L_0 is irradiated at different delivered doses from 0 Gy to 1 kGy. Finally, the RIA is calculated using the following equation:

$$RIA\left[dB.m^{-1}\right]=\frac{-10}{L_0}\log\left\{\frac{I_T(\lambda,t)}{I_T^0(\lambda)}\right\} \quad \text{[Eq. 25]}$$

Where L_0 is the irradiated length of the fiber, $I_T(\lambda,t)$ is the measured light intensity in the irradiated fiber, $I_T^0(\lambda)$ is the reference light intensity of the fiber and λ the reading wavelength of the photocounting system. Figure 42 below shows an example of intensity, normalized intensity, and RIA measured for a probe on channel 1 in function of the dose delivered.

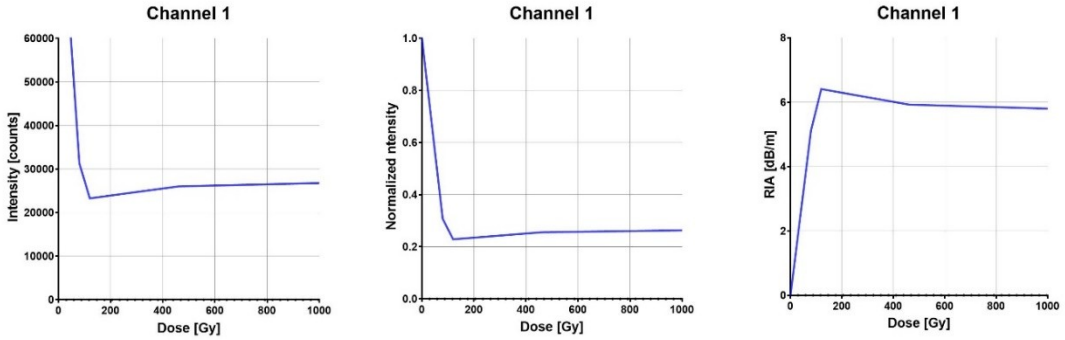

Figure *40*: Example of photometer's channel 1 RIA measurements. From left to right: Intensity, normalized intensity, and RIA are calculated in function of the dose delivered.

A measurement of $I_T(\lambda,t)$ is made at 1 kGy, at the end of the irradiation. This measurement consists of both the last RIA measurement and the first measurement of the probe's recovery properties at T = 0. The

probe's recovery properties are evaluated by measuring $I_T(\lambda, t)$ at different times after the end of the irradiation (T = 0, 1, 6, 20, and 24 h).

In addition, since the RIA is a phenomenon induced by dose deposits, it is right to think that different energy range does not results in the same RIA for the same deposited dose. For this reason, the RIA was calculated using a 6 MV FFF photon beam, at a 600 UM/min dose rate, with a 20 cm x 20 cm field, at a 95 cm Source Surface Distance (SSD) and under 4.7 cm of PMMA plates of 40 cm x 40 cm. The measurements were realized from 0 Gy to 600 Gy using an experimental setup similar to the one described in Figure 39. The same protocol was used in the radiotherapy environment and the recovery properties were evaluated after the irradiation at T = 0 to 14 h.

III.A.1.b. Scintillation decay evaluation

While the previous method is sufficient for evaluating the RIA in the optical guide, it does not give an estimation of a possible radio-induced scintillation loss in the scintillating fiber. To overcome this limitation and evaluate specifically the loss of scintillation alone in the scintillating fiber, a second experimental setup was put in place. This experimental setup consists in connecting both the extremities of the probes directly to the photocounting system and measuring the fiber's scintillation signal without any additional external light source and in function of the cumulated dose deposited in the fiber (Cf. Figure 43). The signal is defined as the mean value of the impulses [counts] measured every 1 ms for a duration of 30 s.

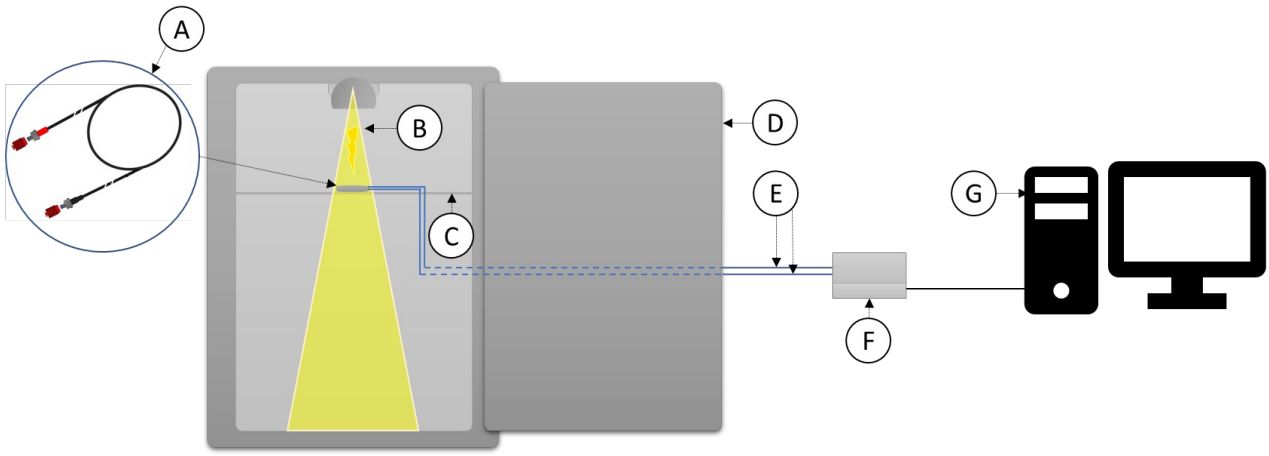

Figure *41*: RIA measurement experimental setup. A: Zoom on the fiber positioned in a spiral shape. B: X-ray from the X-ray tube. C: 0.8 mm plexiglass support. D: Lead radioprotective door. E: Channel 1 and 2 of the scintillating fiber. F: Fibermetrix photometer. G: Computer with in-house signal processing software.

In this configuration, the only signal measured corresponds to the scintillation signal alone. Therefore, the additional part of the attenuation measured in this configuration would correspond to a scintillation difference only. These measurements were performed simultaneously with the previous ones, by switching the

channels. The RIA properties of the fibers used for the IVI-CBCT dosimeter were studied using the methods and equipment detailed above. The results of the study are presented for each type of fiber, with the normalized intensity (NI) measured at different points of the irradiation, then the RIA is presented.

III.A.2. RIA measurements on the optical guide (BCF-98)

In the first place, the study was conducted on the optical guide. Figure 44 shows the variation of normalized intensity (NI) measured for the 3 BCF-98 probes from 0 to 1 kGy.

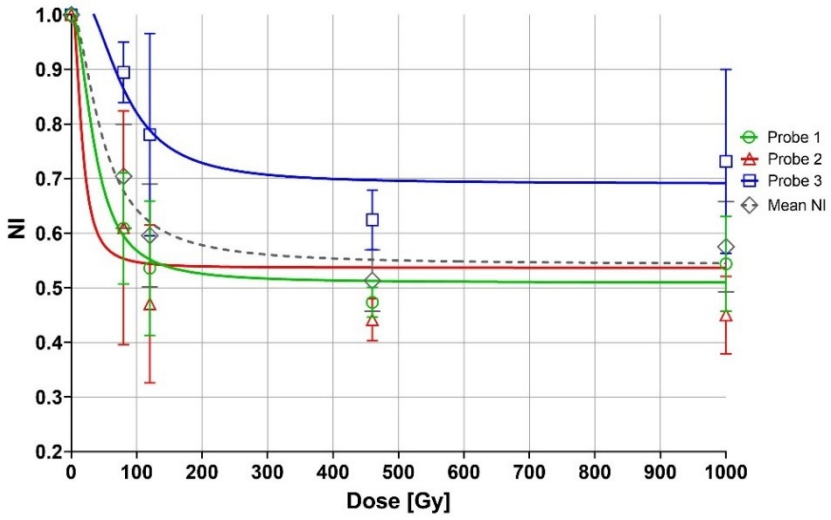

Figure *42*: Normalized intensity (NI) measured in function of the delivered dose for BCF-98 probes. The probe 1, 2, and 3 are represented respectively in green, red, and blue. The mean normalized intensity for the three probes is represented in dashed black lines. The Standard Error of the Mean (SEM) is represented by the error bars.

The probe 1, 2, and 3 are represented respectively in green, red, and blue. For each probe, the mean values for channels 1 and 2 are represented. The mean NI for the three probes is represented in dashed black lines. For all the probes, a relatively quick decrease of 43% of the signal is observed from 0 to 120 Gy followed by a stabilization of the signal until 1 kGy. More specifically, for probe 1 the mean NI fall from 1 to 0.61 at 80 Gy, decreases slowly to 0.54 at 120 Gy, then 0.47 at 460 Gy, and has a slight increase up to 0.54 at 1 kGy. For probe 2 the mean NI fall from 1 to 0.61 at 80 Gy, diminish slowly to 0.47 at 120 Gy, then 0.44 at 460 Gy, and have a slight increase up to 0.45 at 1 kGy. For probe 3 the mean NI fall from 1 to 0.89 at 80 Gy, diminish slowly to 0.78 at 120 Gy, then 0.62 at 460 Gy, and have a slight increase up to 0.73 at 1 kGy.

Figure 45 shows the variation of Radio-Induced Attenuation (RIA) calculated for the 3 BCF-98 probes from 0 to 1 kGy. The probe 1, 2, and 3 are represented respectively in green, red, and blue. For each probe, the mean values for channels 1 and 2 are represented. The mean RIA for the three probes is represented

in dashed black lines. Since the RIA varies as opposed to the intensity (Cf. Eq. 23), it describes the opposite curve of the NI.

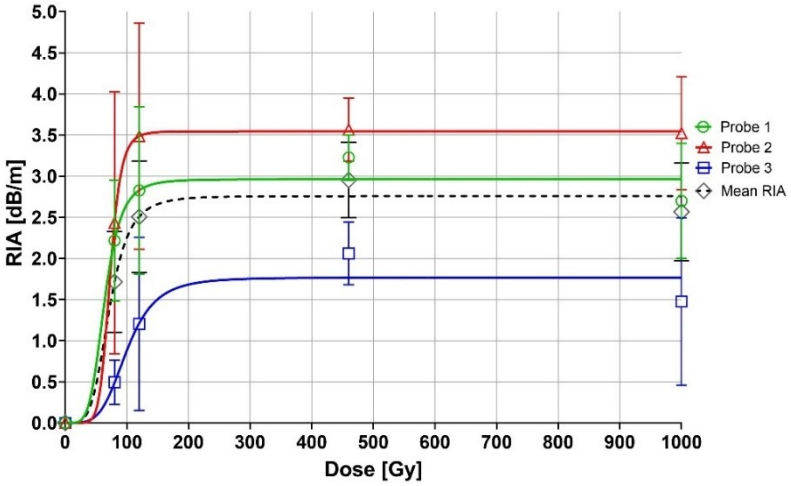

Figure *43*: Radio-Induced Attenuation (RIA) calculated in function of the delivered dose for BCF-98 probes. The probe 1, 2, and 3 are represented respectively in green, red, and blue. The mean RIA for the three probes is represented in dashed black lines. The SEM is represented by the error bars.

As expected following the NI measurements, a relatively quick increase of the RIA is observed from 0 to 120 Gy followed by a stabilization of the RIA until 1 kGy. More specifically, for probe 1 the mean RIA grows from 0 to 2.2 dB/m at 80 Gy, increases slowly to 2.8 dB/m at 120 Gy, then 3.2 dB/m at 460 Gy and has a slight decrease down to 2.7 at 1 kGy. For probe 2 the mean RIA grows from 0 to 2.4 dB/m at 80 Gy, diminishes slowly to 3.5 dB/m at 120 Gy, then 3.6 dB/m at 460 Gy, and has a slight decrease down to 3.5 dB/m at 1 kGy. For probe 3 the mean RIA grows from 0 to 0.49 dB/m at 80 Gy, grows slowly to 1.2 dB/m at 120 Gy, then 2.1 dB/m at 460 Gy, and has a slight decrease down to 1.48 at 1 kGy.

The optical guide, made of BCF-98 shows a stable behavior after a cumulated dose of 200 Gy approximately. The probe's characteristics stop evolving after a cumulated dose value of 460 Gy. Surprisingly, probe 3 presents less attenuation that the two others. This difference in RIA can be due to the high uncertainty associated with some measurement points. Based on these measurements, a systematic pre-irradiation should be required before the fiber’s calibration and installation. The pre-irradiation value, of a minimum of 500 Gy, will be estimated depending on the other fiber’s response to radiation.

The second part of the IVI-CBCT dosimeter is based on scintillating fiber. Two types of scintillating fibers are commercialized by Saint-Gobain, the BCF-12 (blue) and BCF-60 (green), and differ in their chemical composition and physical properties. For example, even if the BCF-12 is the fiber type that is used in the IVIscan dosimeter, the BCF-60 presents better radiation resistance properties and could therefore fit

more to a utilization in RT and high doses environment. For this reason, both types of fibers were tested and are presented in the next two sections.

III.A.3. RIA measurements on the scintillating fiber (BCF- 12)

The following section presents the results of the RIA study on scintillating fibers (BCF-12) used to generate the signal in the IVI-CBCT dosimeter. Even if the scintillating fibers' purpose is to generate a signal following the irradiation, one of the basic requirements is to ensure the generated signal transmission through the scintillating fiber to the optical guide. Figure 46 shows the variation of NI measured for the BCF-12 probe 1 from 0 to 1 kGy. Due to impacts and breaks that happened on the two other probes during the experimentations, almost no signal was measured on probes 2 and 3. For this reason, only probe 1 is represented here.

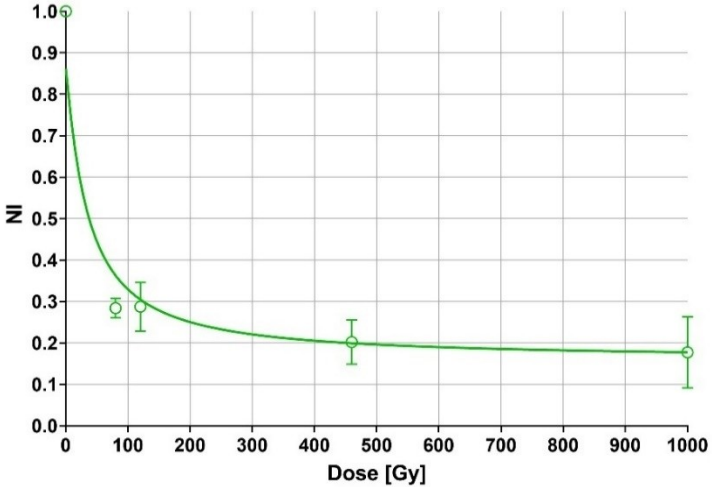

Figure *44*: NI measured in function of the delivered dose for a BCF-12 probe. Probe 1 is represented in green. The SEM is represented by the error bars.

A relatively quick decrease of the signal is observed from 0 to 120 Gy followed by a slight decrease of the signal until 460 Gy. More specifically, the mean NI fall from 1 to 0.28 at 80 Gy, then diminish slowly to 0.20 at 460 Gy and stabilize around this value until 1kGy.

Figure 47 shows the variation of RIA calculated for the BCF-12 probe from 0 to 1 kGy. As for the NI, only probe 1 is represented here.

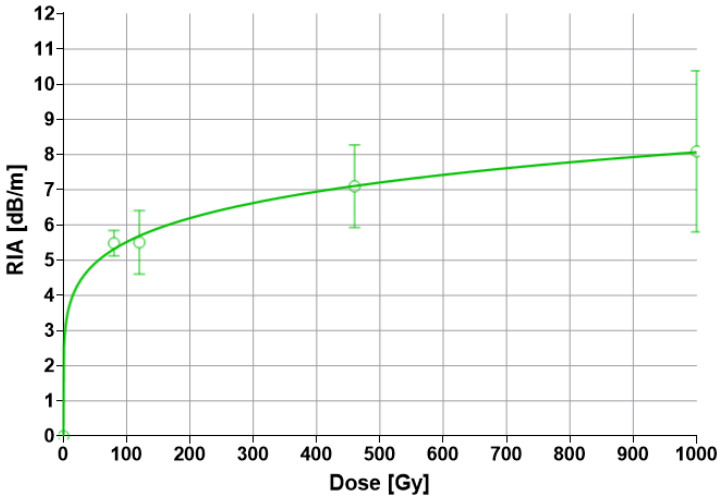

Figure *45*: RIA calculated in function of the delivered dose for a BCF-12 probe. Probe 1 is represented in green. The SEM is represented by the error bars.

A relatively quick increase of the RIA is observed from 0 to 120 Gy followed by a slight increase of the RIA until 460 Gy. More specifically, the mean RIA grows from 0 to 5.5 dB/m at 80 Gy, then diminishes slowly to 7.1 dB/m at 460 Gy and continues to grow up to 8.1 dB/m at 1kGy.

As for the previous fibers, it appears that pre-irradiation is necessary before installing and calibrating the fibers. Even though the RIA grows slower after 500 Gy, its value seems to stabilize after at least 1 kGy of cumulated dose. For industrial use, the BCF-12 and the dosimeters using this fiber would therefore require a minimum pre-irradiation of 1 kGy.

III.A.4. RIA measurements on the scintillating fiber (BCF-60)

Another scintillating fiber type was tested from Saint-Gobain's commercially available scintillating fibers. The BCF-60, Figure 48 shows the variation of NI measured for the 3 BCF-60 probes from 0 to 1 kGy. The probe 1, 2, and 3 are represented respectively in green, red, and blue. For each probe, the mean values for channels 1 and 2 are represented. The mean NI of the three probes is represented in dashed black lines.

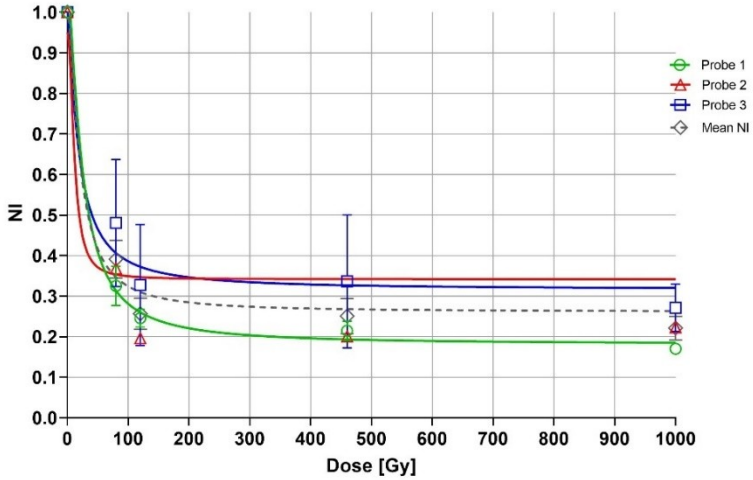

Figure *46*: NI measured in function of the delivered dose for BCF-60 probes. The probe 1, 2, and 3 are represented respectively in green, red, and blue. The mean normalized intensity for the three probes is represented in dashed black lines. The SEM is represented by the error bars.

A relatively quick decrease of the signal is observed from 0 to 120 Gy followed by a slight decrease of the signal until 460 Gy. More specifically, for probe 1 the mean NI fall from 1 to 0.32 at 80 Gy, diminish slowly to 0.25 at 120 Gy, then 0.21 at 460 Gy and have a slight increase up to 0.17 at 1 kGy. For probe 2 the mean NI fall from 1 to 0.37 at 80 Gy, diminish slowly to 0.2 at 120 Gy, and have a slight increase up to 0.22 at 1 kGy. For probe 3 the mean NI fall from 1 to 0.48 at 80 Gy, diminish slowly to 0.33 at 120 Gy, then 0.34 at 460 Gy, and have a slight decrease down to 0.27 at 1 kGy.

Figure 49 shows the variation of RIA calculated for the 3 BCF-60 probes from 0 to 1 kGy. The probe 1, 2, and 3 are represented respectively in green, red, and blue. For each probe, the mean values for channels 1 and 2 are represented. The mean RIA of the three probes is represented in dashed black lines.

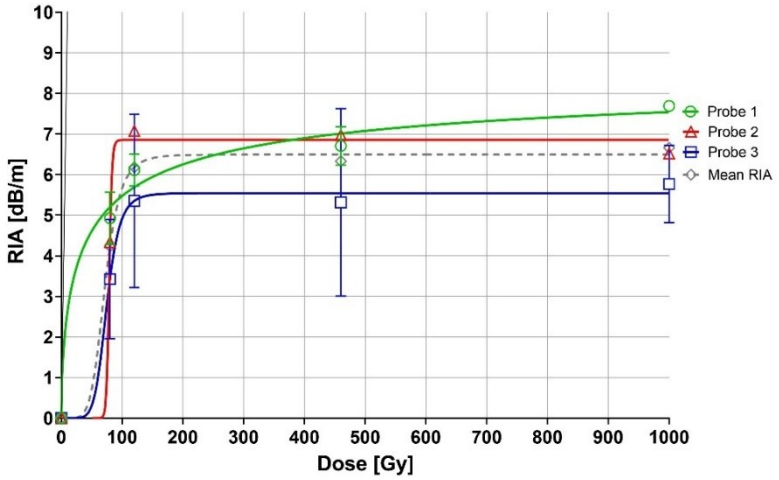

Figure *47*: RIA calculated in function of the delivered dose for BCF-98 probes. The probe 1, 2, and 3 are represented respectively in green, red, and blue. The mean RIA

for the three probes is represented in dashed black lines. The SEM is represented by the error bars.

A relatively fast increase of the RIA is observed from 0 to 120 Gy followed by a slighter increase of the RIA until 1 kGy. More specifically, for probe 1 the mean RIA grows from 0 to 4.93 dB/m at 80 Gy, increases slowly to 6.11 dB/m at 120 Gy, then 6.71 dB/m at 460 Gy, and an increase up to 7.69 dB/m at 1 kGy. For probe 2 the mean RIA grows from 0 to 4.34 dB/m at 80 Gy, increases slowly to 7.08 dB/m at 120 Gy and has a slight decrease down to 6.97 dB/m at 460 Gy and continues to decrease until 6.52 dB/m at 1 kGy. For probe 3 the mean RIA increase from 0 to 3.43 dB/m at 80 Gy, increase slowly to 5.35 dB/m at 120 Gy, then remains stable and has a slight increase up to 5.77 dB/m at 1 kGy. Probe 1 shows a slightly different behavior compared to the two other probes. The slope seems to grow faster in the first Gys delivered. As it was highlighted in the literature[156], even if it increases, the value of the RIA fluctuates considerably between two measurements until 60 Gy approximately.

As for the other type of fibers, pre-irradiation seems to be necessary before installing and calibrating the BCF-60 fibers. The RIA seems to stabilize after between 120 Gy and 1 kGy of cumulated dose. For industrial use, the BCF-60 and the dosimeters using this fiber would therefore require a minimum pre-irradiation of 1 kGy.

In order to visualize all the fibers' RIA on the same figure, Figure 50 shows the mean variation of RIA calculated for the 3 types of fibers from 0 to 1 kGy. The BCF-12, BCF-60, and BCF-98 are represented respectively in blue, green, and red. For each type of fiber, except BCF-12, the mean RIA for three probes is represented.

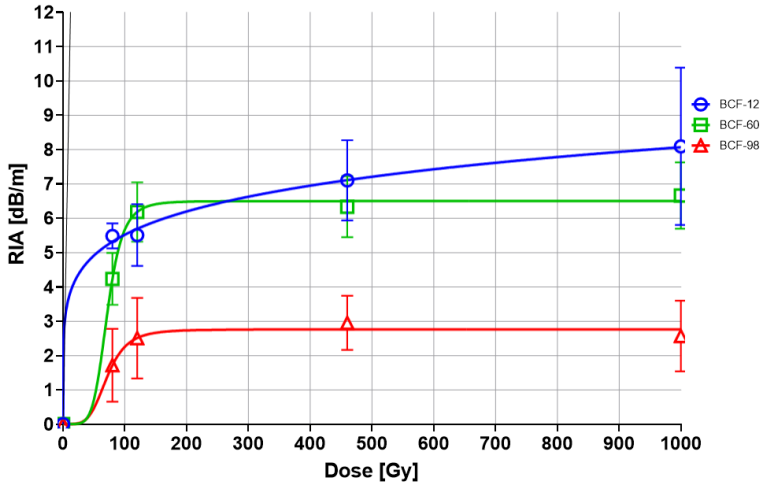

Figure *48*: RIA calculated in function of the delivered dose for BCF-12, BCF-60, and BCF-98 probes represented respectively in blue, green, and red. The SEM is represented by the error bars.

A relatively quick increase of the RIA is observed from 0 to 120 Gy followed by a slighter increase of the RIA until 1 kGy. As expected based on the literature[129, 156], the RIA of the three types of probes grows rapidly until reaching a saturation point. In addition, this rapid growth of RIA for the three types of probes confirms that the RIA is wavelength dependent as it has the same behavior for three probes but not the same amplitude[156]. Although the three types of probes studied show a saturation of RIA at about 120 Gy, it has to be noted that the BCF-98 probes show a significantly lower attenuation than the two others. Moreover, the BCF-12 fiber RIA seems to continue to grow after 120 Gy but at a slowest rate.

Figure 51 shows the mean variation of RIA calculated for the 2 types of fibers from 0 to 1 kGy by taking into account the photons transmitted from the LED added to the scintillation light (solid lines) and the photons from the scintillation only (dashed lines). The BCF-12 and BCF-60 are represented respectively in blue and green.

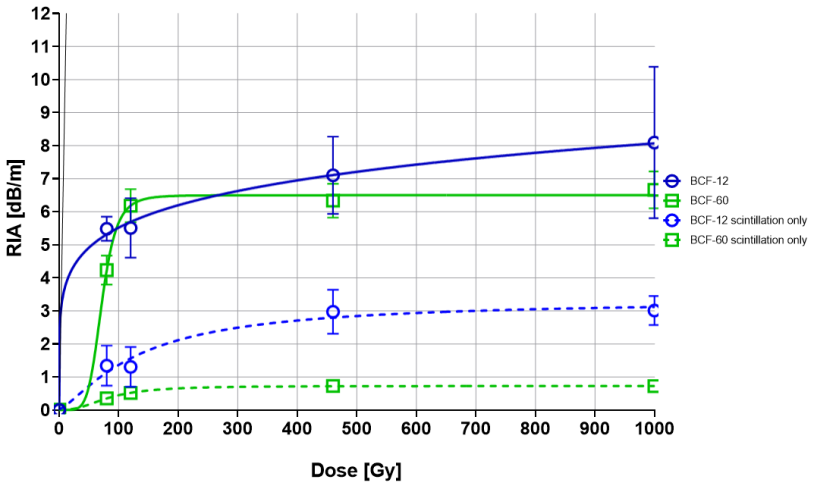

Figure *49*: Mean variation of RIA calculated for the 2 types of fibers from 0 to 1 kGy by taking into account the photons transmitted from the LED added to the scintillation light (in solid lines) and the photons from the scintillation only (dashed lines). The BCF-12 and BCF-60 are represented respectively in blue and green. The SEM is represented by the error bars.

For both types of fibers, a relatively fast increase of the RIA is observed from 0 to 80 Gy followed by a slighter increase of the RIA until 120 Gy and a slow increase of the RIA until 1kGy. Even if describing a similar shape concerning the RIA growth and saturation, the RIA issued from only the scintillation light for the BCF-12 probe is considerably lower than the RIA calculated based on the LED signal transmitted. The same observation is made concerning the RIA from only the scintillation signal for the BCF-12 fiber.

The BCF-60 fiber seems to be less affected by the radiation than the BCF-12 for both transmission and emission (scintillation) components. This radiation resistance is particularly significant when observing the emission component. Moreover, when looking at the BCF-12 RIA slope seems to continue to grow after 1

kGy while the BCF-60 stabilizes after 120 Gy. This difference in radiation resistance is due to the difference in chemical formulation of the BCF-60 which is designed to have a better radiation resistance than other scintillating fibers.

III.A.5. Recovery properties

Figure 52 shows the mean recovery properties of the RIA calculated for the 3 types of fibers from 0 to 24h. The BCF-12, BCF-60, and BCF-98 are represented respectively in blue, green, and red. For each type of fiber, except BCF-12, the mean RIA for three probes is represented.

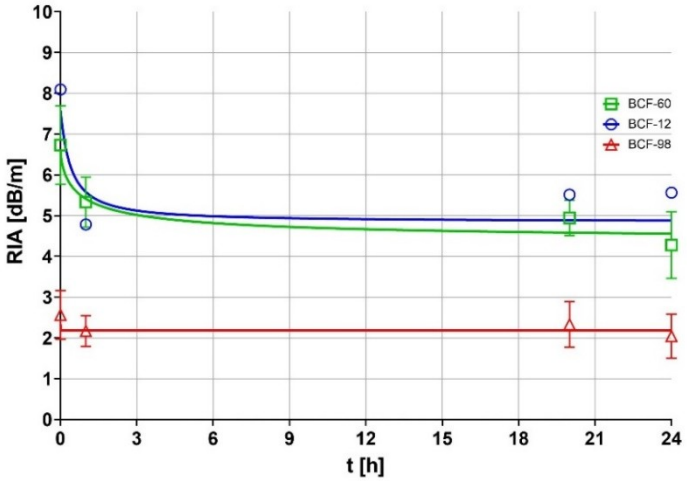

Figure *50*: Mean recovery properties of the RIA calculated for the 3 types of fibers from 0 to 24h. The BCF-12, BCF-60, and BCF-98 are represented respectively in blue, green, and red. For each type of fiber, except BCF-12, the mean RIA for three probes is represented. The SEM is represented by the error bars.

For the BCF-12 probe, a relatively quick decrease of the RIA is observed after the first hour down from 8.09 dB/m to 4.78 dB/m followed by a low increase of the RIA at 6 h to 5.73 dB/m and stabilized RIA at about 5.5 dB/m at 24 h. For the BCF-60 probes, a relatively quick decrease of the RIA is observed after the first hour from 6.73 dB/m to 5.33 dB/m followed by a low decrease of the RIA at 6 h down to 4.68 dB/m and shows an RIA of 4.28 dB/m 24 h after the end of the irradiation. The BCF-98 probes seem not to recover their attenuation properties after the end of the irradiation.

III.A.6. Different energy (6MV) same effect?

Figure 53 shows the mean variation of RIA calculated for the BCF-12 fiber from 0 to 600 Gy using a 6 MV FFF beam.

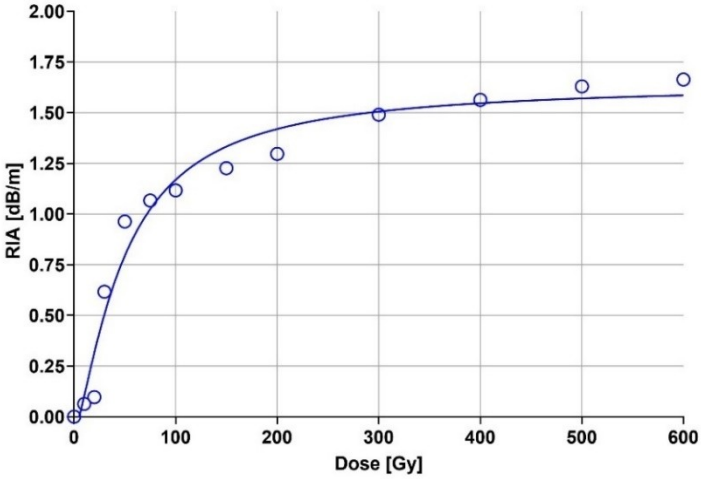

Figure *51*: RIA calculated for BCF12 fiber using a 6MV FFF irradiation beam.

The RIA grows rapidly between 0 and 50 Gy at 0.96 dB/m followed by a slower increase up to 1.66 dB/m at 600Gy. Even if the shape of the curve is similar to the one observed for the BCF-12 fiber at low energies, the RIA absolute values are significantly lower. Here it appears that the RIA calculated with the IVI-CBCT probe, made partially of BCF-12, using a Varian Linac a 1400 UM/min dose rate is much lower than the RIA calculated with the X-Ray generator at a 635.5mGy/min dose rate.

Figure 54 shows the mean recovery properties of the RIA calculated for BCF-12 fiber.

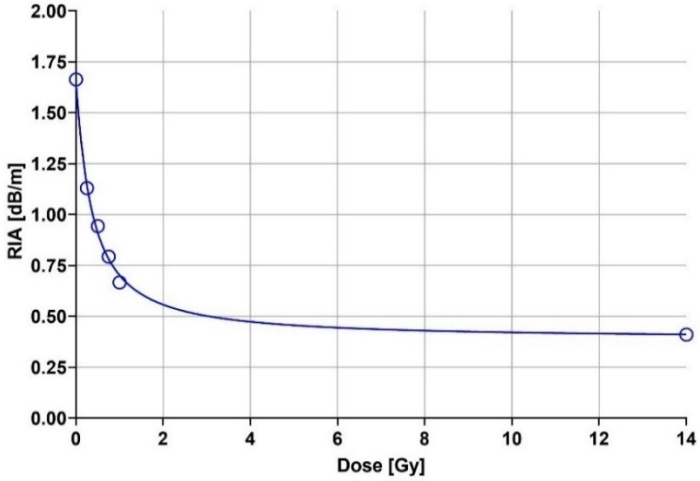

Figure *52*: Recovery fiber properties after the end of the irradiation.

As for the previous studies, a relatively fast decrease of the RIA is observed during the first hour down from 1.66 dB/m to 0.66 dB/m followed by a low decrease of the RIA to 0.41 dB/m at 14 h. Even if the shape of the curve is similar to the one observed for the BCF-12 fiber at low energies, the RIA absolute values are significantly lower.

III.A.7. Conclusions

The RIA study of the 3 types of fibers shows different responses depending on the fiber type. Even though all the fibers present RIA when irradiated with a high cumulated dose, 3 different behaviors were observed. Firstly, the RIA of the optical guide made of BCF-98 grows steeply between 0 and 120 Gy but slowly reaches a limit value after this cumulated dose. This limit appeared to be at least twice lower for BCF-98 than for the other fibers. Since the BCF-98 is made to operate the transmission of the scintillation photons, this lower RIA value makes it an interesting characteristic of the optical guide. Concerning the two scintillating fibers, BCF-12 and BCF-60 seem to have similar properties when looking at the evolution of the RIA with dose, even if the BCF-12 fiber might not have reached its RIA limit at 1 kGy. However, when looking at the evolution of the scintillation with a cumulated dose, it appears that BCF-12 and BCF-60 have different behaviors. Indeed, the attenuation of the scintillation signal in BCF-60 was almost not affected by the cumulated dose in BCF-60. This last characteristic is due to the chemical composition of the BCF-60 with hydroxy flavone for radiation resistance.

Another interesting point of the RIA in PMMA is the recovery properties of the fibers. While the attenuation is almost stable after the end of the irradiation, it showed a net decrease for BCF-12 and BCF-60. The results obtained are in line with the literature. The decrease observed reveals that the fibers regain partially their transmission once the irradiation is stopped. This means the radiation damage is partially repaired inside the fiber.

We also studied the BCF-12 RIA under irradiation of 6 MV photons beam. While the RIA shows similar behavior when a fiber is exposed to a high cumulated dose in kV and MV photons, the value of limit RIA differs when changing from kV to MV photons. Indeed, the RIA grows steeply to 1.24 dB/m until 150 Gy and continues to grow after this cumulated dose value. This value is significatively lower than the one observed under kV beam irradiation. This could be due to an energy dependency aspect of the RIA. To our knowledge, this is the first time that this effect is observed and may be due to a difference in the dose microdeposits inside the fiber when irradiating with a kV or MV photons beam. This aspect of the RIA deserves further investigation.

Following this study, it was decided to pre-irradiate all the fibers used for IVI-CBCT for a dose of at least 1 kGy under a 120 kV photons beam inside the Fibermetrix laboratory X-ray generator. Further study is necessary to evaluate the resistance and aging of the fibers in an RT environment depending on the time, and deposited dose during a consequential time (< 1 year). This study will help to define the time necessary between two calibrations of the dosimeter or even the probe's lifespan. This lifespan time is complex to anticipate due to the energy aspect and the recovery properties of the fibers tested. For example, a similar study was realized on the IVIscan dosimeter and resulted in an estimation of a 5 % loss in 7 years. Nevertheless, the IVIscan is calibrated every 3 years to conform with mandatory calibration period.

III.B. Implementation of a new photodetector in the photocounting system

Due to the cost, size, and perennity of the components as a consequence of the absence of concurrence in the PM modules supplier (Hamamatsu, Shizuoka, Japan, owning 100% of the PM modules and 90% of the PM tubes global market), a part of the work realized during this thesis aimed to replace the PM modules in the detection chain by the SiPM technology. Fibermetrix laboratory has developed an in-house acquisition chain using SiPM (MicroFJ-30035-TSV, ON Semiconductor, Phoenix, Arizona, USA) photodetectors of 3.07 mm x 3.07 mm active surface with 5,676 microcells (Cf. Figure 55) and a wavelength sensitivity range from 200 nm to 900 nm and a peak wavelength at 420 nm instead of a PM module (H10721-110, Hamamatsu, Shizuoka, Japan) (Cf. Figure 56) with a wavelength sensitivity range from 230 nm to 700 nm, a detection peak wavelength at 400 nm.

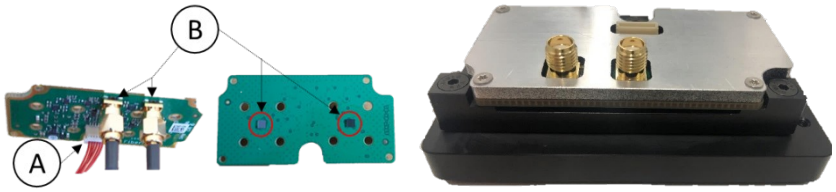

Figure *53*: On the right, the prototype electronic card with 2 SiPMs (3 .07 mm x 3.07 mm active surface). A: Alimentation cable. B: SiPM photosensors. On the left, is an aluminum protection for EMI.

As explained previously, the SiPM has many advantages such as its very low price compared to PM, and its small dimensions, but it is also sensitive to temperature and has a relatively high noise compared to PM modules. The photodetector dimensions were chosen to have an optimal signal-noise ratio (SNR) mainly defined in this case by the ratio between the SiPM optical surface illuminated by the probe and the optical surface not receiving light (therefore generating only noise).

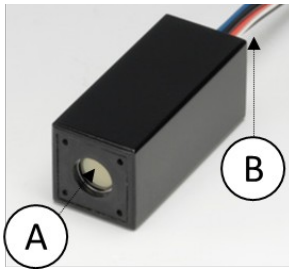

Figure *54*: Hamamatsu PM module. A: Photocathode (Ø 1 cm active surface). B. Alimentation and signal cables.

This study also helped to define the optimal distance between the probe and the SiPM based on the probe's diameter. The acquisition chain used in this characterization work is derived from a functional prototype of the SiPM acquisition chain developed at the Fibermetrix laboratory. The primary signal analysis performed inside the prototype electronic circuit involves signal amplification made of 3 amplificatory levels to make the signal detectable (Cf. Figure 57).

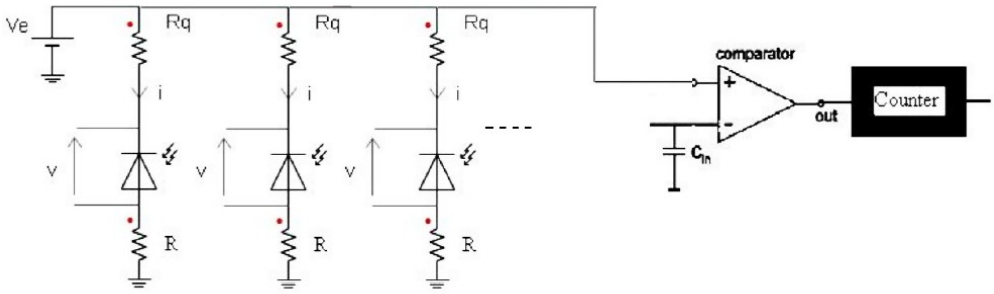

Figure *55*: Three levels amplification system used for the SiPM photocounting system.

An electronic threshold varying from 50 mV to 360 mV and encoded from 0 to 255 is applied to the electronic signal to discriminate the signal impulses (*i.e.* the noise and the electronic signal generated from the interaction of single or multiple photoelectrons) (Cf. Figure 58). In the remainder of the manuscript, the electronic thresholds will be referred to as the encoded value from 0 to 255. The SiPM photocounting chain prototype aims to be used with all the dosimeters developed by Fibermetrix, including the dosimeters for radiotherapy applications. For that purpose, the prototype was characterized once integrated into the Fibermetrix photocounting system.

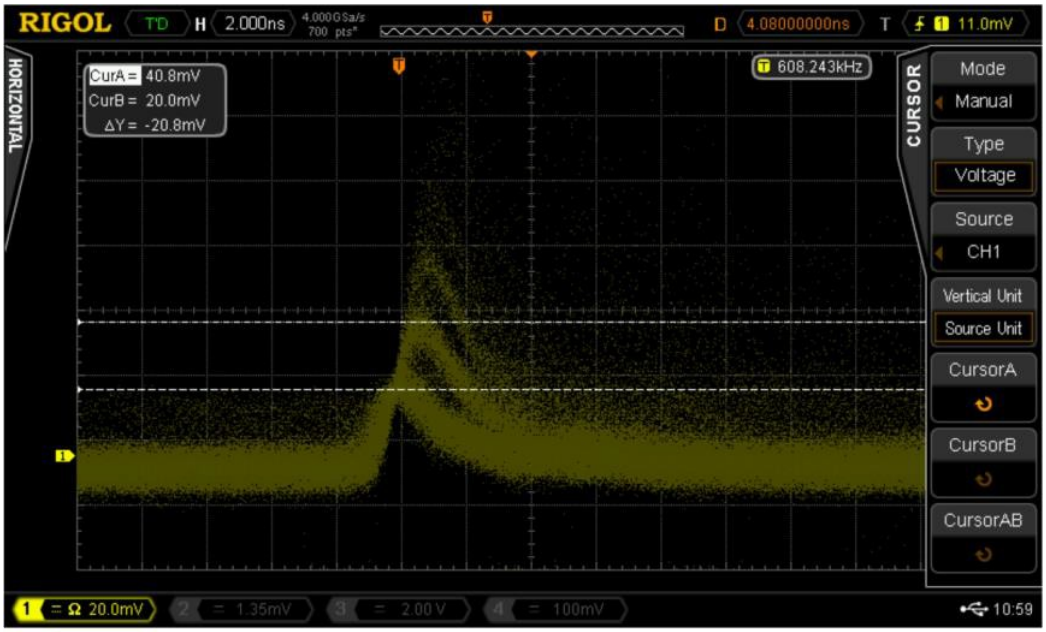

Figure 56: Oscilloscope visualization of the signal generated by a SiPM. The electrical impulsions correspond to a signal generated by 1, 2, or 3 photo-electrons. The noise generated is also visible.

The beginning of the implementation work aimed to characterize the behavior of a SiPM detector according to the chosen threshold. Then, an analysis was performed on the SiPM's noise, and finally on the SiPM's response as a function of time.

III.B.1. Experimental setup and material

The light intensity was programmed to increase linearly following a ramp function increasing the LED power input with an iterations period of 10 000 ms. Therefore, the LED intensity is referred to as light flux from 0 to 10 000, 0 representing the light flux at 0 ms when the LED is not emitting light, and 10 000 being the light flux at 10 000 ms. The experimental setup used is schematized in Figure 59. To follow both measurements at the same time, the PM module was connected to channel 2 and the SiPM to channel 1 of a Fibermetrix photocounting system identical to the photocounting system used for the IVIscan and IVInomad dosimeter.

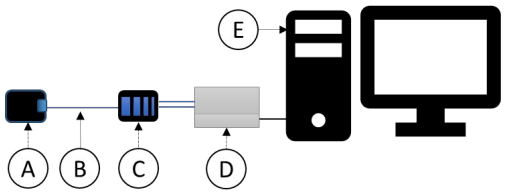

Figure *57*: Experimental setup of the SiPM's characterization. A: LED light. B: Optical guide. C: Attenuator system. D: Fibermetrix photodetection system with one channel

connected to the SiPM and the other channel linked to the PM. E: Computer with in-house dedicated software.

As the PM response is stable in time and linear in function of the photon intensity, this experimental setup allowed carrying the SiPM characterization in function of the PM counting system as a reference and therefore carry the characterization independently from the LED's unintentional power variations or other external interferences.

III.B.2. Electronic counting threshold impact on SiPM

The integration of a SiPM detector in the photocounting system requires first the setting of the electronic threshold applied. In use with PM, a too-low threshold can lead to high sensitivity to external disturbances while a too-high threshold reduces the overall sensitivity of the system. For the PMs, an algorithm had been set up to choose the threshold in a reliable and reproducible way. This study aimed to characterize the SiPM's response in function of the light intensities for different thresholds. Using the results of this characterization, the SiPM's optimal electrical threshold will be defined.

A periodical (t = 10 000 ms) signal was calibrated on the LED with a minimum amplitude of 0 photons and a maximal amplitude of about 175 000 photons. Using the electronic thresholds from 60 to 155, the evolution of the counts measured in function of the light intensity was performed. This section regroups the results of the SiPM response depending on the electronic counting threshold. For readability purposes, the electronic thresholds are represented by groups of 5 on the same figure. It is reminded that the light injected into the SiPM grows strictly in time following a ramp function. For this reason, the increase of time means an increase in the light ramp, this is why the SiPM measurements are represented as a function of time. The figures listed from 60. A to 60. F shows the SiPM response in intensity for thresholds from 92 to 150 during 10 000 ms.

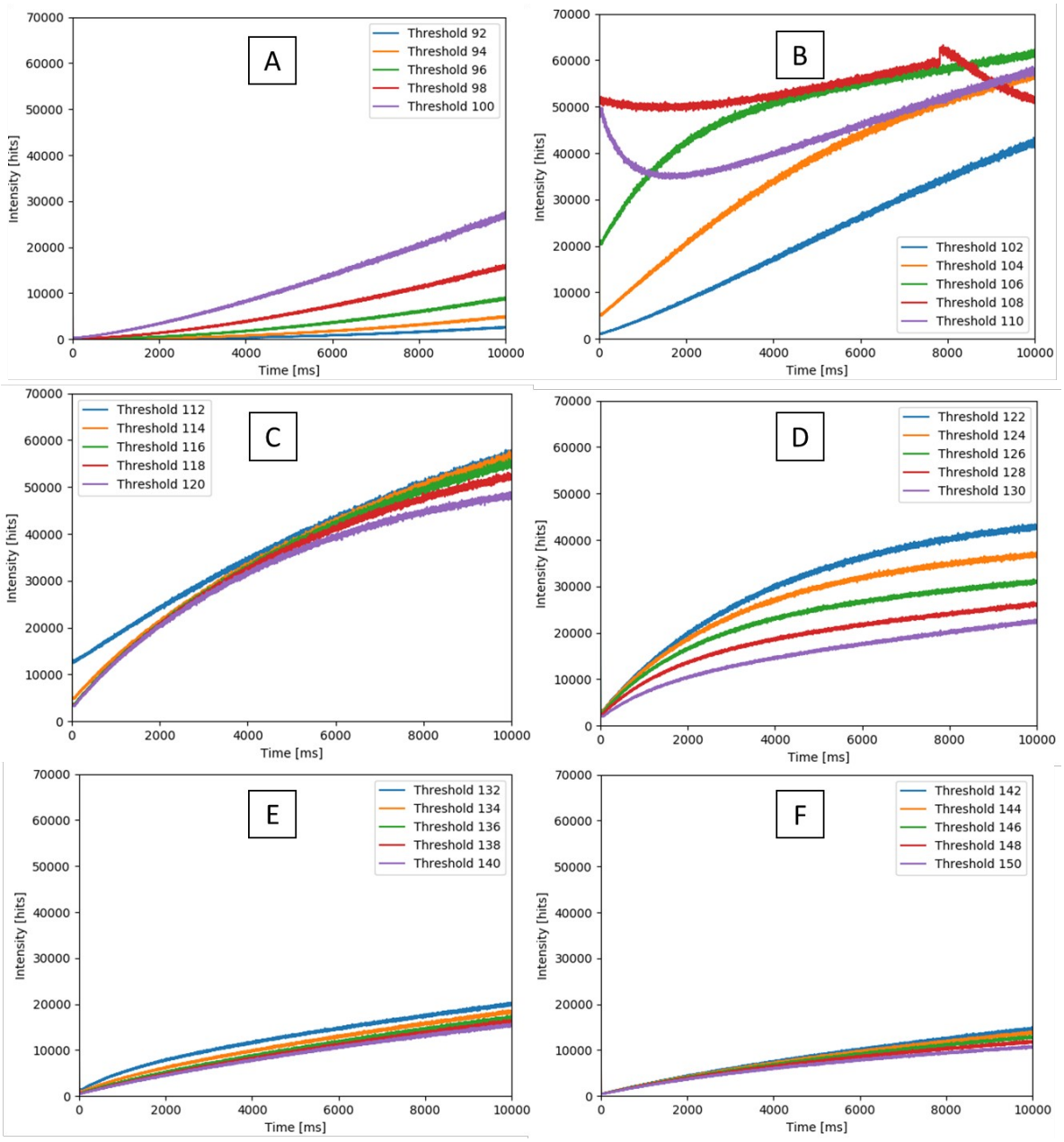

Figure *58*: SiPM response to a linear light signal at different electronic thresholds. A: Thresholds from 92 to 100. B: Thresholds from 102 to 110. C: Thresholds from 112 to 120. D: Thresholds from 122 to 130. E: Thresholds from 132 to 140. F: Thresholds from 142 to 150.

The SiPM's response in function of light intensity varies significantly with the electronic threshold applied. The figure 60.A shows the response of the SiPM for electronic thresholds encoded from 92 to 100 For these thresholds, the intensity at T = 0 ms (at the beginning of the linear light signal) is close to zero, resulting in low dark noise. The evolution of the signal shows a non-linear growth with a maximum intensity relatively low of about 27500 hits. At this range, the light intensity increases strictly with the increases in thresholds. Figure 60. B shows the response of the SiPM for electronic thresholds encoded from 102 to 110. From threshold 102 to 106 the signal at T = 0 ms starts to differ significantly from zero and grows with the

threshold increase. As with the previous thresholds, the signal is strictly increasing until threshold 106. In addition, the intensity grows with the threshold up to 106. Thresholds 108 and 110 seem to have a response that decreases before increasing with the increase of light intensity. Furthermore, saturation seems to appear on threshold 108. Figure 60. C shows the response of the SiPM for electronic thresholds encoded from 112 to 120. From threshold 112 to 120 the signal at T = 0 ms differs significantly from zero and grows with the threshold increase. The measured intensity is strictly increasing with the light intensity (increasing with the time [ms]). Also, the measured intensity is decreasing with the increase of the threshold. Figure 60.D shows the response of the SiPM for electronic thresholds encoded from 122 to 130. From threshold 122 to 130 the signal at T = 0 ms differs significantly from zero and grows with the threshold increase. The measured intensity is strictly increasing with the light intensity (increasing with the time [ms]). Also, the measured intensity is decreasing with the increase of the threshold. Figure 60. E shows the response of the SiPM for electronic thresholds encoded from 132 to 140. From threshold 132 to 140 the signal at T = 0 ms differs significantly from zero and grows with the threshold increase. The measured intensity is strictly increasing with the light intensity (increasing with the time [ms]). Also, the measured intensity is decreasing with the increase of the threshold. Figure 60. F shows the response of the SiPM in intensity for electronic thresholds encoded from 142 to 150. From threshold 142 to 150 the signal at T = 0 ms differs significantly from zero and grows with the threshold increase. The intensity measured is strictly increasing with the light intensity (which increases with time [ms]). Also, the measured intensity is decreasing with the increase of the threshold.

The choice of the optimum threshold T_{opt} must be realized taking into account the possibility to correlate the intensity measured to a dose. In that aim, the slope of the intensity measured must be strictly growing and have an amplitude large enough to differentiate between low and high dose rates. The low (92 - 110) and high (130 – 150) thresholds exhibit a low response even to high light intensities. On the other hand, 108 and 110 thresholds exhibit a response not strictly growing and therefore are not suitable for dose measurements. Following these results, the optimal SiPM threshold is $110 < T_{opt} < 150$. To specify the T_{opt} value inside this interval, the photodetector's response to light intensity must be completed with a complementary study on the SiPM's noise depending on the threshold.

III.B.3. SiPM's noise depending on the applied threshold

Since the SiPM is particularly sensitive to noise generated by the temperature, and knowing that the SiPM's temperature increase when the photocounting system is operating, this study aimed to determine the noise response of the SiPM while the system was operating photocounting iterations. The protocol is repeated on 3 SiPM sensors to evaluate the homogeneity of response through different SiPM of the same batch (results of the 2 other SiPMs are presented in the annex). For each SiPM characterized, the following representations and processing were performed:

- Evolution of the number of counts measured as a function of the injected light level for each threshold tested.
- Evolution of the number of minimum, maximum, and amplitude (maximum – minimum) of the response to a light ramp according to the tested threshold.
- Evolution of the Signal Noise Ratio (SNR) and noise level as a function of the threshold.
    - The noise level and the signal evaluation are done by modeling the response of the number of counts as a function of the injected light:

$$Noise[a.u] = \left| \left(signal_{measured} - signal_{theoretical} \right) \right| \qquad \text{[Eq. 26]}$$

$$SNR[hits] = \frac{amplitude}{Noise} \qquad \text{[Eq. 27]}$$

Despite their low noise level, we choose to avoid the low thresholds (under 110) due to their low-intensity amplitude and low maximum intensity (Cf. Figure 60 above). To describe the response of the SiPMs photodetectors concerning the noise, the maximal, minimal, and amplitude of the signal variations in the SiPMs are represented in function of the threshold for the thresholds from 110 to 160. For each threshold, an estimation of the noise and the SNR is also represented. Figure 61 represents the study of the noise in SiPM #1 depending on the threshold. The left part shows the maximum (yellow), the minimum (blue), and the amplitude (green) of the intensity measured. The left part presents the noise evaluation in blue and the SNR in yellow.

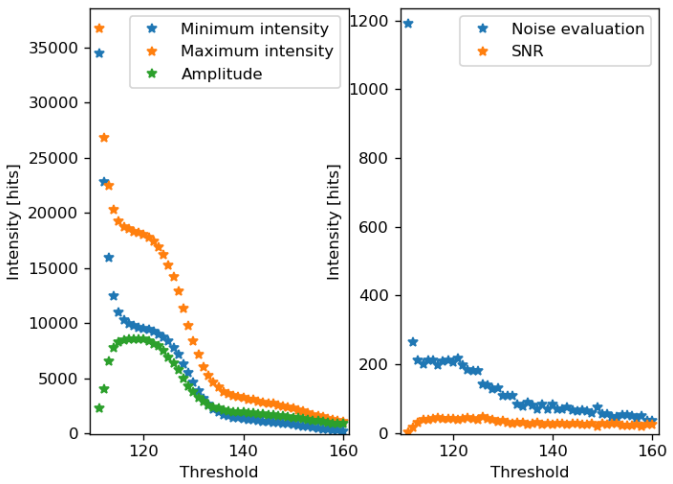

Figure *59*: SiPM #1 noise characterization for thresholds from 110 to 160.

Regarding intensity, different functioning zones can be described depending on the threshold. From 110 to 115, the minimum (from 34500 to 11000) and maximum (from 36500 to 19000) intensity in decreasing

quickly as the amplitude (from 2250 to 8550) and threshold rise. From 115 to 125, the minimum (from 11000 to 8550) and maximum (from 19000 to 15700) intensity in decreasing quickly as the amplitude (from 8550 to 6200) and threshold rise. Then the maximum, minimum, and amplitude decrease progressively until 160. If we look at the noise level and the SNR, although similar functioning zones appear, they're not exactly at the same thresholds. As the noise level decrease (from 1200 to 215) between 110 and 115, the SNR grows (from 8 to 44). Then the noise remains stable until 120, and start to decrease until 160 while conserving similar performances regarding the SNR.

For the three SiPMs studied (the results from SiPM #2 and #3, presented in the annex, are very similar to SiPM#1), we observed the presence of high amplitude zones with relatively good SNR between $115 < T_{opt} < 160$. Another interesting functioning zone is present after 140, although this functioning zone presents significantly lower performances in terms of the signal intensity measured. Following this noise study and the characterization of the SiPM at different thresholds, the thresholds between 115 and 160 were identified as the optimal range of functioning electronic thresholds to integrate the SiPM in the photocounting system. Eventually, following these results, it was chosen to set the threshold to 140 for this SiPM and the other SiPM tested.

III.B.4. SiPM's response stability in time for a definite threshold

The previous measurement protocols aimed to determine the behavior of a SiPM as a function of the photocounting threshold for a short time. The first time stability analyses aimed at observing the stability in time of the dark noise, and therefore, the response to the same injected signal. To evaluate the SiPM's response over a long time, the same setup as before was realized and the light was also injected into a reference PM to control the stability of the LED source in time.

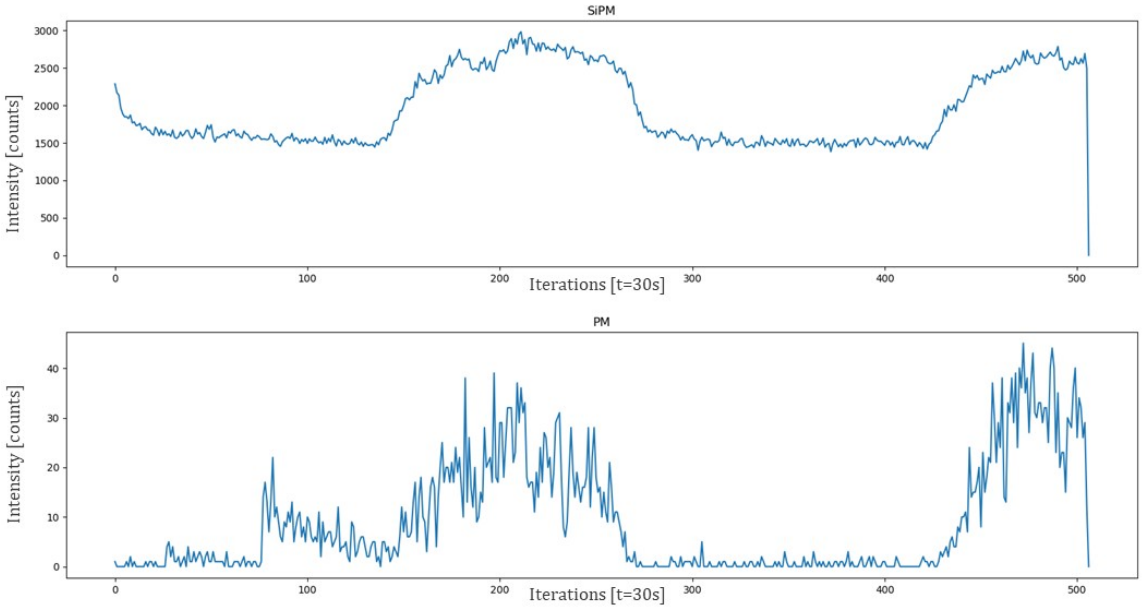

Figure *60*: Noise measurements of SiPM (on the top) and PM (at the bottom) simultaneously. The noise seems to not be heterogeneous through the iterations. After analyses, it corresponds to the noise coming from environmental light (mostly sunlight) through 2 measurement days.

Due to light leakages detected during the first experimental sets (Cf. Figure 62), the measurements were repeated several times before managing to localize and suppress the light leakages coming from millimetric gaps in the experimental SiPM setup. These gaps were suppressed by adding opacifying seals (Cf. Figure 63) on the SiPM photocounting setup first realized in Figure 55 above.

Figure *61*: Opacifying seals added to the SiPM photocounting system to prevent light leakages.

Once the opacifying seals were placed, the evaluation was realized during 48 h. The analyses and representations show:

- The SiPM response at different light intensities in function of time.
- The relative difference between the intensity of the first iteration and the intensity measured through time for different injected light intensities.
- The SiPM's response as a function of the dark noise for a corresponding light intensity

Figure 64. A shows the intensity measured by the SiPM through the iterations for different light incident fluxes. Light flux 0 (in blue) corresponds to the DCR, and the other light flux corresponds to the light

at 2000 ms, 4000 ms, 6000 ms, and 8000 ms on the linear signal generated by the LED with a period of 10 000 ms. Figure 64. B presents the absolute differences at different iterations for a constant light injected.

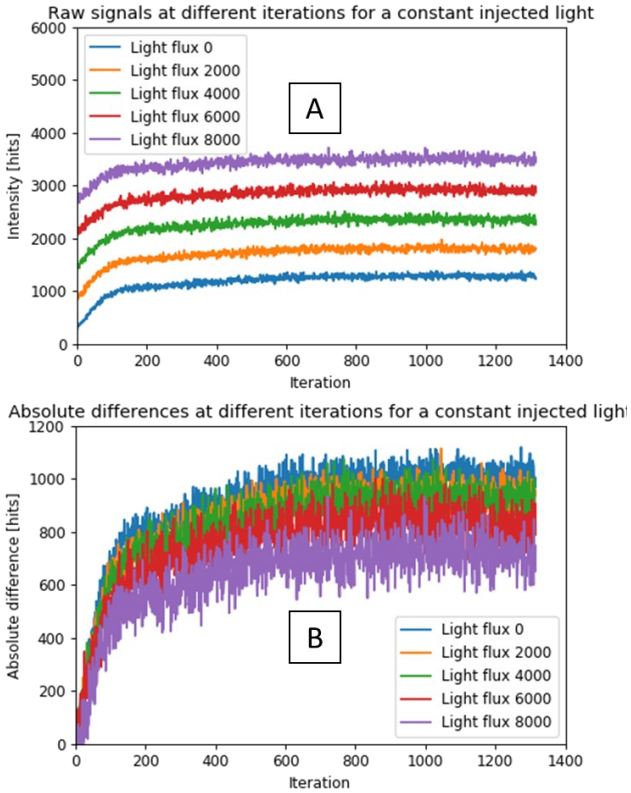

Figure *62*: A: Raw signals at different iterations for a constant injected light. B: Absolute differences at different iterations for a constant injected light.

This figure allows visualizing the intensity growth for each light flux through the iterations. Analyzing Figure 64. A, the light flux evolves in the same way with the intensity measured growing through the first iterations until 114, then only varying around the same value (different for each light flux). The light flux 0, corresponding to the DCR, shows a starting point at 312 counts and an inflection point at 1057 for the 139th iteration. The intensity value at the last iteration is at 1306, meaning that even if the DCR stabilizes through time, it still grows over a long time. Another interesting point to look at in this figure is that the noise from the DCR seems to be addable through the light flux, meaning that it does not vary depending on the light intensity. Looking at Figure 64. B, the first iteration is taken as the reference iteration for comparison with the other ones. As expected, the difference starts at 0 and then increases in time with the iterations. The absolute light intensity difference decreases with the increase of light flux.

Figure 65 represents the intensity relative difference for each light flux compared to the previous iterations (here the reference intensity for each iteration n is the iteration n-1).

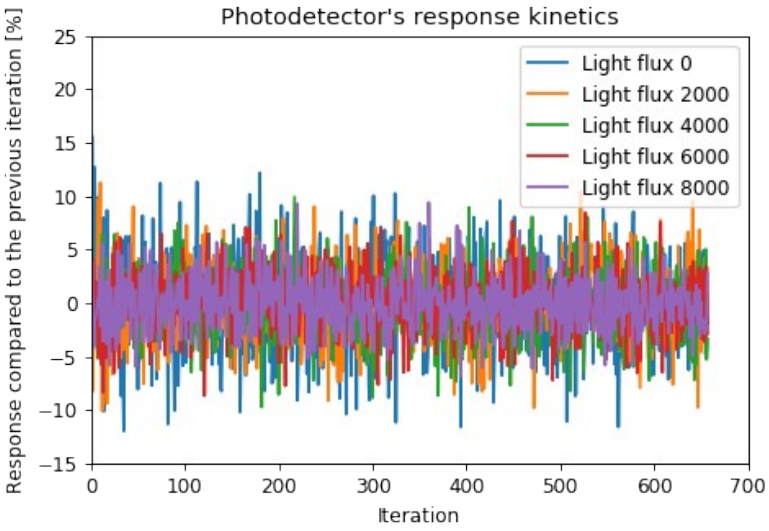

Figure *63*: SiPM's response kinetics.

The response from one iteration to the next varies between 12.4 % and -11.6 %. Although all the light fluxes vary similarly from one iteration to another, it has to be noted that the light flux 0 (representing the DCR) is the one showing the most variability, meaning that most of the variations in the intensity are issued from the DCR. In addition, the mean value is equal to -0.04 % and the standard variation is equal to 2.55 %. Therefore, considering the light flux 0, the mean and the standard deviation values indicate that the noise change from iteration i-1 to i by -0.04 % with an uncertainty of 2.55 %.

III.B.5. Conclusions

The SiPM's characterization, with the aim of implementation in the photodetection system, highlighted the SiPM operating performances depending on the electronic threshold applied, the signal intensity, and the time. The two firsts study allowed us to identify an optimal threshold range from 115 to 160 with a strictly growing signal measured, an intensity amplitude allowing us to discriminate easily low and high light intensity, and an interesting SNR. Also, the noise study allowed us to localize light leakages inside our experimental setup that were not identified before. An easy and reproducible solution was found to remove these millimetric gaps and improve the system SNR by using black seals around the connectors. Following this correction, we've been able to characterize the system's stability in time regarding different light intensities, including no light injected (DCR). We have identified one of the optimal thresholds, *i.e.*140, combining good performances in terms of noise and SNR.

Thanks to this study, the SiPM has been implemented into a beta-test photodetection system. Moreover, it has been decided to select the electronic threshold using the complete methodology used here to identify the optimal threshold range. In addition, optical insulators are now used on all the SiPM photodetectors, and the DCR is corrected in real time from the signal.

As identified during this study, the SiPM presents a noise significantly superior to the one observed in the PM. Even if the SNR resulting is suitable with the use of the detector in our dosimeter, it could still be improved by a noise reduction. One of the perspectives to realize this noise reduction is the reduction of the number of amplification levels from 3 to 2 levels. This would certainly result in a decrease in signal but also noise generated and measured inside the SiPM. Therefore, the next steps of the study need to be done to evaluate how it affects the SNR.

Also, further study needs to be realized in a clinical environment to analyze de SiPM's response in the presence of a linear accelerator or CT scanner. In addition, now that the SiPM has been implemented into the detection system, further work should be required if aiming to pass the regulatory tests to evaluate its conformity to CE markings, European norms regarding electronic devices in the medical environment (e.g. IEC 61674; IEC 60731; NF EN 62366; NF EN 60601-1) and FDA.

Another non-negligible point to assess is the power consumption of this new photodetector compared to the PMs. It could potentially lead to the change of elements inside the power supply chain (e.g. power input and battery) and have to be evaluated. Finally, since the SiPMs' dimensions are considerably lower than the PM's, the photocounting system design could also be edited to either increase the number of channels available on the photocounting system or reduce the system's dimensions while conserving similar performances.

III.C. Dose measurement method developed for CT and CBCT large collimations

As stated above, several methods have been proposed to overcome the problem of dosimetry for wide beam CT scanners or CBCT[4, 32, 41, 61, 63, 88, 118, 152, 173]. In this section, a method using the Fibermetrix dosimeters to evaluate the dosimetric performance of wide beams in computed tomography was developed. This work was published in a scientific article[82]. The part of this article regarding the wide collimations formal analysis and investigations were realized during this thesis. The IVIscan dosimeter and the associated method were compared with a reference IC and validated as a new fiber dosimetry system for mandatory dosimetric quality controls (MDQC). It was proposed to calculate the $CTDI_w$ and the $CTDI_w^{N\times T>40}$ ($CTDI_w$ for large collimations, *i.e.* collimations > 40 mm), using the two methods, in regulatory conditions on multiple CT scans for the thinnest, largest, and usual beam widths used in clinical practices and beyond for the different X-ray tube voltages (kV). The energy dependency of the IVIscan detector was also studied using the kV variation. Then, the relative deviation between the $CTDI_w$ obtained through the reference method using

the reference CT chamber, $CTDI_w^{chamber}$, and the one obtained through the IVIscan method, $CTDI_w^{IVIscan}$ were evaluated.

III.C.1. Materials and methods

III.C.1.a. CT equipment

To validate the IVIscan dosimeter universally, measurements of all CTDIw were carried out with four different CT scans from the three main CT manufacturers. A Siemens SOMATOM® definition AS+ called System Number 1 (SN1), a Canon Medical Aquilion ONE Genesis (SN2), a GE Healthcare Revolution CT (SN3), and a Canon Medical Aquilion ONE/PRISM Edition (SN4). SN2, SN3, and SN4 have collimation widths over 40 mm while SN1 has traditional collimation widths of less or equal to 40 mm. The highest voltage used by the CTs was 140 kV, except for the SN2 and SN4 which use 135 kV.

III.C.1.b. Irradiation parameters

$CTDI_w$ calculation from MDQC tests requires specific CT acquisition parameters such as tube voltage and beam widths. Thus, the aim was to first validate the IVIscan dosimeter under these specific requisites. So, the reference and IVIscan measurements were performed at 120 kV, at the thinnest and largest beam widths used in the clinic, for a head and body protocol with the corresponding phantom, as required by the French regulation related to the quality control of CT scanners[144]. Medical physics experts are unanimous that MDQC should be more closely aligned with clinical practice, especially concerning the protocols used. Therefore, for each case, an X-ray tube current of 200 mA and a tube rotation of 1 s were settled to adapt the dose rate to accurate measurements with the IC (used as a reference in this study).

III.C.1.c. Reference dose indexes

Reference materials:

To measure the parameter of CT radiation dose, the study was conducted using a 100 mm Unfors Raysafe™ X2 IC (Fluke Biomedical, Everett, WA, USA) and standard-sized CTDI PMMA head and body phantoms. The IC was calibrated according to IEC 61223-2-6. Measurements were made with an uncertainty of less than 5% at the 95% confidence level (manufacturer data).

The two standardized PMMA cylindrical phantoms of 16 cm diameter and 32 cm diameter were used for head CT protocols and body CT protocols, respectively. Both phantoms are 15 cm in length and have five 12.4 mm diameter holes. One of them is located at the center and the other four, are 10 mm beneath the surface at 90◦ intervals.

To perform CTDI calculation with beam widths over 40 mm, we used the IAEA method described above and using the same IC as for beam widths < 40 mm. The evaluation was performed over the largest beam widths from 80 to 160 mm according to the CT scan technical possibilities. The CT chamber was then attached to a retort stand on the CT table and aligned at the isocenter of the beam as shown in Figure 66 (left).

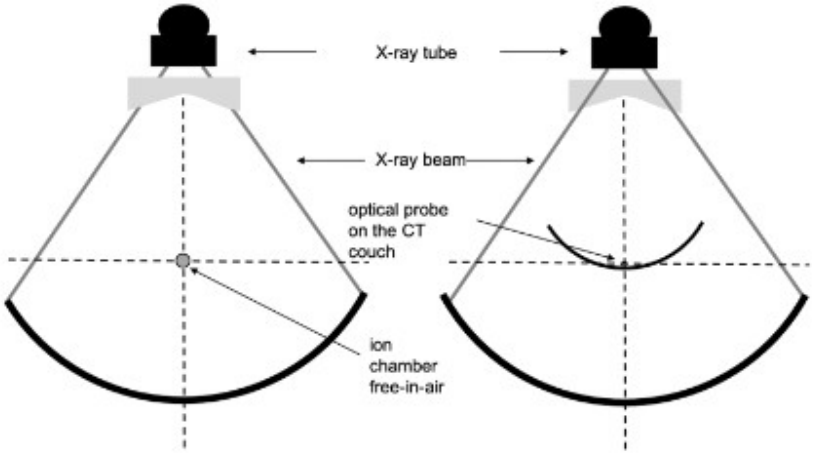

Figure 64: Diagram demonstrating practical measurement of the CT air kerma indexes measured ($CTDI_{air,N\times T>40}$) for beam width N x T > 40 mm with a 100 mm IC free-in-air (left) and with an IVIscan detector on the CT table (right). No phantom is used here.

The table was then stepped through in the z-direction in increments of 100 mm and a beam rotation was performed at each increment step. The IC was placed away from the edge of the table to avoid any scattered radiation from the table. Dose measurements were carried out in three sequential steps as shown in Figure 67, and summed to give $CTDI_{air,N\times T>40}$. Then, $CTDI^{IC}_{w,N\times T>40}$ was calculated according to Equation (3) defined above with a reference beam width of 40 mm.

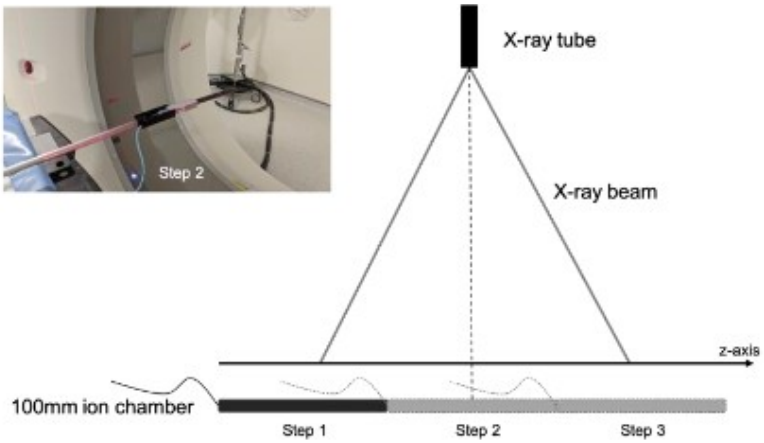

Figure 65: Diagram representation of the recommended three-step in-air measurement method of $CTDI_{air,N\times T>40}$ for beam width N x T > 40 mm with a 100 mm IC.

III.C.1.d. IVIscan dose indexes

IVIscan Scintillating Fiber Detector was calibrated in terms of air Kerma in RQT9 beam quality, which is the reference beam quality in scanography. It was characterized according to IEC 61674 at the Laboratoire National Henri Becquerel (LNHB, CEA LIST, Saclay, France), an independent primary calibration laboratory. A software solution is permanently connected to the dosimeter and the CT scan to recover the measured data and all the implementation parameters of the CT scan for each irradiation protocol. A history of dose measurements and MDQC is available and a quality control report can be easily generated.

Due to the high variability in CT beam quality depending on the examination protocols (*i.e.* tube voltage and beam filtration), the calibration factor $N_{k,RQT9}$ is automatically corrected by the software during the installation of the dosimetry system on each CT scan to offset the energy dependence and give the most accurate dose D(z). Air kerma, and hence dose measurements, were made with an uncertainty of less than 5% at the 95% confidence level (manufacturer data).

For beams less or equal to 40 mm, the method for calculating $CTDI_w$ with IVIscan dosimeter was carried out with only one measurement instead of the five with an IC (*i.e.* one for each phantom hole as required for the usual $CTDI_w$ calculation). A single dose measurement, $CTDI_{2000,table}$ was performed on the table, under the phantom, for a 360◦ X-ray tube rotation. A specific conversion factor NC was then automatically applied by the processing module and the beam width was automatically taken into account to obtain the $CTDI_w^{IVIscan}$ such as:

$$CTDI_w^{IVIscan}[mGy] = CTDI_{2000,table} \times N_C$$

It is to be noted that $CTDI_{2000,table}$ is the dose D(z) measured over the 2000 mm sensor length. The conversion factor N_C is selected from a conversion factor table stored in the memory of the device according to the CT scan acquisition type and basic radiation-matter interaction rules. The table is generated for each CT scan by a set of initial measurements during the commissioning of the dosimeter to take into account the specificity of each CT scan. The N_C factors are acquired for head and body protocols at 120 kV and one beam width only, usually 10 mm. The method used to obtain N_C factors is not detailed in this work. This is largely described in the Fibermetrix patents[125, 170].

For beams over 40 mm, the method involves the measurement of $CTDI_{2000,table,N\times T>40}$ which is a dose measurement on the table too but without any phantom. Then, according to [Eq(5)]:

$$CTDI_{w,N\times T>40}^{IVIscan}[mGy] = CTDI_{2000,table,N\times T>40} \times N_{C*}$$

where $N_{C,*}$ is another specific conversion factor stored in the memory of the device and depending on the anatomical type of the irradiation protocol (head or body). Compared to Equation (3), this conversion factor takes into account the absence of any phantom and the measurement on the CT table instead of free-in-air as for the IAEA methodology for wide-beam MDQC.

Then, the $CTDI_{w,N\times T>40}$ was calculated from a single measurement on the table with the IVIscan method, instead of the multiple measurements in air and in phantom holes required for CTDI calculation with a 100 mm IC. To compare the results between IVIscan and the reference IC methods as accurately as possible, the PSF sensor measurements were carried out together with the reference IC so that there is no additional uncertainty associated with the X-ray emission or another environmental parameter.

III.C.2. Results

Then, we compared the two different methodologies for MDQC on the four different CT scans to validate a new PSF dosimeter and to assess the corresponding accuracy. Hereafter in this paper, the beam width of 38.5 mm for SN1 is treated as a 40 mm beam width to compare results with other CT scans. The results for each CT scan are displayed in Figure 68. Figure 69 shows the mean $\left[\Delta CTDI\right]_{ref}^{IVIscan}$ overall CT scans by protocol type (*i.e.* beam width and anatomic region of head and body).

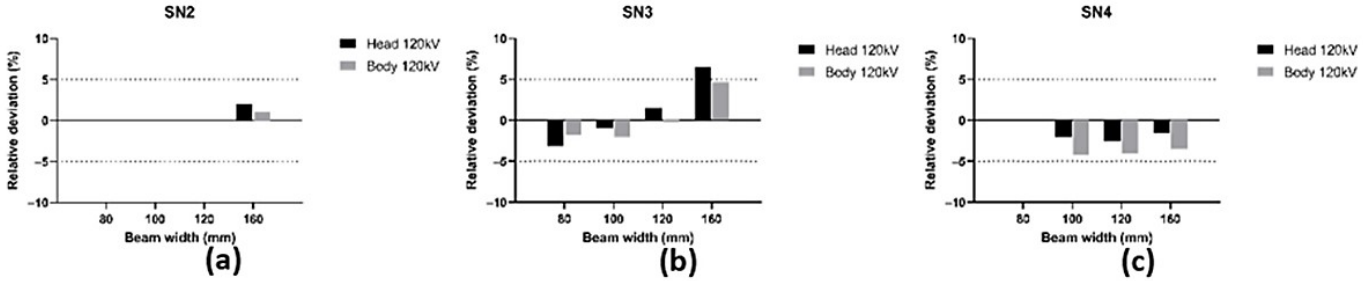

Figure 66: Relative deviation $\left[\Delta CTDI\right]_{ref}^{IVIscan}$ at 120 kV for head and body phantoms over the largest beam width for (a) SN2 with N × T = 160 mm, (b) SN3 with N × T = 80, 100, 120, and 160 mm, (c) SN4 with N × T = 100, 120 and 160 mm.

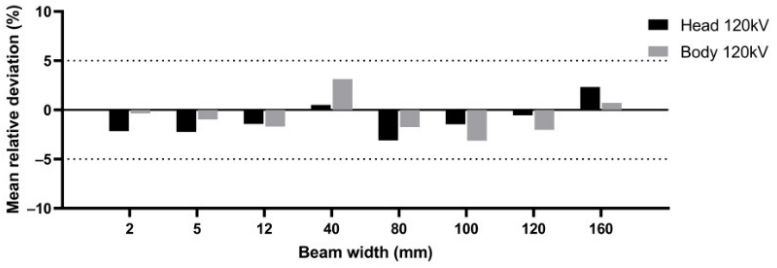

Figure 67: Mean $\left[\Delta CTDI\right]_{ref}^{IVIscan}$ over all centers at 120 kV for each protocol type (head and body and beam width from 2 mm to 160 mm)

The results show a deviation < 5 % for all the beam widths except for SN3, at 160 mm, and a head protocol where a relative deviation of +6.5% is obtained. In all other cases, the relative deviation is between −4.2% and +4.6% and thus does not exceed ±5%. The mean $\left[\Delta CTDI\right]_{ref}^{IVIscan}$ shown in Figure 68 is between −3.13% and +2.33% according to the CT protocol type. Therefore, we can reasonably conclude here as well that both methodologies of calculating the $CTDI_{w,N\times T>40}$ for a beam over 40 mm is equivalent.

III.C.3. Conclusions

As CT is the most radiative imaging modality, it is important to be able to accurately estimate the output radiation and ideally in the conditions of clinical use. Moreover, the dose from CBCT takes a growing part of the overall dose in RT with the increasing use of IGRT. Today, the CTDIw is the reference indicator used for MDQC in both CT and CBCT. However, this indicator suffers from several limitations. First, 100 mm CT chamber and PMMA phantom lengths do not allow for accurate measurement of the larger beam width available on the new wide beam CT scans and on CBCT. The current tools and methods are therefore obsolete in addition to being time-consuming which may interfere with clinical activity. According to current French and international regulations, MDQC is only carried out once a year and as an internal control when changing an X-ray tube or any hardware or software intervention that may influence the X-ray emission. This can lead to the late detection of a dosimetric mismatch. Therefore, a simplified and automated method allowing quick and relevant measurements, without impacting the clinical activity, is needed and could encourage more regular controls.

We observed only one relative deviation above +5 %, and it represents a minority of the total of 16 measurements. Moreover, considering the ±5 % uncertainty related to each dosimetry system and the accuracy of the phantom positioning for each comparative test, it can be assumed that these results highlight an equivalence of the IVIscan method and associated scintillating fiber sensor and usual IC for CTDIw measurements. Thus, these results are very satisfactory and validate the use of the IVIscan dosimeter within the framework of standard regulatory MDQC in computed tomography.

Furthermore, the IVIscan detector and associated methods described in this article could find interesting applications in CBCT. This imaging equipment is increasingly growing in the field of image-guided radiotherapy. It has been henceforth recommended by multiple international institutions to report the imaging dose given through radiotherapy treatment courses and implement a quality control system able to control the X-ray tube performances over time. Since there is no standardized approach to CBCT quality control and dosimetry across all CBCT systems, and the measurement of CTDI on CBCT is very time-consuming, it could be interesting to study the relevance of the scintillating fiber probe for MDQC on this kind of device. This will be the subject of the following sections of the manuscript.

III.D. Dosimeter's development and comparative measurements

As indicated in the sections above, there are already existing solutions to measure the dose from the treatment beam for quality assurance purposes in radiotherapy[58,82-93]. On the contrary, a lack of technical solutions to give a fast and precise measurement of the dose from increasingly used imaging systems was observed. In addition, the bibliography work highlighted the fact that CBCT was the main source of dose from imaging systems[2,9,34,35,50–52]. For this reason, the thesis work focused on the development of an innovative detector for imaging systems in RT. Furthermore, to facilitate its use, the detector should be permanently installed and not require calibration at each use.

III.D.1. Dosimeter's hardware characteristics

III.D.1.a. The probe

Various probes were realized before finding the final prototype of the IVI-CBCT dosimeter. Because the PM wavelength sensibility is calibrated to be more sensitive to visible photons emitted in the blue wavelength, the scintillating part of the probe is assured by a BCF-12 plastic scintillating fiber (PSF) (Saint-Gobain, Courbevoie, France) made of a polystyrene-based core containing a combination of fluorescent dopants and PMMA cladding. Given the high doses of radiotherapy, the possibility of using a radiation-resistant scintillating fiber such as the BCF-60 was considered but was not studied due to its lower scintillating performances and the lower PM sensibility to its emission wavelength. In order to collect the photons emitted and scattered on the entire irradiated length during CBCT acquisitions, the PSF length was set to 1 m. The scintillation photons emitted by the PSF following the CBCT irradiation are transmitted to the PM through a POF.

The POF, constituted of BCF-98 (Saint-Gobain, Courbevoie, France), acts as a light guide and is made of a polystyrene-based core and PMMA cladding. Both fibers have a density of 1.05 g/cm^3. To guarantee a good trapping efficiency of the photons emitted, the core and the cladding of the PSF have a refractive index of 1.6 and 1.49 respectively.

Contrary to IVIscan dosimeter where the splicing between the scintillating and clear fiber is assured by a metallic tube and optical glue, here the splice between the scintillating and the clear fiber is guaranteed by a plastic tube sleeve and an optical epoxy glue from EPO-TEK 353ND to reduce the influence of the probe on treatment and imaging beams while ensuring splice resistance and a maximal transmission of scintillation photons (Cf. Figure 70).

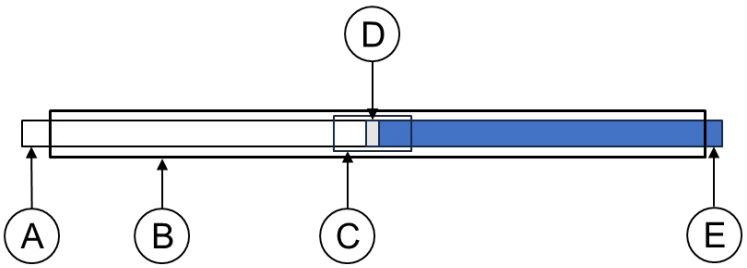

Figure 68: Connection between the clear fiber (A) and the PSF (E) inside the protective sheath (B). The splice guaranteed by a plastic transparent plastic sleeve (C) and an optical glue (D).

This optical glue is a two-component, high-temperature epoxy designed for semiconductor, hybrid, fiber optic, and medical applications. It has a spectral transmission of 50% for 550 nm at 23°C, a refractive index of 1.5694 at 589 nm, and a drying time of approximately 24 h, thus assuring maximal transmission performances at the dosimeter's operating conditions.

A 3 mm outer diameter cladding made of black Hytrel surrounds the entire length of the probe (Cf. Figure 71). The scintillation photons are transformed into signals by PM photodetectors. In addition, the PMs are insulated by a thin copper layer to reduce EMI disturbances from the electronic circuit and noise from scattered photons.

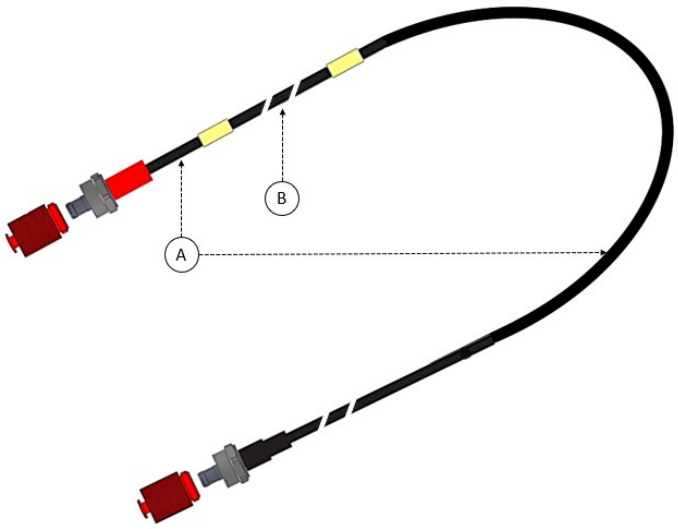

Figure *69*: Example of detector's shape with: A) The clear fiber (POF) #1 and #2. B) The PSF.

III.D.1.b. Dosimeter's positioning and alimentation

Since the two main medical linear accelerator vendors are Varian and Elekta, the prototype dosimeter was developed and installed firstly on a Varian to adapt the system to Elekta devices later in the device development. The dosimeter was installed on the PerfectPitch Exact Couch of a Varian TrueBeam STx

accelerator of the Metz CHR hospital radiotherapy service. It was placed on the back of the couch and connected to the photodetection system that was positioned on the side of the treatment couch (Cf. Figure 72 and 73). The accelerator is equipped with an onboard kV imager capable of acquiring planar kV images as well as kV-CBCT.

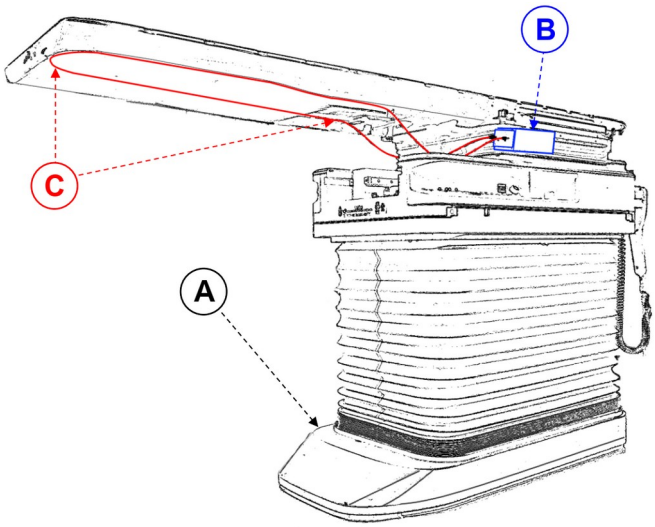

Figure *70*: Schematic depiction of the components of the measurement device and its setup on the treatment couch with: A. the couch of the accelerator, B. the signal treatment unit composed of a battery, two photo-multipliers, an signal analysis controller and a Bluetooth emitter, C. the optical fiber that is securely taped underneath the couch - the two arrows are pointing at the beginning and the end of the scintillating part of the fiber.

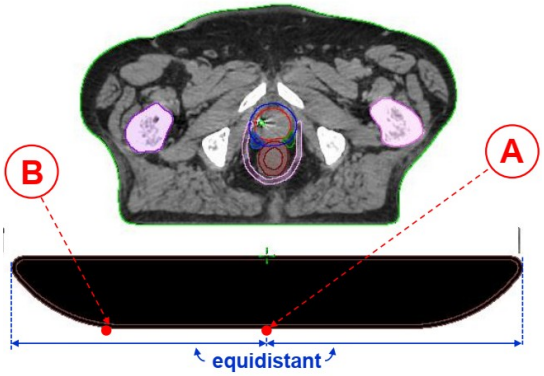

Figure *71*: View of a transverse image from a prostate plan from the TPS Eclipse (Varian, a Siemens Healthineers Company, Palo Alto, USA) with the couch underneath the patient. A: The PSF *i.e.* the scintillating. B: The POF, *i.e.* the non-measuring part. The PSF is centered below the couch.

One of the major concerns was to implement the dosimeter in a radiotherapy environment without influencing the images and the treatment beams or obstructing the patient's and radiation therapist's movements while being able to measure the dose received during CBCT exams. Even though the in-vivo measurements were not achieved during this thesis, it was taken into consideration when implementing the

dosimeter into the clinical environment. In that aim the dosimeter was placed under the treatment table (to avoid obstruction of the patient and radiation therapist's movements or material) at the center while the photometer was placed on the side of the treatment couch (Cf. Figure 73). Contrary to IVIscan, this dosimeter does not involve the presence of a protective mat for two reasons: (i) to minimize the dosimeter's influence on the treatment and imaging beam, and (ii) with the probe placed under the couch, there is no need for a protective material to ensure the probe's protection.

The dosimeter is connected to a wall-mounted receiver via Bluetooth. The receiver is connected via an RJ45 cable to a computer hosting the analysis software on a computer at the treatment control panel. The RJ45 also guarantees the photodetection system alimentation and battery recharge. The number of photons collected by the photodetectors is calculated from the signal collected and is then used in the dose calculations.

The following sections of the dosimeter's development and comparative measurement section is under submission process in the mdpi *sensors* scientific journal.

III.D.2. Dosimeter's influence on the imaging beam

The impact of the fiber was visually assessed on posterior kV images, with and without an in-house 3D printed thoracic phantom, using 2 acquisition protocols: "Extremity" with 65 kV and 3.5 mAs and "Thorax small" with 80 kV and 5.0 mAs. Finally, the impact of the fiber was visually assessed on the CBCT image set without phantom and using the "Head full fan" protocol with 100 kV and 270 mAs.

Figure 74 shows planar images acquired using a posterior incidence, without (A and B) and with (C and D) an in-house 3D printed thoracic phantom, using 2 acquisition protocols: "Extremity" with 65 kV and 3.5 mAs (A and C) and "Thorax small" with 80 kV and 5.0 mAs (B and D).

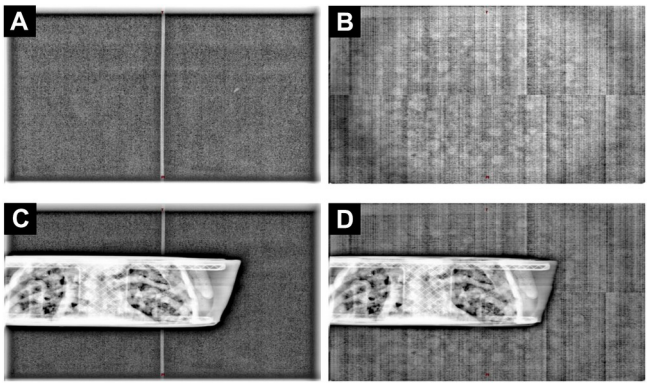

Figure *72*: Planar images acquired using a posterior incidence, without (A and B) and with (C and D) an in-house 3D printed thoracic phantom, using 2 acquisition

protocols: “Extremity” with 65 kV and 3.5 mAs (A and C) and “Thorax small” with 80 kV and 5.0 mAs (B and D).

Looking at Figure 74, the fiber can be seen in the middle (left/right direction) of the kV images when acquired at 65 kV (A and C) but not at 80 kV (B and D). Also, the fiber is not visible anymore on the pixels covered by the thoracic phantom (C). This indicates that the fiber is visible at low kV but not anymore from 80 kV. Furthermore, when the PSF is visible at low kV, it does not obstruct or deteriorate the visibility of the image.

III.D.3. Dosimeter’s influence on the treatment beam

A first look at Figure 75 shows the attenuation coefficients of water, soft tissue, and polystyrene at MeV energy. These indicate similar attenuation coefficients between water, soft tissue, and polystyrene.

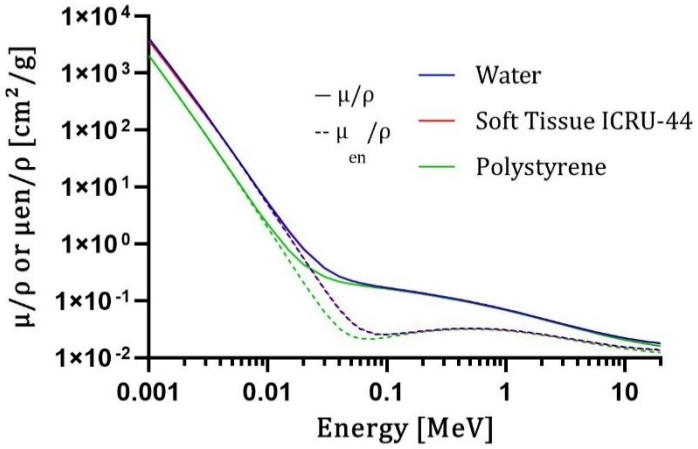

Figure 73: X-Ray mass attenuation coefficient for water (blue) soft tissue according to the ICRU report 44 (red) and polystyrene (green). Adapted from the NIST database on X-Ray attenuation coefficient.

Following these data, the fiber dosimeter made mainly of polystyrene, is assumed to attenuate the treatment beams as much as a 3 mm diameter cylinder of water. Even if this perturbation seems qualitatively negligible, it had to be quantitatively evaluated in order to estimate the influence of the PSF on the treatment beams.

To assess whether the presence of the fiber dosimeter would modify the delivery of the treatment it was first compared with a posterior (linac positioned at a 180° angle) 10 cm x 10 cm 6 MV FFF 6 MV with flattering filter and 18 MV portal [133] images acquired with the EPID of the TrueBeam with the fiber versus without the fiber. During these measurements, a 10 cm thick RW3 slab phantom (PTW-Freiburg, Freiburg, Germany) was placed on the couch at the isocenter. The DICOM images were analyzed using the open-source image processing program ImageJ[128] where a large region of interest (ROI) encompassing the majority of the beam was used to compute an average profile in the left/right direction (Figure 76).

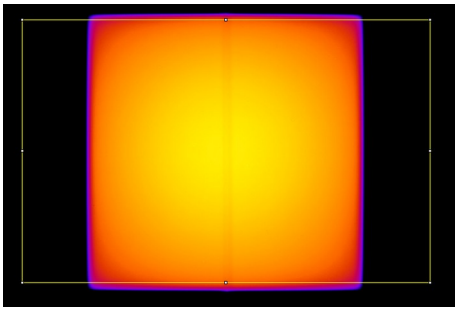

Figure *74*: Example of a 10 cm x 10 cm 6 MV flattening filter-free (FFF) portal image acquired with the electronic portal imaging device (EPID) in the presence of the fiber with a 10 cm thick RW3 phantom at the isocenter. The figure shows the rectangular region of interest (ROI) that was used to compute average profiles in the left/right direction to assess the impact of the optic fiber.

Figure 77 shows portal profiles acquired with the electronic portal imaging device (EPID) in the presence of the fiber with a 10 cm thick RW3 phantom at the isocenter and absolute differences between the profiles with/without the fiber for three beam energies (6 MV FFF, 6 MV, and 18 MV).

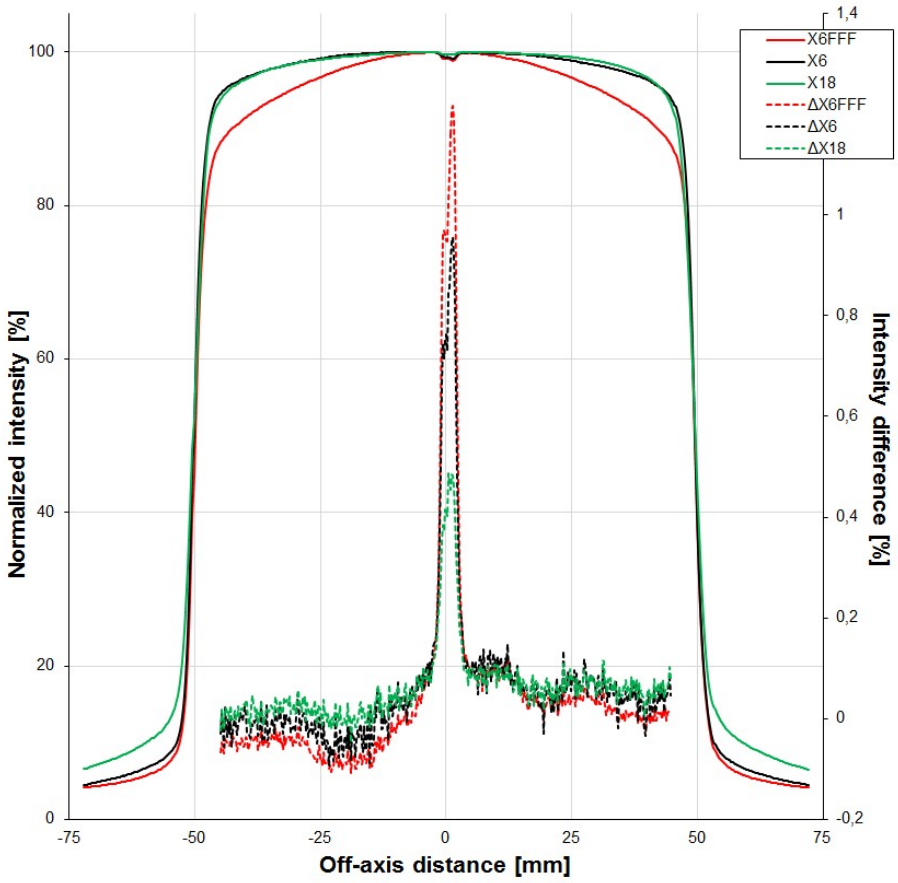

Figure 75: Profiles (solid lines, left vertical axis) of 10 cm x 10 cm 6 MV flattening filter free (FFF), 6 MV, and 18 MV obtained from portal images acquired with the electronic portal imaging device (EPID) in the presence of the fiber with a 10 cm thick RW3 phantom at the isocenter and absolute differences (dashed lines, right vertical axis) between the profiles with/without the fiber.

A decrease in the signal is observed in the center of the profile (from -2 mm to +2 mm) for all three energies. The drop is higher for the 6 MV FFF beam (maximum -1.2%), than the 6 MV beam (maximum -1.0%), and is lower for the 18 MV beam (maximum -0.5%). This decrease in the measured fluence indicates a diminution of the photons measured behind the PSF. However, based on the EPID oversensitivity to lower energy photons[68, 122, 157], a change in fluence does not necessarily indicates a change in dose. For that reason, another measurement tool was used to assess the dose variation.

An EBT3 Gafchromic film (Ashland Advanced Materials, Bridgewater, NJ, USA) was used to verify the impact of the presence of the fiber on the dose using the following setup: the film was placed at the isocenter in the middle of a 10 cm RW3 slab phantom and irradiated at the dose of 2 Gy with a posterior 10 cm x 10 cm 6 MV FFF beam. The film was scanned before and after irradiation with an Epson Expression 10000XL scanner (Seiko Epson Corp., Suwa, Japan). The dose analysis was performed with in-house Java software in which 3-color conversion and film homogeneity correction were implemented by using the non-irradiated image. The analysis was conducted using the same methodology as for the EPID images except that the reference profile (without the fiber) was calculated in the Varian Eclipse 16.1 TPS (Varian Medical Systems, Palo Alto, CA, USA) using the Acuros XB 15.6.04 algorithm with a 1 mm calculation grid size and the same geometry.

Figure 78 shows dose profiles obtained from an EBT3 film placed at the isocenter in the middle of a 10 cm thick RW3 phantom in the presence of the fiber and the corresponding dose calculated in the TPS Eclipse for the 6 MV FFF beam only and absolute differences between the aforementioned dose profiles.

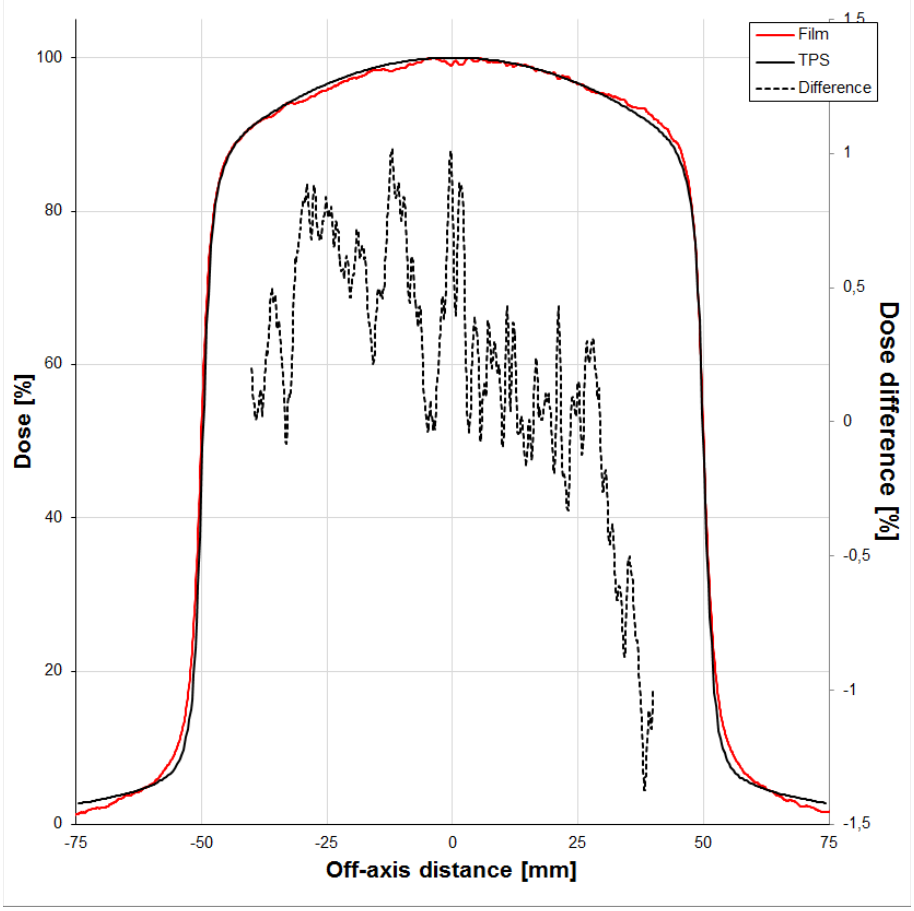

Figure *76*: Dose profiles (solid lines, left vertical axis) of 10 cm x 10 cm 6 MV flattening filter free (FFF) obtained from an EBT3 film placed at the isocenter in the middle of a 10 cm thick RW3 phantom in the presence of the fiber and the corresponding dose calculated in the TPS Eclipse and absolute differences (dashed line, right vertical axis) between the aforementioned dose profiles.

No relevant differences between the film and the TPS can be seen, even in the middle of the profiles where the fiber is placed. Therefore, the PSF does not influence the treatment dose when installed under the treatment couch.

III.D.4. Signal uniformity and calibration methods

III.D.4.a. Signal uniformity along the scintillating fiber

Photon attenuation phenomena in optical fibers are well-known. Various phenomena contribute to the overall photon attenuation in the probe, and they can be classified into two groups: fiber absorptions, characterized by the PSF and the attenuation length of clear optical fiber, and point losses resulting from splicings between the PSF and clear optical fiber, as well as the SMA connectors. These point losses represent the largest portion of total attenuation in the probe. Therefore, the uniformity of the signal measured also varies depending on the position of the irradiated PSF section. To evaluate this variation, the signal uniformity

along the PSF was simulated mathematically. In that aim, the overall attenuation along the PSF was evaluated using the known attenuation of each component of the probe (*i.e.* the connectors, the optical guide length, the splice, and the scintillating fiber length) and the following formula:

$$N_i(x)[u.a] = N_0 \times 10^{-A} \qquad \text{[Eq. 28]}$$

With $N_i(x)$ the number of photons measured on channel i when irradiating the PSF at the position x, N_0 is the number of photons initially generated inside the PSF and A the sum of the attenuations from all the components traversed by the photons before reaching the PM. The attenuation from every components (Cf. Table 5) is given by the average attenuation measured or given by the technical characteristics of the components.

The uniformity variation U was thus determined using the following formula:

$$U[\%] = \frac{\frac{N_{max} - N_{min}}{\overline{N}}}{2} \times 100 \qquad \text{[Eq. 29]}$$

With N_{max} and N_{min} respectively the maximal and minimal number of photons collected by the PMs, and $\overline{N}$ the mean number of photons collected by the PMs. Two different scenarios were simulated: (i) Using the photons measured from only one channel to compute the dose. (ii) Using the photons measured from the two channels to compute the dose. The main advantage of the first scenario is that it makes one channel available for an eventual complementary measurement with another probe (e.g. punctual entrance or transmitted dose) at the same time. Given that the device will be used in MDQC and measurements, it would therefore be easy to set a reference position for the couch and therefore always irradiate the same section of the PSF.

Table 4: Probe's components attenuation

Probe component	Attenuation (dB)
Channel connector #1	0.5
POF #1	0.11
Splice #1	0.5
PSF	1
Splice #2	0.5
POF #2	0.41
Channel connector #2	0.5
Maximal insertion loss	6
Additional loss from channel #1	1.1
Additional loss from channel #2	1.378

Using the [Eq. 28] and the known attenuation factor of each component, the variation of the uniformity of the signal was estimated to vary by ± 9.21 % and ± 0.83 % respectively for the first and second scenarios (Cf. Figure 79).

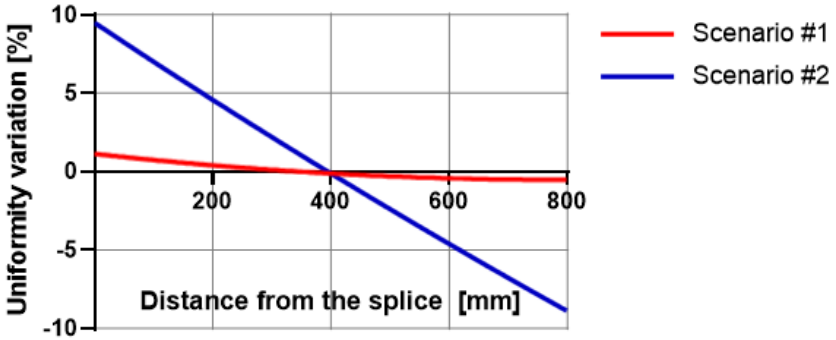

Figure 77: Uniformity deviation along the PSF in scenario #1 (2 channels connected) and scenario #2 (1channel connected).

Based on this simulation, the uniformity variation in function of the PSF irradiated section was not acceptable in the first scenario if not corrected. However, given that the PSF will always be placed at the exact same position for the MDQC and measurements, and because of the large collimations involved in CBCT acquisitions, it is therefore not required to use both channels for the IVI-CBCT device. Therefore leaving another free channel on the photocounting system to acquire punctual measurements at the same time. Although the choice of using one channel for MDQC and studies is suitable for this application, it is reminded that the device must be calibrated and used with the two channels if used for measurements with various couch positions such as patient dose measurements.

III.D.4.b. Calibration methods

To perform the cross-calibration, the dosimeter, and the ionization chamber are placed at the same position as the ionization chamber during CTDI measurements, *i.e.* the isocenter. To do so, the probe is placed at the center of the treatment couch using the Linac gantry at 180°, collimator 0°, and with the widest collimator aperture so the projection of the crossbar appears on the back of the treatment couch. The treatment couch is then translated along the z-axis so the projection of the crossbar can be used to place the totality of the PSF sensitive length (1 m). The lateral lasers are used to position the PSF at the isocenter height when calibrating the detector.

To realize the CTDI measurements, the ionization chamber is placed inside the CTDI phantom at the central and peripheral inserts. Concerning the air Kerma measurements needed to calculate the CTDI for wide collimations according to the report n°5 of the IAEA cited in the sections above, the ionization chamber was placed on a polystyrene plate, then the plate was placed at the treatment table's extremity, in front of the Linac so that the center of the chamber is placed at the isocenter. Then two verification acquisitions were realized by acquiring a planar kV-2D image in frontal and sagittal plans (Cf. Figure 80).

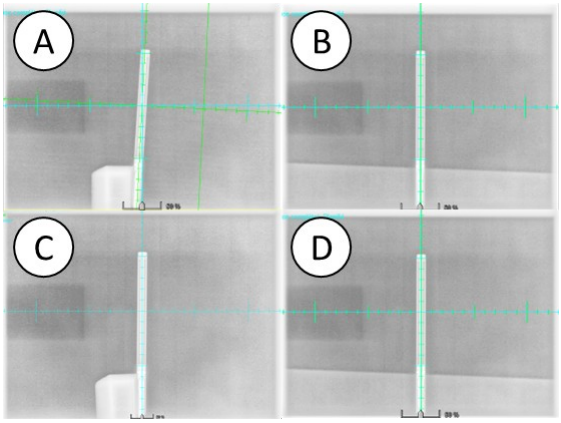

Figure *78*: 2D-kV acquisitions. A: Acquisition with the gantry at 270° before repositioning. B: Acquisition with the gantry at 0° before repositioning. C: Acquisition

with the gantry at 270° after repositioning. D: Acquisition with the gantry at 0° after repositioning.

The dosimeter was cross-calibrated with a pencil ionization chamber, that had been calibrated in a Primary Standards Laboratory, for each CBCT protocol. For each protocol, the CTDI cross-calibration factor N_c was defined as follows:

$$N_{c,\,protocol}\ [mGy.hits^{-1}] = CTDI_{ref,\,IC} / M_{ref,\,IVI\text{-}CBCT} \quad [Eq.\ 30]$$

Here $CTDI_{ref,\,IC}$ was measured during the reference acquisitions using a 10 cm PTW (PTW-Freiburg, Freiburg, Germany) pencil IC model 30009 connected to a PTW DIADOS E model T11035 electrometer and placed in a dedicated PTW model T40027 CT body phantom using the methodology developed earlier in the thesis[82] based on the IAEA HUMAN HEALTH REPORTS No. 5 methodology[173] and $M_{ref,\,IVI\text{-}CBCT}$ is the integrated number of counts measured by the IVI-CBCT device during the reference acquisitions.

Concerning the CTDI measurements, a reference supero-inferior collimation of 2 cm and a nominal beam width of 17.5 or 18.5 cm depending on the CBCT protocol was used with the following formula:

$$CTDI_{100,\,nominal\,width}[mGy] = CTDI_{100,20} \times \frac{CTDI_{free--air,\,nominal\,width}}{CTDI_{free--air,20}} \quad [Eq.\ 31]$$

$CTDI_{100,\ nominal\ width}$ representing the CTDI calculated in the phantom for the nominal beam width, $CTDI_{100,20}$ representing the CTDI measured in the phantom for the reference beam width (20 mm), $CTDI_{free\text{-}in\text{-}air,\ nominal\ width}$ being the CTDI measured in the air for the nominal beam width at 3 incremented supero-inferior positions: -10 cm, 0 cm and +10 cm from the isocenter and $CTDI_{free\text{-}in\text{-}air,20}$ representing the CTDI measured in the air for the reference beam width.

The CTDI is then determined for each acquisition by the following formula:

$$CTDI_{IVI\text{-}CBCT}\ [mGy] = N_{c,\,protocol} \times M_{IVI\text{-}CBCT} \quad [Eq.\ 31]$$

With $CTDI_{IVI\text{-}CBCT}$ representing the CTDI measured by the IVI-CBCT system and $M_{IVI\text{-}CBCT}$ the integrated number of counts measured by the IVI-CBCT device during the acquisition.

All the calibrations and formulas mentioned above are integrated into the pre-commercial analysis software (Cf. Figure 81) developed specifically for the fiber dosimeter measurement system. The software was developed using C# and is installed on a computer running on Windows present at the control desk. The communication with the dosimeter is assured by an RJ45 cable through the bunker's cable conduits. The software allows the operators to register a calibration factor for each CBCT protocol used (Cf. Figure 81). Depending on the time between two CBCT-emitted pulses (Cf. Figure 82) and the probe's DCR noise, the user

can also determine other signal processing parameters like a cutting parameter between two pulses or a DCR threshold parameter (Cf. Figure 81).

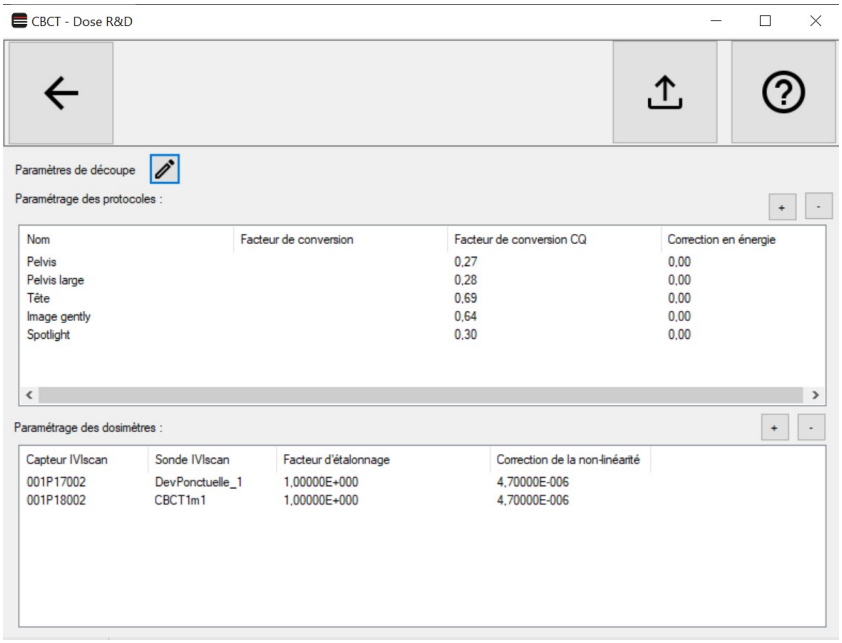

Figure *79*: In-house dedicated software.

Other acquisition parameters can be customized for the calibration of the system such as the sampling time and the noise threshold to take into account for every acquisition protocol including low dose protocols with a low signal-to-noise ratio and/or fast and widely separated pulses. The count rate is displayed during the acquisition as shown in the following figure (Cf. Figure 82).

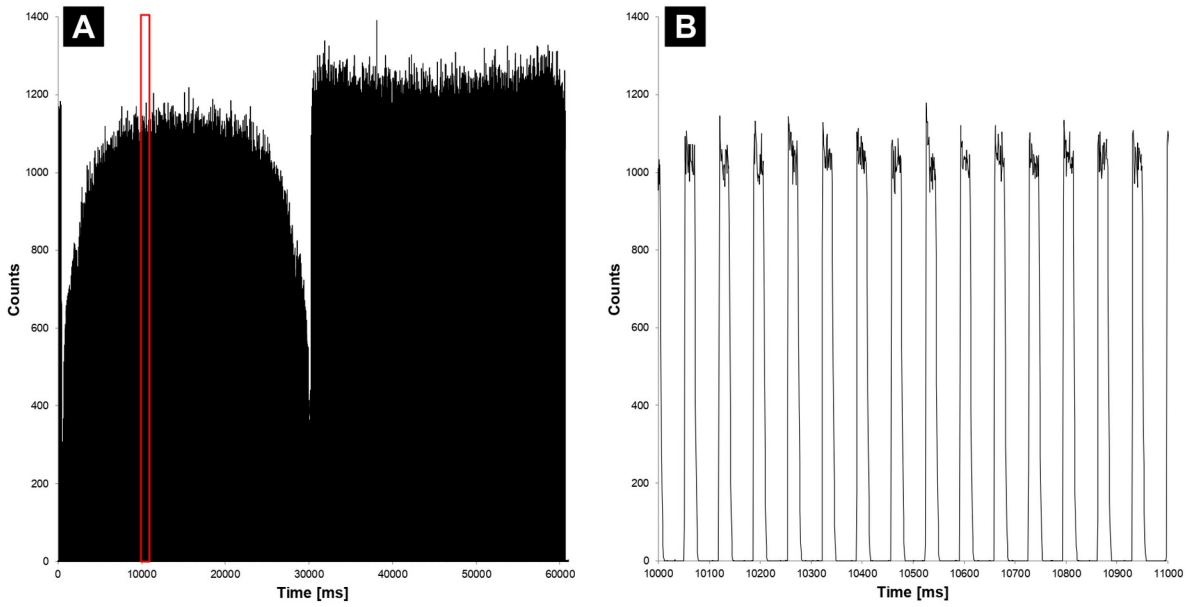

Figure *80*: Counts in function of the time (ms) for an acquisition of a CBCT with a 360° rotation of the source (A). A zoomed view of (A) inside the red boundaries shows the pulsed emission of X-rays by the kV source (B).

III.D.5. Repeatability and comparative performances

The CTDI measured with the IVI-CBCT dosimeter (acquisitions profiles recorded in the air with the fiber at the isocenter - couch vertical axis at +5,4 cm) was compared with the pencil chamber used for the calibration several days after the calibration process. The measurements were done for the 3 protocols detailed in Table 6.

Table *5*: Details of the CBCT protocols used for the comparison of the CTDI.

CBCT protocols	Pelvis	Pelvis Large	Spotlight
Fan type	Half fan	Half fan	Full fan
Trajectory	Full	Full	Full
Start angle [°]	180	180	180
End angle [°]	180E	180E	180E
Tube voltage [kV]	125	140	125
mAs	1080	1687.5	1350
Field of view [cm]	46.5	46.5	26.2
Collimation [cm]	17.5	17.5	18.5

[1]E stands for Extended

The repeatability was assessed by realizing 10 CTDI measurements for each protocol and each detector. The mean value and standard deviation of these measurements were recorded and the coefficient of variation was calculated. The theoretical CTDI value calculated by the accelerator was also recorded and compared to the mean values of measurements. Results of the repeatability evaluation are plotted in Figure 83 as a bar chart (the values are resumed in Table 14 in the annex).

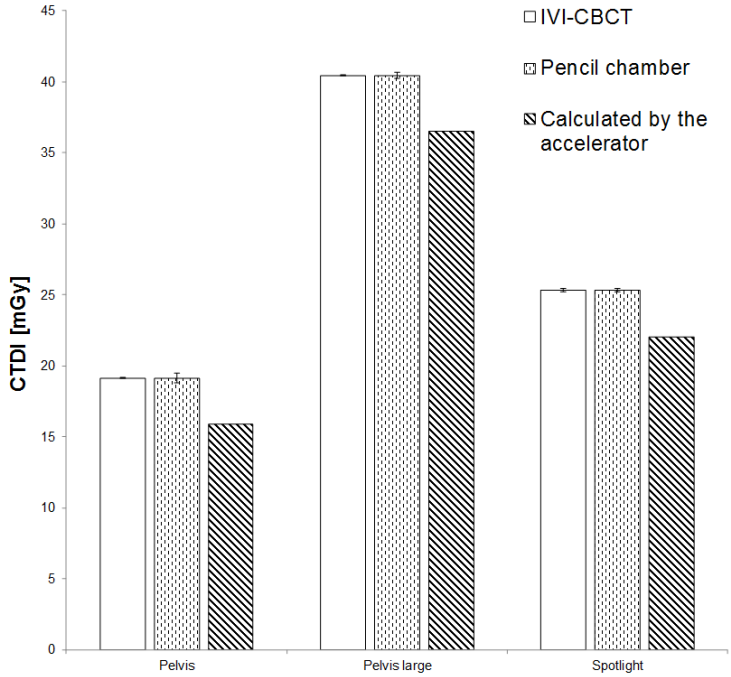

Figure *81*: Bar charts of the mean CTDI [mGy] measured by the IVI-CBCT device, the pencil chamber, or calculated by the accelerator. Error bars are standard deviations.

It appeared that the CTDI measured with the pencil IC and the IVI-CBCT device are consistently similar, with low uncertainty in the measurements. Conversely, the CTDI calculated by the Linac is systematically lower than the ones measured. This could be originated from a constructor measurement methodology that was not suitable for CBCT large collimations.

Then the variation of the CTDI with some acquisition parameters of the pelvis protocol, namely the tube voltage (100 or 125 kV), intensity (20, 60 or 100 mA), collimation (2, 4, 10, 15 or 17.5 cm), and images per second (IPS) (3 or 15 IPS), was assessed with both detectors. The measurements were done using the dosimeter only for the protocols in Table 6. All the measurements were normalized to the standard collimation used respectively for each protocol.

Table *6*: Details of the CBCT measurement protocols used for the comparison of the collimator aperture factor.

CBCT protocols	Pelvis	Pelvis Large	Spotlight	Image Gently
Fan type	Half fan	Half fan	Full fan	Full fan
Trajectory	Full	Full	Full	Full fan
Start angle [°]	180	180	180	180
End angle [°]	180E	180E	180E	180E
Tube voltage [kV]	125	140	125	80
mAs	1080	1687.5	1350	180
Field of view [cm]	46.5	46.5	26.2	26.2
Collimation [cm]	17.5	17.5	18.5	18.5

The CTDI was measured for all the protocols listed in Table 6 with the PTW pencil IC using the standard methodology and compared to the IAEA HUMAN HEALTH REPORTS No. 5 methodology. The results of the variation of the CTDI with acquisition parameters are shown in Figure 84.

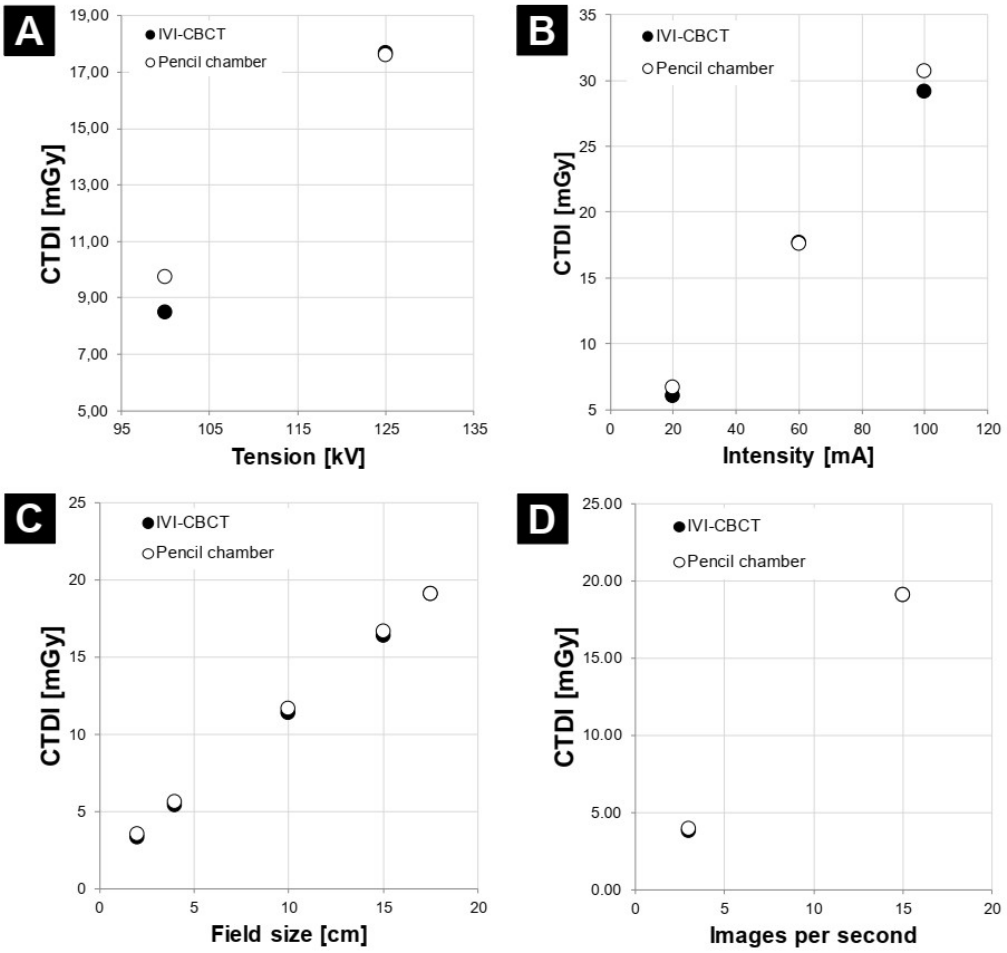

Figure *82*: Plots showing the variation of the CTDI [mGy] measured by the IVI-CBCT device or the pencil chamber in function of the tube tension [kV] (A), the tube intensity [mA] (B), the field size [cm] (C) and the number of images per second (D).

The relative difference observed was -2.6% (-0.1 mGy) when changing the IPS from 3 to 15 and respectively -4.6% (-0.3 mGy) and -0.8% (-0.3 mGy) when changing the mA to 20 and 100 mAS. When dropping the tension from 125 to 100 kV, the relative dose difference was -8.7% (-0.9 mGy). Except for the tension, the comparison with the pencil chamber shows similar CTDI values when changing the acquisition parameters. It indicates that the measures performed by the IVI-CBCT dosimeter are independent of the variation in intensity, field size, or images per second. The study on the collimation response of the detector was extended to all the protocols used in clinical routine, with collimations from 2 cm to the respective collimation of the protocol. Figure 87 shows the dose variation in the IVI-CBCT device depending on the collimation size for each clinical protocol.

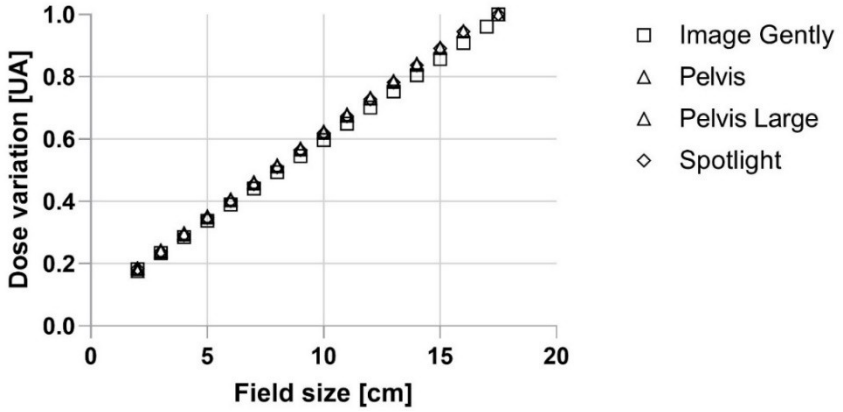

Figure *83*: Dose variation depending on the collimation for each clinical CBCT protocol.

The dose variation measured by the IVI-CBCT dosimeter evolves linearly with the field size. These results suggest that the calculation methodology used for the measurement of the CTDI with the IVI-CBCT device is efficient regardless of the collimation (small collimations and wide collimations). When varying the field size, the maximum relative dose difference of -7.2% (-0.3 mGy) at a field size of 2 cm.

Additionally, even if the dosimeter developed is used for dosimetric QA, investigations were realized to evaluate its behavior if used for patients' CBCT dosimetry. As the treatment couch is generally not positioned at the isocenter during treatment, the response of the IVI-CBCT was studied depending on the treatment couch position in the sagittal, longitudinal, and frontal plane. The Air Kerma was measured for the protocols listed in Table 6 with the IVI-CBCT and with the PTW pencil ionization chamber, translating independently from -6cm to +21cm in the frontal plane with a 3cm increment, and from -5cm to +5cm in sagittal plan with a 1cm increment. The difference in incremental movements in sagittal and frontal plans is explained due to the high number of measurements required to perform the CTDI measurement with the IC for a wide collimation field (5 acquisitions for each phantom position = 15 acquisitions per position in the sagittal or frontal plan). Therefore, the CTDI at different couch positions was compared to the CTDI at the isocenter for both the IVI-CBCT and IC measurements and compared between both dosimeters. Figure 88 shows the dose variation for different treatment couch translations in frontal and sagittal plans measured by IC and the IVI-CBCT dosimeter for different CBCT protocols.

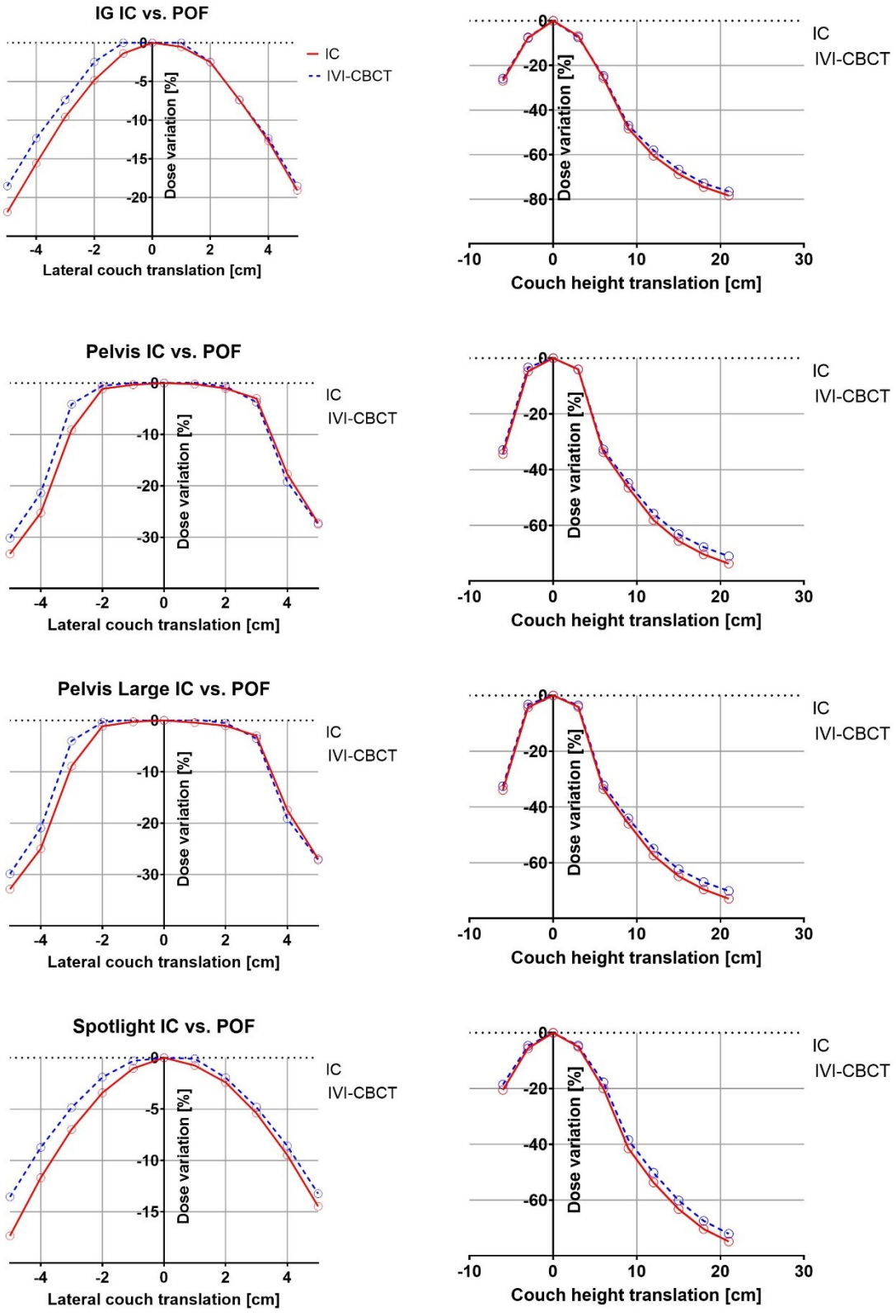

Figure *84*: Dose variation for different treatment couch translations in frontal and sagittal plans measured by IC and the IVI-CBCT dosimeter for different CBCT protocols.

When translating the treatment couch laterally, the dose variation observed by the IC and the developed dosimeter is consistently in line, except for the extreme negative lateral positions. Similar behavior is observed when translating the treatment couch in height. On the other hand, the study shows dose variations compared to the dose at the isocenter of up to 80%. These considerable dose differences highlight the need for a couch position correction factor if measuring the dose with the couch translated from the isocenter.

III.D.6. Conclusion

In the continuity of the previous sections, this work helped to define the dosimeter's components and hardware characteristics while comparing it to reference dosimeters in IGRT.

Firstly, the components and positioning of the probe were defined to have the least impact on the treatment and imaging beam while maintaining the performances of the device. These choices proved to be appropriate following the tests carried out on the dosimeter's influence. Regarding the images, the probe is visible at low voltage (65 kV) but disappears from the image once at 80 kV. Given that the CBCT protocols present on the linac used all involve a voltage starting at 80 kV, the probe can be considered invisible from the CBCT. Nevertheless, the interference of the probe was not evaluated for all the imaging protocols available on the linac such as Exactrac (Brainlab, Munich, Germany) or MV-2D images, and may be visible on low-dose imaging protocols using voltage < 80 kV. Concerning the treatment beam, when measured with the EPID it appears that the probe interfere slightly (<1.2 %) with the photons fluence at the center of the profile for the 6 MV, 18 MV, and 6 MV FFF photon beams tested. Based on the documented EPID oversensitivity to low energy photons[68, 122, 157], the question was then whether the IVI-CBCT probe interference with the fluence also had an impact on the dose. When evaluated with the Gafchromic films, this interference was not detected, thereby not resulting in a change of the dose. According to this measurement, the fluence difference measured by the EPID may be due to the probe's attenuation of low energy photons that may not significatively participate in the dose distribution. The tests of the probe's interaction with the imaging beams could suggest that the probe's interaction with the photons beam is not detectable above 80 kV and therefore that it does not impact significantly the photons fluence above this value. Further tests should be realized to confirm this hypothesis.

In addition, a sustainable installation was found to guarantee the power supply and signal transmission of the dosimeter. Also, the signal uniformity across the PSF was assessed, and two solutions were identified, depending on the application. If performing MDQC, the issue no longer arises since the couch position can be identically specified for all the QC. In that case, the dosimeter only requires the presence of one measurement channel, leaving the second channel available for another simultaneous punctual measurement. This solution could be particularly useful in the case of dosimetric studies involving several measurements (e.g. CBCT dose

optimization studies). On the other hand, for patient dosimetry applications, the dosimeter would require a two-channel measurement to correct the signal uniformity.

The calibration method was defined based on the large collimation dosimetry methods described above. This calibration was then tested by repeatability and comparative measurements. The repeatability showed equal values between the IVI-CBCT and the IC dose measurements and a maximum variation of 0.5% for the IVI-CBCT dosimeter which is equal to the maximum variation observed with the IC. Therefore, the IVI-CBCT dosimeter performances are then considered equal to the IC performances for the protocols studied. Also, when tested with different irradiation parameters (*i.e.* tube voltage, ips, mA, collimation). Again, the IVI-CBCT measurements agreed with the IC when altering the ips, mA, and collimation. Concerning the tube voltage, the results show an alteration of the IVI-CBCT measurement when changing the tube voltage from 125 to 100 kV. This result is in line with a previous study suggesting an energy dependence on the fiber[57]. An obvious solution to this issue would be to calibrate the dosimeter for the range of tube voltage used by CBCT protocols. Although this solution would be sufficient for MDQC, it would be insufficient for patient dosimetry and therefore need to be addressed for such application.

Finally, the dose variation compared to the isocenter was measured with couch lateral and height translations. This study revealed dose variations of up to 80% due to couch translation. Considering these differences, it appears essential to correct the dose measurements from the couch position when measuring the dose at a different position from the isocenter.

III.E. Discussion

III.E.1. Plastic fibers Radio-induced attenuation

This thesis work first started by evaluating the fibers' transmission and emission properties in high-cumulated dose environments by evaluating three types of fibers' RIA. The main difficulty of these measurements resides in the fact that each probe had to be manufactured specifically for these tests, and cannot be reused again for the same test once they have been irradiated because of the radiation-induced damage. Another main issue was to find the optimal dose rate to be able to perform the measurements at different dose ranges up to 1 kGy.

The BCF-98, BCF-12, and BCF-60 probes showed a quick decay of normalized intensity before the first 120 Gy and then stabilized approximately at 400 Gy. These measurements are in line with the literature[156]. Nevertheless, the RIA in the optical guide appears to be significantly lower than the blue and green scintillator probes. This difference would be explained by the fact that even if they have the same base material (PMMA), the BCF-12 and BCF-60 are fluor-doped fibers.

Considering the recovery of the properties of the fiber probes, the BCF-98 (corresponding to the optical guide) seems to not recover its previous attenuation properties even after a long time. On the other hand, both BCF-12 and BCF-60 recover partially their properties after the end of the irradiation, despite the recoveries remaining incomplete. Following these results, it appears that even if they are less detectable, the damage caused by radiations to the optical guide is irreversible at the dose rate studied, or recovers after a far longer time period. On the contrary, the damages caused in the scintillating fibers BCF-12 and BCF-60 are more noticeable but seem to recover partially after 24 h. This corroborates the results of the literature concerning the PMMA fiber's properties recovery in time[59, 60, 90, 113]. The difference in damage recoveries could be due to the different formulations between the scintillating fibers and the optical guide.

The investigation of a scintillation loss in function of the dose showed that the scintillation decrease is significantly lower for both the scintillators than the RIA, with lower values for the green scintillator. Following the literature[59, 60, 90, 113, 156], the RIA observed varies significantly depending on the observed wavelength. Since the LED didn’t have the exact same wavelength spectrum as the scintillating fibers emission, it was expected to have a difference in RIA observed between both experiments. Nevertheless, this change in wavelength is relatively low and could not explain such a difference in RIA observed between the BCF-12 scintillation signal and the LED signal. Since the signal collected in the first experiments was made of two components (*i.e.* the scintillation plus the LED light transmitted through the fibers), while the scintillation RIA is composed of only the scintillation signal, the difference between the RIA resulting from both measurements can result from a scintillation loss only. The lower RIA (better transmission) observed for the scintillating signal can be explained by the fact that the scintillating fibers formulation was studied to be transparent to its own scintillation wavelengths, but not to other wavelengths. In addition, when observing the scintillation only, the RIA is much lower for the BCF-60 probes. This can be explained by two things: The RIA is inversely proportional to the wavelength observed. And mostly, the chemical composition of BCF-60 is specified to contain higher radiation resistance materials such as 3-hydroxyflavone[171]. It also has been reported in the literature[164] that the presence of a wavelength shifter in BCF-60 (shifting the scintillating photons from blue to green wavelength) can impact the response to the temperature of the BCF-60 compared to BCF-12, suggesting that the BCF-60 composition play a role in its response to energy transfer (*i.e.* thermal, or radio-induced). Therefore, BCF-60 remains a more desirable option for measuring high-dose radiations (e.g. radiotherapy treatment beams). It has to be noted that some points are associated with strong uncertainties. Since the difference in RIA between the BCF-12 and BCF-60 remains in the uncertainty range, further studies should be realized to differentiate more precisely the impact of radio-induced damage in the two types of fibers. Also, following this study, we have decided to pre-irradiate all the probes at 1 kGy before installation and calibration. In addition, as a perspective of improvements, future RIA measurements could include the measurement of a sham-irradiated reference probe

in parallel with the measurements of the irradiated probes to abstain the measurements from variations of the LED output or photocounting system.

It has to be noted that the BCF-98 POF will not receive as much dose as the PSF given that the POF is positioned outside the primary beam range. In addition, although the fibers used for the RIA measurements are the same categories of fibers that are used in the IVI-CBCT prototype, the IVI-CBCT final product will involve similar fibers but from a different manufacturer (Toray Industries, Tokyo, Japan) due to better cost and delays. While several studies showed the RIA presence in BCF-12 and BCF-60 fibers, no evidence has been found in the literature concerning RIA on Toray fibers, it would be interesting to confirm the final choice of fiber by a similar RIA study on Toray plastic POFs.

Although the usual dose in radiotherapy doesn't involve the delivery of doses as high as the ones present in this RIA study, the use of POF RIA, with the right wavelength and fiber type selected, could find an interest in FLASH-RT dosimetry where high doses are delivered with a dose-rate ≥ 40 Gy/s. Recently, several studies have shown promising results regarding this POF application[69, 93]. In addition, the use of BCF-60 fibers could be an interesting choice even for conventional radiotherapy MV beam dosimetry due mainly to its peak emission wavelength at 530 nm facilitating the Cherenkov correction.

III.E.2. Characterization of SiPM photodetector for scintillation dosimetry

Following the light path from the fiber, the second study of this thesis focused on the implementation of a new photodetector, *i.e.* the SiPM, into the photocounting system. The SiPM photodetector's characterization highlighted the presence of different functioning patterns depending on the electronic threshold applied in function of the time. The study started by changing the electronic thresholds to evaluate the SiPM's response depending on the threshold applied. When selecting the threshold, the purpose was to find the optimum value, presenting a low DCR and a variation in function of the injected signal allowing the detection and discrimination of low, intermediate, and high light flux. This part of the characterization allowed us to highlight the presence of three operating regimes concerning the thresholds (Cf. Figure 89): (i) At low thresholds, within the range of 92 and 106, the SiPM presents a low DCR but also experiments with low maximum intensity. (ii) Between 108 and 112, presenting an unregular response, these latter thresholds are particularly hard to use in a counting system due to their measured intensity being not strictly increasing. (iii) Above 112, resulting in a relatively low DCR, a strictly increasing measured intensity, and counting dynamics allowing the precise measurement of high and low light intensities.

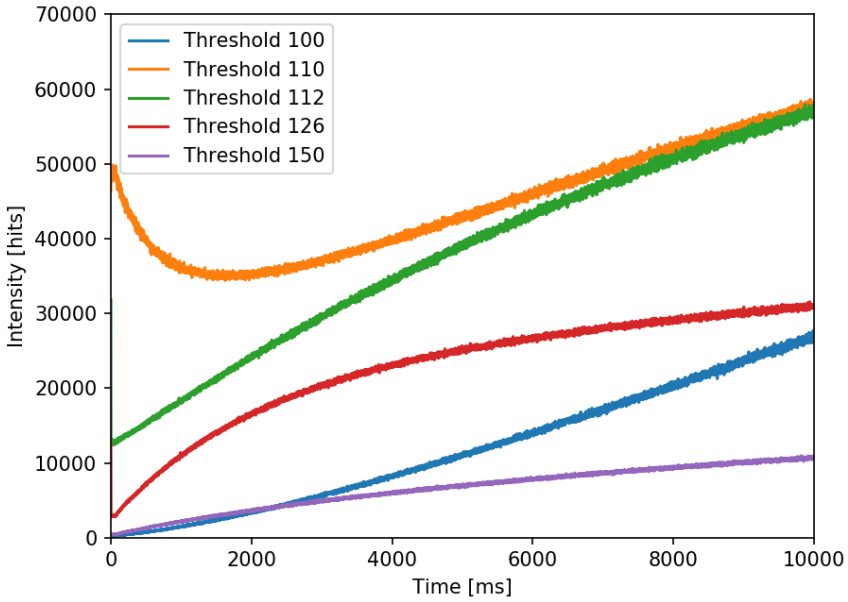

Figure *85*: SiPM response to a linear light signal for different threshold regimes.

The detailed noise study clarified the thresholds operating regimes description. A first type of response is observed below threshold 115, where the signal amplitude grows before reaching a stable region until decreasing above 125. Parallelly, the noise level decrease, and the SNR increase to 115, before remaining stable until both decrease above 120. The same behavior is observed for the two other SiPM tested for thresholds slightly different.

Following this noise study and the characterization of the SiPM at different thresholds, the thresholds between 115 and 140 were identified as the optimal range of functioning electronic thresholds to integrate the SiPM in the photocounting system. The noise study also indicated that the characterization, even if resulting in similar behaviors, has to be performed for each SiPM in order to find the ad hoc threshold.

The analysis of the SiPM performance stability through time also helped to get a better understanding of the SiPM noise by the study of the different light fluxes through time. The light flux n°0, representing the DCR, increased during the first 80 iterations (800 s), then continued to increase slowly through time indicating an augmentation of the noise when the SiPM is operating. This phenomenon was expected according to the literature[2] describing the high sensibility of the SiPM with the temperature, as the temperature rises inside the photocounting system when operating. Since the intensity measured varies identically to the DCR through time for all the light flux studied, it indicates the additive character of the SiPM's DCR. In addition, the study of the photodetector kinetics reveals a variation through time relatively more important for the DCR than for the other light flux.

Following this study, we have decided to place the electronic threshold on the SiPM #1 at 140 and installed it in a beta-test center. The methods to define the optimal threshold was also defined following the methodology used in this study.

III.E.3. CBCT dosimeter development and characterization

The device consists of an optical fiber that is placed beneath the treatment couch of the accelerator and is connected to a signal treatment unit affixed to the side of the couch. Since it communicates with a wall-mounted receiver via Bluetooth, it can be considered a wireless device, which adds to its utility. Nevertheless, the detector still needs to be charged periodically and the battery can last up to 48 h if the dosimeter is used continuously, which is unlikely to happen. A possible improvement to the dosimeter integration could be to connect the photometer through the treatment couch base to an RJ45 cable assuring both the recharging and the communication with an external computer.

The tests of the device started with analyses of the impact of the probe on the dose that is delivered. The EPID signal changed at the exact position of the fiber beneath the couch: the maximum difference was -1.2%, which was observed with the 6 MV FFF beam (Cf. Figure 77). This change could be caused by the known over-sensitivity of amorphous silicon EPIDs to lower energy photons compared to water-equivalent detectors; this is due to the increased photoelectric effect in the copper/phosphor screen[68, 122, 157]. The notion that the EPID signal change observed is due to EPID's over-sensitivity to low-energy photons is supported by the fact that the fiber did not affect the dose measurements of the film (Cf. Figure 78). Thus, the presence of the fiber does not appear to alter the delivery of the therapeutic dose.

While the fiber was visible on 65 kV planar kV-images (Extremity protocol), this mark was blocked when a thoracic phantom was placed before the beam. The fiber was also not visible at energies ≥ 80 kV (Figure 74). Moreover, on kV-CBCT images, the fiber was only visible as a small dot under the table. Thus, the presence of the fiber underneath the couch also does not appear to bias the imaging process.

During this thesis, since the device was a prototype, it was not calibrated in a Primary Standard Laboratory but it has been cross-calibrated with a pencil chamber that itself has been calibrated in a Primary Standards Laboratory. Nevertheless, the future products based on this prototype will benefit from a calibration from a Primary Standard Laboratory and the dose will be assessed using the methodology developed by the Fibermetrix laboratory[57]. To test the accuracy of the device, the cross-calibration of the device was repeated for three acquisition CBCT protocols (Pelvis, Pelvis Large, and Spotlight) that require different kV adjustments (125 or 140 kV) and fans (half fan or full fan): these protocols were chosen because previous evaluations of the detector with CT scanners showed a non-negligible dependence of the response of the fiber on the energy of the beam (up to 31% of dose deviations between a scintillating fiber dosimeter and a pencil

ionization chamber[57]). Thus, 10 measurements were acquired for each detector and each protocol, and found that the probe displayed better constancy (coefficient of variation ranged from 0.1% to 0.5%) than the pencil chamber (0.5% to 1.7%). Notably, compared to the CTDIs measured by the device or pencil chamber, the CTDIs calculated by the accelerator were consistently lower. This could be attributed to the dose-estimation methodology of the accelerator. The analyses with the three CBCT protocols also showed that the dose involved in the imaging ranges from 19 to 45 mGy depending on the protocol. While it is unlikely to happen, it is possible for a patient to undergo several CBCT acquisitions at each treatment fraction. Therefore, in this specific case, the findings support a previous study by Marinello et al. showing that the overall dose from kV-CBCT imaging can reach up to 3 Gy by the end of the treatment[118].

The accuracy of the device was also tested when the acquisition parameters in one of the CBCT protocols (Pelvis) were altered. Again, the IVI-CBCT dosimeter agreed well with the pencil chamber. Specifically, the relative differences were -2.6% (-0.1 mGy) when changing the IPS from 3 to 15 and respectively -4.6% (-0.3 mGy) and -0.8% (-0.3 mGy) when changing the mA to 20 and 100 mAS. Considering these differences, no IPS or mA correction factor is required for the dosimeter if used within the ranges applied above. As expected from previous studies on scintillating fiber dosimeter[57], when dropping the tension from 125 to 100 kV, the relative dose difference was -8.7% (-0.9 mGy). Even if it represents a low absolute value when operating a single measurement (e.g. dosimetric QA), the relative difference due to energy variation can become notable if applied to repeated CBCT patient dose measurements. This highlights the need for an energy correction factor Nk* in addition to a Primary Standard Laboratory calibration factor Nk for patient dose applications. When varying the field size, the maximum relative dose difference of -7.2% (-0.3 mGy) at a field size of 2 cm. Given that the cross-calibrations were performed at the respective collimation (17.5 and 18.5 cm) and the fact that the collimations are unlikely to reach values < 10 cm for clinical applications, the dosimeter does not require an additional correction factor for the collimation. On average, the trends in the variation of the responses of the pencil ionization chamber and the scintillating fiber dosimeter with dose parameters are the same showing that the IVI-CBCT device could be used to detect variations in the tube output over time.

On the other hand, the study of the variation of the dose in function of the treatment couch position showed good agreement between the dose measured by the IC and the IVI-CBCT dosimeter. This suggests that the dosimeter can be used to detect variations in the table position. Moreover, it also underlined the necessity of an additional correction factor based on the couch position to use the detector for patient dosimetry application. Following these findings, the use of the dosimeter for dosimetric quality assurance only requires the use of a calibration factor N_k.

Finally, we deducted the minimal time requested for each of the two dosimeters based on the CBCT acquisition duration and the number of acquisitions needed for each dosimeter. Although it is highly time-consuming, we didn't consider the time needed to change the IC position in the CTDI phantom's inserts or the time needed to change the CTDI's phantom position between each measurement (*i.e.* door opening, entering the room, changing insert, moving the phantom/checking the phantom's position) because this part is also highly operator and center dependent. Nevertheless, it has to be noted that the IVI-CBCT dosimeter, as opposed to the ionization chamber, requires a unique measure while the IC requires multiple measures to assess the CTDI. This results in a minimum requested time of 60 s to measure the CTDI with the IVI-CBCT dosimeter, whereas the pencil IC requests a minimum of 900 s to perform the same measurement. Due to its design, the device generates the CTDI very quickly, namely, the time needed to conduct a CBCT acquisition. This is considerably faster than the reference IAEA method, which takes at least 15 times this duration for a complete set of acquisitions. This reflects the fact that these latter measurements must be conducted in a dedicated phantom and free-in-air and that great care must be paid to the ionization chamber position. Specifically, the phantom must be positioned, and measurements in the five holes and free-in-air must be conducted in three positions. In addition, the medical physicist's time in radiotherapy is often spread into numerous tasks, resulting in the need for fast and accurate tools. In this context, the device presented in this thesis presents a significant advantage in terms of the timeliness to provide the CTDI.

These promising properties suggest that the dosimeter developed could be useful for tube output monitoring over time, periodic CTDI verifications (*i.e.* following an intervention of the vendor), and protocol optimization purposes. However, further studies are required to determine how well the device performs with a variety of CBCT protocols, including cranial CBCT protocols or optimized low-dose protocols, and other onboard CBCT manufacturers.

III.F. Conclusions regarding the specifications, dosimetric performances, and clinical constraints / Experimental development conclusions

During this work, many steps of the dosimeter's initial requirements were validated, from the probe's design, installation in the treatment room, and compatibility with the RT environment and high doses to the definition of the calibration method and the characterization and validation of the dosimeter installed in the treatment room.

The RIA study gave interesting results concerning the behavior of POF and PSF in the presence of high doses. Following this study, pre-calibration irradiation of 1 kGy has been defined for all the new probes.

Further evaluation will be done to assess the physical properties of POF and PSF depending not only depending on the deposited dose but also on time.

The dosimeter's perennity was assessed by the investigation of SiPM implementation into the photocounting system. Thanks to this study, the SiPM photodetectors can be implemented into the IVI-CBCT photocounting system. In addition to the cost and dimensions criteria, this study took place in a global context of shipping restrictions and delays in electronic manufacturing across the globe. It showed very interesting results, and the SiPM photocounting system will be progressively incorporated into all the IVI dosimetry solutions starting in January 2024. The remaining work needs to be done to estimate the impact on the power supply and the possibility to decrease the noise while conserving a similar SNR.

Also, the method was defined for large collimations dosimetry and the main clinical constraints inherent to the RT environment were assessed since the dosimeter's influence on imaging and treatment beams was evaluated and considered negligible. Moreover, the dose measured with IVI-CBCT was similar to the one measured with IC and showed good repeatability. These results are very encouraging for MDQC.

As mentioned in the sections above, limitations remain regarding the patient dosimetry application of the system. Among them, uniformity correction, couch position correction, and energy correction should be assessed to evaluate the patient dose. While the uniformity correction can be easily corrected by the use of the 2 channels, the couch position correction needs further investigation.

Nevertheless, concerning the energy correction, previous evaluation of the fiber mass attenuation coefficients variation at 0° and 180° (when the difference of energy spectrum seen by the fiber is maximal) using a CTDI body 32cm phantom and an 80 kV and 140 kV X-ray source showed a maximal difference of 6,9 % between the two angles[77]. Moreover, with the phantom positioned on the table, the dose contribution from the anterior angles (e.g. 0°) to the overall measured dose can be considered minor compared to the dose contribution from the posterior angles (e.g. 180°). Therefore, the maximal difference of 6.9% in mass attenuation coefficient, when put regarding the anterior angles dose contribution, has a minor impact on the dose measured. Given the rationale aforementioned, no energy correction factor should be needed for CBCT dosimetry in the presence of scattering volume (*i.e.* a patient or a phantom).

Eventually, another dosimeter (IVInomad) was used during the radiobiological studies in order to measure the punctual dose delivered in proximity to the cell culture medium. It allowed us to evaluate the DNA repair mechanisms involved in IGRT in the frame of a preliminary study of the AR phenomenon in IGRT using the IVInomad dosimeter. The following section details this preliminary study.

IV. Radiobiological aspect

The entanglement between medical physics and radiobiology is present since the birth of these domains and has profoundly improved the research in both fields. A deep understanding of the issues on one side only comes in conjunction with progress and technological advancements on the other side. For this purpose, and because it is Fibermetrix and the Unit 1296 belief that technological innovations in medical physics must benefit all related fields, this thesis proposes to explore an application of the imaging dose evaluation from a radiobiological perspective. The Unit 1296 "Radiation: Defense, Health Environment" was created with the support of the National Institute of Health and Medical Research (INSERM), the Ministry of the Armed Forces, the Armed Forces Health Service (SSA), and the Léon-Bérard Center in Lyon (CLB). Directed by Nicolas Foray, Director of Research at INSERM, Michel Drouet, Chief Medical Officer (SSA), and Béatrice Fervers, clinical epidemiologist (CLB), the main mission of this Unit is to better understand the biological consequences of exposure to radiation DNA-breaking agents in a clinical, military, environmental, space or professional context, by studying more particularly the impact of the individual factor in the repair and signaling of DNA damage.

The next section suggests reviewing the radiobiological basic concepts. Then, the following sections will investigate, in the frame of a preliminary study, the effects of low imaging doses in combination with high treatment doses on DNA repair.

IV.A. State of the art

IV.A.1. Radio-induced risk models

Radio-induced risks can be quantified following models based on epidemiological studies. The main issues and uncertainty in these epidemiological studies reside in the quantification of the effects of the low doses (< 100 mGy) on radio-induced cancers[172, 162]. As public medical exposure is rising every year, the effect of low doses became of public health interest. To assess the radio-induced risk, epidemiologists have considered two models based on wide cohorts: the Linear-no-threshold (LNT) and Non-linear threshold (NLT) models. Based on the precaution principle, the LNT model assumes that the risk is strictly proportional to the absorbed dose and is null if there is no absorbed dose. At the end of the 1950s, the International Commission on RadioProtection (ICRP) adopted the LNT principle as a precaution principle due to the lack of mechanistic models explaining the dose-response and carcinogenesis[36]. Even today, this model is still preconized[37, 96, 150] and is at the origin of the ALARA (As Low As Reasonably Achievable) radioprotection principle. Following the analysis of the Hiroshima and Nagasaki events, the first model appears to overestimate the occurrence of radio-induced cancers[21]. This led to the introduction of a second model based on the presence of a dose threshold at 100 mSv, followed by a proportional link between dose and radio-induced cancer. While the Hiroshima data (the largest dataset ever obtained on radio-induced

cancers) converged to the NLT model, the assessment of the associated risks under the threshold, and the threshold dose, remained the major issues in the field. Studies suggest the existence of an augmentation of the cancer risk at lower absorbed doses (between 10 and 100 mSv) for different fractionation[22, 31] (Cf. Figure 88).

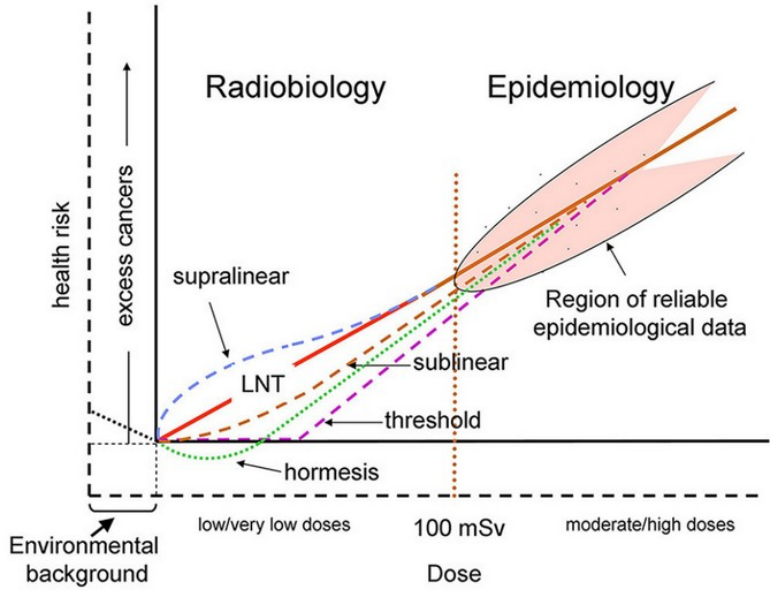

Figure *86*: Schematic representation of possible dose-response relationships for radiation-induced cancer risk including low dose (< 100 mGy) and moderate/high doses (> 100 mGy)[22].

In addition to these two models, other patterns specific to low doses tend to make the risk assessment more difficult. Under 100 mSv, the literature[38, 55] suggests the possibility of the existence of a protective effect (*i.e.* Hormesis effect) of low doses on the cells. In contrast to this effect, the principle of hypersensitivity to low doses suggests a more detrimental effect of the low doses, particularly between 100 and 200 mSv[119]. These two effects, when compared to the LNT and NLT, contribute to the reconsideration of both the LNT and NLT models. The linear description of the risk in the low-dose range of the imaging field is challenged by these phenomena. Additionally, the gradual link between these phenomena and individual factors was not previously considered in discussions on low-dose radiation[123]. The disagreement between those who support the LNT and the NLT models highlights the societal challenge still undergoing in the understanding of radiation's low-dose effects.

In opposition to low doses, the radiation-induced effects of high doses are well documented in the literature. However, one of the modern radiobiological issues that have not been studied is the combined effect of low and high doses during radiotherapy treatments.

IV.A.2. Hormesis and adaptive response

IV.A.2.a. Hormesis

T.D. Luckey first introduced the term "hormesis" to the field of radiation research in the 1980s to describe a J- or U-shaped dose-dependent phenomenon[115], implying that hormesis is a continuous function of dose (or dose rate). Therefore, it suggested the existence of a specific threshold dose below which exposure to stress is “positive” and above which stress is “harmful”[35]. The non-linear nature of the hormesis phenomenon has been an important aspect of the debate on the linear no-threshold model[40, 142]. Consequently, the notion of a stimulatory effect has gradually been replaced by the notion of a beneficial effect, as opposed to the toxic effect observed at high doses.

IV.A.2.b. Adaptive response

Adaptive response (AR) is defined in biology as “an adaptive process that allows survival under adverse conditions”[147]. In 1984, Olivieri et al. first introduced the term into the field of radiation research to describe a radiobiological phenomenon that occurs after two successive doses[130]: The first, called "priming dose" (d_{AR}), precedes a certain time (Δt_{AR}) and a higher dose called the "challenging dose" (D_{AR}). Thus, the AR phenomenon occurs when the effect of $d_{AR}+\Delta t_{AR}+D_{AR}$ is smaller than that of D_{AR} alone (Cf. Figure 89 and 90)[130]. While the D_{AR} dose consistently produces deleterious and/or lethal effects, the primary d_{AR} the dose is generally interpreted as stimulating cellular defenses[34, 94] to respond to D_{AR}. However, the nature of these defenses has not been clearly identified until now.

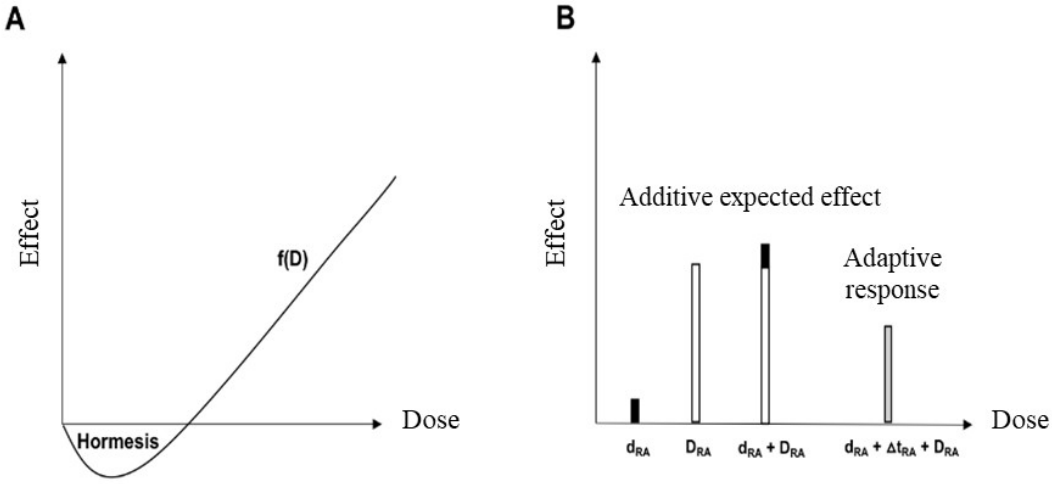

Figure *87*: Difference between the hormesis and the adaptive response. Hormesis is defined as a continuous function of the dose where a stimulating effect occurs at sub-inhibitor doses. It is the effect of a single dose or a single dose rate (can appear when irradiated by a chronic exposure). B: The adaptive response is defined by an infra-

additive effect observed after the succession of a priming dose d_{AR} followed by a challenging dose D_{AR} separated by a time period of Δt_{AR} (adapted from Devic et al. [58]).

AR can lead to a reduction in risk from a high dose (D_{AR}) by another lower dose (d_{AR}), whereas hormesis describes beneficial biological effects without the induction of another dose. Furthermore, hormesis and AR do not necessarily occur in the same dose range: D_{AR} is generally equivalent to a few Gy, whereas hormesis is observed at much lower doses ranging from mGy to cGy such as d_{AR}.

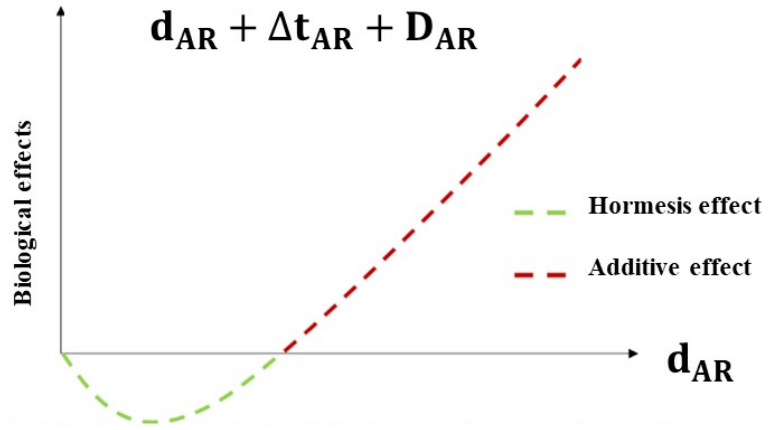

Figure *88*: Hormesis effect without adaptive response in function of d_{AR} (adapted from Devic et al.[56]).

The molecular mechanisms of the adaptive response and hormesis are not well known but could be very similar since AR can be considered a hormetic phenomenon. When reviewing AR protocols, it is remarkable that the priming dose of AR is, in more than 90% of the studies, less than 0.05 Gy but greater than 0.001 Gy. Oxidative stress caused by 1 Gy of X-ray or γ radiation simultaneously induces approximately 10,000 BDs, 1,000 SSBs, and 40 DSBs per human diploid cell. Therefore, priming dose d_{AR} typically induces less than 500 BDs, 50 SSBs, and two DSBs per cell. It corresponds to significantly less oxidative stress than that induced by the spontaneous DNA damage typically observed in radioresistant human cells[79]. Such DNA damage cannot significantly affect cell survival or genomic instability. In contrast, in radiosensitive cells, oxidative stress due to spontaneous genomic instability causes a small but significant amount of DNA damage, greater than that observed in radioresistant cells[79]. Therefore, one of the possible hypotheses proposed is that spontaneous oxidative stress added to that caused by the initial d_{AR} dose can result in a significant amount of DNA damage only in radiosensitive cells[58]. Thus, if a certain level of oxidative stress is required for the occurrence of an AR phenomenon, it should preferably occur in radiosensitive cells[58].

In external radiotherapy, some indications require the use of 3-dimensional (3D) imaging (kV-CBCT or MVCT) recurrently for repositioning (e.g. head and neck, rectum, prostate) resulting in deposited doses

rarely or not taken into account into the treatment plan. Therefore, this thesis also aimed to perform a preliminary study to evaluate the effect of the low dose of kV-CBCT or MVCT imaging during radiotherapy sessions on DNA repair mechanisms and cell survival.

In head and neck squamous cell carcinoma (HNSCC), early complications of the RT are observed from the beginning of the treatment to a few months after its end. Among them, oral mucositis and dysphagia, which are the most frequently observed in HNSCC patients, can significantly reduce their quality of life[26] and may interfere with or even permanently interrupt treatments[160]. Mucositis is an irritation of the mucous membranes lining the oral cavity and can lead to the development of mouth ulcers. Dysphagia is characterized by difficulty swallowing, often linked to a swallowing problem. These toxicities will prevent the patient from eating normally, worsening his quality of life and leading to weight loss. This loss of weight is synonymous with stopping the treatment for the oncologist. Therefore, the following methods were used on healthy tissues from cancer patients and in the case of radiosensitive group II genetic syndromes[67].

IV.B. Methods and experimental setup

We have focused on cancers localized in the head and neck region (Head and Neck Cancers: HNC). Indeed, HNSCC is typically diagnosed at a locally advanced stage[30], and while early-stage cases can be treated with surgery and/or RT, locally advanced HNSCC is usually treated with RT with at least one CBCT per fraction, depending on the primary site and stage[155].

IV.B.1. Cell lines

A Primary Dermal Fibroblast; Normal, Human, Adult (HDFa) (from ATCC ref: PCS-201-012) was used. 2 non-metastatic HNSCC patients (called TS1 and TS14) treated with definitive radio(chemo)therapy between 1st January 2017 and 1st June 2017 were included. Radiation therapy was delivered either by Intensity Modulated Radiotherapy (IMRT) or Volumetric Modulated Arc Therapy (VMAT). Among them, all accepted to enter the Collection number: 2017-A00086-47. The study was approved by the local Ethical Committee (number: 2017-A00086-47). All patients were informed and signed consent. The following data were collected: sex, the primary site of HNSCC, radiotherapy details including dosimetry and technique, and chemotherapy details such as type of chemotherapy (Cf. Table 7).

Cells from a skin biopsy were cultured in monolayer with Dulbecco's modified Eagle's minimum medium (DMEM) (Gibco, NY, USA) supplemented with 20% fetal calf serum (FSS, Gibco, Brazil), 1% penicillin, and streptomycin (PS) (Gibco, NY, USA) for the lines. Cells were incubated in an incubator at 37°C and 5% CO2. The study was done for each cell line using three biological replicates (triplicates).

Table 7: Clinical data from the patients' cell lines TS1 and TS14.

NUMBER	TS1	TS14
PRIMARY LOCALIZATION	Base Tongue	Oropharynx
GENDER	M	M
STAGE T	T4	T3
STAGE N	N2c	N2a
CHEMOTHERAPY/DRUG	FLUORO-URACILE CISPLATIN	Erbitux (Cetuximab)
TYPE OF RT	Neo-Adjuvant	Concomitant
TECHNIQUE	IMRT	VMAT
DOSE (GY)	Split course: 45 Gy (3 Gy/fraction)	70 Gy (2 Gy/fraction)
TOXICITIES (CTCAE)	Grade 2	Grade 3
TUMOR RESPONSE (RECIST)	Partial response (PR)	Progressive Disease (PD)

IV.B.2. Biomarkers

To evaluate the effect of CBCT on the DNA repair mechanisms, the DNA repair was observed using the pATM and phosphoH2AX immunostaining at 10 min and 24 h post-irradiation. In addition, the micronuclei were also counted at 24h post-irradiation.

IV.B.3. Irradiation and fixation protocol

IV.B.3.a. Irradiation protocol

The irradiation condition mimics a standard HNC RT treatment fraction with one CBCT acquisition followed 3min later by a 2 Gy irradiation. To separate the influence of each dose (imaging dose, and 2 Gy) in the irradiation sets, the irradiations were repeated for imaging dose only, 2 Gy only, and imaging dose combined with 2 Gy. Figure 91 below gives the detail of each irradiation protocol.

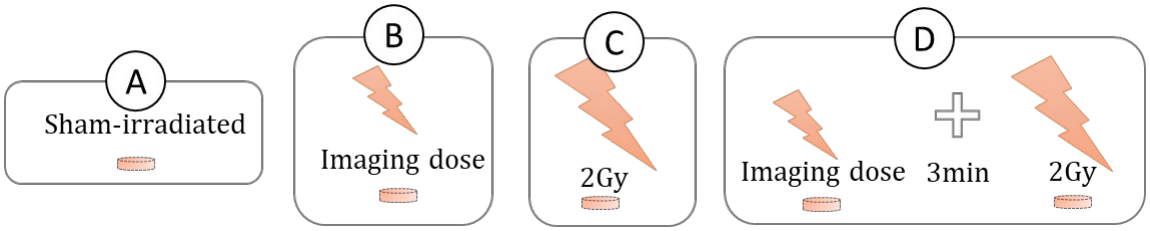

Figure *89*: Irradiation sets. A: Sham-irradiated cells; B: Imaging dose (kV-CBCT or MVCT) alone. C: 2Gy alone. D: Imaging dose (kV-CBCT or MVCT) + 3min + 2Gy, respectively $d_{AR}+\Delta t_{AR}+D_{AR}$.

Before this thesis work, the radiobiology irradiation experimental setups involved the presence of a 1 cm PMMA plate above and below the irradiated petri box, without an additional scattering medium and the boxes being half filled with the nutrient medium as presented in Figure 92. This configuration, although very simple, also includes a lot of dose uncertainties due to the presence of heterogeneities.

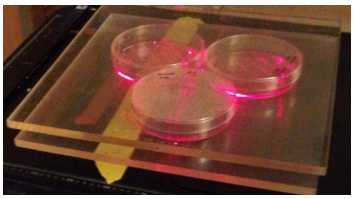

Figure *90*: Previous irradiation setup.

To improve this experimental setup by reducing the dose distribution heterogeneities and guarantee a homogeneous repartition of the dose delivered through the petri boxes and flasks, they were placed inside in-house inserts made inside a bolus (BOLUSIL, Kerjean Biotechnologies, Aubergenville, France) with a 1.05g/cm^3 density (Cf. Figure 93). In addition, to avoid air gaps inside the cell petri boxes, they were filled with nutrient medium.

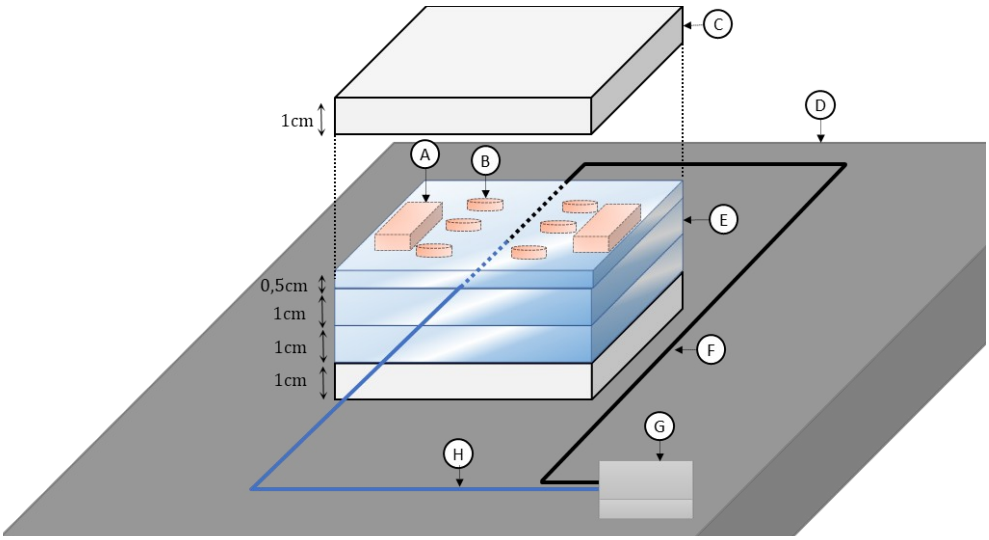

Figure *91*: Experimental setup for the cellular irradiations. A: Cells flasks. B: Petri boxes. C: Upper 1cm PMMA plates. D: Treatment couch. E: BOLUSIL bolus. F: Fiber dosimeter channel 1. G: Photometer. H: Fiber dosimeter channel 2.

Using the experimental setup presented in Figure 93, the dose delivered by the kV-CBCT is measured using an IVInomad dosimeter developed for this study and plugged into channel 2 of the photocounting device. Initially, the first channel was supposed to be used to measure the dose from the 6 MV beam, but it was eventually not used because the probe was not functional. As the effect of the dose also depends on the energy of the incident particles, the AR effect was investigated using kV and MV pretreatment imaging. The irradiations were delivered using two medical accelerators: an Elekta Versa HD (Stockholm, Sweden) delivering a 6MV treatment beam and equipped with a kV-CBCT imaging system, and a Tomotherapy (Accuray, Sunnyvale, CA, USA) delivering a 6 MV photons beam and equipped with a 3.5 MV MVCT imaging system. The dose delivered by the kV-CBCT imaging system was measured on the first irradiation with an IVInomad system specially designed for the study and was considered similar to the other irradiation repetitions. The IVInomad probe used for the study is made of a 1 cm diameter and 1 mm long PSF sensitive volume and a 2 m long POF. The dose delivered by the Tomotherapy irradiator was calculated using the Precision TPS (Cf. Figure 94). The dose delivered by the MVCT Tomotherapy system was estimated based on the dosimetric quality control (1.5 - 1.6 cGy) and following the literature[139] on MVCT dose estimations.

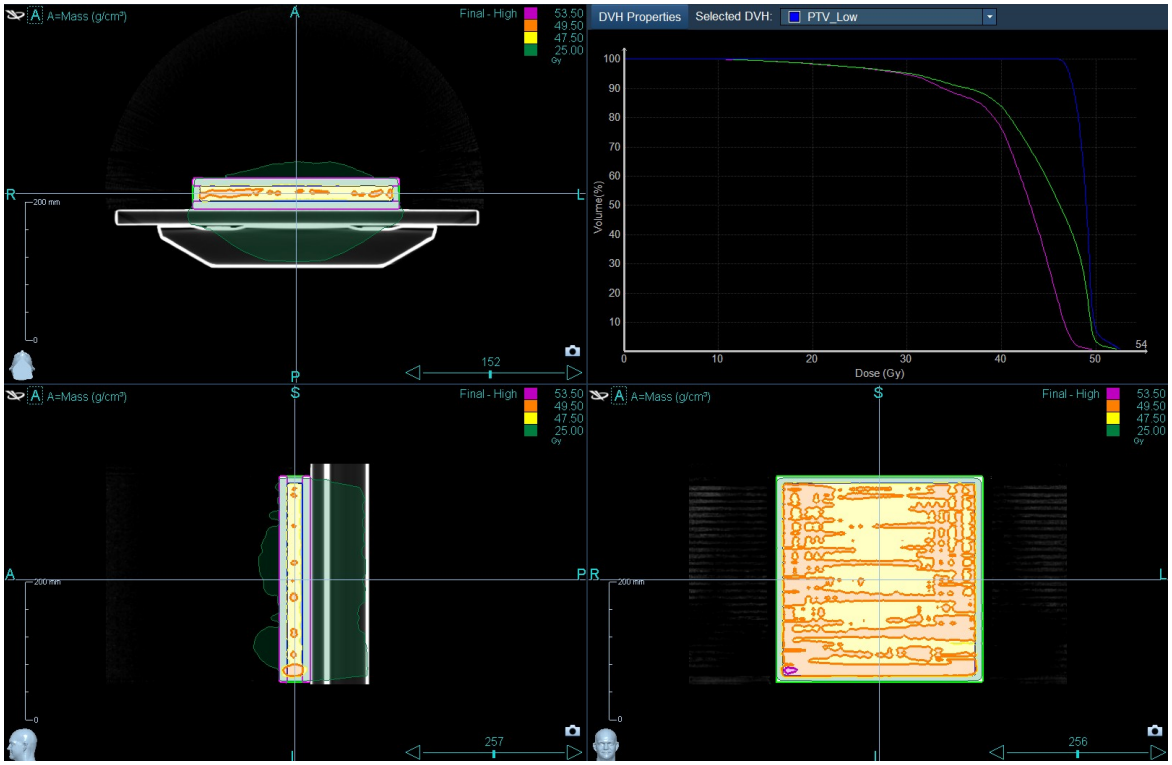

Figure *92*: Dose repartition inside the experimental phantom for the Tomotherapy irradiations. The dose is calculated using the Precision TPS.

IV.B.3.b. Fixation protocol

The cells on the lamellas are irradiated following the conditions enumerated in figure 91 and a timer is stated after the end of the irradiation. The cells are fixed at different times t = 0 min, t = 10 min, and t = 24 h. The cells are rinsed twice with PBS1X, then a 4% paraformaldehyde + 2% sucrose solution is placed on each slide, under the chemical hood. After 15 minutes of waiting at room temperature, the cells are rinsed again with PBS1X, then PBS1X is placed in each dish and they are stored at 4°C.

IV.B.3.c. Immunofluorescence

Then, the cell membranes are permeabilized with a lysis solution [sucrose, MgCl2, Hepes, NaCl, Triton]. Immunostaining is done with two antibodies: anti-phospho-ATM primary antibody, directed against pATM protein [mouse monoclonal antibody diluted in PBS/BSA 3% (Millipore, USA)] and anti-phospho-histone H2AX primary antibody, directed against γH2AX protein [mouse monoclonal antibody diluted in PBS/Bovine Serum Albumin (BSA) 3%, Millipore, USA] are prepared before manipulation and deposited on the corresponding coverslips. The whole is incubated for 1 hour, at 37°C and 5% CO2. The secondary antibody used is coupled to the fluorochrome fluorescein isothiocyanate (FITC) [anti-mouse Immunoglobulin C produced by a goat, (Sigma-Aldrich, USA)]. A drop of Di Amidino Phenyl Indole (DAPI) (Vectashield, Vector Laboratories, USA) is deposited on slides previously cleaned with alcohol (Cf. Figure 95).

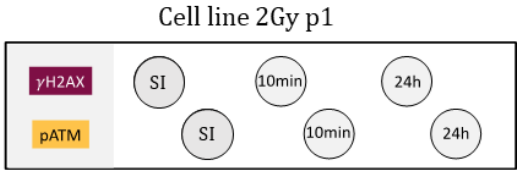

Figure *93*: Example of cell line on a lamella.

The lamellas are placed on the drop of DAPI which will allow the observation of the nucleus by binding to the DNA. The next day, the lamellas are varnished and stored at 4°C in the dark while waiting for the reading. Cells are observable under a fluorescence microscope at 460 nm for DAPI and 521 nm for pATM and γH2AX foci. Foci of 50 cells are counted for each antibody and time. Micronuclei are counted per 100 cells. Averages for each replicate are calculated.

IV.C. Results

The aim of this preliminary study was to determine whether the imaging (priming) dose may impact the final response of tissues to a challenging dose of 2 Gy. In addition, the kV CBCT (priming dose delivered at 100 kV) effect was compared to the MV CBCT (priming dose delivered at 3.5 MV) effect. Before investigating the occurrence of a possible adaptative response (AR) effect ($d + \Delta t + D < D$), the cell lines must be characterized in order to know if they are likely to have a potential AR effect.

IV.C.1. Radiobiological characterization of the patient's cell lines

Table 8 shows the numbers of γH2AX foci per Gy assessed at 10 min and 24 h post-irradiation on the Linac device (CLB, Lyon). It is noteworthy that, by considering the difficulties of access to irradiators, the control of the repair time may have been flawed with errors of a few mins. Hence for the 10 min γH2AX data (*i.e.* the highest values of foci), we have systematically applied a 7.5% relative error, as a large intercomparison data campaign between U1296 and Neolys Diagnostics laboratories suggested it.

Table 8: Amount of γH2AX foci per Gy assessed 10 min and 24h post-irradiation on the Linac device (CLB, Lyon). The results are presented such as: Amount of γH2AX ± SEM. SEM stands for the standard error of the mean.

Cell lines	10min	24h
TS1	21 ± 2	0.2 ± 0.1
TS14	15 ± 1	0.2 ± 0.1

At 10 min post-irradiation, the cell lines present a lack of damage recognition. This lack of recognition, not being followed by a lack of repairs at 24h is indicative of a radiosensitivity group II cells[95].

IV.C.2. Combination of d + Δt + D in IGRT using kV-CBCT: Effect on DNA repair deduced from γH2AX foci

Thereafter was examined whether the irradiation scenario d + Δt + D provides a different number of γH2AX foci than exposure to D alone for a low dose d delivered by kV-CBCT prior to a treatment dose D delivered by a 6 MV treatment beam. Table 9 represents the amount of γH2AX foci assessed 10 min and 24 h after no exposure, exposure to d, (d + Δt + D), or D with the imaging dose being delivered by the kV-CBCT. The results from Table 9 are compiled in Figure 99 in the annex.

Table *9*: Amount of γH2AX foci assessed 10 min and 24 h after exposure to D or (d + Δt + D) using the kV-CBCT to deliver the low dose d. The results are presented such as: Amount of γH2AX ± SEM. SEM stands for the standard error of the mean.

Cell lines	10 min D vs. (d + Δt + D)	p	24 h D vs. (d + Δt + D)	p
HDF	45.4 ± 0.6 vs 45.4 ± 0.6	- p > 0.999	0.9 ± 0.1 vs 0.8 ± 0.1	- p = 0.549
TS1	43.2 ± 1.1 vs 45.0 ± 1.0	- p = 0.310	1.1 ± 0.1 vs 1.1 ± 0.1	- p = 0.979
TS14	30.7 ± 0.6 vs 32.3 ± 0.7	- p = 0.067	0.8 ± 0.1 vs 1.2 ± 0.1	<< p = 0.013

Here ">>" or "<<" mean (d + Δt + D) >> D and (d + Δt + D) << D, respectively; "-" means no significative difference between the two irradiation scenarios. The p-value is indicated.

Following the results presented, a supralinear effect (an increase of γH2AX foci amount) was observed only for the TS14 cell line at 24 h post-irradiation. While this effect is statistically significant, the difference in absolute value cannot be considered significant. No significative variation was observed for all the other cell lines tested at 10 min and 24 h post-irradiation.

IV.C.3. Different d_{AR} energy (kV-CBCT vs. MVCT): Same effects?

It was verified that i) the challenging dose D (2 Gy delivered by a photon beam of 6 MV) alone provides the same data whatever the treatment device and ii) The priming dose d provides the same data when delivered by kV-CBCT or MVCT. Table 10 shows the numbers of γH2AX foci per Gray assessed at 10 min and 24 h post-irradiation of the Tomotherapy device (CHR Metz-Thionville, Metz) for the TS1 and TS14 cell lines.

Table *10*: Amount of γH2AX foci per Gy assessed 10 min and 24h post-irradiation on the Tomotherapy device (CHR of Metz-Thionville, Metz). The results are presented such as: Amount of γH2AX ± SEM. SEM stands for the standard error of the mean.

Cell lines	10min	24h
TS1	20 ± 2	0.5 ± 0.2
TS14	18 ± 2	0.4 ± 0.1

As expected, the results observed in Table 10 are corroborating the ones observed in Table 8. This lack of recognition, not being followed by a lack of repairs at 24h is indicative of a radiosensitivity group II cells[95].

Since the number of DSB and SSB generated after irradiation depends not only on the absorbed dose but also on the energy micro-depositions and therefore on the beam energy, it was examined thereafter whether the irradiation scenario d + Δt + D may have a different impact on DNA repair assessed by the amount of γH2AX for d delivered by the MVCT imaging modality. Table 11 represents the numbers of γH2AX foci assessed 10 min and 24 h after no exposure, exposure to d, (d + Δt + D), or D with the imaging dose being delivered by the MVCT. The results from Table 11 are compiled in Figure 100 in the annex.

Table *11*: Amount of γH2AX foci assessed at 10 min and 24 h after exposure to D or (d + Δt + D) using the MVCT to deliver the low dose d. The results are presented such as: Amount of H2Ax ± SEM. SEM stands for the standard error of the mean.

Cell lines	10 min D vs. (d + Δt + D)	p	24 h D vs. (d + Δt + D)	p
HDF	31.9 ± 0.6 vs 31.8 ± 0.7	-	2.2 ± 0.3 vs 1.6 ± 0.3	- p = 0.116
TS1	40.8 ± 1 vs 32.5 ± 0.6	>> p < 0.001	1.8 ± 0.3 vs 0.9 ±0.1	>> p < 0.01
TS14	35.6 ± 0.9 vs 35.4 ± 0.6	-	1.5 ± 0.2 vs 1.6 ±0.2	-

Here ">>" or "<<" mean (d + Δt + D) >> D and (d + Δt + D) << D, respectively; "-" means the difference is not statistically significative. The p-values are indicated.

A sublinear (possibly AR) effect is observed for the TS1 cell lines at 10 min and 24 h (significative decrease of γH2AX foci) (Cf. Table 11) but not for the two other cell lines (no difference in γH2AX foci) at the same time points.

Figure 96 shows representative immunofluorescence photos of DNA DSB assessed by γH2AX foci at 10 min and 24 h for the TS1 cells line following 0 Gy, d, d + Δt + D, and D, with d being delivered by kV-CBCT and MVCT irradiation.

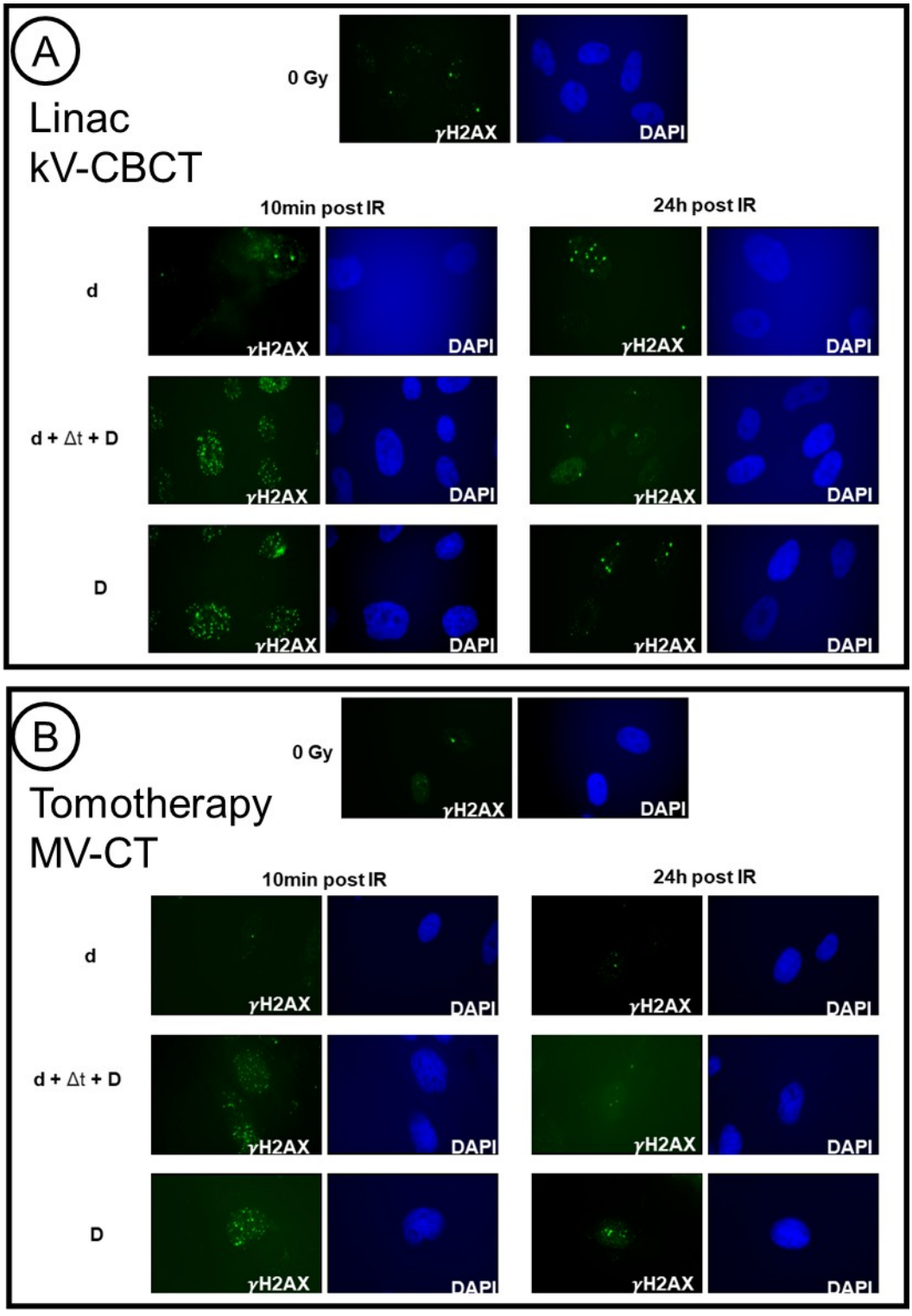

Figure *94*: Kinetics of γH2AX foci with different radiation types. A) Immunofluorescence against γH2AX was applied to the patient cell line TS1 with four irradiation conditions with the kV-CBCT device. B) Immunofluorescence against γH2AX was applied to the patient cell line TS1 with four irradiation conditions with the Tomotherapy device. Nuclei are visualized using DAPI immunostaining.

IV.C.4. Different markers: same effects? Occurrence of an effect deduced from micronuclei?

By applying the same as for the γH2Ax, all the micronuclei data at 24 h were gathered in Table 12.

Table 12: Amount of micronuclei assessed 24 h after exposure to D or (d + Δt + D). The results are presented as: Amount of micronuclei ± SEM. SEM stands for the standard error of the mean.

Cell lines	kV-CBCT D vs. (d + Δt + D)	p	MVCT D vs. (d + Δt + D)	p
HDF	14.7 ± 1.8 vs 15.3 ± 2.3	- p = 0.951	11.3 ± 1.7 vs 9.3 ± 0.7	- p = 0.568
TS1	5.3 ± 0.7 vs. 8.7 ±1.3	- p = 0.108	5.7 ± 1.2 vs. 5.0 ± 1.2	- p = 0.933
TS14	12 ± 1.2 vs. 3.7 ± 0.3	>> p < 0.001	5.3 ± 0.7 vs. 11.7 ± 1.5	<< p = 0.011

Here ">>" or "<<" mean (d + Δt + D) >> D and (d + Δt + D) << D, respectively; "-" means the difference is not statistically significative. The p-values are indicated.

No significant effect was observed with HDF, whatever the conditions. Concerning TS1 at kV-CBCT, while not statistically significant, an effect was observed suggesting a supralinear effect of the dose d. Concerning the TS14 line, the results show opposite effects of the priming dose for kV-CBCT and MV-CT.

IV.D. Discussion

This study aimed to perform a preliminary experiments to ask whether the imaging dose may affect the biological response to the challenging dose (2 Gy). The number of cell lines available was limited and caution should be taken to not over-interpret the data. Only one fibroblast and two cell lines issued from patients who received a head & neck radiotherapy treatment were tested. In addition, due to the availability time of the irradiators, the repair kinetics were assessed only at 10 min and 24h.

Before investigating the occurrence of a possible adaptive response effect ($d+\Delta t+D < D$), we verified the radiosensitivity group of the TS1 and TS14 cell lines. The double strand break induction rate was found systematically lower than 40 γH2AX foci per Gy ($p<0.0001$), the DSB induction rate generally obtained with radioresistant (group I) fibroblasts[25]. This observation support that all the cell lines tested belong to group II of radiosensitivity. As it was expected, these data were not found different significantly for the Linac and the Tomotherapy, suggesting that the 6MV photons treatment beams from both the irradiators produce equivalent biological consequences. In addition, the priming dose d provides the same data when delivered by kV-CBCT or MVCT.

When the number of γH2AX foci was used as an endpoint, it appears for TS1 using the MVCT that a priming dose d applied Δt min before the challenging dose D may have a sublinear effect on the toxicity of the challenging dose D. To our knowledge, it is the first time that the energy dependence of the AR effect is pointed out. When the number of micronuclei was used as an endpoint, with regard to the TS14 line, the results show opposite effects of the priming dose for kV-CBCT and MV-CT. Since this latter effect is observed only on the TS14 line, it does not suggest an energy effect. Micronuclei are the cytogenetic result of the propagation of unrepaired DNA breaks from G1 to G2/M[80]. However, micronuclei do not provide the same interpretation vis-à-vis the individual response to radiation as γH2AX foci. Indeed, ATM monomers recognize DSB that will be managed by NHEJ (α-type DSB). In parallel, another subset of DSB is not recognized by NHEJ, the so-called β-type DSB, that will be recognized by another pathway or not recognized at all. Among each type of DSB, a small fraction will contribute to the lethal effect. Hence, micronuclei are generated by some α-type and some β-type DSB, which makes more complex the relationship between residual γH2AX foci and micronuclei: the γH2AX foci reveal the unrepaired DSB managed by NHEJ only while micronuclei reflect the genomic instability of DSB that is not necessarily recognized by NHEJ. These results suggest that this endpoint may be less appropriate to reveal and quantify a priming dose effect.

IV.E. Conclusion

Analyzing our results in the frame of the clinical background and reality of the TS1 and TS14 patients, it is reminded that both patients were treated for head and neck cancer using IMRT techniques and therefore were likely to benefit from daily IGRT using 3-dimension imaging during their treatments to correct the patient setup errors at each fractions[54, 99, 100, 167]. In this context, it is suggested that the observations obtained during our study could therefore be applied to their treatments. Nevertheless, the toxicity resulting from RT is complex and influenced by various patient-tumor-and treatment-related factors, such as concomitant chemoradiotherapy, altered fractionations, and dosimetric parameters[28, 39, 66, 75, 117, 131, 145, 165]. Hence, even though an AR effect was observed in our results for TS1, our radiobiological group II characterizations of the healthy tissues are in line with the toxicities grade 2 and 3 toxicities observed

respectively for TS1 and TS14. This suggests that the AR effect in IGRT, when observed in healthy tissues of group II, does not supplant the effect of individual radiosensitivity. To our knowledge, it is the first time that this observation is realized. Furthermore, both patients of TS1 and TS14 had respectively a partial response and an evolutive response to the radiotherapy and chemotherapy treatments. Combined with the patients' healthy tissues' radiosensitivity determined above, it indicates the worst-case scenario for both patients: Low or no tumor response to radiotherapy treatment combined with a radiosensitivity of the healthy tissues. In this frame, the possibility of an AR effect regarding the tumor cells should be investigated to understand the possible implication of a priming dose in the tumor response.

V. General conclusions and perspectives

V.A. General conclusions

V.A.1. Development and characterization of the fiber's light measurement technology for CBCT

When this thesis work started, one of the first, yet difficult, questions to answer was to determine the dosimeter specific applications in radiotherapy. Considering the different advantages of the plastic scintillating fiber technology, numerous interesting choices were available, e.g. imaging dose measurement, small fields dosimetry, dosimetric QA, treatment in-vivo dosimetry, and Linac commissioning. This information, in conjunction with the lack of a suitable technical solution for imaging dosimetry in radiotherapy, and the presence of already commercialized fiber dosimeters dedicated to high-energy photons, has motivated us to engage in the development of the CBCT dosimeter.

We decided to begin by characterizing the probe constituting materials (*i.e.* scintillating and clear plastic fiber) behavior in the presence of a high cumulated dose. At this time, COVID-19 epidemy was on course as well as restrictive measures, making access to radiotherapy installations even more challenging than it is under the ordinary situation. For this reason, a significant part of the radiation-induced characterization work has been performed at the Fibermetrix laboratory with an X-Ray generator delivering low-energy photons. As seen above in the results, it appeared that the fibers available at this time (BCF-12; BCF-60; and BCF-98) all responded to a high level of cumulated doses with an increase in signal attenuation. On top of this attenuation, a decrease in scintillation was also observed for both scintillating fibers, with BCF-12 being more affected than BCF-60. Following these results, it appeared that the fiber dosimeter could not be used as is for high doses applications. Rather, the scintillating fibers' response to low doses was well documented and studied by the Fibermetrix laboratory.

Nevertheless, the 3HF radiation hardness formulation of the BCF-60 and its better performances in presence of a high cumulated dose showed encouraging results for high energy dosimetry. This formulation is also present in the SCSF-3HF (1500) fibers from Kuraray (Tokyo, Japan) and will be investigated for high energy and cumulated dose applications since it also facilitates the Cherenkov signal correction.

We also studied the possibility of replacing the PM modules in the detection chain with the SiPM technology for reasons of cost, size, and perennity of the components due to the absence of concurrence in the PM modules supplier (Hamamatsu, Hamamatsu, Japan, owning 100% of the PM modules and 90% of the PM tubes global market). Overall, the characterization of the SiPM photodetector for scintillation dosimetry gave promising results. The optimal functioning parameters range has been found, in addition to a better understanding of the operating regimes of the SiPM photodetector. Although complex, this study also helped

us to improve the SiPM experimental setup to reduce light leakages in the photocounting system. After the electronic threshold, one of the major limitations identified during the characterization was the noise due to an increase in temperature inside the photocounting system.

As seen in the section concerning SiPM photodetectors, one of the main sources of DCR is due to the increase in temperature when the SiPM is operating. Looking at Figure 57 describing the amplification levels, which are at the origin of a part of the system temperature increase, an interesting possibility could be to remove one of the three amplification levels to significatively reduce the noise while investigating the SNR ratio. Since the end of the SiPM study, the SiPM photodetector has been implemented in photocounting systems to perform complementary investigations in clinical environments for both radiotherapy and radiology applications.

A part of the thesis work consisted of the development of the CBCT dosimeter. We first started with designing the probes for the CBCT application and treatment couch and then adapted the photocounting system to be able to measure the dose using only 1 channel (conversely to the IVIscan system which required simultaneous 2 channels measurement), allowing the possible acquisition of a second signal (e.g. from a punctual/linear probe) parallelly to the CBCT dose. The hardware development was followed by the development of dedicated software recording each acquisition data by patient name and date, and converting the photocount into measured dose with ad hoc calibration factors. Hence, the work realized in this thesis also resulted in the development of the methodology to calculate the CTDI and the air kerma calibration factors.

V.A.2.Dosimetric QA applications

Our study suggests that the IVI-CBCT dosimeter proposed in this thesis may be promising for fast accurate MDQC or dose optimization of the CBCT acquisitions on dedicated radiotherapy linear accelerators. Moreover, we demonstrated that the presence of the detector has little to no influence on the MV treatment beams or kV-images in either 2- or 3-dimensional modes.

Unsurprisingly, the recently published French decision related to the quality controls of external radiotherapy and radiosurgery installations (*i.e.* IMRT and radiotherapy in stereotactic conditions installations) in France still doesn't involve MDQC for CBCT or any imaging devices in radiotherapy[169]. Albeit this decision ignored the recommendations of the EFOMP, IAEA, and ESTRO[88] by not assessing dosimetry quality assurance of the imaging devices in radiotherapy, it can be easily explained by the previous lack of technical solutions to perform fast and accurate MDQC of the imaging installations. Therefore, in anticipation of regulatory changes, this thesis provides a commercial dosimeter for CBCT dosimetric quality control.

The primary and secondary functions of the dosimeter established in the introduction of this manuscript were completely fulfilled (Cf. Table 13). In addition, if requested by CBCT users, further developments will be realized to assess the dose to patients during CBCT exams.

Table 13: Dosimeter's primary and secondary functions.

Primary functions		Secondary functions	
Measure the dose from CBCT imaging systems in RT	✓ for QC	Having little or no influence on treatment and imaging beams	✓
Display a signal proportional to the delivered dose	✓	No obstruction to the patient's, or radiation therapist's movements	✓
Dose measurement is at least as accurate as the reference dosimeter for the same applications	✓	Access to the follow-up of the measurements	✓
Display good repeatability	✓		

V.A.3.From physics to radiobiology: A radiobiological perspective on the effects of the low doses from CBCT

How do the imaging low doses, followed by high treatment doses, affect the DNA repair of patients undergoing radiotherapy treatments? The radiobiological section of the manuscript aimed to provide an answer to this question. In this frame, the thesis exploratory work was aiming to include the radiobiology perspective in the physical study of low doses in IGRT.

Considering the γH2Ax markers, an AR effect was observed for TS1. Put in regard to the radiobiological characterization and the clinical data, it appears that the observed AR effect of the priming dose was not significant enough to observe consequences on the toxicities' outcome. Moreover, this AR effect was observed only for the kV-CBCT, suggesting an energy effect of the priming dose.

V.B. Perspectives

In light of these results, it is expected that the dosimeter presented will find applications in leading radiotherapy services aiming to measure and control the dose issued from CBCT devices. The work led to the realization of a pre-commercial prototype set up in a beta testing center in Metz. The system is used by the teams for QC and dose assessment (cumulative CTDI).

Thanks to the SiPM integration, the photocounting system can now be redesigned to reduce its size, cost, and energy consumption. This improvement in design and energy consumption will undoubtedly benefit

the development of the detector for radiotherapy applications (e.g. the CBCT dosimeter) as it will help the detector to blend into the radiotherapy environment and tend to make it as “invisible” as possible to the operators and patients. Another possible development made possible by the implementation of the SiPM photodetector is the addition of more counting channels into the photocounting system (2 channels on the actual photocounting system). As an example, this would allow the photocounting system to process measurements from more than 2 fiber dosimeters at once. This could be of particular interest in the optic of a dosimeter able to measure in-vivo dose from both treatment and imaging sources at the same time.

Currently, the acquisition protocols (and therefore the calibration factors associated) still have to be selected manually in the in-house dedicated software, but in order to use the system routinely for patients dosimetry a major improvement would be to retrieve the acquisition parameters (e.g. the couch position, the CBCT protocol, the rotation trajectory) and patient information in real-time from the Record & Verify or the treatment machines to apply the ad hoc calibration and correction factors. In order to solve this issue, we are currently trying to connect the system with the Varian local database of the radiotherapy service.

Given the dosimeter installation and geometry, this technology could find interesting applications in helicoidal accelerators for IGRT dosimetry. Furthermore, if provided with the correction factors for energy, uniformity, and Cherenkov correction, it could also find interesting applications in IVD or pre-treatment QA dosimetry.

Notably, Figure 82 shows how the counts measured by the detector varied over time and therefore also the X-ray source angle. The measured signal was highly dependent on the X-ray tube position and therefore on the treatment couch attenuation. Thus, the shape of the signal could be used to assess for example the position of the fiber beneath the couch or any modification in the tube rotation geometry.

Moreover, given the efficiency of this methodology with regard to quality control or dose optimization measurements, it is of interest to determine whether it can be used to measure the CBCT doses that are delivered to the patient during radiotherapy treatment. This latter issue also points to the CBCT patient dose metrics topic, with no consensus yet from the literature. In this context, an innovative measurement approach could help delineate the shape of uniform practices and be of great interest to the medical physics community. Despite the limitations cited above, the dosimeter could be used in combination with dose calculation algorithms (e.g. Monte Carlo-based, or artificial intelligence algorithm) and irradiation parameters in order to evaluate more precisely the imaging dose distribution in the patient for each radiotherapy session. Since the CTDI and its derived indicators represent the mean dose in a volume or slice and are initially meant to be quality assurance indicators, this perspective could allow us to evaluate the patient dose from an imaging device with more suitable indicators.

In addition to the patient dose measurement, many questions on the IGRT dose remain unanswered. Do we “simply” deduce the IGRT dose from the treatment plan? Does the imaging low dose affect the biological mechanisms the same way as high treatment doses do? Does individual radiosensitivity plays a role and how is it different for high doses and low doses? Then, regarding these aspects, what is the place of personalized dosimetry? Moreover, as explained above, radiobiological reactions of X-rays are not simply a question of dose but also depend on the beam’s energy, the radiobiological time, and the patient’s radiosensitivity. This is even more true when considering the combination of low and high doses. These questions highlight the multidisciplinary aspect of the doses in IGRT. In this context, a radiobiological characterization of the healthy tissues' radiosensitivity and AR effect prior to the treatment could help to anticipate the treatment toxicities and therefore help to adapt the patients’ supportive care. Moreover, it has to be investigated whether an AR effect is present regarding the tumor cells and how this possible effect could potentially combine with a tumoral radiobiological characterization (*i.e.* possible combination of an AR effect with the radioresistant or radiosensitive character of tumor cells).

V.C. Personal conclusions

From a personal point of view, the thesis was a unique occasion to consolidate and improve my skills in a multidisciplinary environment. This instructive framework was made possible through the CIFRE collaboration between the laboratories of INSERM U1296 and Fibermetrix. Thanks to this context, I have worked in association with various actors in public health research, from fundamental researchers to industrial innovators and clinical actors.

The implementation of clinical partnerships, particularly the one with the Metz-Thionville CHR, was a key component of my thesis. Working in collaboration with healthcare professionals provided valuable clinical data for our studies. These partnerships also strengthened our relationship with the medical community, which is essential for ensuring the real impact of our research.

Project management was one of the most important aspects of my work, as I had to coordinate my personal efforts with the ones of several teams to achieve our objectives. This experience taught me to be both organized and flexible, to deal with unforeseen events while keeping focused on our final results. As a supervisor of interns, I was as well able to put my mentoring and supervisory skills into practice. This also allowed me to pass on my research knowledge to younger generations while learning new approaches and ideas from them.

Acquiring multidisciplinary skills was an important dimension of my thesis. As a medical physicist, my former education was focused on fundamental physics and its medical applications. Through my thesis, I have developed my expertise in various fields such as the conception of optical fiber probes, scintillation

dosimetry, signal processing, Monte Carlo dose calculations, and radiobiology. Working at the interface of industry and academic research allowed me to interact, with experts from various backgrounds, exchange ideas, and learn from their experiences to develop a comprehensive understanding of the issues faced by each party. This unique industry perspective also enriched my vision of health research, emphasizing the importance of innovation and its commercialization.

In addition to my work on my CIFRE thesis, I also had the opportunity to actively participate in the national (French medical physics society (SFPM) administrative board) and international (junior leader to the ESTRO physics workshop on kV-imaging dose justification and optimization in radiotherapy) institutions, which enriched my professional experience and broadened my perspectives. These experiences have been instrumental in shaping my personal and professional goals, as they have taught me the importance of being an active participant in the scientific community and using my knowledge and skills to make a positive impact. It has enabled me to broaden my perspectives, develop new skills, and contribute to the advancement of health research on a broader scale. I believe that continued participation in these institutions will be essential for advancing the field of health research and improving healthcare outcomes for individuals and communities around the world.

In conclusion, my CIFRE thesis was a very enriching professional and personal experience. Project management, the implementation of clinical partnerships, supervising interns, acquiring multidisciplinary skills, and contributing to the scientific community were key elements that shaped my vision of health research. This experience made me realize that health research & innovation is a team effort and requires close collaboration between industry and academic research professionals to advance the field and improve patients' lives.

VI. Annexes

VI.A. Article: Characterization of an Innovative Detector Based on Scintillating Fiber for Personalized Computed Tomography Dosimetry

sensors

MDPI

Article

Validation of a New Scintillating Fiber Dosimeter for Radiation Dose Quality Control in Computed Tomography

Nicolas Guillochon [1], Mamoutou Balde [1], Christian Popotte [1,2], Selena Pondard [3], Corentin Desport [3], Nicolas Kien [3], Fanny Carbillet [4], Ramiro Moreno [3] and Mélodie Munier [1,4,*]

[1] Fibermetrix, 7 Allée de l'Europe, 67960 Entzheim, France
[2] INSERM U1296 Radiations: Défense, Santé, Environnement, 69008 Lyon, France
[3] ALARA Expertise, 67960 Entzheim, France
[4] ALARA Group, 67960 Entzheim, France
* Correspondence: melodie.munier@fibermetrix.fr

Abstract: (1) Background: The IVIscan is a commercially available scintillating fiber detector designed for quality assurance and in vivo dosimetry in computed tomography (CT). In this work, we investigated the performance of the IVIscan scintillator and associated method in a wide range of beam width from three CT manufacturers and compared it to a CT chamber designed for Computed Tomography Dose Index (CTDI) measurements. (2) Methods: We measured weighted CTDI (CTDIw) with each detector in accordance with the requirements of regulatory tests and international recommendations for the minimum, maximum and the most used beam width in clinic and investigated the accuracy of the IVIscan system based on the assessment of the CTDIw deviation from the CT chamber. We also investigated the IVIscan accuracy for the whole range of the CT scans kV. (3) Results: We found excellent agreement between the IVIscan scintillator and the CT chamber for the whole range of beam widths and kV, especially for wide beams used on recent technology of CT scans. (4) Conclusions: These findings highlight that the IVIscan scintillator is a relevant detector for CT radiation dose assessments, and the method associated with calculating the CTDIw saves a significant amount of time and effort when performing tests, especially with regard to new CT technologies.

Keywords: IVIscan; scintillation detector; optical fiber; dosimetry; CTDI; computed tomography; wide-beam; diagnostic

Citation: Guillochon, N.; Balde, M.; Popotte, C.; Pondard, S.; Desport, C.; Kien, N.; Carbillet, F.; Moreno, R.; Munier, M. Validation of a New Scintillating Fiber Dosimeter for Radiation Dose Quality Control in Computed Tomography. *Sensors* **2023**, *23*, 2614. https://doi.org/10.3390/s23052614

Academic Editors: José Manuel Almeida and Luís C. Coelho

Received: 5 February 2023
Revised: 23 February 2023
Accepted: 25 February 2023
Published: 27 February 2023

1. Introduction

The Computed Tomography Dose Index (CTDI) was introduced more than 40 years ago [1] and has facilitated government regulation and dosimetry standardization for computed tomography (CT) manufacturers [2]. It was developed to provide a standardized method to compare radiation output levels between different CT scanners. Today, it is also used for quality assurance purposes such as to monitor the deviation over time of CT scans in a relative way, and for optimization of patient radioprotection. It represents the average dose over a single slice in a standard cylindrical polymethyl methacrylate (PMMA) dose phantom of 15 cm in length, and 16 cm and 32 cm diameter for head and body examination, respectively. Theoretically, the CTDI should be measured from plus to minus infinity. Since in practice the pencil ion chamber to measure CTDI, called CT chamber, is typically 100 mm long, the International Electrotechnical Commission (IEC) has specifically defined the $CTDI_{100}$ measured in IEC 60601-2-44 Ed3.0 as

$$CTDI_{100} = \int_{-50mm}^{+50mm} \frac{D(z)}{N \times T} dz, \quad (1)$$

where $D(z)$ is a dose profile in air kerma along the longitudinal axis z. The number of detector channels and the width of each channel are N and T, respectively. $N \times T$ represents the total beam width.

The weighted computed tomography dose index, $CTDI_w$, which consists of a combination of central and peripheral measurements of $CTDI_{100}$ defined in Equation (1), in the PMMA dose phantom with applied weighted factors, corresponding to a linear decrease of the dose along the radial direction as

$$CTDI_w = \frac{1}{3} CTDI_{100,center} + \frac{2}{3} \langle CTDI_{100,peripheral} \rangle, \quad (2)$$

where $CTDI_{100,center}$ is the value measured at the center hole of the standard PMMA phantoms, and $\left\langle CTDI_{100,peripheral} \right\rangle$ is the average value measured at the four peripheral holes.

$CTDI_{100}$ and $CTDI_w$, were used in the past, but with the advent of modern scanners providing helical acquisitions, $CTDI_{vol}$ has been introduced and defined as the ratio between the $CTDI_w$ and the helical pitch. The pitch is generally defined as the ratio between the displacement of the table in one rotation of the gantry and the beam width. As all the acquisitions during mandatory controls are made in axial mode, the $CTDI_{vol}$ is rarely, if ever, used in the mandatory radiation dose quality control (RDQC) of CT scanners and is equal to the $CTDI_w$.

However, these indicators and the current method of obtaining them have major limitations and are not suitable for the new CT scan technologies [3,4] and tools such as wide-beam CT scanners. With the advent of multi-detector scanners, beam widths on the z-axis and the length of the scan have increased significantly. It has been shown on numerous occasions that for beam widths greater than 40 mm, the 100 mm CT chamber does not consider a large part of the primary and scattered radiation and the $CTDI_{100}$ underestimates the delivered dose by about 30–40% for a body phantom and 10–20% for a head phantom for the widest beams [5,6]. Today, CT scans can use beam widths up to 160 mm allowing to cover larger anatomical areas with clinical applications such as cardiac and head CT using the axial mode [7].

The IEC has described a two-tiered approach to the definition of CTDI. The first tier uses the conventional definition of $CTDI_{100}$ and is applied for beam widths < 40 mm. The second tier is used for beam widths > 40 mm.

In this new approach, it is assumed that the ratio between the $CTDI_w$ at two different beam widths is equal to the ratio of the $CTDI_{air}$, measured free-in-air, at these beam widths. Thus, it is proposed to calculate $CTDI_{w,N\times T>40}$, which is the weighted CT air kerma index for a beam width of $N \times T > 40$ mm as follows:

$$CTDI_{w,N\times T>40} = CTDI_{w,ref} \times \left(\frac{CTDI_{air,N\times T>40}}{CTDI_{air,ref}}\right), \quad (3)$$

$CTDI_{air,N\times T>40}$ and $CTDI_{air,ref}$ are the CT air kerma indexes measured free-in-air for a beam width > 40 mm and a beam width < 40 mm, respectively. $CTDI_{w,ref}$ is the weighted CT air kerma index for a reference beam width < 40 mm.

Several methods have been proposed to overcome this problem of dosimetry for wide beam CT scanners including small point detectors, multiple steps of a 100 mm CT chamber [8] or a 300 mm CT chamber [9–11]. Especially, the multiple steps method consists of multiple contiguous position measurements with step increments equal to the ion chamber length, i.e., 100 mm. However, this alternative method is rarely used because it is complex to set up and time consuming. On the other hand, the specific 300 mm CT chamber required for wide beams is quite fragile and expensive, and therefore it is rarely used. The small ionization chambers are dedicated to radiotherapy and so need a specific calibration for CT dosimetry. Solid-state detectors might suffer from energy and angular dependence so their use in CT application for CTDI measurements is not really appropriate.

It is clear that even though the regulatory texts and international recommendations require that radiation dose evaluation be performed under conditions as close as possible to clinical use [12]; in practice, the wide beams are still not always verified today. Indeed,

RDQC should have meaningful results using a quick measurement, and be accessible and reproducible.

The Fibermetrix®company has developed a measurement method and associated device named IVIscan®, based on a plastic scintillating fiber sensor of two meters long [13,14]. Devic et al. have mainly characterized the system and demonstrated its accuracy in terms of air kerma measurements in the CT scan energy range [15]. Scintillating optic fiber has been under development for several years for medical dosimetry applications [16–18] and is based on various materials such as doped silica fiber or plastic scintillating fiber. The Exradin W1 and W2 (Standard Imaging Inc., Middleton, WI, USA) [19–21] have especially been developed for radiotherapy applications and have been marketed for a few years. The IVIscan real-time dosimeter is an in vivo dosimetry solution dedicated to medical imaging. It is the first commercially available dosimetry solution that is permanently placed on the CT table, operates in full autonomy, and could have applications in RDQC [22,23]. Moreover, the two meter sensor length allows the integration of the dose even on wide-beams acquisition and all along the explored length in clinical examinations.

This study evaluates dosimetric performance of this scintillating fiber detector as part of the CT scan RDQC with a particular focus on detector response in wide-beam scanners. So, we compared the IVIscan dosimeter and the method associated with a reference CT chamber and validated it as a new fiber dosimetry system for RDQC. We proposed to calculate the $CTDI_w$ and the $CTDI_{w,N\times T>40}$ defined in Equations (2) and (3) by the two measurement methods, in regulatory conditions on multiple CT scans for thinnest, largest and usual beam widths used in clinical practices and beyond for the different X-ray tube voltages (kV). The kV variation allows us to study the energy dependency of the IVIscan detector. Then we evaluated the relative deviation between the CTDIw obtained through the reference method using the reference CT chamber, $CTDI_w^{chamber}$, and the one obtained through the IVIscan method, $CTDI_w^{IVIscan}$.

2. Materials and Methods

2.1. Computed Tomography Equipment

In order to validate IVIscan dosimeter in a universal way, measurements of all $CTDI_w$ were carried out with four different CT scans from the three main CT manufacturers. A Siemens SOMATOM®definition AS+ called System Number 1 (SN1), a Canon Medical Aquilion ONE Genesis (SN2), a GE Healthcare Revolution CT (SN3) and a Canon Medical Aquilion ONE/PRISM Edition (SN4). SN2, SN3 and SN4 have beam widths over 40 mm while SN1 has traditional beam widths of less or equal to 40 mm. The highest voltage used by the CTs was 140 kV, with the exception of the SN2 and SN4 which use 135 kV.

2.2. Irradiation Parameters

CTDIw calculation from RDQC tests requires specific CT acquisition parameters as tube voltage and beam width. Thus, the aim was to first validate the IVIscan dosimeter under these specific requisites. So, the reference and IVIscan measurements were performed at 120 kV, at the thinnest and largest beam width used in clinic, for a head and body protocol with the corresponding phantom, as required by the French regulation related for the quality control of CT scanners [24]. Medical physics experts are unanimous that RDQC should be more closely aligned with clinical practice, especially with respect to the protocols used. Thus, we carried out measurements at the most common beam width used in clinical routine too. For each case, we settled an X-ray tube current of 200 mA and a tube rotation of 1 s, in order to adapt the dose rate to accurate measurements with the CT chamber, which is the reference in this study.

In addition, we evaluated the IVIscan dosimeter repeatability in terms of CTDIw calculation on a wide range of dose rate and beam qualities available on CT scans. For this purpose, IVIscan measurements were carried out on the entire range of SN1 tube voltage, from 70 to 140 kV, and two beam widths of 5 mm and 38.5 mm. Assuming that the protocol

type, head or body, has less impact on the dosimeter repeatability than the tube voltage or dose rate, we chose only head protocols for this test.

We also wanted to investigate the energy dependence of IVIscan dosimeter. In this way, further measurements were carried out beyond the RDQC requisites with the CT chamber and IVIscan dosimeter, for the whole range of SN2 tube voltage, i.e., 80, 100, 120 and 135 kV, and beam widths of 2 mm and 40 mm. Given the high number of measurements to be carried out with the CT chamber, we also considered that it was sufficient to carry out these tests with a single protocol type. Thus, we chose body protocol.

2.3. *Reference Dose Indexes*

2.3.1. Reference Materials

To measure the parameter of CT radiation dose, the study was conducted using a 100 mm Unfors Raysafe^{TM} X2 CT chamber (Fluke Biomedical, Everett, WA, USA) and standard-sized CTDI PMMA head and body phantoms. The CT chamber was calibrated according to IEC 61223-2-6. Measurements were made with an uncertainty of less than 5% at the 95% confidence level (manufacturer data).

The two standardized PMMA cylindrical phantoms of 16 cm diameters and 32 cm diameters were used for head CT protocols and body CT protocols, respectively. Both phantoms are 15 cm in length and have five 12.4 mm diameter holes. One of them is located at the center and the other four, 10 mm beneath the surface at 90° intervals.

2.3.2. Reference Measurements

- CT scan Compliance

Firstly, an evaluation of the conformity of the four scanners was carried out by a primary RDQC with a CT chamber in standard quality control conditions. According to international regulation, the $CTDI_{vol}$ value displayed by the scanner must not deviate by more than ±20% from the measured $CTDI_w^{chamber}$ [25]. Then the relative deviation between $CTDI_{vol}$ displayed by the CT scan and $CTDI_w^{chamber}$ was defined in percent as

$$[\Delta CTDI]_{ref}^{CT} = \left(\frac{CTDI_{vol} - CTDI_w^{chamber}}{CTDI_w^{chamber}}\right) \times 100, \quad (4)$$

$CTDI_{vol}$ is calculated by dividing $CTDI_w$ with the pitch. Since all measurements are made with axial acquisitions with pitch = 1, $CTDI_{vol}$ is equal to $CTDI_w$.

- Beam Width < 40 mm

$CTDI_w^{chamber}$ was calculated according to Equation (2) defined above from the five measurements in the phantom holes. Figure 1 shows the practical measurement of CTDIw for beam width < 40 mm. The CT chamber setup is on the left side on the figure. The evaluation was performed over the thinnest beam width (2 mm for SN2 and SN4 and 5 mm for SN1 and SN3) and the most used beam width for clinical protocols (38.5 mm for SN1 and 40 mm for SN2, SN3, and SN4). A width of 12 mm was tested for SN4 as well.

- Beam Width > 40 mm

To perform CTDI calculation with beam widths over 40 mm, we used the International Atomic Energy Agency (IAEA) method described in the paper introduction and using the same CT chamber as for beam width < 40 mm. The evaluation was performed over the largest beam widths from 80 to 160 mm according to the CT scan technical possibilities. The CT chamber was then attached to a retort stand on the CT table and aligned at the isocenter of the beam as shown in Figure 2 (left). The table was then stepped through in the z-direction in increments of 100 mm and a beam rotation was performed at each increment step. The CT chamber was placed away from the edge of the table to avoid any scattered radiation from the table. Dose measurements were carried out in the three sequential steps as shown in Figure 3, and summed to give $CTDI_{air,N\times T>40}$. Then, $CTDI_{w,N\times T>40}^{chamber}$ was calculated according to Equation (3) defined above with a reference beam width of 40 mm.

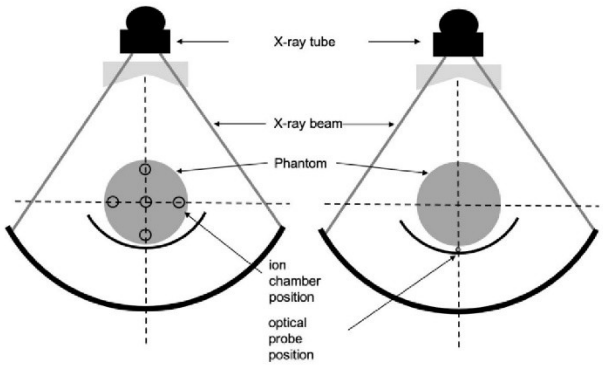

Figure 1. Diagram demonstrating practical measurement of weighted CT air kerma index ($CTDI_w$) for beam width < 40 mm with a 100 mm CT chamber (**left**) and IVIscan detector (**right**). The phantom is placed on the CT table in both cases.

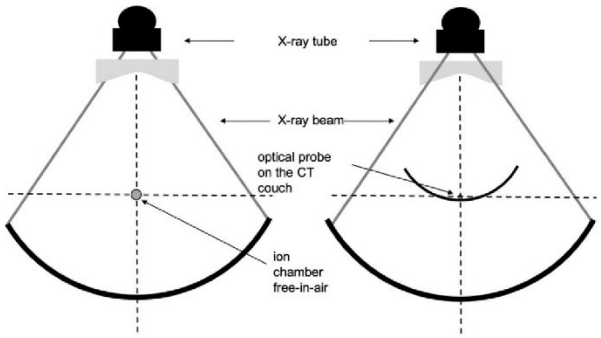

Figure 2. Diagram demonstrating practical measurement of the CT air kerma indexes measured ($CTDI_{air,N\times T>40}$) for beam width $N \times T$ larger than 40 mm with a 100 mm CT chamber free-in-air (**left**) and with IVIscan detector on the CT table (**right**). No phantom is used here.

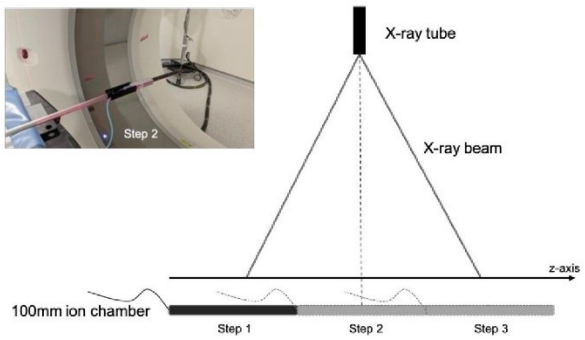

Figure 3. Diagram representation of the recommended three-step in-air measurement method of $CTDI_{air,N\times T>40}$ for beam width $N \times T$ larger than 40 mm with a 100 mm CT chamber.

2.4. IVIscan Dose Indexes

2.4.1. IVIscan Scintillating Fiber Detector

The IVIscan®(Fibermetrix®, Entzheim, France) is a commercially available dosimeter dedicated to automatic dose measurements and dose index calculations on CT scans [26]; it

is composed of a two-ended scintillating probe and an electronic part, named the photometer, detecting the light emitted by the probe. The probe consists of a scintillating plastic fiber sensor of 2 m long connected to a clear plastic optical fiber, acting as a light guide, at each sensor end. The total probe length is thus about 6 m. The material composition of the probe has been described in previous work [15]. It is permanently installed under the CT couch forming a U-shape at the head side of the table (Figure 4) and thus, it is not visible. The 2 m sensor is longer than the maximum exposed length on the CT table, and therefore it is possible to carry out dose measurements everywhere on the CT table. The probe is connected to the two-channel photometer, which measures the scintillation light emitted by the probe due to ionizing radiation interactions with the scintillating fiber and converts it into radiation dose. IVIscan dosimeter was calibrated in terms of air Kerma in RQT9 beam quality, which is the reference beam quality in scanography. It was characterized according to IEC 61674 at the Laboratoire National Henri Becquerel (LNHB, CEA LIST, Saclay, France), an independent primary calibration laboratory. A software solution is permanently connected to the dosimeter and the CT scan both to recover the measured data and all the implementation parameters of the CT scan for each irradiation protocol. History of dose measurements and RDQC is available and a quality control report can be easily generated.

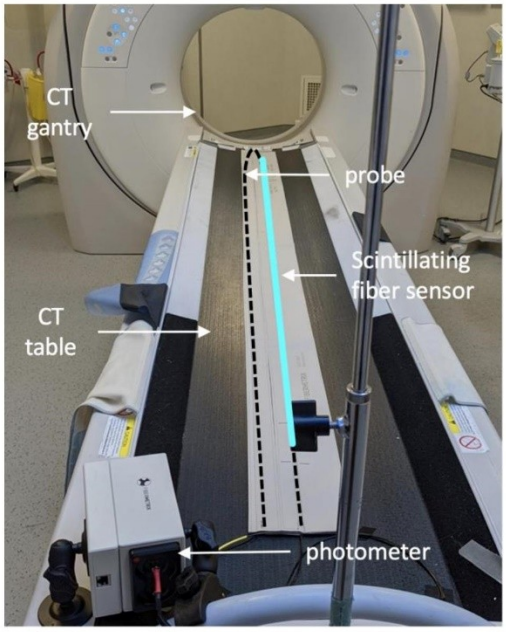

Figure 4. IVIscan system installed on a CT scan. The probe is placed on the CT table forming a U-shape at the head side of the table (black dotted line) and is connected to the photometer fixed at the feet side of the table. The scintillating fiber sensor (blue line) is placed in line to measure air kerma all along the exposure area on the CT table.

Due to the high variability in CT beam quality depending on the examination protocols (i.e., tube voltage and beam filtration), the calibration factor $N_{k,RQT9}$ is automatically corrected by the software during the installation of the dosimetry system on each CT scan to offset the energy dependence and give the most accurate dose $D(z)$. This correction method was also detailed in the previous work cited above. Air kerma, and hence dose measurements, were made with an uncertainty of less than 5% at the 95% confidence level (manufacturer data).

2.4.2. IVIscan Measurement Method

For beams less or equal to 40 mm, the method for calculating $CTDI_w$ with IVIscan dosimeter was carried out with only one measurement instead of the five with a CT chamber, i.e., one for each phantom hole, required for the usual $CTDI_w$ calculation (Figure 1). A single dose measurement, $CTDI_{2000table}$, was performed on the table, under the phantom, for a 360° X-ray tube rotation. A specific conversion factor N_C was then automatically applied by the processing module and the beam width was automatically taken into account to obtain the $CTDI_w^{IVIscan}$ such as

$$CTDI_w^{IVIscan} = CTDI_{2000table} \times N_C, \quad (5)$$

It is to be noted that $CTDI_{2000table}$ is the dose $D(z)$ measured over the 2000 mm sensor length. The conversion factor N_C is selected from a conversion factor table stored in the memory of the device according to the CT scan acquisition type and basic radiation-matter interaction rules. The table is generated for each CT scan by a set of initial measurements during the commissioning of the dosimeter so as to take into account the specificity of each CT scan. The N_C factors are acquired for head and body protocols at 120 kV and one beam width only, usually 10 mm. The method of obtaining N_C factors is not detailed in this work. This is largely described in the Fibermetrix patents [27,28].

For beams over 40 mm, the method involves the measurement of $CTDI_{2000table,\ N\times T>40}$ which is a dose measurement on the table too but without any phantom. Then, according to Equation (5):

$$CTDI_{w,N\times T>40}^{IVIscan} = CTDI_{2000table,N\times T>40} \times N_{C^*}, \quad (6)$$

where N_{C^*} is another specific conversion factor stored in the memory of the device and depending on the anatomical type of the irradiation protocol (head or body). Compared to Equation (3), this conversion factor takes into account the absence of any phantom and the measurement on the CT table instead of free-in-air as for the IAEA methodology for wide-beam RDQC.

Then, the $CTDI_{w,N\times T>40}$ was calculated from a single measurement on the table with the IVIscan method, instead of the multiple measurements in air and in phantom holes required for CTDI calculation with a 100 mm CT chamber. To compare the results between IVIscan and the reference CT chamber methods as accurately as possible, the scintillating fiber sensor measurements were carried out together with the reference CT chamber so that there is no additional uncertainty associated with the X-ray emission or another environmental parameter.

2.5. Statistical Analysis

2.5.1. Repeatability

A first step of $CTDI_{2000table}$ and $CTDI_{2000table,N\times T>40}$ measurements was carried out to evaluate the repeatability of the IVIscan measurement method. Mean $CTDI_w^{IVIscan}$ and $CTDI_{w,N\times T>40}^{IVIscan}$, and relative standard deviation (RSD) were calculated on the basis of three replicates on SN1.

2.5.2. Energy Dependence

The relative deviation of the CTDIw between the scintillating fiber sensor and the reference CT chamber was calculated in RDQC conditions according to the following equation:

$$[\Delta CTDI]_{ref}^{IVIscan} = \left(\frac{CTDI_w^{IVIscan} - CTDI_w^{chamber}}{CTDI_w^{chamber}}\right) \times 100, \quad (7)$$

Lastly, mean $[\Delta CTDI]_{ref}^{IVIscan}$ and RSD associated were calculated on the basis of three replicates on SN2 for the four available tube voltages.

3. Results

3.1. CT Scan Compliance

Figure 5 shows the deviation $[\Delta CTDI]_{ref}^{CT}$ between $CTDI_w$ displayed by the CT scan, and $CTDI_w^{chamber}$ and $CTDI_{w,N\times T>40}^{chamber}$ measurements using the 100 mm CT chamber for a standard RDQC performed on the four CT scanners SN1, SN2, SN3 and SN4. Both head and body protocols were controlled each time for the thinnest, largest and most beam width used in clinic.

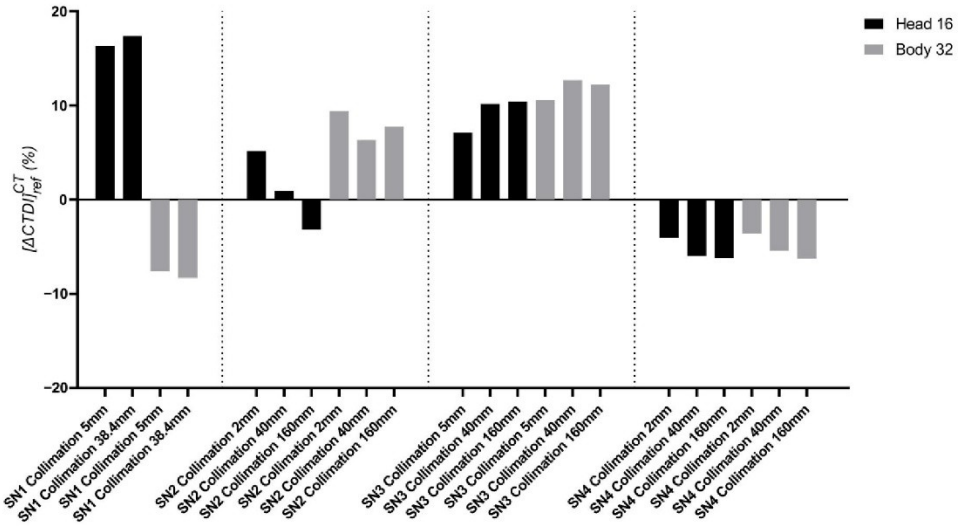

Figure 5. Relative deviation between $CTDI_w$ displayed by the CT scan and CT chamber, $[\Delta CTDI]_{ref}^{CT}$, for standard 120 kV radiation dose quality control (RDQC) performed on a Siemens SOMATOM®definition AS+ (SN1), a Canon Medical Aquilion ONE Genesis (SN2), a GE Healthcare Revolution CT (SN3) and a Canon Medical Aquilion ONE/PRISM Edition (SN4). The measurements were performed at the minimum, maximum and most used beam widths for head and body protocols.

A great disparity from −6.26% to +17.4% is observed between the different CT scanners, the different beam widths and the different phantoms used. The highest deviations are observed for SN1 for the head phantom at 5 mm and 40 mm beam width with 16.3% (±0.64) and 17.4% (±0.46), respectively. However, the deviation does not exceed ±20%, so the four CT scanners SN1, SN2, SN3 and SN4, meet the criteria for acceptable RDQC and can be used in this study.

For the remainder of this study, the $CTDI_w$ displayed by the CT scan will not be considered. Only the results obtained with the 100 mm CT chamber and IVIscan dosimeter will be compared.

3.2. IVIscan Validation

3.2.1. Repeatability

First, Table 1 shows the mean $CTDI_w^{IVIscan}$ obtained with the IVIscan method and the relative standard deviations associated for head protocols at 70, 100, 120 and 140 kV SN1 tube voltages, and 5 mm and 38.5 mm beam widths. The relative standard deviation is between 0.02% for 140 kV and 38.5 mm beam width and 0.21% for 70 kV and 5 mm beam width. We characterized the IVIscan repeatability in terms of air kerma in reference beam qualities in a previous study [15], and demonstrated that the specific uncertainty was about 0.02% for dose rate close to the minimum dose rates used in CT (<1 mGy). So, we can reasonably assume that the relative standard deviations (RSDs) observed here are

mainly due to the stability of the CT X-ray emission, and especially for low dose rates. However, these results indicate very good repeatability with the scintillating fiber sensor methodology.

Table 1. Mean $CTDI_w$ measured with IVIscan, $CTDI_w^{IVIscan}$, and relative standard deviation (RSD) associated for three replicates on SN1 for head protocols at 70, 100, 120 and 140 kV and for beam widths of 5 mm and 38.5 mm.

Beam width (mm)	5				38.5			
Tube voltage (kV)	70	100	120	140	70	100	120	140
Mean $CTDI_w^{IVIscan}$ (mGy)	3.78	12.77	21.52	32.19	4.31	14.43	24.11	35.70
RSD (%)	0.21%	0.07%	0.10%	0.16%	0.05%	0.11%	0.10%	0.02%

3.2.2. Deviation between $CTDI_w^{IVIscan}$ and $CTDI_w^{chamber}$

Then, we compared the two different methodologies for RDQC on the four different CT scans to validate a new scintillating fiber dosimeter and to assess the corresponding accuracy. Hereafter in this paper, the beam width of 38.5 mm for SN1 is treated as a 40 mm beam width to compare results with other CT scans. The results for each CT scan are displayed in Figure 6 for beam width < 40 mm and Figure 7 for beam width > 40 mm. Figure 8 shows the mean $[\Delta CTDI]_{ref}^{IVIscan}$ over all CT scans by protocol type, i.e., beam width and anatomic region of head and body.

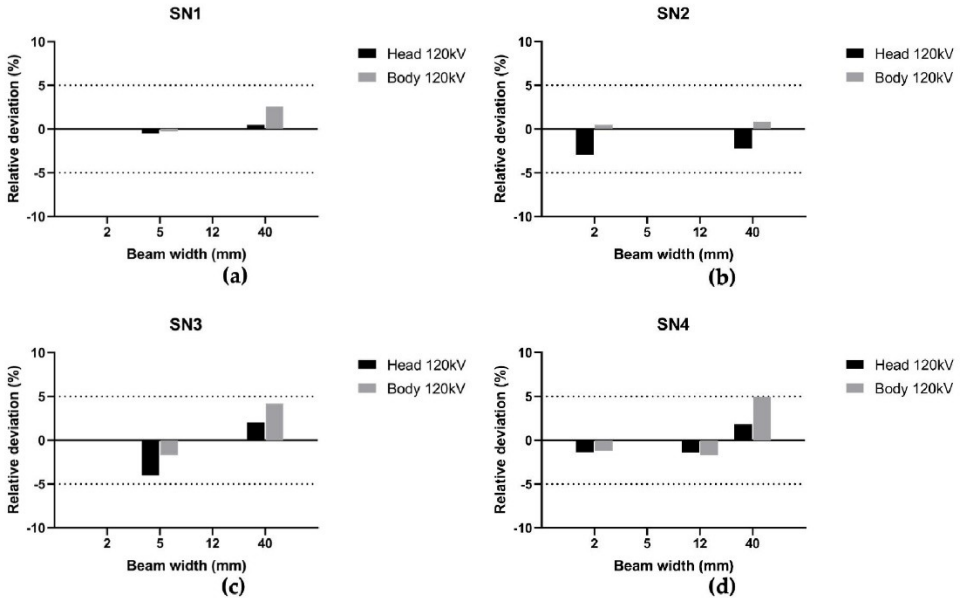

Figure 6. Relative deviation between $CTDI_w^{IVIscan}$ and $CTDI_w^{chamber}$, $[\Delta CTDI]_{ref}^{IVIscan}$, at 120 kV for head and body phantoms over the thinnest and the most used beam width in clinic for (**a**) SN1, (**b**) SN2, (**c**) SN3 and (**d**) SN4.

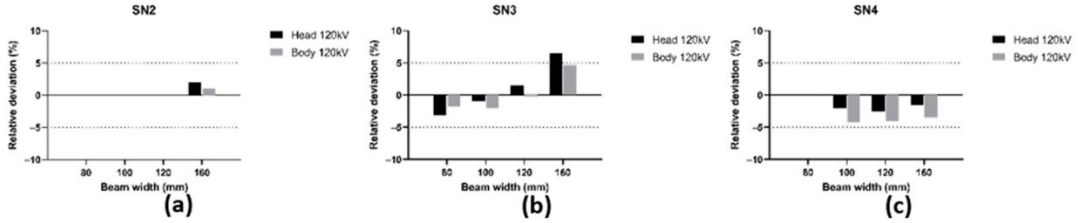

Figure 7. Relative deviation $[\Delta CTDI]_{ref}^{IVIscan}$ at 120 kV for head and body phantoms over the largest beam width for (**a**) SN2 with $N \times T$ = 160 mm, (**b**) SN3 with $N \times T$ = 80, 100, 120 and 160 mm, (**c**) SN4 with $N \times T$ = 100, 120 and 160 mm.

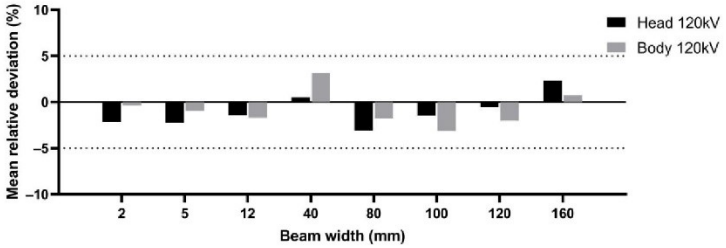

Figure 8. Mean $[\Delta CTDI]_{ref}^{IVIscan}$ over all centers at 120 kV for each protocol type (head and body and beam width from 2 mm to 160 mm).

Regarding beam width < 40 mm, results presented show a relative deviation between −3.9% and +4.9%. The maximum value relates to SN4, 40 mm beam width and body protocol (Figure 6d). Considering all measurements, the relative deviation does not exceed ± 5% regardless of the CT scan and protocol used and the mean $[\Delta CTDI]_{ref}^{IVIscan}$ ranges from −2.25% to +3.14% according to the CT protocol type (Figure 8). In view of the respective uncertainty of the two dosimeters, we can conclude that the two methodologies of calculating the $CTDI_w$ are equivalent for RDQC with beam < 40 mm, and the N_C factor is independent of the beam width.

Similar results are obtained for beam width > 40 mm except for SN3, at 160 mm, and a head protocol where a relative deviation of +6.5% is obtained. In all other cases, the relative deviation is between −4.2% and +4.6% and thus does not exceed ±5%. The mean $[\Delta CTDI]_{ref}^{IVIscan}$ shown in Figure 8 is between −3.13% and +2.33% according to the CT protocol type. Therefore, we can reasonably conclude here as well that both methodologies of calculating the $CTDI_{w,N\times T>40}$ for a beam over 40 mm are equivalent.

3.2.3. Energy Dependence

Even though the regulations require RDQC to be performed at a fixed energy of 120 kV, we wanted to study the relative deviation $[\Delta CTDI]_{ref}^{IVIscan}$ on the entire energy range of a CT scan. Figure 9 shows the results obtained for SN2 at 80, 100, 120 and 135 kV for body CT acquisition and two different beam widths.

Relative deviation $[\Delta CTDI]_{ref}^{IVIscan}$ ranges from −1.23% (±1.92) to +2.28% (±1.62) and does not exceed ±5% regardless of the beam width used. Therefore, we can assume that the IVIscan method does not depend on the beam quality. This makes it possible to carry out RDQC for different kV parameters with the same accuracy, especially for the specific control of pediatric protocols which are often 100 kV or high body mass index (BMI) protocols which are often 140 kV.

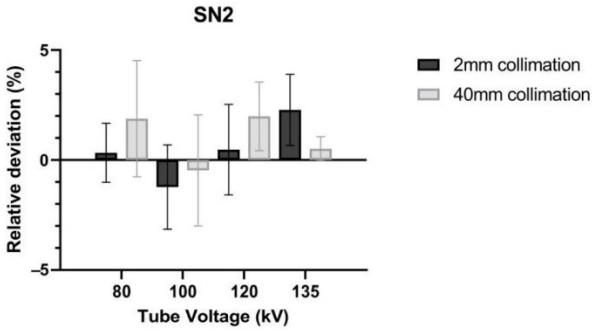

Figure 9. Relative deviation $[\Delta CTDI]_{ref}^{IVIscan}$ calculated for SN2 Head CT protocols over the thinnest beam (2 mm beam width) and the most used in clinic (40 mm beam width) for the entire CT energy range. The standard deviations are represented as error bars.

4. Discussion and Conclusions

As CT is the most radiative imaging modality, it is important to be able to accurately estimate the output radiation and ideally in the conditions of clinical use. Today, the $CTDI_w$, is the reference indicator used for RDQC. However, this indicator suffers from several limitations. First, 100 mm CT chamber and PMMA phantom lengths do not allow for accurate measurement of the larger beam width available on the new wide beam CT scans. The current tools and methods are therefore obsolete in addition to being time consuming which may interfere with clinical activity. According to current French and international regulations, RDQC is only carried out once a year and as an internal control when changing an X-ray tube or any hardware of software intervention that may influence the X-ray emission. This can lead to the late detection of a dosimetric mismatch. Therefore, a simplified and automated method allowing quick and relevant measurements, without impacting the clinical activity, is needed and could encourage more regular controls.

The results presented in this work show a good correlation between IVIscan and the usual CT chamber method, no matter which scanner, phantom, energy or beam width is used. We observed only one relative deviation above +5%, and it represents a minority of the total of 34 measurements, comprising 16 measurements over 40 mm beam width. Moreover, considering the $\pm$5% uncertainty related to each dosimetry system and the accuracy of the phantom positioning for each comparative test, it can be assumed that these results highlight an equivalence of the IVIscan method and associated scintillating fiber sensor and usual CT chamber for CTDIw measurements. Thus, these results are very satisfactory and validate the use of the IVIscan®dosimeter within the framework of standard regulatory RDQC in computed tomography. Complementary results with kV variation show the non-dependency of IVIscan methodology with the beam energy that is convenient for performing quality controls closer to the clinic.

The competent authorities are currently considering changing the quality control procedures to address the various issues outlined above and thus come closer to clinical practices. With its sensor shape and radiolucency, allowing measurements during clinical examinations, and its detection length, the IVIscan device would overcome these difficulties both for wide beams and helical acquisitions which make it possible to imagine RDQC that are close to the current clinical practices in CT.

Furthermore, the IVIscan detector and associated methods described in this article could find interesting applications in other fields (e.g., radiotherapy) with the use of Cone Beam CT (CBCT) imaging equipment, which has the particularity to also have a wide beam. This imaging equipment is increasingly growing in the field of image-guided radiotherapy. It has been henceforth recommended by multiple international institutions to report the imaging dose given through radiotherapy treatment courses and implement a quality control system able to control the X-ray tube performances over time. Since there is no

standardized approach to CBCT quality control and dosimetry across all CBCT systems, and the measurement of CTDI on CBCT is very time-consuming, it could be interesting to study the relevance of the IVIscan dosimeter for RDQC on this kind of device. This will be the subject of future work.

Author Contributions: Conceptualization, M.M. and F.C.; methodology, N.G. and M.M.; validation, N.G. and M.M.; formal analysis, N.G., M.B., C.P. and M.M.; investigation, M.B., C.P., S.P., C.D., N.K. and R.M.; resources, M.M. and F.C.; data curation, N.G. and M.B.; writing—original draft preparation, N.G., M.M., M.B. and C.P.; writing—review and editing, N.G. and M.M.; visualization, N.G. and M.B.; supervision, M.M.; project administration, M.M. and F.C.; All authors have read and agreed to the published version of the manuscript.

Funding: This research received no external funding.

Acknowledgments: We would like to thank the medical imaging departments from the CH Haguenau, CHU Rangueil in Toulouse, Centre Léon Bérard in Lyon, Robert Debré Hospital from APHP in Paris and especially the heads of departments and medical physicists for allowing us to use their CT scans to complete our measurements.

Conflicts of Interest: The first two authors and the last author work on the development of the IVIscan®dosimeter within the Fibermetrix®company.

References

1. Shope, T.B.; Gagne, R.M.; Johnson, G.C. A Method for Describing the Doses Delivered by Transmission X-ray Computed Tomography. *Med. Phys.* **1981**, *8*, 488–495. [CrossRef]
2. Dixon, R.L.; Anderson, J.A.; Bakalyar, D.M.; Boedeker, K.; Boone, J.M.; Cody, D.D.; Fahrig, R.; Jaffray, D.A.; Kyprianou, I.S.; Mc Collough, C.H.; et al. *Comprehensive Methodology for the Evaluation of Radiation Dose in X-ray Computed Tomography*; Report TG n°111; AAPM: Alexandria, VA, USA, 2010. Available online: https://www.aapm.org/pubs/reports/RPT_111.pdf (accessed on 4 January 2023).
3. Dixon, R.L.A. New Look at CT Dose Measurement: Beyond CTDI. *Med. Phys.* **2003**, *30*, 1272–1280. [CrossRef] [PubMed]
4. Perisinakis, K.; Damilakis, J.; Tzedakis, A.; Papadakis, A.; Theocharopoulos, N.; Gourtsoyiannis, N. Determination of the Weighted CT Dose Index in Modern Multi-Detector CT Scanners. *Phys. Med. Biol.* **2007**, *52*, 6485–6495. [CrossRef] [PubMed]
5. Boone, J.M. The Trouble with CTDI100: The Trouble with CTDI100. *Med. Phys.* **2007**, *34*, 1364–1371. [CrossRef]
6. Damilakis, J. CT Dosimetry: What Has Been Achieved and What Remains to Be Done. *Investig. Radiol.* **2021**, *56*, 62–68. [CrossRef]
7. Lambert, J.W.; Phillips, E.D.; Villanueva-Meyer, J.E.; Nardo, L.; Facchetti, L.; Gould, R.G. Axial or Helical? Considerations for Wide Collimation CT Scanners Capable of Volumetric Imaging in Both Modes. *Med. Phys.* **2017**, *44*, 5718–5725. [CrossRef] [PubMed]
8. Bujila, R.; Kull, L.; Danielsson, M.; Andersson, J. Applying Three Different Methods of Measuring CTDIfree Air to the Extended CTDI Formalism for Wide-Beam Scanners (IEC 60601–2–44): A Comparative Study. *J. Appl. Clin. Med. Phys.* **2018**, *19*, 281–289. [CrossRef] [PubMed]
9. Dixon, R.L.; Ballard, A.C. Experimental Validation of a Versatile System of CT Dosimetry Using a Conventional Ion Chamber: Beyond CTDI100: A Versatile CT Dosimetry System. *Med. Phys.* **2007**, *34*, 3399–3413. [CrossRef] [PubMed]
10. International Atomic Energy Agency. *Status of Computed Tomography Dosimetry for Wide Cone Beam Scanners*; Human Health Reports n°5; IAEA: Vienna, Austria, 2011. Available online: https://www-pub.iaea.org/mtcd/publications/pdf/pub1528_web.pdf (accessed on 4 January 2023).
11. International Atomic Energy Agency. *Quality Assurance Program for Computed Tomography: Diagnostic and Therapy Applications*; Human Health Series n°19; IAEA: Vienna, Austria, 2012. Available online: https://www-pub.iaea.org/mtcd/publications/pdf/pub1557_web.pdf (accessed on 4 January 2023).
12. American College of Radiology. *Computed Tomography Quality Control Manual*; ACR: Reston, VA, USA, 2017. Available online: https://www.acr.org/-/media/ACR/Files/Clinical-Resources/QC-Manuals/CT_QCManual.pdf (accessed on 4 January 2023).
13. Gillet, P.; Munier, M.; Arbor, N.; Carbillet, F.; El Bitar, Z. Evaluation of an Optical Scintillating Fiber Detector for CT Dosimetry. *Radiat. Meas.* **2018**, *119*, 125–131. [CrossRef]
14. Gillet, P. Validation d'un Dosimètre Patient Temps Réel Basé Sur Fibre Optique Pour La Tomodensitométrie X à l'aide de Simulation Monte Carlo. Ph.D. Thesis, Université de Strasbourg, Strasbourg, France, 2018.
15. Devic, C.; Plagnard, J.; Munier, M. Characterization of an Innovative Detector Based on Scintillating Fiber for Personalized Computed Tomography Dosimetry. *Sensors* **2021**, *22*, 90. [CrossRef] [PubMed]
16. Veronese, I.; Chiodini, N.; Cialdi, S.; d'Ippolito, E.; Fasoli, M.; Gallo, S.; La Torre, S.; Mones, E.; Vedda, A.; Loi, G. Real-time dosimetry with Yb-doped silica optical fibres. *Phys. Med. Biol.* **2017**, *62*, 4218. [CrossRef] [PubMed]

17. Zubair, H.T.; Oresegun, A.; Mizanur Rahman, A.K.M.; Ung, N.M.; Mat Sharif, K.A.; Zulkifi, M.I.; Muhd Yassin, S.Z.; Maah, M.J.; Yusoff, Z.; Abdul-Rashid, H.A.; et al. Real-time radiation dosimetry using P-doped silica optical fiber. *Measurement* **2019**, *146*, 119–124. [CrossRef]
18. Horner, M.R.; Stepusin, E.J.; Hyer, D.; Hintenlang, D.E. Characterizing energy dependence and count rate performance of a dual scintillator fiber-optic detector for computed tomography: Performance of a Dual Scintillator Fiber-Optic Detector. *Med. Phys.* **2015**, *42*, 1268–1279. [CrossRef] [PubMed]
19. Thrower, S.; Prajapati, S.; Holmes, S.; Schüler, E.; Beddar, S. Characterization of the plastic scintillator detector system Exradin W2 in a high dose rate flattening-filter-free Photon Beam. *Sensors* **2022**, *22*, 6785. [CrossRef] [PubMed]
20. Galavis, P.E.; Hu, L.; Holmes, S.; Das, I.J. Characterization of the plastic scintillation detector Exradin W2 for small field dosimetry. *Med. Phys.* **2019**, *46*, 2468–2476. [CrossRef] [PubMed]
21. Underwood, T.S.A.; Rowland, B.C.; Ferrand, R.; Vieillevigne, L. Application of the Exradin W1 scintillator to determine Ediode 60,017 and microdiamond 60,019 correction factors for relative dosimetry within small MV and FFF fields. *Phys. Med. Biol.* **2015**, *60*, 6669–6683. [CrossRef] [PubMed]
22. Popotte, C.; Devic, C.; Munier, M.; Moreno, R.; Rousseau, H.; Perlongo, S.; Pilleul, F.; Paul, D. Multicentric comparative study of dose indexes using an "in vivo" optical fiber detection system. *Phys. Med. Int. J. Med. Phys.* **2021**, *92*, S127–S128. [CrossRef]
23. Popotte, C.; Devic, C.; Guillochon, N.; Munier, M.; Paul, D. Evaluation of the IVIscan Detector for Dosimetric Quality Control and Dose Measurements for Cone Beam Computed Tomography in Radiotherapy. *Phys. Med. Eur. J. Med. Phys.* **2022**, *104*, S32. [CrossRef]
24. American Association of Physicists in Medicine. *Performance Evaluation of Computed Tomography Systems*; Report Task Group 233; AAPM: Alexandria, VA, USA, 2019; Available online: https://www.aapm.org/pubs/reports/RPT_233.pdf (accessed on 4 January 2023).
25. Agence Nationale de Sécurité du Médicament et des Produits de Santé. *Annexe de la Décision du 22/11/2007 Fixant les Modalités du Contrôle de Qualité des Scanographes Modifiée par la Décision du 11/03/2011*; ANSM: Saint Denis, France, 2019. Available online: https://www.legifrance.gouv.fr/jorf/id/JORFTEXT000023850697 (accessed on 4 January 2023).
26. Fibermetrix. IVIscan. Available online: https://fibermetrix.com/wp-content/uploads/2022/10/Fiche_produit_IVI_ENG.pdf (accessed on 4 January 2023).
27. Munier, M.; Sohier, T.; Torche, F.; Carbillet, F. Dispositif de Détermination D'une Dose Déposée et Procédé Associé. FR Patent 3053799 (B1), 30 August 2019.
28. Munier, M.; Carbillet, F.; Prudhomme, P.-B.; Guillochon, N. Procédé de Traitement des Données Relatives à un Examen Radiologique D'un Patient. FR Patent 3110708 (B1), 22 April 2022.

VI.B. SiPM noise study for different SiPMs

Figure 97 represents the study of the noise in SiPM #2 depending on the threshold. The part on the left shows the maximum (yellow), the minimum (blue), and the amplitude (green) of the intensity measured. The part on the right presents the noise evaluation in blue and the SNR in yellow.

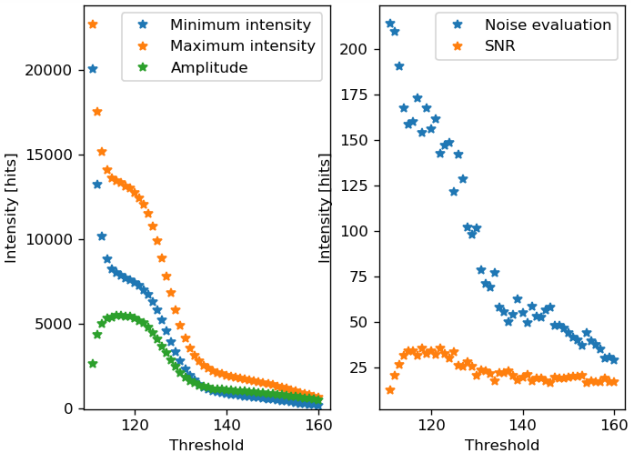

Figure *95*: SiPM #2 noise characterization for thresholds from 110 to 160.

Although the inflection points are different, SiPM#2 shows the same response as the previous SiPM regarding its functioning zones.

Figure 98 below represents the study of the noise in SiPM #3 depending on the threshold.

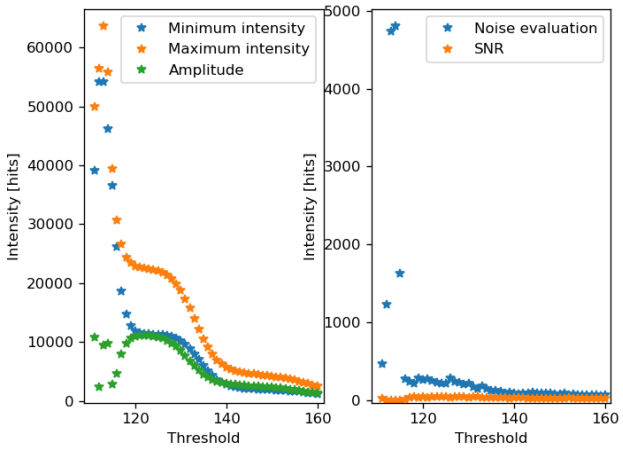

Figure *96*: SiPM #3 noise characterization for thresholds from 110 to 160.

The part on the left shows the maximum (yellow), the minimum (blue), and the amplitude (green) of the intensity measured. The part on the right presents the noise evaluation in blue and the SNR in yellow. Although the inflection points are different, SiPM#3 shows the same response as the previous SiPM regarding its functioning zones.

VI.B. IVI-CBCT repeatability

Table *14*: Mean, standard deviation, coefficient of variation of 10 repeated CTDI measurements (AIEA method) with the IVI-CBCT device, the pencil chamber as well as the linac calculated values.

CBCT protocols	Pelvis	Pelvis Large	Spotlight
Mean value IVI-CBCT [mGy]	19.14	40.45	25.34
Standard deviation IVI-CBCT [mGy]	0.02	0.03	0.11
Coefficient of variation IVI-CBCT [%]	0.1%	0.1%	0.5%
Mean value pencil chamber [mGy]	19.14	40.45	25,34
Standard deviation pencil chamber [mGy]	0.33	0.15	0,12
Coefficient of variation pencil chamber [%]	0,017	0.5%	0,005
Calculated by the accelerator [mGy]	15.89	36.54	22.02

VI.C. Radiobiological aspects

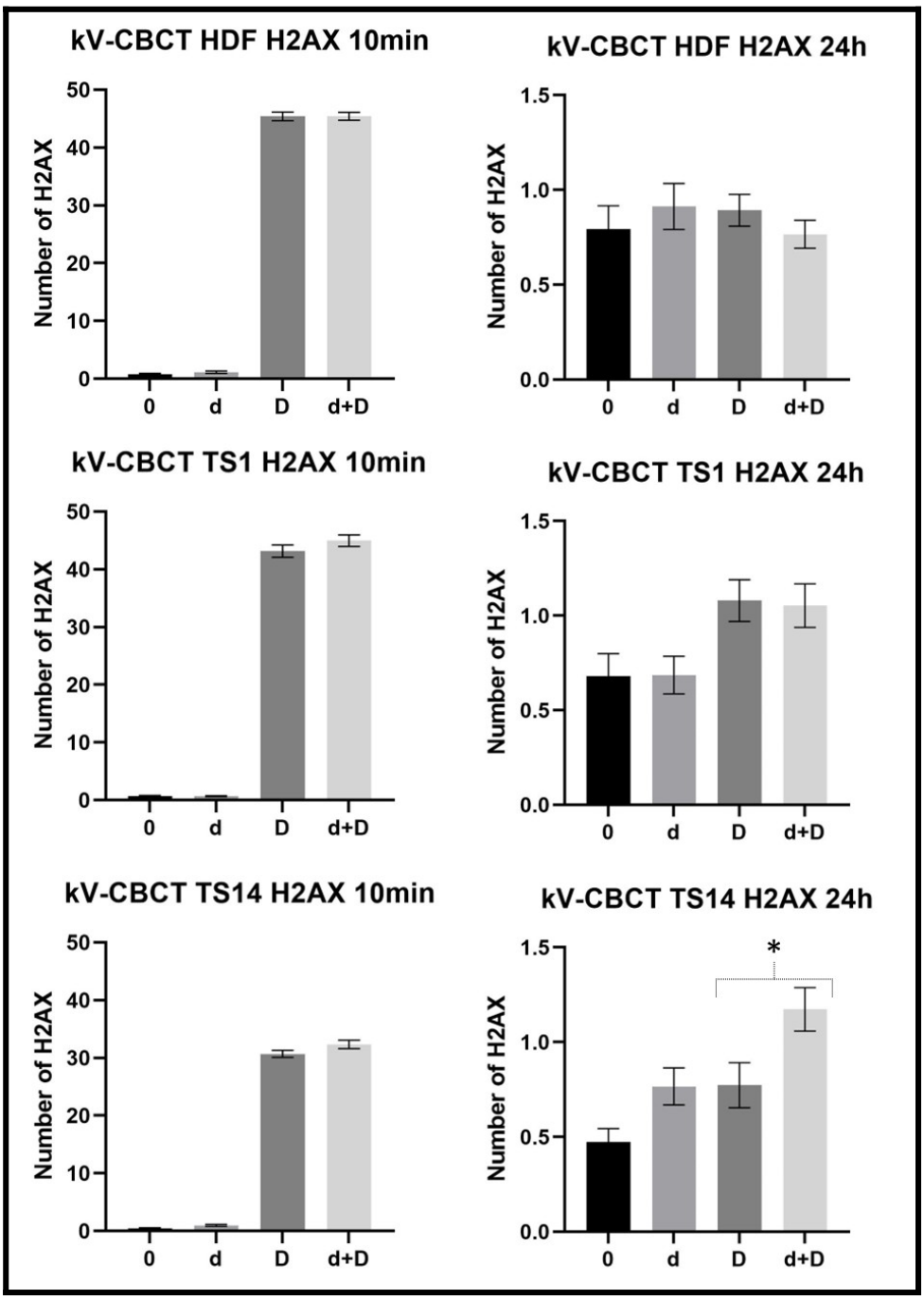

Figure *97*: Repair kinetics of non-irradiated and irradiated cells at d, D alone, and (d + Δt + D), with the dose d being delivered by the kV-CBCT. The kinetics are characterized by the amount of γH2AX foci assessed at 10 min and 24 h. "d" = low dose from kV-CBCT; "D" = dose from one treatment fraction (2 Gy), and "Δt" = time between d and D (3min). "*" stands for $p < 0.05$.

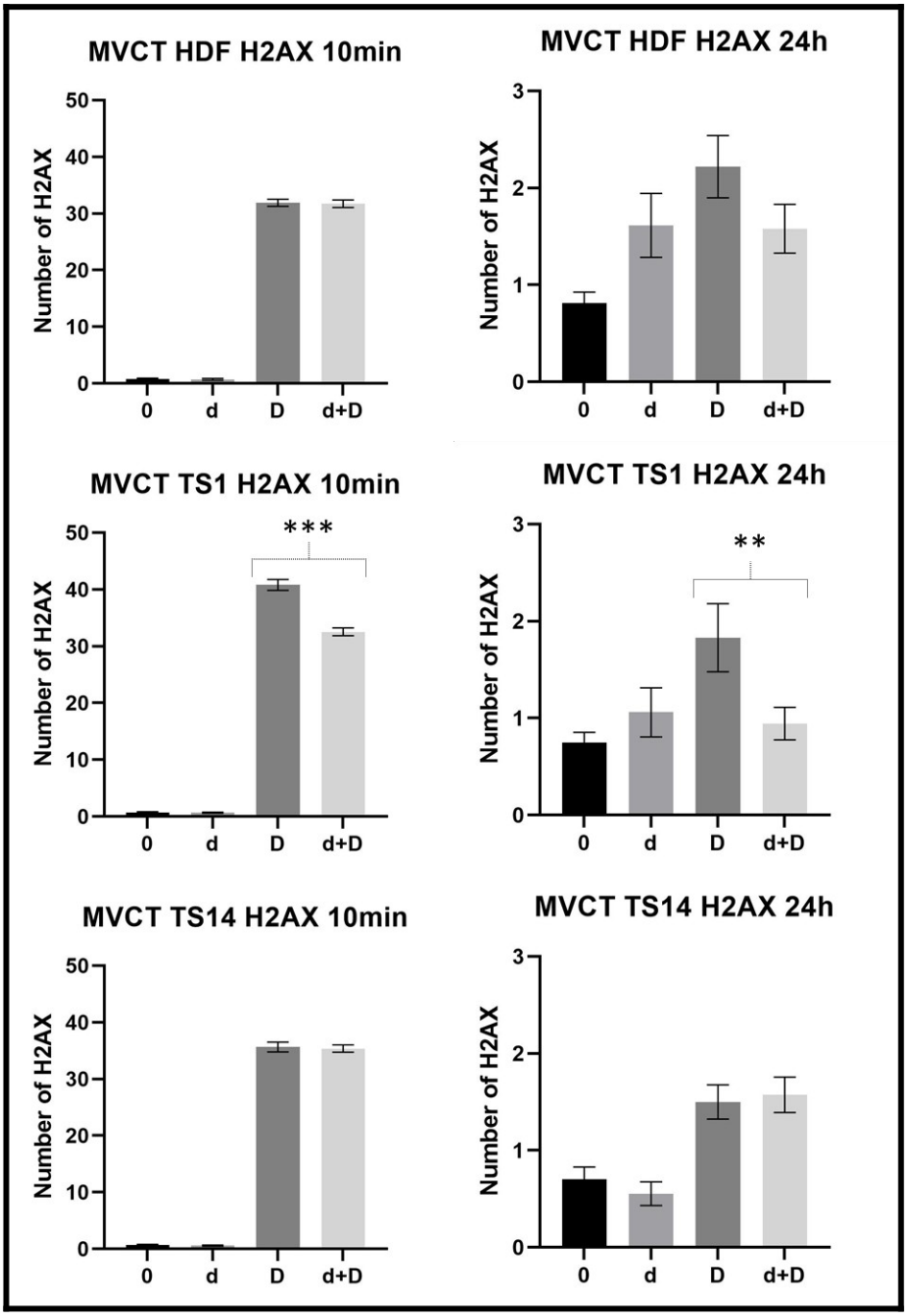

Figure *98*: Repair kinetics of non-irradiated and irradiated cells at d, D alone, and (d + Δt + D), with the dose d being delivered by the MVCT. The kinetics are characterized by the amount of γH2AX foci assessed at 10 min and 24 h. "d" = low dose from MVCT; "D" = dose from one treatment fraction (2 Gy), and "Δt" = time between d and D (3min). "*" stands for $p < 0.05$; "" stands for $p < 0.01$; and "***" stands for $p < 0.001$.**

VII. References

[1] Abuhaimed, A. et al. 2023. Assessment of organ and size-specific effective doses from cone beam CT (CBCT) in image-guided radiotherapy (IGRT) based on body mass index (BMI). *Radiation Physics and Chemistry*. 208, (Jul. 2023), 110889. DOI:https://doi.org/10.1016/j.radphyschem.2023.110889.

[2] Acerbi, F. et al. 2019. Understanding and simulating SiPMs. *Nuclear Instruments and Methods in Physics Research Section A: Accelerators, Spectrometers, Detectors and Associated Equipment*. 926, (May 2019), 16–35. DOI:https://doi.org/10.1016/j.nima.2018.11.118.

[3] Ahmad, M. et al. 2011. Four-dimensional volume-of-interest reconstruction for cone-beam computed tomography-guided radiation therapy. *Medical Physics*. 38, 10 (2011), 5646–5656. DOI:https://doi.org/10.1118/1.3634058.

[4] Alaei, P. et al. 2015. Imaging dose from cone beam computed tomography in radiation therapy. *Physica Medica*. 31, 7 (Nov. 2015), 647–658. DOI:https://doi.org/10.1016/j.ejmp.2015.06.003.

[5] Alsanea, F. et al. 2018. A real-time method to simultaneously measure linear energy transfer and dose for proton therapy using organic scintillators. *Medical Physics*. 45, 4 (2018), 1782–1789. DOI:https://doi.org/10.1002/mp.12815.

[6] Amer, A. et al. 2007. Imaging doses from the Elekta Synergy X-ray cone beam CT system. *British Journal of Radiology*. 80, 954 (2007), 476–482. DOI:https://doi.org/10.1259/bjr/80446730.

[7] Archambault, L. 2005. Élaboration D'Un Dosimètre À Fibres Scintillantes. (2005), 206–206.

[8] Archambault, L. 2005. Élaboration D'Un Dosimètre À Fibres Scintillantes. (2005), 206–206.

[9] Archambault, L. et al. 2006. Measurement accuracy and Cerenkov removal for high performance, high spatial resolution scintillation dosimetry. *Medical Physics*. 33, 1 (2006), 128–135. DOI:https://doi.org/10.1118/1.2138010.

[10] Archambault, L. et al. 2006. Measurement accuracy and Cerenkov removal for high performance, high spatial resolution scintillation dosimetry. *Medical Physics*. 33, 1 (2006), 128–135. DOI:https://doi.org/10.1118/1.2138010.

[11] Archer, J. et al. 2020. 2D photon dosimetry with a scintillation fibre optic dosimeter. *Radiation Physics and Chemistry*. 166, April 2019 (2020), 108490–108490. DOI:https://doi.org/10.1016/j.radphyschem.2019.108490.

[12] Archer, J. et al. 2019. High spatial resolution scintillator dosimetry of synchrotron microbeams. *Scientific Reports*. 9, 1 (2019), 1–7. DOI:https://doi.org/10.1038/s41598-019-43349-6.

[13] Badran, B.M. et al. 2002. Influence of γ-irradiation on poly(methyl methacrylate). *Journal of Applied Polymer Science*. 85, 4 (2002), 886–895. DOI:https://doi.org/10.1002/app.10706.

[14] Beaulieu, L. et al. 2013. Current status of scintillation dosimetry for megavoltage beams. *Journal of Physics: Conference Series*. 444, 1 (2013). DOI:https://doi.org/10.1088/1742-6596/444/1/012013.

[15] Beaulieu, L. et al. 2016. Review of plastic and liquid scintillation dosimetry for photon, electron, and proton therapy. *Physics in Medicine and Biology*. 61, 20 (2016), R305–R343. DOI:https://doi.org/10.1088/0031-9155/61/20/R305.

[16] Becquerel, H. et al. 1901. Action physiologique des rayons du radium. *Compt. Rend. Acad. Sci*. 132, (1901), 1289–1291.

[17] Beddar, A.S. et al. 1992. Cerenkov light generated in optical fibres and other light pipes irradiated by electron beams. *Physics in Medicine and Biology*. 37, 4 (1992), 925–935. DOI:https://doi.org/10.1088/0031-9155/37/4/007.

[18] Beddar, A.S. et al. 2004. Plastic scintillation dosimetry for radiation therapy: Minimizing capture of Cerenkov radiation noise. *Physics in Medicine and Biology*. 49, 5 (2004), 783–790. DOI:https://doi.org/10.1088/0031-9155/49/5/009.

[19] Beddar, A.S. et al. 1992. Water-equivalent plastic scintillation detectors for high-energy beam dosimetry: I. Physical characteristics and theoretical considerations. *Physics in Medicine and Biology*. 37, 10 (1992), 1883–1900. DOI:https://doi.org/10.1088/0031-9155/37/10/006.

[20] Beddar, S. Scintillation dosimetry: Review, new innovations and applications. 49.

[21] Beebe, G.W. et al. 1962. Studies of the Mortality of A-Bomb Survivors: I. Plan of Study and Mortality in the Medical Subsample (Selection I), 1950-1958. *Radiation Research*. 16, 3 (1962), 253–280. DOI:https://doi.org/10.2307/3571157.

[22] Belli, M. et al. 2020. The Response of Living Organisms to Low Radiation Environment and Its Implications in Radiation Protection. *Frontiers in Public Health*. 8, (Dec. 2020), 601711. DOI:https://doi.org/10.3389/fpubh.2020.601711.

[23] Bergonie, J. et al. 1905. L'aspermatogenèse expérimentale complète obtenue par les rayons X est-elle definitive. *Compt. Rend. Soc. Biol.* 58, (1905), 678–680.

[24] Bergonié, J.-A. et al. 1906. *Action des rayons X sur le testicule*. G. Gounouilhou.

[25] Berthel, E. et al. 2019. The Nucleoshuttling of the ATM Protein: A Unified Model to Describe the Individual Response to High- and Low-Dose of Radiation? *Cancers*. 11, 7 (Jun. 2019), 905. DOI:https://doi.org/10.3390/cancers11070905.

[26] Bhide, S.A. et al. 2010. Advances in radiotherapy for head and neck cancer. *Oral Oncology*. 46, 6 (Jun. 2010), 439–441. DOI:https://doi.org/10.1016/j.oraloncology.2010.03.005.

[27] Bissonnette, J.-P. et al. 2012. Quality assurance for image-guided radiation therapy utilizing CT-based technologies: A report of the AAPM TG-179. *Medical Physics*. 39, 4 (2012), 1946–1963. DOI:https://doi.org/10.1118/1.3690466.

[28] Blanchard, P. et al. 2011. Mixed treatment comparison meta-analysis of altered fractionated radiotherapy and chemotherapy in head and neck cancer. *Journal of Clinical Epidemiology*. 64, 9 (Sep. 2011), 985–992. DOI:https://doi.org/10.1016/j.jclinepi.2010.10.016.

[29] Bouche, E. et al. 2008. Guide pour la pratique quotidienne de la Dosimétrie in Vivo en radiothérapie externe. (2008), 30–32.

[30] Bray, F. et al. 2018. Global cancer statistics 2018: GLOBOCAN estimates of incidence and mortality worldwide for 36 cancers in 185 countries. *CA: A Cancer Journal for Clinicians*. 68, 6 (2018), 394–424. DOI:https://doi.org/10.3322/caac.21492.

[31] Brenner, D.J. et al. 2003. Cancer risks attributable to low doses of ionizing radiation: Assessing what we really know. *Proceedings of the National Academy of Sciences*. 100, 24 (Nov. 2003), 13761–13766. DOI:https://doi.org/10.1073/pnas.2235592100.

[32] Buckley, J.G. et al. 2018. Investigation of the radiation dose from cone-beam CT for image-guided radiotherapy: A comparison of methodologies. *Journal of Applied Clinical Medical Physics*. 19, 1 (2018), 174–183. DOI:https://doi.org/10.1002/acm2.12239.

[33] Buranurak, S. et al. 2016. Fiber-coupled Al2O3:C radioluminescence dosimetry for total body irradiations. *Radiation Measurements*. 93, (2016), 46–54. DOI:https://doi.org/10.1016/j.radmeas.2016.05.001.

[34] Calabrese, E.J. et al. 2007. Biological stress response terminology: Integrating the concepts of adaptive response and preconditioning stress within a hormetic dose–response framework. *Toxicology and Applied Pharmacology*. 222, 1 (Jul. 2007), 122–128. DOI:https://doi.org/10.1016/j.taap.2007.02.015.

[35] Calabrese, E.J. 2008. Hormesis: Why it is important to toxicology and toxicologists. *Environmental Toxicology and Chemistry*. 27, 7 (2008), 1451–1474. DOI:https://doi.org/10.1897/07-541.1.

[36] Calabrese, E.J. 2013. Origin of the linearity no threshold (LNT) dose–response concept. *Archives of Toxicology*. 87, 9 (Sep. 2013), 1621–1633. DOI:https://doi.org/10.1007/s00204-013-1104-7.

[37] Calabrese, E.J. 2013. Origin of the linearity no threshold (LNT) dose–response concept. *Archives of Toxicology*. 87, 9 (Sep. 2013), 1621–1633. DOI:https://doi.org/10.1007/s00204-013-1104-7.

[38] Calabrese, E.J. et al. 2000. Radiation hormesis: its historical foundations as a biological hypothesis. *Human & Experimental Toxicology*. 19, 1 (Jan. 2000), 41–75. DOI:https://doi.org/10.1191/096032700678815602.

[39] Chemoradiotherapy for locally advanced head and neck cancer: 10-year follow-up of the UK Head and Neck (UKHAN1) trial - ScienceDirect: *https://www.sciencedirect.com/science/article/pii/S1470204509703067*. Accessed: 2023-04-14.

[40] Chen, W.L. et al. 2007. Effects of Cobalt-60 Exposure on Health of Taiwan Residents Suggest New Approach Needed in Radiation Protection. *Dose-Response*. 5, 1 (Jan. 2007), dose-response.0. DOI:https://doi.org/10.2203/dose-response.06-105.Chen.

[41] Chow, J.C.L. 2009. Cone-beam CT dosimetry for the positional variation in isocenter: A Monte Carlo study. *Medical Physics*. 36, 8 (2009), 3512–3520. DOI:https://doi.org/10.1118/1.3166934.

[42] Clift, M.A. et al. 2002. A temporal method of avoiding the Cerenkov radiation generated in organic scintillator dosimeters by pulsed mega-voltage electron and photon beams. *Physics in Medicine and Biology*. 47, 8 (2002), 1421–1433. DOI:https://doi.org/10.1088/0031-9155/47/8/313.

[43] Comparison of radiation doses between cone beam CT and multi detector CT: TLD measurements | Radiation Protection Dosimetry | Oxford Academic: *https://academic.oup.com/rpd/article-abstract/132/3/339/1596435*. Accessed: 2023-02-06.

[44] Conrad, M. et al. 2018. Determination of the effective dose delivered by image guided radiotherapy in head & neck and breast treatments. *Zeitschrift für Medizinische Physik*. 28, 4 (Dec. 2018), 276–285. DOI:https://doi.org/10.1016/j.zemedi.2018.01.001.

[45] Costa, A.M. et al. 2010. In vivo dosimetry with thermoluminescent dosimeters in external photon beam radiotherapy. *Applied Radiation and Isotopes*. 68, 4–5 (2010), 760–762. DOI:https://doi.org/10.1016/j.apradiso.2009.09.039.

[46] Damilakis, J. 2021. CT Dosimetry : What has been achieved and what remains to be done. 56, (2021), 62–68. DOI:https://doi.org/10.1097/RLI.0000000000000727.

[47] Darafsheh, A. et al. 2017. On the origin of the visible light responsible for proton dose measurement using plastic optical fibers. *Design and Quality for Biomedical Technologies X*. 10056, (2017), 100560V-100560V. DOI:https://doi.org/10.1117/12.2252695.

[48] Darafsheh, A. et al. 2017. Proton therapy dosimetry using the scintillation of the silica fibers. *Optics Letters*. 42, 4 (2017), 847–847. DOI:https://doi.org/10.1364/ol.42.000847.

[49] De Angelis, C. et al. 2002. An investigation of the operating characteristics of two PTW diamond detectors in photon and electron beams. *Medical Physics*. 29, 2 (2002), 248–254. DOI:https://doi.org/10.1118/1.1446101.

[50] De Angelis, C. et al. 2007. Present limitations of CVD diamond detectors for IMRT applications. *Nuclear Instruments and Methods in Physics Research, Section A: Accelerators, Spectrometers, Detectors and Associated Equipment*. 583, 1 (2007), 195–203. DOI:https://doi.org/10.1016/j.nima.2007.08.186.

[51] De Boer, S.F. et al. 1993. Optical filtering and spectral measurements of radiation-induced light in plastic scintillation dosimetry. *Physics in Medicine and Biology*. 38, 7 (1993), 945–958. DOI:https://doi.org/10.1088/0031-9155/38/7/005.

[52] De, D.D.E.L. a R. 2014. La radioprotection des travailleurs. *Irsn*. (2014), 1–118.

[53] Debnath, S.B.C. et al. 2020. High spatial resolution inorganic scintillator detector for high-energy X-ray beam at small field irradiation. *Medical Physics*. 47, 3 (2020), 1364–1371. DOI:https://doi.org/10.1002/mp.14002.

[54] Den, R.B. et al. 2010. Daily Image Guidance With Cone-Beam Computed Tomography for Head-and-Neck Cancer Intensity-Modulated Radiotherapy: A Prospective Study. *International Journal of Radiation Oncology*Biology*Physics*. 76, 5 (Apr. 2010), 1353–1359. DOI:https://doi.org/10.1016/j.ijrobp.2009.03.059.

[55] Department of Public Health, Environmental Health Sciences, Morrill I, N344 et al. 2014. Hormesis: a fundamental concept in biology. *Microbial Cell*. 1, 5 (May 2014), 145–149. DOI:https://doi.org/10.15698/mic2014.05.145.

[56] Devic, C. 2020. *Cassures double-brin de l'ADN et influence du facteur individuel dans la réponse aux faibles doses de radiation : cas particulier des examens par scanner*. Université Claude Bernard.

[57] Devic, C. et al. 2021. Characterization of an Innovative Detector Based on Scintillating Fiber for Personalized Computed Tomography Dosimetry. *Sensors*. 22, 1 (Dec. 2021), 90. DOI:https://doi.org/10.3390/s22010090.

[58] Devic, C. et al. 2018. Influence of Individual Radiosensitivity on the Adaptive Response Phenomenon: Toward a Mechanistic Explanation Based on the Nucleo-Shuttling of ATM Protein. *Dose-Response*. 16, 3 (Jul. 2018), 155932581878983. DOI:https://doi.org/10.1177/1559325818789836.

[59] Di Francesca, D. et al. 2019. Dosimetry Mapping of Mixed-Field Radiation Environment Through Combined Distributed Optical Fiber Sensing and FLUKA Simulation. *IEEE Transactions on Nuclear Science*. 66, 1 (Jan. 2019), 299–305. DOI:https://doi.org/10.1109/TNS.2018.2882135.

[60] Di Francesca, D. et al. 2018. Radiation-Induced Attenuation in Single-Mode Phosphosilicate Optical Fibers for Radiation Detection. *IEEE Transactions on Nuclear Science*. 65, 1 (Jan. 2018), 126–131. DOI:https://doi.org/10.1109/TNS.2017.2778314.

[61] Ding, G.X. et al. 2008. Accurate patient dosimetry of kilovoltage cone-beam CT in radiation therapy. *Medical Physics*. 35, 3 (2008), 1135–1144. DOI:https://doi.org/10.1118/1.2839096.

[62] Ding, G.X. et al. 2009. Radiation Dose From Kilovoltage Cone Beam Computed Tomography in an Image-Guided Radiotherapy Procedure. *International Journal of Radiation Oncology*Biology*Physics*. 73, 2 (Feb. 2009), 610–617. DOI:https://doi.org/10.1016/j.ijrobp.2008.10.006.

[63] Dixon, R. et al. 2010. *Comprehensive Methodology for the Evaluation of Radiation Dose in X-Ray Computed Tomography*. AAPM.

[64] Downes, P. et al. 2009. Monte Carlo simulation and patient dosimetry for a kilovoltage cone-beam CT unit. *Medical Physics*. 36, 9Part1 (2009), 4156–4167. DOI:https://doi.org/10.1118/1.3196182.

[65] Dunn, L. et al. 2013. Commissioning of optically stimulated luminescence dosimeters for use in radiotherapy. *Radiation Measurements*. 51–52, (2013), 31–39. DOI:https://doi.org/10.1016/j.radmeas.2013.01.012.

[66] Eisbruch, A. et al. 2011. Chemo-IMRT of Oropharyngeal Cancer Aiming to Reduce Dysphagia: Swallowing Organs Late Complication Probabilities and Dosimetric Correlates. *International Journal of Radiation Oncology*Biology*Physics*. 81, 3 (Nov. 2011), e93–e99. DOI:https://doi.org/10.1016/j.ijrobp.2010.12.067.

[67] El Nachef, L. et al. 2022. Cancer and Radiosensitivity Syndromes: Is Impaired Nuclear ATM Kinase Activity the Primum Movens? *Cancers*. 14, 24 (Dec. 2022), 6141. DOI:https://doi.org/10.3390/cancers14246141.

[68] Elmpt, W. van et al. 2008. A literature review of electronic portal imaging for radiotherapy dosimetry. *Radiotherapy and Oncology*. 88, 3 (Sep. 2008), 289–309. DOI:https://doi.org/10.1016/j.radonc.2008.07.008.

[69] Favaudon, V. et al. 2019. Time-resolved dosimetry of pulsed electron beams in very high dose-rate, FLASH irradiation for radiotherapy preclinical studies. *Nuclear Instruments and Methods in Physics Research, Section A: Accelerators, Spectrometers, Detectors and Associated Equipment*. 944, March (2019), 162537–162537. DOI:https://doi.org/10.1016/j.nima.2019.162537.

[70] Fontbonne, J.M. et al. 2002. Scintillating fiber dosimeter for radiation therapy accelerator. *IEEE Transactions on Nuclear Science*. 49 I, 5 (2002), 2223–2227. DOI:https://doi.org/10.1109/TNS.2002.803680.

[71] Foray, N. 2016. Victor Despeignes, the Forgotten Pioneer of Radiation Oncology. *International Journal of Radiation Oncology*Biology*Physics*. 96, 4 (Nov. 2016), 717–721. DOI:https://doi.org/10.1016/j.ijrobp.2016.07.019.

[72] Francois Therriault-Proulx, R.P., James N. Yang, A. Sam Beddar 2019. Quality assurance for gamma knife perfexion using the exradin W1 plastic scintillation detector and Lucy phantom. (2019). DOI:https://doi.org/10.1016/j.snb.2007.07.003.

[73] Frelin, A.M. et al. 2005. Spectral discrimination of Čerenkov radiation in scintillating dosimeters. *Medical Physics*. 32, 9 (2005), 3000–3006. DOI:https://doi.org/10.1118/1.2008487.

[74] Galavis, P.E. et al. 2019. Characterization of the plastic scintillation detector Exradin W2 for small field dosimetry. *Medical Physics*. 46, 5 (2019), 2468–2476. DOI:https://doi.org/10.1002/mp.13501.

[75] Geets, X. et al. 2007. Adaptive biological image-guided IMRT with anatomic and functional imaging in pharyngo-laryngeal tumors: Impact on target volume delineation and dose distribution using helical tomotherapy. *Radiotherapy and Oncology*. 85, 1 (Oct. 2007), 105–115. DOI:https://doi.org/10.1016/j.radonc.2007.05.010.

[76] Giaddui, T. et al. 2013. Comparative dose evaluations between XVI and OBI cone beam CT systems using Gafchromic XRQA2 film and nanoDot optical stimulated luminescence dosimeters. *Medical Physics*. 40, 6Part1 (2013), 062102. DOI:https://doi.org/10.1118/1.4803466.

[77] Gillet, P. et al. 2018. Evaluation of an optical scintillating fiber detector for CT dosimetry. *Radiation Measurements*. 119, (Dec. 2018), 125–131. DOI:https://doi.org/10.1016/j.radmeas.2018.09.012.

[78] Girard, S. et al. 2013. Radiation Effects on Silica-Based Optical Fibers: Recent Advances and Future Challenges. *IEEE Transactions on Nuclear Science*. 60, 3 (Jun. 2013), 2015–2036. DOI:https://doi.org/10.1109/TNS.2012.2235464.

[79] Granzotto, A. et al. 2016. Influence of Nucleoshuttling of the ATM Protein in the Healthy Tissues Response to Radiation Therapy: Toward a Molecular Classification of Human Radiosensitivity. *International Journal of Radiation Oncology*Biology*Physics*. 94, 3 (Mar. 2016), 450–460. DOI:https://doi.org/10.1016/j.ijrobp.2015.11.013.

[80] Grote, S.J. et al. 1981. Observations of Radiation-induced Chromosome Fragment Loss in Live Mammalian Cells in Culture, and Its Effect on Colony-forming Ability. *International Journal of Radiation Biology and Related Studies in Physics, Chemistry and Medicine*. 39, 4 (Jan. 1981), 395–408. DOI:https://doi.org/10.1080/09553008114550491.

[81] Grusell, E. et al. 1986. Evaluation of temperature effects in p-type silicon detectors. *Physics in Medicine and Biology*. 31, 5 (1986), 527–534. DOI:https://doi.org/10.1088/0031-9155/31/5/005.

[82] Guillochon, N. et al. 2023. Validation of a New Scintillating Fiber Dosimeter for Radiation Dose Quality Control in Computed Tomography. 23, 5 (2023), 2614.

[83] H. Yoshida et al. 1995. Temperature effect on the radiation-degradation of PMMA. 46, 4 (1995), 921–924.

[84] Hempel, D. et al. 2020. Testicular dose contributed by X-ray volume image-(XVI)-guided intensity-modulated radiotherapy (IMRT) in prostate cancer patients. *Biuletyn Polskiego Towarzystwa Onkologicznego Nowotwory*. 5, 2 (2020), 64–70.

[85] de las Heras Gala, H. et al. 2017. Quality control in cone-beam computed tomography (CBCT) EFOMP-ESTRO-IAEA protocol (summary report). *Physica Medica*. 39, (Jul. 2017), 67–72. DOI:https://doi.org/10.1016/j.ejmp.2017.05.069.

[86] Hsu, S.M. et al. 2007. Synthesis and physical characteristics of radiophotoluminescent glass dosimeters. *Radiation Measurements*. 42, 4–5 (2007), 621–624. DOI:https://doi.org/10.1016/j.radmeas.2007.01.053.

[87] Hu, N. et al. 2014. Measurement of radiotherapy CBCT dose in a phantom using different methods. *Australasian Physical & Engineering Sciences in Medicine*. 37, 4 (Dec. 2014), 779–789. DOI:https://doi.org/10.1007/s13246-014-0301-x.

[88] Hugo, de las H.G. et al. 2017. *QUALITY CONTROL IN CONE-BEAM COMPUTED TOMOGRAPHY (CBCT) EFOMP-ESTRO-IAEA PROTOCOL*. European Federation of Organisations for Medical Physics.

[89] ICRU Report 80, Dosimetry Systems for Use in Radiation Processing – ICRU: *https://www.icru.org/report/dosimetry-systems-for-use-in-radiation-processing-icru-report-80/*. Accessed: 2023-02-20.

[90] Implementation of Optical-Fiber Postmortem Dose Measurements: A Proof of Concept | IEEE Journals & Magazine | IEEE Xplore: *https://ieeexplore.ieee.org/abstract/document/8865620*. Accessed: 2023-02-20.

[91] Islam, M.K. et al. 2006. Patient dose from kilovoltage cone beam computed tomography imaging in radiation therapy. *Medical Physics*. 33, 6Part1 (2006), 1573–1582. DOI:https://doi.org/10.1118/1.2198169.

[92] Jaffray, D.A. et al. 1999. A radiographic and tomographic imaging system integrated into a medical linear accelerator for localization of bone and soft-tissue targets. *International Journal of Radiation Oncology*Biology*Physics*. 45, 3 (Oct. 1999), 773–789. DOI:https://doi.org/10.1016/S0360-3016(99)00118-2.

[93] Jeong, D.-H. et al. 2021. Optical Filter-Embedded Fiber-Optic Radiation Sensor for Ultra-High Dose Rate Electron Beam Dosimetry. *Sensors*. 21, 17 (Aug. 2021), 5840. DOI:https://doi.org/10.3390/s21175840.

[94] Joiner, M.C. et al. 1999. Adaptive response and induced resistance. *Comptes Rendus de l'Académie des Sciences - Series III - Sciences de la Vie*. 322, 2 (Feb. 1999), 167–175. DOI:https://doi.org/10.1016/S0764-4469(99)80040-7.

[95] Joubert, A. et al. 2008. DNA double-strand break repair defects in syndromes associated with acute radiation response: At least two different assays to predict intrinsic radiosensitivity? *International Journal of Radiation Biology*. 84, 2 (Jan. 2008), 107–125. DOI:https://doi.org/10.1080/09553000701797039.

[96] Jr, J.D.B. et al. Members of the Main Commission of the ICRP.

[97] Jucius, R.A. et al. 1977. Radiation Dosimetry In Computed Tomography (CT). *Application of Optical Instrumentation in Medicine VI* (Dec. 1977), 286–295.

[98] Jursinic, P.A. 2007. Characterization of optically stimulated luminescent dosimeters, OSLDs, for clinical dosimetric measurements. *Medical Physics*. 34, 12 (2007), 4594–4604. DOI:https://doi.org/10.1118/1.2804555.

[99] Kaur, I. et al. 2016. Dosimetric impact of setup errors in head and neck cancer patients treated by image-guided radiotherapy. *Journal of Medical Physics / Association of Medical Physicists of India*. 41, 2 (2016), 144–148. DOI:https://doi.org/10.4103/0971-6203.181640.

[100] Kearney, M. et al. 2020. A review of Image Guided Radiation Therapy in head and neck cancer from 2009–2019 – Best Practice Recommendations for RTTs in the Clinic. *Technical Innovations & Patient Support in Radiation Oncology*. 14, (Jun. 2020), 43–50. DOI:https://doi.org/10.1016/j.tipsro.2020.02.002.

[101] Kim, D.W. et al. 2013. Imaging Doses and Secondary Cancer Risk From Kilovoltage Cone-beam CT in Radiation Therapy. *Health Physics*. 104, 5 (May 2013), 499. DOI:https://doi.org/10.1097/HP.0b013e318285c685.

[102] Kim, D.W. et al. 2013. Imaging doses and secondary cancer risk from kilovoltage cone-beam ct in radiation therapy. *Health Physics*. 104, 5 (2013), 499–503. DOI:https://doi.org/10.1097/HP.0b013e318285c685.

[103] Kim, S. et al. 2010. ESTIMATION OF COMPUTED TOMOGRAPHY DOSE INDEX IN CONE BEAM COMPUTED TOMOGRAPHY: MOSFET MEASUREMENTS AND MONTE CARLO SIMULATIONS. *Health Physics*. 98, 5 (May 2010), 683. DOI:https://doi.org/10.1097/HP.0b013e3181cd3ec3.

[104] Koivisto, J.H. et al. 2015. Characterization of MOSFET dosimeters for low-dose measurements in maxillofacial anthropomorphic phantoms. *Journal of Applied Clinical Medical Physics*. 16, 4 (2015), 266–278. DOI:https://doi.org/10.1120/jacmp.v16i4.5433.

[105] Krebs, A.T. 1955. Early History of the Scintillation Counter. *Science*. 122, 3157 (Jul. 1955), 17–18. DOI:https://doi.org/10.1126/science.122.3157.17.

[106] Kry, S.F. et al. 2017. AAPM TG 158: Measurement and calculation of doses outside the treated volume from external-beam radiation therapy. *Medical Physics*. 44, 10 (2017), e391–e429. DOI:https://doi.org/10.1002/mp.12462.

[107] Lambert, J. et al. 2006. A plastic scintillation dosimeter for high dose rate brachytherapy. *Physics in Medicine and Biology*. 51, 21 (2006), 5505–5516. DOI:https://doi.org/10.1088/0031-9155/51/21/008.

[108] Lambert, J. et al. 2010. A prototype scintillation dosimeter customized for small and dynamic megavoltage radiation fields. *Physics in Medicine and Biology*. 55, 4 (2010), 1115–1126. DOI:https://doi.org/10.1088/0031-9155/55/4/014.

[109] Lambert, J. et al. 2008. Cerenkov-free scintillation dosimetry in external beam radiotherapy with an air core light guide. *Physics in Medicine and Biology*. 53, 11 (2008), 3071–3080. DOI:https://doi.org/10.1088/0031-9155/53/11/021.

[110] Lanson, J.H. et al. 1999. In vivo dosimetry during conformal radiotherapy: Requirements for and findings of a routine procedure. *Radiotherapy and Oncology*. 52, 1 (Jul. 1999), 51–59. DOI:https://doi.org/10.1016/S0167-8140(99)00074-2.

[111] Leo, W.R. 1994. *Techniques for nuclear and particle physics experiments: a how-to approach*. Springer.

[112] Létourneau, D. et al. 1999. Miniature scintillating detector for small field radiation therapy. *Medical Physics*. 26, 12 (1999), 2555–2561. DOI:https://doi.org/10.1118/1.598793.

[113] Li Vecchi, G. et al. 2020. Infrared radiation Induced attenuation of radiation sensitive optical fibers: influence of temperature and modal propagation. *Optical Fiber Technology*. 55, (Mar. 2020), 102166. DOI:https://doi.org/10.1016/j.yofte.2020.102166.

[114] Linares Rosales, H.M. et al. 2019. Optimization of a multipoint plastic scintillator dosimeter for high dose rate brachytherapy. *Medical Physics*. 46, 5 (2019), 2412–2421. DOI:https://doi.org/10.1002/mp.13498.

[115] Luckey, T.D. 1980. Hormesis with ionizing radiation. CRC. *Inc. Boca Raton, Fl*. (1980).

[116] Madden, L. et al. 2019. First measurements with a plastic scintillation dosimeter at the Australian MRI-LINAC. *Physics in Medicine & Biology*. 64, 17 (Sep. 2019), 175015. DOI:https://doi.org/10.1088/1361-6560/ab324b.

[117] Maria, O.M. et al. 2017. Radiation-Induced Oral Mucositis. *Frontiers in Oncology*. 7, (2017).

[118] Marinello, G. et al. *Systèmes d ' imagerie intégrés ou associés aux appareils de radiothérapie Coordonné par Ginette Marinello et Jianji Pan*.

[119] Marples, B. et al. 2008. Low-Dose Hyper-Radiosensitivity: Past, Present, and Future. *International Journal of Radiation Oncology*Biology*Physics*. 70, 5 (Apr. 2008), 1310–1318. DOI:https://doi.org/10.1016/j.ijrobp.2007.11.071.

[120] Martin, C.J. et al. 2021. An international survey of imaging practices in radiotherapy. *Physica Medica*. 90, (Oct. 2021), 53–65. DOI:https://doi.org/10.1016/j.ejmp.2021.09.004.

[121] Micke, A. et al. 2011. Multichannel film dosimetry with nonuniformity correction. *Medical Physics*. 38, 5 (2011), 2523–2534. DOI:https://doi.org/10.1118/1.3576105.

[122] Mijnheer, B. 2017. EPID-based dosimetry and its relation to other 2D and 3D dose measurement techniques in radiation therapy. *Journal of Physics: Conference Series*. 847, 1 (May 2017), 012024. DOI:https://doi.org/10.1088/1742-6596/847/1/012024.

[123] Moulay Lakhdar, I. et al. 2021. Fibroblasts from Retinoblastoma Patients Show Radiosensitivity Linked to Abnormal Localization of the ATM Protein. *Current Eye Research*. 46, 4 (Apr. 2021), 546–557. DOI:https://doi.org/10.1080/02713683.2020.1808998.

[124] Munier, M. et al. 2014. A new scintillating fiber dosimeter for real-time measurement in radiology and radiotherapy. *Physica Medica*. 30, (Dec. 2014), e129. DOI:https://doi.org/10.1016/j.ejmp.2014.10.026.

[125] MUNIER, M. et al. 2019. Dispositif de détermination d'une dose déposée et procédé associé. 3053799. Aug. 30, 2019.

[126] Munier, M. 2018. Real-time patient dose measurement in CT Scan : An innovative solution to improve radiation awareness. (2018), 800 words. DOI:https://doi.org/10.1594/ESI2018/ESI-0086.

[127] Murphy, M.J. et al. 2007. The management of imaging dose during image-guided radiotherapy: Report of the AAPM Task Group 75. *Medical Physics*. 34, 10 (2007), 4041–4063. DOI:https://doi.org/10.1118/1.2775667.

[128] NIH Image to ImageJ: 25 years of image analysis | Nature Methods: *https://www.nature.com/articles/nmeth.2089.* Accessed: 2023-02-06.

[129] O'Keeffe, S. et al. 2009. Polymer Optical Fibre for in Situ Monitoring of Gamma Radiation Processes. *International Journal on Smart Sensing and Intelligent Systems*. 2, 3 (2009), 490–502. DOI:https://doi.org/10.21307/ijssis-2017-363.

[130] Olivieri, G. et al. 1984. Adaptive Response of Human Lymphocytes to Low Concentrations of Radioactive Thymidine. *Science*. 223, 4636 (Feb. 1984), 594–597. DOI:https://doi.org/10.1126/science.6695170.

[131] Orlandi, E. et al. 2019. Predictors of Patient-Reported Dysphagia Following IMRT Plus Chemotherapy in Oropharyngeal Cancer. *Dysphagia*. 34, 1 (Feb. 2019), 52–62. DOI:https://doi.org/10.1007/s00455-018-9913-8.

[132] Our solutions | Fibermetrix: *http://fibermetrix.com/en/our-solutions/*. Accessed: 2023-03-06.

[133] Pardo, E. et al. 2016. On flattening filter-free portal dosimetry. *Journal of Applied Clinical Medical Physics*. 17, 4 (2016), 132–145. DOI:https://doi.org/10.1120/jacmp.v17i4.6147.

[134] Pasquino, M. et al. 2017. Dosimetric characterization and behaviour in small X-ray fields of a microchamber and a plastic scintillator detector. *British Journal of Radiology*. 90, 1069 (2017). DOI:https://doi.org/10.1259/bjr.20160596.

[135] Pazzaglia, S. et al. 2022. Out-of-field effects: lessons learned from partial body exposure. *Radiation and Environmental Biophysics*. 61, 4 (Nov. 2022), 485–504. DOI:https://doi.org/10.1007/s00411-022-00988-0.

[136] Popotte, C. et al. 2022. Dose Quantificaiton from Daily CBCT Exams During VMAT Prostate Radiotherapy Treatments Using an Innovative Plastic Scintillating Detector. 104, Supplement 1 (2022), S114. DOI:https://doi.org/10.1016/S1120-1797(22)02385-7.

[137] Popotte, C. et al. 2021. Multicentric comparative study of dose indexes using an in vivo optical fiber detection system. 92, Supplement (2021), S127–S128. DOI:https://doi.org/10.1016/S1120-1797(22)00272-1.

[138] Popotte, C. et al. 2021. Multicentric comparative study of dose indexes using an "in vivo" optical fiber detection system. *Physica Medica*. 92, (Dec. 2021), S127–S128. DOI:https://doi.org/10.1016/S1120-1797(22)00272-1.

[139] QA for helical tomotherapy: Report of the AAPM Task Group 148a) - Langen - 2010 - Medical Physics - Wiley Online Library: *https://aapm.onlinelibrary.wiley.com/doi/full/10.1118/1.3462971*. Accessed: 2023-03-19.

[140] Qi, Z.-Y. et al. 2007. Verification of the plan dosimetry for high dose rate brachytherapy using metal–oxide–semiconductor field effect transistor detectors. *Medical Physics*. 34, 6Part1 (2007), 2007–2013. DOI:https://doi.org/10.1118/1.2736288.

[141] Raman, S.P. et al. 2013. CT Dose Reduction Applications: Available Tools on the Latest Generation of CT Scanners. *Journal of the American College of Radiology*. 10, 1 (Jan. 2013), 37–41. DOI:https://doi.org/10.1016/j.jacr.2012.06.025.

[142] Rithidech, K.N. et al. 2008. Evidence for Radiation Hormesis after *In Vitro* Exposure of Human Lymphocytes to Low Doses of Ionizing Radiation. *Dose-Response*. 6, 3 (Jul. 2008), dose-response.0. DOI:https://doi.org/10.2203/dose-response.07-024.Rithidech.

[143] Rodríguez, M.L. et al. 2008. Implementation of in vivo Dosimetry with Isorad™ Semiconductor Diodes in Radiotherapy Treatments of the Pelvis. *Medical Dosimetry*. 33, 1 (2008), 14–21. DOI:https://doi.org/10.1016/j.meddos.2007.04.004.

[144] Samei, E. et al. 2019. Performance evaluation of computed tomography systems: Summary of AAPM Task Group 233. *Medical Physics*. 46, 11 (2019), e735–e756. DOI:https://doi.org/10.1002/mp.13763.

[145] Sanguineti, G. et al. 2012. Effect of Radiotherapy and Chemotherapy on the Risk of Mucositis During Intensity-Modulated Radiation Therapy for Oropharyngeal Cancer. *International Journal of Radiation Oncology*Biology*Physics*. 83, 1 (May 2012), 235–242. DOI:https://doi.org/10.1016/j.ijrobp.2011.06.2000.

[146] Scandurra, D. et al. 2014. A dosimetry technique for measuring kilovoltage cone-beam CT dose on a linear accelerator using radiotherapy equipment. *Journal of Applied Clinical Medical Physics*. 15, 4 (2014), 80–92. DOI:https://doi.org/10.1120/jacmp.v15i4.4658.

[147] Schwab, M. 2008. *Encyclopedia of Cancer*. Springer Science & Business Media.

[148] Shi, M. et al. 2020. GPU-accelerated Monte Carlo simulation of MV-CBCT. *Physics in Medicine & Biology*. 65, 23 (Nov. 2020), 235042. DOI:https://doi.org/10.1088/1361-6560/abaeba.

[149] Shope, T.B. et al. 1981. A method for describing the doses delivered by transmission x-ray computed tomography. *Medical Physics*. 8, 4 (1981), 488–495. DOI:https://doi.org/10.1118/1.594995.

[150] Shore, R.E. et al. 2018. Implications of recent epidemiologic studies for the linear nonthreshold model and radiation protection. *Journal of Radiological Protection*. 38, 3 (Sep. 2018), 1217–1233. DOI:https://doi.org/10.1088/1361-6498/aad348.

[151] Soriani, A. et al. 2007. Setup verification and in vivo dosimetry during intraoperative radiation therapy (IORT) for prostate cancer. *Medical Physics*. 34, 8 (2007), 3205–3210. DOI:https://doi.org/10.1118/1.2750965.

[152] Spezi, E. et al. 2009. Monte Carlo simulation of an x-ray volume imaging cone beam CT unit. *Medical Physics*. 36, 1 (2009), 127–136. DOI:https://doi.org/10.1118/1.3031113.

[153] Spezi, E. et al. 2012. Patient-Specific Three-Dimensional Concomitant Dose From Cone Beam Computed Tomography Exposure in Image-Guided Radiotherapy. *International Journal of Radiation Oncology*Biology*Physics*. 83, 1 (May 2012), 419–426. DOI:https://doi.org/10.1016/j.ijrobp.2011.06.1972.

[154] Sporea, D. et al. 2012. Optical Fibers and Optical Fiber Sensors Used in Radiation Monitoring. *Selected Topics on Optical Fiber Technology*. Moh. Yasin, ed. InTech.

[155] Squamous cell carcinoma of the oral cavity, larynx, oropharynx and hypopharynx: EHNS–ESMO–ESTRO Clinical Practice Guidelines for diagnosis, treatment and follow-up† - Annals of Oncology: *https://www.annalsofoncology.org/article/S0923-7534(20)39949-X/fulltext*. Accessed: 2023-04-14.

[156] Stajanca, P. et al. 2016. Effects of gamma radiation on perfluorinated polymer optical fibers. *Optical Materials*. 58, (2016), 226–233. DOI:https://doi.org/10.1016/j.optmat.2016.05.027.

[157] Stevens, S. et al. 2018. An assessment of a 3D EPID-based dosimetry system using conventional two- and three-dimensional detectors for VMAT. *Physica Medica: European Journal of Medical Physics*. 45, (Jan. 2018), 25–34. DOI:https://doi.org/10.1016/j.ejmp.2017.11.014.

[158] Swinnen, A. et al. 2004. Feasibility study of entrance in vivo dose measurements with mailed thermoluminescence detectors. *Radiotherapy and Oncology*. 73, 1 (2004), 89–96. DOI:https://doi.org/10.1016/j.radonc.2004.07.021.

[159] Testicular dose contributed by X-ray volume image-(XVI)-guided intensity-modulated radiotherapy (IMRT) in prostate cancer patients | Hempel | Biuletyn Polskiego Towarzystwa Onkologicznego Nowotwory: *https://journals.viamedica.pl/biuletyn_pto/article/view/68398*. Accessed: 2023-02-06.

[160] The pathobiology of mucositis | Nature Reviews Cancer: *https://www.nature.com/articles/nrc1318*. Accessed: 2023-04-14.

[161] Therriault-Proulx, F. et al. 2018. Effect of magnetic field strength on plastic scintillation detector response. *Radiation Measurements*. 116, March (2018), 10–13. DOI:https://doi.org/10.1016/j.radmeas.2018.06.011.

[162] United Nations Scientific Committee on the Effects of Atomic Radiation 2015. *Sources, Effects and Risks of Ionizing Radiation, UNSCEAR 2012 Report: Report to the General Assembly, with Scientific Annexes A and B*. UN.

[163] Werneck, M.M. et al. 2019. *Plastic Optical Fiber Sensors: Science, Technology and Applications*. CRC Press.

[164] Wootton, L. et al. 2013. Temperature dependence of BCF plastic scintillation detectors. *Physics in Medicine and Biology*. 58, 9 (May 2013), 2955–2967. DOI:https://doi.org/10.1088/0031-9155/58/9/2955.

[165] Xu, C. et al. 2017. Chemoradiotherapy Versus Radiotherapy Alone in Stage II Nasopharyngeal Carcinoma: A Systemic Review and Meta-analysis of 2138 Patients. *Journal of Cancer*. 8, 2 (Jan. 2017), 287–297. DOI:https://doi.org/10.7150/jca.17317.

[166] Yin, Z. et al. 2004. Response corrections for solid-state detectors in megavoltage photon dosimetry. *Physics in Medicine and Biology*. 49, 16 (2004), 3691–3702. DOI:https://doi.org/10.1088/0031-9155/49/16/015.

[167] Zamri, N.A.M. et al. 2017. Setup Uncertainty of Head and Neck Cancer (HNC) patients treated with Image Guided Intensity Modulated Radiotherapy (IG-IMRT). (2017).

[168] Brevet WO2008009917A2 - ...erefor - Google Brevets.pdf.

[169] Décision du 28/02/2023 fixant les modalités du contrôle de qualité des installations de radiothérapie externe et de radiochirurgie. Agence Nationale de Sécurité du Médicament et des produits de santé.

[170] *Medical diagnostic X-ray equipment. Radiation conditions for use in the determination of characteristics:*. BSI British Standards.

[171] Saint-Gobain fibers product sheet.

[172] 2016. *Sources, effects and risks of ionizing radiation: United Nations Scientific Committee on the Effects of Atomic Radiation : UNSCEAR 2012 report to the General Assembly with scientific annexes*. United Nations.

[173] 2011. *Status of Computed Tomography Dosimetry for Wide Cone Beam Scanners*. Technical Report #5. IAEA Human Health Reports n°5.

[174] WO03101528A2_Original_document_20200420110317.pdf.

[175] WO2004043542A1_Original_document_20200420115210.pdf.

[176] WO2008125759A2_Original_document_20200420131334.pdf.

[177] WO2019180380A1_Original_document_20200414153814.pdf.